ISSN 0912-1803

PHOTON FACTORY ACTIVITY REPORT

1993

#11

NATIONAL LABORATORY FOR HIGH ENERGY PHYSICS, KEK

Photon Factory Activity Report 1993

Staff members and visitors of the Photon Factory gathered in front of the PF office building.

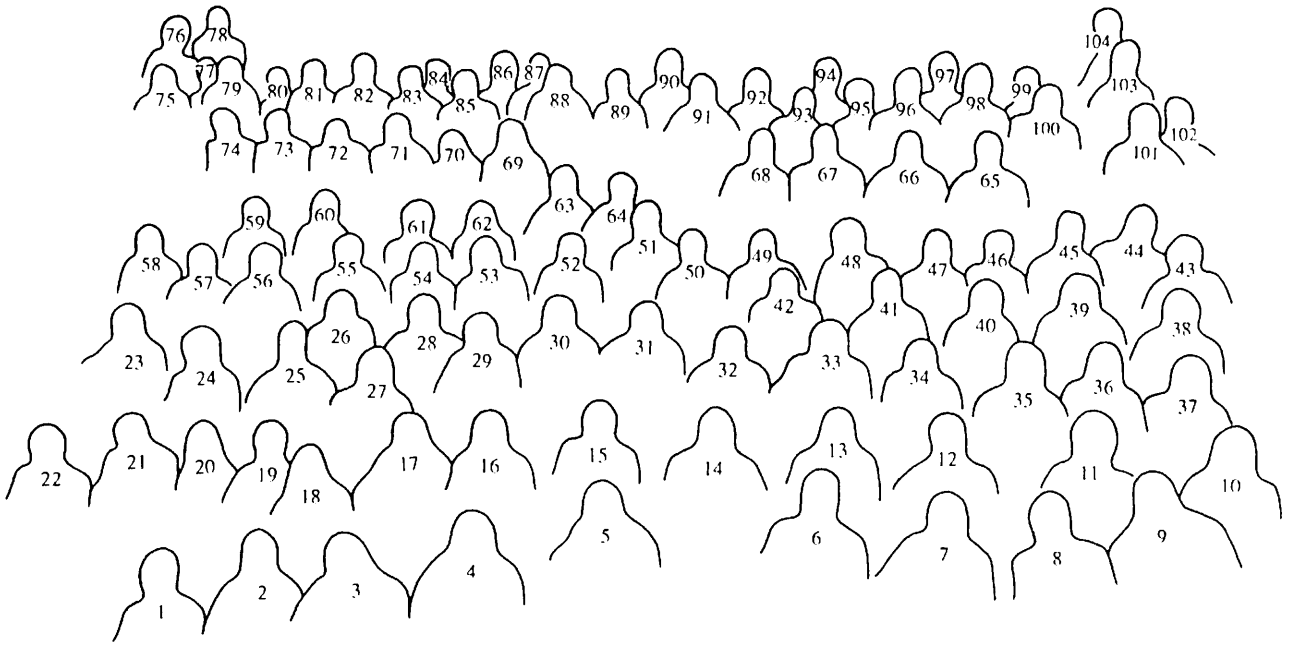

1. K. Nakahigashi
2. H. Ishibashi
3. K. Ohsumi
4. K. Taga
5. H. Kobayashi
6. S. Yamamoto
7. S. Anami
8. K. Nasu
9. T. Miyahara
10. T. Kosuge
11. K. Tamura
12. M. Kobayashi
13. M. Isawa
14. T. Matsushita
15. H. Iwasaki
16. H. Kobayakawa
17. A. Mikuni
18. M. Kimura
19. N. Sakabe
20. Y. Hakuta
21. H. Kitamura
22. I. Sato
23. T. Kikuchi
24. T. Kasuga
25. E. Arakawa
26. T. Oguchi
27. T. Azuma
28. Y. Amemiya
29. K. Hirano
30. T. Kamitani
31. R. Matsuda
32. M. Yokota
33. A. Ueda
34. S. Sakanaka
35. K. Tsuchiya
36. N. Nakamura
37. Y. Takiyama
38. T. Araki
39. K. Ohmi
40. J. Y. Choi
41. T. Kurihara
42. T. Urano
43. Y. Kagoshima
44. H. Sugiyama
45. Y. Sato
46. N. Usami
47. S. Asaoka
48. K. Tanaka
49. K. Kakihara
50. K. Furukawa
51. A. Lazos
52. H. Watanabe
53.
54.
55. H. Maezawa
56. K. Kobayashi
57. S. Kishimoto
58. A. Nakagawa
59.
60. T. Nogami
61. M. Noji
62. A. Kikuchi
63. R. R. Chistyakov
64. H. Kawata
65. C. O. Pak
66. K. Haga
67. I. Abe
68. S. Fukuda
69. M. C. Kida
70. H. Ando
71. M. Tanaka
72. T. Suwada
73. Y. Oku
74. M. Tadano
75. T. Shioya
76. N. Kamikubota
77. T. Honda
78. T. Tsubo
79. S. Tokumoto
80. K. Ito
81. N. Watanabe
82. T. Koide
83. Y. Koyama
84. M. Ando
85. K. Mori
86. M. E. E. Harju
87. B. Mantsyzov
88. T. Mitsuhashi
89. T. Kikegawa
90. Y. Kitajima
91. A. Koyama
92. T. Sekitani
93. Y. Otake
94. T. Hatano
95. K. Iwano
96. Y. Uchida
97. J. D. Wang
98. Y. Kobayashi
99. S. Yamaguchi
100. Y. Hori
101. A. Toyoshima
102. J. Y. Zhon
103. T. Shidara
104. Y. Ogawa

PREFACE

In 1993 the 2.5-GeV injector linac and the 2.5-GeV storage ring of the Photon Factory were operated almost as initially scheduled, and users could carry out various kinds of experiments using synchrotron radiation without any serious cancellation of their beamtime. The total operation time was 5300 hours for the linac and 4900 hours for the ring. Synchrotron-radiation experiments, although in the parasitic mode, were also carried out at the 6.5-GeV TRISTAN Accumulation Ring with successful results.

New projects have been started aimed at upgrading the facilities of the Photon Factory. One is to increase the beam energy of the linac, from 2.5 GeV to 8.0 GeV. This will enable us to inject electrons with full energy into the Accumulation Ring and to provide electrons and positrons having a larger current for the B-Factory experiments for high-energy physics, which are scheduled to begin in 1997 at the TRISTAN Main Ring. The other is to reduce the emittance of the 2.5-GeV ring, and thus, to increase the brightness of the radiation by approximately five times. Additional quadrupole and sextupole magnets will be installed in the ring along with a minor modification of the bean channels.

Eleven years have passed since the construction of the beamlines at an early stage of the operation of the 2.5 GeV ring. Discussions have been made about scrapping and rebuildng of the old beamlines so that they conform to recent progress in synchrotron-radiation science. A facility has recently become available at the ring, in which experiments on radioactive and nuclear materials can be carried out. It is used to study radiation biology and actinide physics.

Planning of experiments using the radiation emitted from an undulator to be in stalled in the TRISTAN Main Ring is in progress. The aim is to measure the emittance of the radiation when the big ring is operated at a beam energy of 10 GeV, and to exploit new possibilities at the 4th-generation ring. These are, however, feasibility studies and the conversion of the Main Ring to the storage ring has been postponed until the B-Factory experiments are finished.

A generator of slow positrons was constructed together with a beam guide utilizing the acceleration facilities at the injector linac. It can be used for studying the momentum distribution of electrons and lattice defects in solids. This is one of the advanced applications of the accelerator being developed at KEK.

The official opening of the Australian National Beamline at BL-20B at the 2.5-GeV ring was made on 15 October, 1993, with the attendance of Mr. C. Schacht, Minister of Science and Small Business, Australia, Mr. T. Amemiya, Deputy Director General, Ministry of Education, Science and Culture, Japan and many other guests. Interesting experimental results of have already been obtained at this beamline.

Prof. T. Kasuga has joined the Light Source Division of the Photon Factory. He will contribute to the progress in studies of the beam dynamics in the storage ring. Prof. N. Sakabe was awarded the Tsukuba Prize for his outstanding contributions to the development of synchrotron-radiation diffraction instruments for protein crystallography.

H. Iwasaki

Director of the Photon Factory

Acknowledgments

The editors would like to thank Ms. Miyako Kimura and Sumie Imai for their help in editing this issue.

KEK Progress Report 94-1 A/M

KEK Reports are available from:

Technical Information & Library
National Laboratory for High Energy Physics
1-1 Oho, Tsukuba-shi
Ibaraki-ken, 305
JAPAN

Phone: +81-298-64-1171
Fax: +81-298-64-4604
e-mail: LIBRARY@KEKVAX.KEK.JP
Telex: 3652-534 (Domestic)
(0)3562-534 (International)
Cable: KEKOHO

CONTENTS

OUTLINE OF THE PHOTON FACTORY

INTRODUCTION

The Photon Factory (PF) is a national synchrotron radiation research facility affiliated with the National Laboratory for High Energy Physics(KEK) supervised by the Ministry of Education, Science and Culture. It is located at the northern end of Tsukuba Science City, which is about 60 km north-east of Tokyo. The PF consists of a 2.5-GeV electron/positron linear accelerator, a 2.5-GeV electron/positron storage ring as a dedicated light source, TRISTAN accumulation ring as a parasitic light source and beamlines and experimental stations for exploiting synchrotron radiation in studies involving such research fields as physics, chemistry, biology, medical sciences, pharmacology, earth sciences and lithography. All of the facilities for synchrotron radiation research are open to scientists of universities and research institutes belonging to the government, public organizations, private enterprises and those of foreign countries. The members of institutions affiliated with the Ministry of Education, Science and Culture are given the highest priority among all users. Applications from other organizations are also admitted.

OVERVIEW OF THE FACILITY

The plan view of the facility is shown in Fig. 1. The 2.5-GeV linac housed in a 450 m long enclosure is used as an injector for both the PF storage ring and the accumulation ring (AR) of TRISTAN main ring. The PF storage ring was already equipped with the flexibility of storing positrons in place of electrons. A part of the AR has been used as a high energy synchrotron radiation source producing radiation from its bending magnet and two insertion devices. One of the insertion devices produces elliptically polarized radiation, and the other highly brilliant radiation in the X-ray region. The AR has been operated for synchrotron radiation users with an energy range from 5.8 to 6.5 GeV.

ORGANIZATION AND STAFF

The organization of KEK is shown in Fig. 2. The PF is composed of three divisions: Injector Linac, Light Source and Instrumentation. A working group has been organized for the design study of the use of the TRISTAN Main Ring for synchrotron radiation science. The organization of the PF including its personnel is shown in Fig. 3. The Advisory Council for the PF was established to discuss scientific programs and management of the PF. The council consists of twenty one senior scientists including ten non-KEK members (Table 1). The term of membership is two years. The Program Advisory Committee (PAC) consisting of the members listed in Table 2 receives proposals of users and decides priorities for the experiments.

In Table 3 the names of the staff members are listed in alphabetical order to help make direct contact. Also, the numbers of staff members and visiting scientists are summarized in Table 4.

BUDGET AND OPERATION TIME

The budget of the PF is supplied by the Ministry of Education, Science and Culture. The annual budget after commissioning of the facilities is shown in Table 5. The numbers of beam channels in each year are shown in Table 6.

The machine operation time is divided into three terms per year. Summary and timetable of the machine operation in FY 1993 are shown in Tables 7 and 8, respectively.

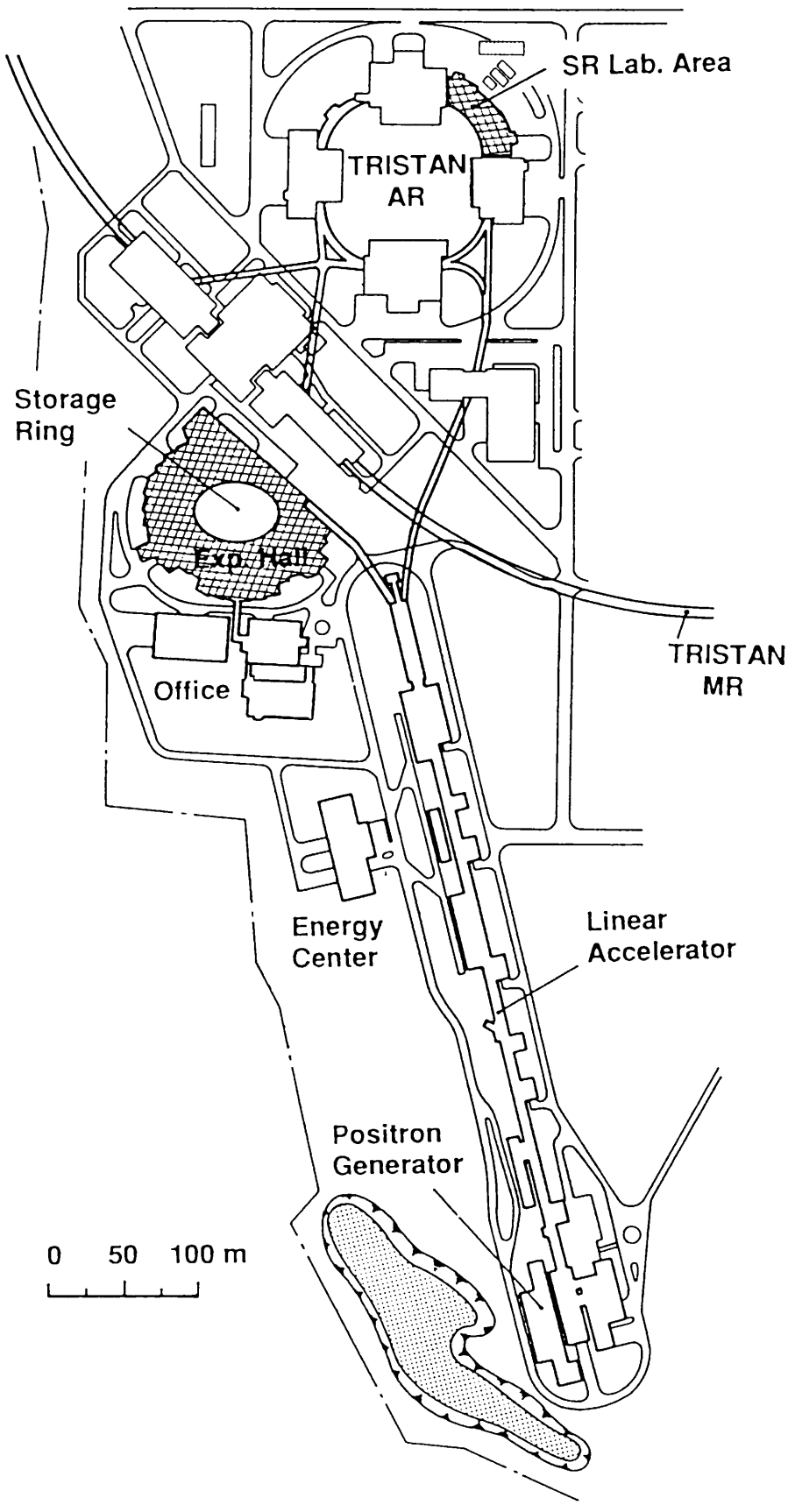

Fig. 1 Plan view of the Photon Factory

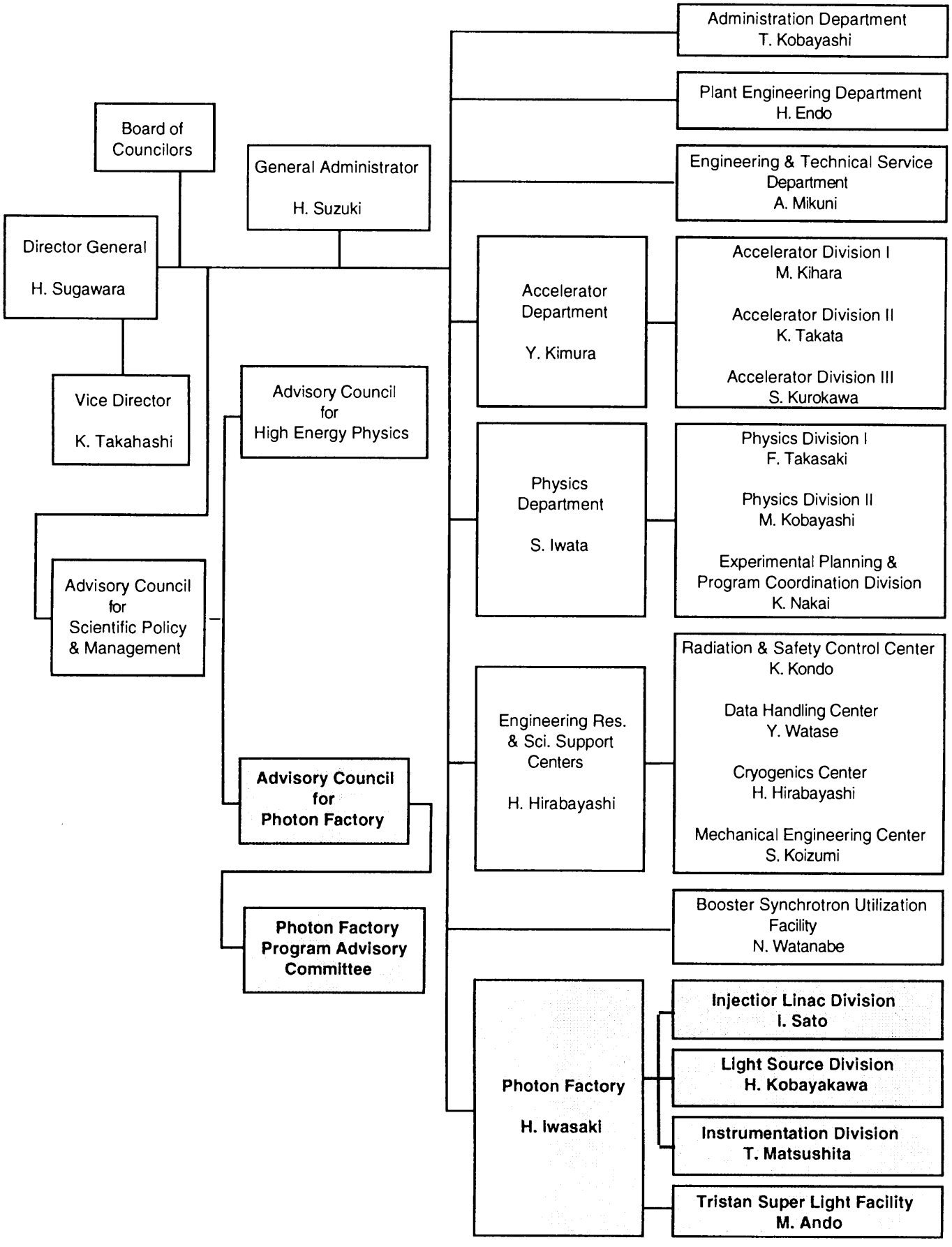

Fig. 2 Organization of KEK

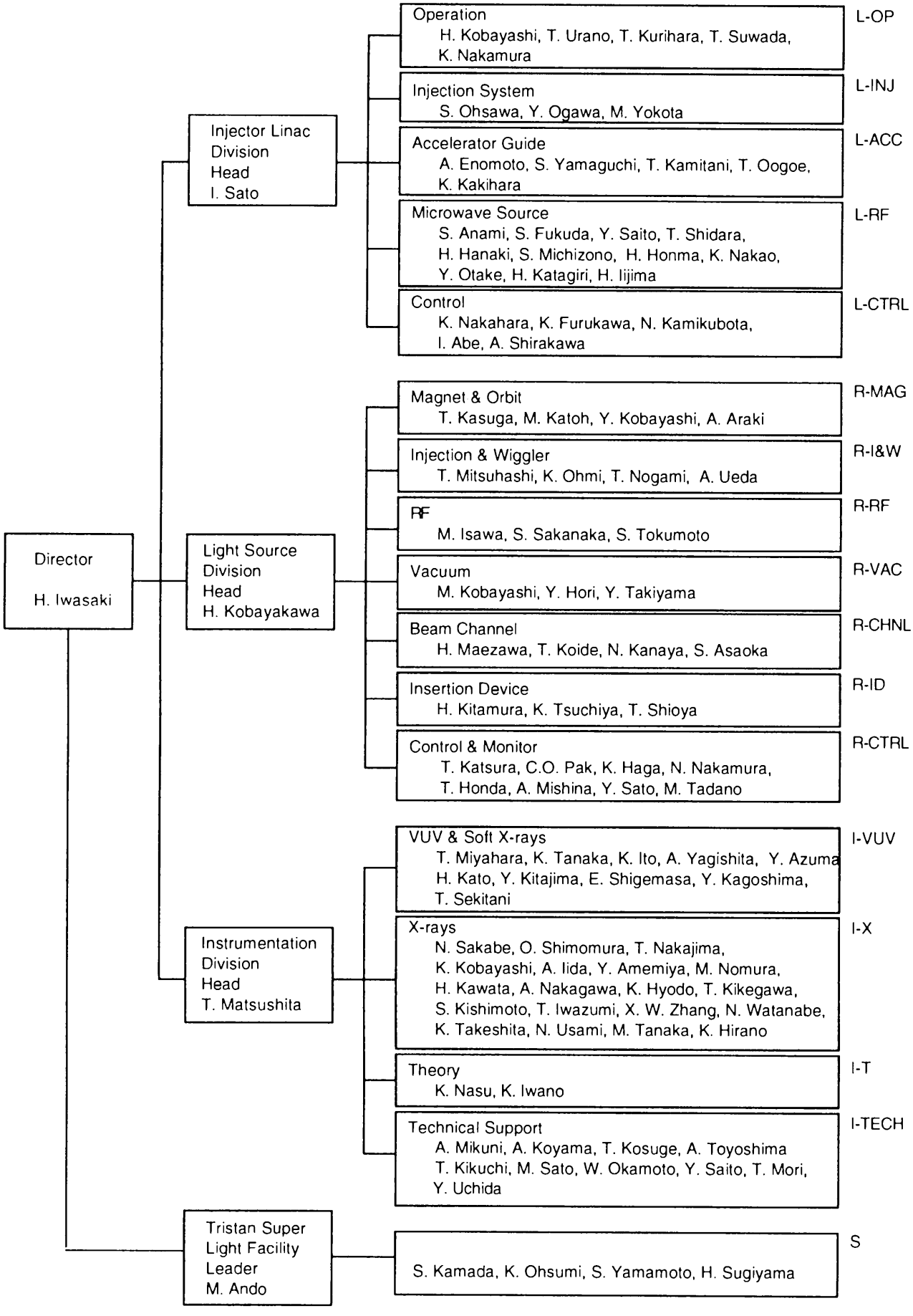

Fig. 3 Organization of the Phton Factory

Table 1 Members of Advisory Council

** Chairman * Vice-Chairman

ANAMI, Shozo	Injector Linac Division, PF, KEK
ANDO, Masami	Tristan Super Light Facility, PF, KEK
FUJII, Yasuhiko	Institute for Solid State Physics, University of Tokyo
HARADA, Jinpei	Faculty of Engineering, Nagoya University
HIEDA, Kotaro	Faculty of Science, Rikkyo University
ISHII, Takehiko*	Institute for Solid State Physics, University of Tokyo
ITO, Kenji	Instrumentation Division, PF, KEK
KATSUBE, Yukiteru	Institute for Protein Research, Osaka University
KIKUTA, Seishi	Faculty of Engineering, University of Tokyo
KOBAYAKAWA, Hisashi	Light Source Division, PF, KEK
KOBAYASHI, Hitoshi	Injector Linac Division, PF KEK
KOBAYASHI, Masanori	Light Source Division, PF, KEK
MAEZAWA, Hideki	Light Source Division, PF, KEK
MATSUSHITA, Tadashi	Instrumentation Division, PF, KEK
NAKAJIMA, Tetsuo	Instrumentation Division, PF, KEK
NITTONO, Osamu	Faculty of Engineering, Tokyo Institute of Technology
OHTA, Toshiaki	Faculty of Science, Hiroshima University
SAKABE, Noriyoshi	Instrumentation Division, PF, KEK
SATO, Isamu**	Injector Linac Division, PF, KEK
SUZUKI, Kenji	Institute for Materials Research, Tohoku University
TOKONAMI, Masayasu	Faculty of Science, University of Tokyo

Table 2 Members of Program Advisory Committee

* Chairman

KOBAYAKAWA, Hisashi	Light Source Division, PF, KEK
KOSUGI, Nobuhiro	Institute for Molecular Sicnece
MATSUSHITA, Tadashi*	Instrumentation Division, PF, KEK
MURATA, Takatoshi	Department of Physics, Kyoto University of Education
NASU, Keiichiro	Instrumentation Division, PF, KEK
OHTA, Toshiaki	Faculty of Science, Hiroshima University
SAKATA, Makoto	School of Engineering, Nagoya University
SATO, Isamu	Injector Linac Division, PF, KEK
SHIMOMURA, Osamu	Instrumentation Division, PF, KEK
SUEMATSU, Hiroyoshi	Faculty of Science, University of Tokyo
TANAKA, Nobuo	Faculty of Bioscience and Biotechnology, Tokyo Institute of Technology
TANIGUCHI, Masaki	Faculty of Science, Hiroshima University
TOKUNAGA, Fumio	Faculty of Science, Osaka University
YAGISHITA, Akira	Instrumentation Division, PF, KEK
YOSHIDA, Satohiro	Faculty of Engineering, Kyoto University
UEKI, Tatsuo	Institute of Physical and Chemical Research

Table 3 Staff members of the Photon Factory; Oct. '92 ~ Sept. '93

Name	Responsibility(*)	e-mail address
Research Staff		
IWASAKI, Hiroshi	Director	
ANAMI, Shozo	L-RF	
ENOMOTO, Atsushi	L-ACC	ENOMOTOA@KEKVAX.KEK.JP
FUKUDA, Shigeki	L-RF	SFUKUDA@KEKVAX.KEK.JP
FURUKAWA, Kazuro	L-CTRL	FURUKAWA@KEKVAX.KEK.JP
HANAKI, Hirofumi	L-RF	HANAKI@KEKVAX.KEK.JP
KAMIKUBOTA, Norihiko	L-CTRL	KAMI@KEKVAX.KEK.JP
KAMITANI, Takuya	L-ACC	KAMITANI@KEKVAX.KEK.JP
KOBAYASHI, Hitoshi	L-OP	HITOSHIK@KEKVAX.KEK.JP
KURIHARA, Toshikazu	L-OP	TKURIHAR@KEKVAX.KEK.JP
MICHIZONO, Shin'ichiro	L-RF	MICHIZON@KEKVAX.KEK.JP
NAKAHARA, Kazuo	L-CTRL	
OGAWA, Yujiro	L-INJ	OGAWAYJ@KEKVAX.KEK.JP
OHSAWA, Satoshi	L-INJ	OHSAWA@KEKVAX.KEK.JP
SAITO, Yoshio	L-RF	
SATO, Isamu	L-Head	
SHIDARA, Tetsuo	L-RF	SHIDARA@KEKVAX.KEK.JP
SUWADA, Tsuyoshi	L-OP	SUWADA@KEKVAX.KEK.JP
URANO, Takao	L-OP	URANO@KEKVAX.KEK.JP
YAMAGUCHI, Seiya	L-RF	SYAMA@KEKVAX.KEK.JP
HAGA, Kaiichi	R-CTRL	HAGA@KEKVAX.KEK.JP
HONDA, Tohru	R-CTRL	HONDAT@KEKVAX.KEK.JP
HORI, Yoichiro	R-VAC	HORI@KEKVAX.KEK.JP
ISAWA, Masaaki	R-RF	ISAWA@KEKVAX.KEK.JP
KANAYA, Noriichi	R-CHNL	KANAYA@KEKVAX.KEK.JP
KATOH, Masahiro	R-MAG	KATOHM@KEKVAX.KEK.JP
KATSURA, Tomotaro	R-CTRL	KATSURA@KEKVAX.KEK.JP
KITAMURA, Hideo	R-ID	KITAMURA@KEKVAX.KEK.JP
KOBAYAKAWA, Hisashi	R-Director	KOBAYAKA@KEKVAX.KEK.JP
KOBAYASHI, Masanori	R-VAC	KOBYASIMR@KEKVAX.KEK.JP
KOBAYASHI, Yukinori	R-MAG	
KOIDE, Tsuneharu	R-CHNL	
MAEZAWA, Hideki	R-CHNL	MAEZAWAH@KEKVAX.KEK.JP
MITSUHASHI, Toshiyuki	R-I&W	MITSUHAS@KEKVAX.KEK.JP
NAKAMURA, Norio	R-CTRL	NORIO@KEKVAX.KEK.JP
OHMI, Kazuhito	R-I&W	OHMI@KEKVAX.KEK.JP
PAK, Cheol On	R-CTRL	PAK@KEKVAX.KEK.JP
SAKANAKA, Shyogo	R-RF	SAKANAKA@KEKVAX.KEK.JP
TSUCHIYA, Kimichika	R-ID	TSUCHIYA@KEKVAX.KEK.JP
AMEMIYA, Yoshiyuki	I-X	AMEMIYA@KEKVAX.KEK.JP
HYODO, Kazuyuki	I-X	HYODO@KEKVAX.KEK.JP
IIDA, Atsuo	I-X	AIIDA@KEKVAX.KEK.JP
ITO, Kenji	I-VUV	ITO@KEKVAX.KEK.JP
IWAZUMI, Toshiaki	I-X	IWAZUMI@KEKVAX.KEK.JP
KAGOSHIMA, Yasushi	I-VUV	KAGOSIMA@KEKVAX.KEK.JP
KATO, Hiroo	I-VUV	HIROO@KEKVAX.KEK.JP
KAWATA, Hiroshi	I-X	KAWATA@KEKVAX.KEK.JP
KIKEGAWA, Takumi	I-X	KIKEGAWA@KEKVAX.KEK.JP
KISHIMOTO, Syunji	I-X	KISIMOTO@KEKVAX.KEK.JP
KITAJIMA, Yoshinori	I-VUV	KITAJIMA@KEKVAX.KEK.JP
KOBAYASHI, Katsumi	I-X	KOBAYASK@KEKVAX.KEK.JP
MATSUSHITA, Tadashi	I-Head	MATSUS@KEKVAX.KEK.JP

Name	Responsibility(*)	e-mail address
MIYAHARA, Tsuneaki	I-VUV	MIYAHARA@KEKVAX.KEK.JP
NAKAGAWA, Atsushi	I-X	NAKAGAWA@KEKVAX.KEK.JP
NAKAJIMA, Tetsuo	I-X	TETSUO@KEKVAX.KEK.JP
NOMURA, Masaharu	I-X	NOMURAM@KEKVAX.KEK.JP
SAKABE, Noriyoshi	I-X	SAKABE@KEKVAX.KEK.JP
SHIGEMASA, Eiji	I-VUV	SIGEMASA@KEKVAX.KEK.JP
TAKESHITA, Kunikazu	I-X	TAKESHIT@KEKVAX.KEK.JP
TANAKA, Ken'ichiro	I-VUV	TANAKAK@KEKVAX.KEK.JP
TANAKA, Masahiko	I-X	MASAHIKO@KEKVAX.KEK.JP
USAMI, Noriko	I-X	USAMI@KEKVAX.KEK.JP
WATANABE, Nobuhisa	I-X	NOBUHISA@KEKVAX.KEK.JP
YAGISHITA, Akira	I-VUV	YAGISITA@KEKVAX.KEK.JP
ZHANG, Xiaowei	I-X	XIAOWEI@KEKVAX.KEK.JP
ANDO, Masami	S-Leader	ANDO@KEKVAX.KEK.JP
KAMADA, Susumu	S	KAMADA@KEKVAX.KEK.JP
OHSUMI, Kazumasa	S	OHSUMIK@KEKVAX.KEK.JP
SUGIYAMA, Hiroshi	S	HIROSHIS@KEKVAX.KEK.JP
YAMAMOTO, Shigeru	S	SHIGERU@KEKVAX.KEK.JP
Supporting Staff		
ABE, Isamu	L-CTRL	ABEI@KEKVAX.KEK.JP
HONMA, Hiroyuk	L-RF	
IIJIMA, Hitoshi	L-RF	
KAKIHARA, Kazuhisa	L-ACC	KAKIHARA@KEKVAX.KEK.JP
KATAGIRI, Hiroaki	L-RF	
NAKAMURA, Kie	L-OP	KIE@KEKVAX.KEK.JP
NAKAO, Katsumi	L-RF	
OOGOE, Takao	L-ACC	OOGOE@KEKVAX.KEK.JP
OTAKE, Yuji	L-OP	OTAKE@KEKVAX.KEK.JP
SHIRAKAWA, Akihiro	L-CTRL	SIRAKAWA@KEKVAX.KEK.JP
YOKOTA, Mitsuhiro	L-INJ	
ARAKI, Akira	R-MAG	
ASAOKA, Seiji	R-CHNL	
MISHINA, Atsushi	R-CTRL	MISHINA@KEKVAX.KEK.JP
NAKAMURA, Hajime	R-CTRL	
NOGAMI, Takashi	R-I&W	NOGAMI@KEKVAX.KEK.JP
SATO, Yoshihiro	R-CTRL	YOSHIHIR@KEKVAX.KEK.JP
SHIOYA, Tatsuro	R-ID	SHIOYA@KEKVAX.KEK.JP
TAKIYAMA, Youichi	R-VAC	
TOKUMOTO, Shuichi	R-RF	TOKUMOTO@KEKVAX.KEK.JP
UEDA, Akira	R-I&W	
KIKUCHI, Takashi	I	KIKUCHI@KEKVAX.KEK.JP
KOSUGE, Takashi	I	KOSUGE@KEKVAX.KEK.JP
KOYAMA, Atsushi	I	KOYAMA@KEKVAX.KEK.JP
MIKUNI, Akira	I	MIKUNI@KEKVAX.KEK.JP
MORI, Takeharu	I	MORIT@KEKVAX.KEK.JP
OKAMOTO, Wataru	I	OKAMOTOW@KEKVAX.KEK.JP
SAITO, Yuuki	I	YSAITO@KEKVAX.KEK.JP
SATO, Masato	I	SATOM@KEKVAX.KEK.JP
TOYOSHIMA, Akio	I	TOYOSIMA@KEKVAX.KEK.JP
UCHIDA, Yoshinori	I	UCHIDA@KEKVAX.KEK.JP

Members who left the PF in this period are also shown, and those who joined in this period will appear in the next issue.

(*) Refer to Fig. 3 for abbreviations.

Table 4 Annual numbers of staff & visiting scientists

Position	Department	1983	1984	1985	1986	1987	1988	1989	1990	1991	1992	1993
Chief Director		1	1	1	1	1	1	1	1	1	1	1
	Injector Linac	3	3	3	4	4	4	3	3	4	3	3
Professor	Light Source	4	4	3	4	4	4	4	5	5	4	5
	Instrumentation	1	1	2	3	4	5	5	5	6	8	9
Associate	Injector Linac	2	2	2	1	2	3	5	7	6	7	7
Professor	Light Source	3	5	5	3	3	3	5	4	3	3	3
	Instrumentation	5	5	8	7	9	7	10	9	8	10	10
Research	Injector Linac	8	9	10	11	10	10	9	8	9	9	9
Associate	Light Source	7	6	8	9	12	12	9	11	11	12	12
	Instrumentation	10	10	10	13	13	14	11	15	15	15	18
Technical	Injector Linac	5	6	6	7	8	9	10	11	11	11	11
Staff	Light Source	6	6	6	7	7	8	10	10	10	10	10
	Instrumentation	2	4	4	8	9	11	10	9	10	10	10
Visiting	Injector Linac	2	2	2	2	2	2	2	2	2	2	1
Scientist	Light Source	4	4	4	4	4	4	4	4	4	4	3
	Instrumentation	6	6	6	6	6	6	6	6	7	6	6
Total		69	74	80	90	98	103	104	110	112	115	118

Table 5 Budget in each fiscal year (in million yen)

Item	1983	1984	1985	1986	1987	1988	1989	1990	1991	1992	1993
Salary	474	484	510	561	561	642	757	764	859	898	939
PF Storage Ring (channel, insertion device, etc.)	0	0	153	131	647	0	0	196	103	0	0
PF Experiments	153	134	184	190	196	237	341	367	399	375	366
PF Operation & Maintenance	477	552	653	820	907	962	1,078	1,107	1,107	1,042	1,015
Computer Rentals	135	135	135	136	136	141	145	145	145	145	145
Positron Source & Electric Plant Operation	0	0	41	138	208	258	300	308	300	253	224
Cooling System & Electric Operation	111	124	180	211	214	217	231	235	240	218	212
Electricity	226	257	338	381	331	355	425	423	423	423	418
PF-Industrial Cooperative Experiments	94	84	95	185	166	302	219	171	174	154	132
AR Construction and Experiments					398	267	387	250	260	148	145
Miscellaneous	134	115	127	162	120	301	243	287	388	564	877
Total	1,804	1,885	2,416	2,915	3,884	3,682	4,126	4,253	4,398	4,220	4,473

Table 6 Yearly account of beam channels

Belonging	1983	1984	1985	1986	1987	1988	1989	1990	1991	1992	1993
PF	8	8	10	12	13	13	15	15	17	20	21
Institutes	0	1	1	1	3	4	4	4	4	3	2
Industry	1	2	4	4	4	4	4	4	4	4	4
Total	9	11	15	17	20	21	23	23	25	27	27

Table 7 Summary of operation in FY 1993 (April 1993 - March 1994) (hours)

Cycle	Linac	PF Ring	Users' time	AR	Dedicated to SR at AR
1	2128	2028	1627	2109	1903
2	1937	1728	1245	1710	1020
3	1235	1152	888	1215	957
Total	5300	4908	3760	5034	3880

Table 8 Timetable of the Machine Operation in FY 1993.

PF : PF ring AR :TRISTAN accumulation ring

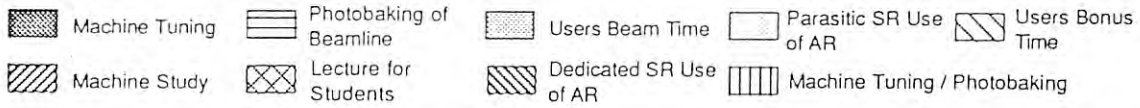

Cycle	Time	MON 9 17	TUE 9 17	WED 9 17	THU 9 17	FRI 9 17	SAT 9 17	SUN 9 17	MON 9 17	TUE 9 17	WED 9 17	THU 9 17	FRI 9 17	SAT 9 17	SUN 9 17	MON 9 17	TUE 9 17	WED 9 17	THU 9 17	FRI 9 17	SAT 9 17	SUN 9 17
1 - 1	Date	4/5	6	7	8	9	10	11	12	13	14	15	16	17	18	19	20	21	22	23	24	25
	Linac																					
	PF																					
	AR																					
1 - 1 / 1 - 2	Date	26	27	28	29	30	5/1	2	3	4	5	6	7	8	9	10	11	12	13	14	15	16
	Linac																					
	PF																					
	AR																					
1 - 2	Date	17	18	19	20	21	22	23	24	25	26	27	28	29	30	31	6/1	2	3	4	5	6
	Linac																					
	PF																					
	AR																					
1 - 3	Date	7	8	9	10	11	12	13	14	15	16	17	18	19	20	21	22	23	24	25	26	27
	Linac																					
	PF																					
	AR																					
1 - 4	Date	28	29	30	7/1	2	3	4	5	6	7	8	9	10	11	12	13	14	15	16	17	18
	Linac																					
	PF																					
	AR																					
2 - 1	Date	9/27	28	29	30	10/1	2	3	4	5	6	7	8	9	10	11	12	13	14	15	16	17
	Linac																					
	PF																					
	AR																					
2 - 1 / 2 - 2	Date	18	19	20	21	22	23	24	25	26	27	28	29	30	31	11/1	2	3	4	5	6	7
	Linac																					
	PF																					
	AR																					
2 - 2 / 2 - 3	Date	8	9	10	11	12	13	14	15	16	17	18	19	20	21	22	23	24	25	26	27	28
	Linac																					
	PF																					
	AR																					
2 - 3	Date	29	30	12/1	2	3	4	5	6	7	8	9	10	11	12	13	14	15	16	17	18	19
	Linac																					
	PF																					
	AR																					
2 - 3	Date	20	21	22	23	24	25	26	27	28	29	30	31	1/1	2	3	4	5	6	7	8	9
	Linac																					
	PF																					
	AR																					
3 - 1	Date	2/7	8	9	10	11	12	13	14	15	16	17	18	19	20	21	22	23	24	25	26	27
	Linac																					
	PF																					
	AR																					
3 - 1 / 3 - 2	Date	28	3/1	2	3	4	5	6	7	8	9	10	11	12	13	14	15	16	17	18	19	20
	Linac																					
	PF																					
	AR																					
3 - 2	Date	21	22	23	24	25	26	27	28	29	30	31	4/1	2	3	4	5	6	7	8	9	10
	Linac																					
	PF																					
	AR																					

SEMINARS, MEETINGS AND PUBLICATIONS

Nine seminars were given by sa staff and visiting cientists who visited the PF in 1993. Ten users' meetings were held in FY 1993, including the annual PF symposium. The PF publishes its quarterly "PHOTON FACTORY NEWS" in Japanese for communication between users and staff.

PF Seminars

West, J. B. (Daresbury Synchrotron Radiation Source)
Experiments in Atomic and Molecular Science at the Daresbury Synchrotron Radiation Source — March 19, 1993

King, G. C. (Department of Physcs, Unversity of Manchester)
Threshold Photoionization Studies of Atoms and Molecules — March 29, 1993

Mitsuhashi, T. (Photon Factory, KEK)
Commissioning of the ESRF — May 12, 1993

Creagh, D. (University College UNSW, Australia)
Atomic Form Factors & Anomalous Scattering Factors — July 21, 1993

Rek, Z. U. (SSRL)
Characterization of YB_{66} Crystals for Use as a New Soft X-ray Monochromator with Synchrotron Radiation — August 20, 1993

Perkins, S. (Royal Free Hospital School of Medicine, University of London)
Recent Developments in Neutron and X-ray Scattering Applied to the Solution Structures of the Complement Proteins of Immune Defence and to Time-Course Studies of the Oxidative Modification of Low Density Lipoproteins — October 5, 1993

Haensel, R. (ESRF)
Synchrotron Radiation Experiment with 3rd Generation Source: New Possibilities, New Challenges — November 16, 1993

Pianetta, P. (SSRL)
X-ray Fluorescence Analysis of Trace Contaminants on Si Wafers — November 17, 1993

Lindau, I. (University of Lund)
High-Resolution Core Level Spectroscopy Using Synchrotron Radiation — November 17, 1993

Users' Meetings

2nd Workshop on Utilization of the MR for a SR Super Brilliant Light Source	January 12-13, 1993
Workshop on High Heat Load in Optical Elements	April 21, 1993
Users' Meeting on Small Angle X-ray Scattering at BL-10C	June 25, 1993
Users' Meeting on BL-2	September 13-14, 1993
Users' Meeting on Structure and Phase Transition of Phospholipid Membrane	November 1, 1993
Users' Meeting on at BL-4C Diffractometer	December 17, 1993
PF Slow-Positron Source Workshop	December 21-22, 1993
The 11th Photon Factory Symposium (Annual Users' Meeting)	January 10-11, 1994
Workshop on the Reconstruction of BL-11 at the Photon Factory	March 14, 1994
Workshop on the Study of Protein Structure by Time-Resolved X-ray Solution Scattering: Present and Perspective	March 23-24, 1994

Publications

PHOTON FACTORY NEWS ISSN 0916-0604 Vol.11, No.1-4

GRADUATE UNIVERSITY FOR ADVANCED STUDIES

The National Graduate University was established in 1988. It has the following three schools:

School of Cultural Studies
School of Mathematical and Physical Sciences
School of Life Sciences.

KEK has participated in the University to form the Department of Synchrotron Radiation Science and the Department of Accelerator Science, both of which belong to the School of Mathematical and Physical Sciences.

Students in the Department of Synchrotron Radiation Science are expected to study the basic theory of emission of synchrotron radiation, its characteristics, and interaction of radiation with matter, and then engage in research by using various facilities at the PF. The research field includes the development of radiation sources, optical elements, and instruments for diffraction, scattering, spectroscopy, and irradiation experiments as well as exploration of new areas of applying synchrotron radiation to science and technology.

PROPOSAL GUIDELINES FOR EXPERIMENTERS AT PHOTON FACTORY

1. HOW TO SUBMIT A PROPOSAL

Photon Factory is open to everybody in scientific research. A proposal should be filed on an application form which is available on request from the Research Cooperation Section of the Administration Department of KEK. An applicant should carefully read the guide before filing an application. A spokesperson should get the agreement of the members to join the team.

An overseas applicant is requested to find an appropriate "contact person in Japan (CPJ)", who will mediate between the applicant and KEK*. Please contact the person in charge of the experimental station you want to use if you do not know any appropriate CPJ. He/She will introduce the person appropriate for the applicant's research plan. A list of the people in charge of the experimental stations can be found in this report.

All experimental proposals are subject to approval of the Photon Factory Program Advisory Committee (PF-PAC). The CPJ will be informed about the decision.

* The contact person in Japan will help you translate Japanese and English, assist with visa applications and your experiments. In order to assure his/her agreement the signature or seal imprint of the CPJ is required.

2. CATEGORY OF PROPOSALS

2.1 For University Researchers etc.

There are four categories of application; G(eneral), S(pecial), P(reliminary) and U(rgent). The character, process of approval and terms of validity are different among those categories.

G is the category for general experiments using synchrotron radiation. Deadlines of application and valid terms are as follows:

Deadlines:
July 8, 1994 (a) and January 13, 1995 (b)
Valid terms:
from October, 1994 to September, 1995 for (a)
from April, 1995 to March, 1997 for (b)

P is the category for preliminary experiments in order to determine the feasibility of proposals for categories G or S and for the new comers in this field. There are some limitations as listed below.

1) The maximum beamtime for one project is less than about 72 hours.
2) One spokesperson can have only one project at a time.
3) More than three proposals of this category cannot be approved for an experimental station at a PF-PAC.

Deadlines:
July 8, 1994 (a) and January 13, 1995 (b)
Valid terms:
from October, 1994 to September, 1995 for (a)
from April, 1995 to March, 1996 for (b)

S is the special category for those experiments that may be difficult to do but may have extremely high scientific value. Among those could be experiments for the development of a difficult technique or those requiring special operation of the storage ring. Photon Factory supports the projects of this category financially within certain limits; the funds cannot be used for travel expenses or salary. At least one Japanese scientist should be included in a team. The process of judgement is different from other categories. An applicant has to express his/her plan orally before the PF-PAC. Deadline and valid term are as follows:

Deadline: late September, 1994
Valid term: from April, 1995 to March, 1998.

The progress report should be presented at the "Photon Factory Symposium" which takes place every year.

U is the category for urgent proposals which cannot be postponed until the next deadline and which are of extremely high scientific value. Once approved, these projects may exclude already assigned beamtime for other projects. Applicants can apply at any time but the valid terms are limited as follows:

a project approved between October and March: until end of March
a project approved between April and September: until end of September.

Results of a project should be reported at the "Photon Factory Symposium."

2.2 For Researchers in Private Companies etc.

Photon Factory is also open for scientists working in private corporations within certain limits. However, a fee is charged for beamtime.

3. ACCOMMODATION

KEK provides guest houses at low cost for visiting scientists. In the case of domestic experimenters, please contact the person in charge of your experimental station. Overseas experimenters should ask the CPJ to book rooms. KEK supports travel and living expenses for domestic experimenters within certain limits but does not do so for overseas experimenters.

4. OTHERS

(1) Experimenters must obey the safety rules at KEK and PF.
(2) Further procedure may be requested in order to carry out an experiment.
(3) If there are question regarding procedures please contact

Research Cooperation Section,
Administration Department,
National Laboratory for High Energy Physics,
Oho, Tsukuba 305, Japan
FAX: +81-298-64-4602.

Table 9 Number of proposals approved by the PAC.

Research Field	1983	1984	1985	1986	1987	1988	1989	1990	1991	1992	1993
(A) EXAFS	42	26	35	40	61	66	57	71	69	67	81
(B) Biology	18	18	28	28	32	38	57	61	75	89	92
(C) X-Ray	24	29	75	54	73	65	61	80	92	109	111
(D) VUV & Soft X-Ray	19	12	27	26	28	28	36	27	45	44	55
Total	103	85	165	148	194	197	211	239	281	309	339

区分 category	G型、P型、S型、U型

高エネルギー物理学研究所放射光実験施設共同利用実験申請書
Application form for synchrotron radiation experiments at Photon Factory (PF)

高エネルギー物理学研究所長殿

申請日 (Date)

実験責任者 Spokesperson

氏名 (Name)　　印 (Signature)

所属、職名 Affiliation Position

連絡先住所 Mailing Address 〒

Tel.　　FAX　　E-mail

下記の通り申請します

実験課題名 Proposal title	(日本語)
	(英訳)

I. 実験組織 team

ローマ字 氏名 Name	所属 Affiliation[1] (大学、学部、学科)	職名[2] Position	電話番号[3] Tel.	PFの利用経験[4] Experience at PF	分担事項 Role in the team

1. 大学院生は所属大学、研究科、専攻　2. 大学院生は課程、学年　3. 内線を含む　4. ステーション名及び習熟度 (excellent, good, fair, poor, none)
欄が不足する場合は同寸別紙に記入の上5枚目に添付

II. 希望ビームタイム schedule

ステーション Station	希望時期 year/month	希望時間[5] beam time
総計 total		

5. 時間または日単位で記入 in units of hours or days

III. 希望ステーションとその理由
(Name of stations and why you chose them)

第1希望

第2希望

第3希望

For overseas applications, describe the contact person in Japan (Name, mailing address, tel. and FAX)

氏名　　印　　Tel.　　FAX

所属、職名

連絡先住所 〒

Office use

受理年月日	※
受理番号	※

List of proposals accepted in FY 1993

Proposal Number	Spokesperson	Title
93-G001	A. Nakamura Faculty of Science, Osaka Univ.	EXAFS studies of metal-ligand bonding of Cd^{II}-peptide complexes
93-G002	M. Hidaka Faculty of Science, Kyushu Univ.	Localized structural analysis of layer compounds by EXAFS
93-G003	M. Ichikawa Catalysis Research Center, Hokkaido Univ.	EXAFS characterization of bimetallic Pd catalysts for freon conversion
93-G004	H. Endo Faculty of Science, Kyoto Univ.	Structure of tellurium-droplets in strongly supercooled liquid states
93-G005	T. Tanaka Faculty of Engineering, Kyoto Univ.	Identification of niobium oxide species in metal oxide matrix
93-G006	I. Watanabe Faculty of Science, Osaka Univ.	XAFS study of nickel hydroxide obtained by electrolytic redox reaction
93-G007	K. Shibata Institute for Materials Research, Tohoku Univ.	EXAFS study about the structure and its influence on amorphous super ionic conductor CuI-Cu_2MoO_4
93-G008	A. Tomita Institute for Chemical Research Science, Tohoku Univ.	A study on the local structure of coal liquefaction catalyst
93-G009	T. Hashimoto Research Laboratory of Engineering, Tokyo Institute of Technology	Analysis of dependence of chemical state of Bi and Pb in $BaPb_{1-x}Bi_xO_{3-5}$ on oxygen nonstoichiometry
93-G010	K. Aika Graduate School at Nagatsuda, Tokyo Institute of Technology	A study on active structures of surface-anchored ruthenium clusters for ammonia-related catalysis
93-G011	S. Suga Faculty of Engineering Science, Osaka Univ.	1s-XANES, EXAFS and MCD of Cu_2Sb and M_xTiS_2
93-G012	T. Murata Kyoto Univ. of Education	EXAFS studies of structure of supercritical state of CB~F_3
93-G013	T. Moriga Faculty of Engineering, Tokushima Univ.	XAFS analysis of additives in ZnO varistors
93-G014	H. Yamashita College of Engineering, Osaka Univ. of Prefecture	EXAFS studies on Fe-based bimetallic catalysts dispersed on carbon

Proposal Number	Spokesperson	Title
93-G015	H. Kanai Faculty of Living Science, Kyoto Prefectural Univ.	Microstructural analysis of the interaction between Ti and Si in the titania-silica mixed oxides prepared by rapid hydrolysis
93-G016	Y. Iwasawa Faculty of Science, Univ. of Tokyo	EXAFS analysis for active structures of advanced tiegler catalysts
93-G017	M. Sakurai Institute for Materials Research, Tohoku Univ.	Local structure of nano-scale Fe cluster produced by ICB deposition
93-G018	S. Emura Institute of Scientific Industrial Research, Osaka Univ.	EXAFS study on coordination of Eu ions
93-G019	H. Kageyama Government Industrial Research Institute, Osaka	XAFS analysis of implanted metal ions in silica glass and alumina
93-G020	T. Miyanaga Faculty of Science, Hirosaki Univ.	Studies of anharmonic potential effect in EXAFS for metal complexes
93-G021	K. Lu Institute of Physics, Chinese Academy of Sciences	XAFS study of some molten oxides and chlorides
93-G022	K. Oki Interdisciplinary Graduate School of Engineering Science, Kyushu Univ.	High pressure fluorescence XANES measurements in Ce alloys
93-G023	M. Adachi Research Institute for Advanced Science and Technology, Univ. of Osaka Prefecture	EXAFS measurement of nanostructured ceramic and metallic materials
93-G024	M. Inui College of General Education, Kyushu Univ.	The local structure of molten silver halide mixtures
93-G025	N. Ishizawa Research Laboratory for Engineering, Tokyo Institute of Technology	EXAFS analysis of Ag-containing glass
93-G026	M. Itoh Institute of Atomic Energy, Kyoto Univ.	EXAFS study on the local structures of CdS, CuCl and ZnTe superclusters
93-G027	E. Huang Institute of Earth Science Academia Sinica	High Pressure studies of diaspore by synchrotron radiation
93-G028	F. Rocca Centro di Fisica S.A.I.I., CNR	EXAFS study on the α-AgI phase stabilized at room temperature in a glass matrix

Proposal Number	Spokesperson	Title
93-G029	T. Ohta Faculty of Science, Univ. of Tokyo	Enhanced anharmonicity in the S-Ni bonds of the c(2×2)S/Ni(110) system
93-G030	I. Nakai Faculty of Education, Tottori Univ.	EXAFS study of amorphous Gd-Y-Ag alloys
93-G031	V. J. James School of Physics, Univ. of New South Wales	Consolidation of proposed structural changes in mammalian collagen and keratin with ageing and disease
93-G032	K. O. Hodgson Department of Chemistry, Stanford Univ.	Stopped-flow time-resolved small-angle X-ray scattering studies of protein folding intermediates
93-G033	Y. Umazume Jikei Univ. School of Medicine	Molecular structure changes in isolated skinned fibers of skeletal muscle
93-G034	M. Kato Institute of Physical and Chemical Research	Small-angle X-ray scattering studies of the solution structure of proteins under high pressure
93-G035	N. Yagi School of Medicine, Tohoku Univ.	An X-ray diffraction study on frog skeletal muscle during shortening
93-G036	T. Hamanaka Faculty of Engineering Science, Osaka Univ.	X-ray diffraction studies on light induced structural change of cephalopods visual cell outer segments
93-G037	A. Ikai Faculty of Bioscience and Biotechnology, Tokyo Institute of Technology	Dynamics of proteinase trapping by α2-macroglobulin
93-G038	T. Fujisawa Institute of Physical and Chemical Research	Structural study on the subunit configuration of olygomeric proteins by using solution X-ray scattering
93-G039	M. Anpo College of Engineering, Univ. of Osaka Prefecture	EXAFS studies on Cu and Ag ions photocatalysts anchored in zeolite
93-G040	K. Ichimura Dokkyo Univ. School of Medicine	Static and kinetic studies on structural change of transferrin on various metal-bindings
93-G041	H. Kihara School of Nursing, Jichi Medical School	Kinetic study on the refolding process of apomyoglobin by stopped-flow X-ray solution scattering, focused on the role of heme
93-G042	K. Wakabayashi Faculty of Engineering Science, Osaka Univ.	Small-angle X-ray scattering studies on actomyosin complex in solution
93-G043	K. Wakabayashi Faculty of Engineering Science, Osaka Univ.	X-ray medium & wide-angle diffraction studies of thin filament during contraction of skeletal muscle

Proposal Number	Spokesperson	Title
93-G044	H. Morimoto Faculty of Engineering of Science, Osaka Univ.	X-ray crystallographic analysis of the coformation change of metal substituted hybrid hemoglobins
93-G045	M. Matsuura Miyagai National College of Technology	XAFS studies on the structural effects of Ga addition in the NdFeB alloys
93-G046	N. Sasaki Muroran Institute of Technology	Studies on mechanical properties of calcified collagen by small angle X-ray diffraction
93-G047	M. Hirai Faculty of Engineering, Gunma Univ.	Structural properties of ganglioside-water system and role in Physiological Function
93-G048	Y. Igarashi Dokkyo Univ. School of Medicine	Structural kinetic studies on the self-assembly of GroEL by using stopped-flow X-ray scattering
93-G049	H. Sakaguchi National Institute of Materials and chemical Research	Self assembly and intermolecular cooperativity of glycerophospholipids
93-G050	N. Miyoshi Fukui Medical School	Development of method of clarification of mechanism in nucleaus DNA damaged by monochromatic X-ray irradiation
93-G051	K. Horiuchi Oita Medical Univ.	Time-resolved X-ray diffraction study on the contraction following photorelease of ATP in skinned muscle fibers
93-G052	N. Sakabe Photon Factory, KEK	Studies on millisecond order dynamics of protein crystal structure using synchrotron radiation
93-G053	M. Hidaka Faculty of Science, Kyushu Univ.	Structural analysis of modified chicken-lysozyme and pokeweed anti-viral protein
93-G054	N. Yasuoka Faculty of Science, Himeji Institute of Technology	Synchrotron radiation study of rubredoxin and related proteins from sulfate reducing bacteria
93-G055	Y. Mitsui Faculty of Engineering, Nagaoka Univ. of Technology	Refined crystal structure of human and murine interferon-β
93-G056	K. Fukuyama Faculty of Science, Osaka Univ.	X-ray crystallographic analysis of cytochrome bc_1 complex
93-G057	Y. Hata Institute for Chemical Research, Kyoto Univ.	X-ray crystal structure analysis of a metalloprotein from *P. aeruginosa*
93-G058	T. Yamane School of Engineering, Nagoya Univ.	Crystal structure analyses of phospholipase A_2 and its isozymes
93-G059	T. Tsukihara Faculty of Engineering, Tokushima Univ.	X-ray crystal structural analysis of a timer protein

Proposal Number	Spokesperson	Title
93-G060	N. Kamiya Institute of Physical and Chemical Research	Crystal structure analysis of nitrile hydratase
93-G061	M. Tanokura Faculty of Science, Univ. of Tokyo	X-ray crystallography of acid proteinase A from *Aspergillus niger* var. *macrosporus*
93-G062	H. Yamaguchi Institute for Protein Research, Osaka Univ.	Cryocrystallography of glutathione synthetase
93-G063	Y. Higuchi Faculty of Science, Himeji Institute of Technology	X-ray crystal analysis of hydrogenase from sulfate reducing bacteria
93-G064	Y. Morimoto Faculty of Engineering, Tokushima Univ.	X-ray structure analysis of monocyte/macrophage colony-stimulating factor (MCSF)
93-G065	K. Miki Research Laboratory Resources Utilization, Tokyo Institute of Technology	Crystallographic studies of energy-conversion proteins in photosynthesis
93-G066	K. Miki Research Laboratory Resources Utilization, Tokyo Institute of Technology	Crystallographic studies of protein subunits of thermus ATPase
93-G067	K. Miki Research Laboratory Resources Utilization, Tokyo Institute of Technology	X-ray crystal structure analysis of streptomyces macromolecular antitumor antibiotic
93-G068	T. Nishioka Institute for Chemical Research, Kyoto Univ.	Crystallographic structure analysis of glutathione synthetase at steady state
93-G069	T. Nonake Faculty of Engineering, Nagaoka Univ. of Technology	Elucidation of catalytic mechanism of 7α-hydroxysteroid dehydrogenase based on X-ray crystal structure analysis
93-G070	E. F. Pai Dept. of Biochemistry, Univ. of Toronto	Crystal structure of xanthine oxidase
93-G071	W. R. Chang Institute of Biophysics, National Laboratory of Macromolecule	Collection of diffraction data of proteins; R-PF, insulin analogue 8 F1-ATPase
93-G072	S. W. Suh Dept. of Chemistry, College of Natural Science, Seoul National Univ.	X-ray crystallographic studies of proteins and enzymes using synchrotron radiation
93-G073	S. K. Burley Howard Hughes Medical Institute, Rockefeller Univ.	High-resolution X-ray diffraction data collection of eukaryotic transcription factors: TBP-2, TBP-1, HNF-3γ, Myn/Max, USF

Proposal Number	Spokesperson	Title
93-G074	J. J. Birktoft Dept. of Biochemistry & Molecular Biophysics, Washington Univ. School of Medicine	X-ray crystallographic study of thermostable malate dehydrogenase and its mutants
93-G075	S. J. Lippard MIT Chemistry Department	X-ray crystallographic studies of methane monooxgenase
93-G076	N. Ishizawa Research Laboratory for Engineering, Tokyo Institute of Technology	Structure analysis of rare-earth tantalum complex oxides utilizing anomalous scattering effects
93-G077	S. Iida Faculty of Science, Toyama Univ.	Development of a high energy X-ray topography and its application to characterization of lattice defects in semiconductor crystals
93-G078	I. Hatta School of Engineering, Nagoya Univ.	Development of the simultaneous measuring system of X-ray diffraction and differential scanning calorimetry
93-G079	K. Kojima Faculty of Liberal Arts and Science, Yokohama City Univ.	Dislocation structure and motion in organic crystals
93-G080	T. Ozaki Faculty of Science, Hiroshima Univ.	X-ray topographic observation of the ferroelectric domain structure in CsH_2PO_4
93-G081	K. Ishida Faculty of Science and Technology, Science Univ. of Tokyo	Polarization analysis of ATS scattering
93-G082	K. Ishida Faculty of Science and Technology, Science Univ. of Tokyo	X-ray diffraction study of strain distributions in ion implanted crystals
93-G083	R. Uno College of Humanities Science, Nihon Univ.	Independent determination of the temperature factor of Ga in a GaAs powder sample
93-G085	T. Hondoh Institute of Low Temperature Science, Hokkaido Univ.	Measurements of dislocation velocities in ice close to the melting temperature
93-G086	M. Tanaka Photon Factory, KEK	Mineral texture analyses by X-ray diffraction
93-G087	T. Ohba School of Science and Engineering, Teikyo Univ.	Crystal structure of Nd-Fe-B composite crystal
93-G088	S. Nojima School of Engineering, Nagoya Univ.	Morphology formation by combined effect of microphase separation and crystallization in an ε-caprolactone-butadiene diblock copolymer

Proposal Number	Spokesperson	Title
93-G089	H. Suematsu Faculty of Science, Univ. of Tokyo	Structural study of fullerene compounds
93-G090	E. Matsubara Institute for Advanced Materials Processing, Tohoku Univ.	Structure study of hydroxide gel by the anomalous X-ray scattering method
93-G091	K. Nakayama National Research Laboratory of Metrology	X-ray wavelength calibration with a compact spectrometer
93-G092	K. Uosaki Faculty of Science, Hokkaido Univ.	Structural study of ferrocenylalkanethiol monolayers on Au electrodes by surface X-ray diffraction
93-G093	K. Ohshima Institute of Applied Physics, Univ. of Tsukuba	Intra- and inter-layer correlation and phase stability in layered compounds
93-G094	K. Aoki National Institute of Materials and Chemical Research	High-pressure powder X-ray diffraction experiments on CO_2
93-G095	N. Shimojo Institute of Community Medicine, Univ. of Tsukuba	Micro analysis of trace elements in biological samples by nondestructive SR-XRF
93-G096	A. Iida Photon Factory, KEK	Characterization of thin film by surface sensitive XRF and reflectometry
93-G097	A. Inaba Faculty of Science, Osaka Univ.	Structure and phase Transition of sulfur hexafluoride monolayer adsorbed on the surface of graphite
93-G098	K. Izumi Faculty of Engineering, Univ. of Tokyo	Structural analysis of metal-silicon interface by X-ray
93-G099	I. Shirotani Muroran Institute of Technology	Phase transitions of phosphorus-arsenic alloys at low temperatures and high pressures
93-G100	T. Yagi Institute for Solid State Physics, Univ. of Tokyo	Development of the high resolution powder X-ray diffraction technique under high pressure using analyzer crystal
93-G101	T. Yagi Institute for Solid State Physics, Univ. of Tokyo	In situ observation of the silicate-metal-water system under lower
93-G102	Y. Katayama Faculty of Science and Technology, Keio Univ.	Structure of isolates selenium chain under pressure
93-G103	H. Kawamure Faculty of Science, Himeji Institute of Technology	Pressure-induced phase transition in sulfur

Proposal Number	Spokesperson	Title
93-G104	A. Matsumuro School of Engineering, Nagoya Univ.	Structure and properties of Mg-based icosahedral quasicrystal under high pressure
93-G105	K. Takemura National Institute for Research in Inorganic Materials	High-pressure powder X-ray diffraction experiments on sodium
93-G106	N. Hamaya Faculty of Science, Ochanomizu Univ.	Mechanism of pressure-induced phase transition in MnF_2
93-G107	H. Miyajima Faculty of Science and Technology, Keio Univ.	Study of Magnetic phase transitions in FeRh and FeRh-Ir alloys by high pressure X-ray diffraction
93-G108	T. Ishikawa Faculty of Engineering, Univ. of Tokyo	X-ray optics for circular polarization using phase retarders
93-G109	T. Takahashi Institute for Solid State Physics, Univ. of Tokyo	Structural studies on Si(111)-Au by surface X-ray diffraction
93-G110	S. Aoki Institute of Applied Physics, Univ. of Tsukuba	Evaluation of grazing incidence focusing mirrors by using partially coherent X-rays
93-G111	T. Masujima School of Medicine, Hiroshima Univ.	Micro-imaging by scintillation effect
93-G112	N. Kamiya Institute of Physical and Chemical Research	Test of double-focusing monochromator for small crystal protein structure analysis
93-G113	K. Ohsumi Photon Factory, KEK	Analysis and refinement of textures and structures of crystals in a microregion
93-G114	S. Ohba Faculty of Science and Technology, Keio Univ.	X-ray structure analyses of ultramicro-magnetic crystals
93-G115	Y. Kashiwase College of General Education, Nagoya Univ.	Study of GIAR-film as nuclear resonance scattering filter
93-G116	K. Mori Japan Atomic Energy Research Institute	Magnetic kerr rotation at X-ray quadrupole scattering from rare earth ferromagnets
93-G118	S. Kikuta Faculty of Engineering, Univ. of Tokyo	Research and development of X-ray optical components for nuclear resonant scattering
93-G119	K. Namikawa Tokyo Gakugei Univ.	Spectroscopic study of 3d transition metal oxide by means of X-ray resonance magnetic scattering

Proposal Number	Spokesperson	Title
93-G120	M. J. Cooper Department of Physics, Univ. of Warwick	Magnetic compton scattering studies of spin density in rare earth and actinide ferromagnetic compounds
93-G121	K. Ishida Faculty of Science and Technology, Science Univ. of Tokyo	Polarization analysis of X-ray magnetic scattering
93-G122	S. Shik Synchrotron Radiation Laboratory, Institute of Solid State Physics, Univ. of Tokyo	Resonant photoemission of Ti oxides
93-G123	K. Ruth Institute of Atomic and Molecular Sciences	Interfacial reactions of Si and Ge grown on modified SiC and diamond surfaces studied by SRPES
93-G124	T. Nakayama Faculty of Science and Technology, Kinki Univ.	Surface modification of ceramics by synchrotron radiation irradiation
93-G125	M. Okusawa Faculty of Education, Gunma Univ.	Transition-metal L emission spectra of transition-metal compounds excited with monochromatized undulator radiation
93-G126	Y. Kagoshima Photon Factory, KEK	Observation of biological specimens by a 50 nm-resolution soft X-ray microscope
93-G127	S. Kravis Institute of Physical and Chemical Research	Production and study of highly-charged photoionized ions
93-G128	S. Nakai Faculty of Engineering, Utsunomiya Univ.	X-ray M emission study of rare earth compounds
93-G129	O. Aita College of Engineering, Univ. of Osaka Prefecture	Resonant X-ray emission spectroscopy in La_2CuO_4 and CuO
93-G130	T. Ohta Faculty of Science, Univ. of Tokyo	Electric conducting properties of organic conductor DMIT salts studied by photoelectron spectroscopy
93-G131	T. Nagata Faculty of Science and Technology, Meisei Univ.	Photoionization processes of rare-earth atoms in the 4d region
93-G132	H. Daimon Faculty of Engineering Science, Osaka Univ.	Photo-stimulated desorption of NO, Cl on Si surface
93-G133	Y. Aiura Electrotechnical Laboratory	Angle-resolved photoemission spectroscopy of $CaTiO_3$, $SrTiO_3$ and $SrVO_3$ Single Crystals
93-G134	H. Sato Faculty of Science, Hiroshima Univ.	Mn 3d partial density of states and p-d hybridization in $Zn_{1-x}Mn_xY$ (Y=S, Se, Te)

Proposal Number	Spokesperson	Title
93-G135	K. Obi Faculty of Science, Tokyo Institute of Technology	Study of photochemical surface reactions by optical emission spectroscopy
93-G136	K. Yoshino Harvard-Smithsonian Center for Astrophysics	High-resolution photoabsorption measurements for molecules of astrophysical and atmospheric importance
93-G137	Y. Azuma Photon Factory, KEK	Non-dipolar effects in the angle resolved photoelectron spectra of rare gases
93-G138	T. Hanyu Faculty of Science, Tokyo Metropolitan Univ.	$M_{2,3}$ magnetic circular dichroism of 3d transition metal-Pd alloys
93-G141	K. Ohshima Institute of Applied physics Univ. of Tsukuba	Study on the short-range ordering in disordered Cu-Pt alloys by DAFS Technique
93-G142	Y. Kubozono Faculty of Science, Okayama Univ.	EXAFS of aromatic radical anions with alkali metals
93-G143	H. Kageyama Government Industrial Research Institute, Osaka	XAFS study on crystallization process of Nd-Fe-B type melt-spun amorphous alloys
93-G144	T. Yamamura Faculty of Science, Science Univ. of Tokyo	XAFS experiment on metallo peptides in terms of zinc finger motifs
93-G145	I. Ouchi Faculty of General Education, Tottori Univ.	Structure of CoCr and CoCrX thin films by means of EXAFS and FY-EXAFS
93-G146	H. Yoshitake Faculty of Engineering, Yokohama National Univ.	Structure transformation of metal fine particle electrodes by UPD alkali metal cation
93-G147	M. Arai Institute for Chemical Reaction Science, Tohoku Univ.	Characterization of supported Pt catalysts prepared by low-temperature reduction
93-G148	H. Wakita Faculty of Science, Fukuoka Univ.	XAFS study on metal-metal interaction of polynuclear metal complexes
93-G149	T. Yamamoto Research Institute for Advanced Science and Technology, Univ. of Osaka Prefecture	Iron EXAFS in nanostructured iron-silver composit materials
93-G150	K. Aika Graduate School at Nagatsuda, Tokyo Institute of Technology	X-ray absorption analysis of the promoting mechanism on ruthenium catalysts modified by thin layer of rare earth metal oxides
93-G151	K. Aika Graduate School at Nagatsuda, Tokyo Institute of Technology	X-ray absorption study on the structure of ruthenium clusters attached to C_{60} with alkali metal dopant for ammonia synthesis

Proposal Number	Spokesperson	Title
93-G152	M. Niwa Faculty of Engineering, Tottori Univ.	Analysis on structure of GeO_2 monolayer prepared by CVD method on metal oxide
93-G153	K. Kikuchi Faculty of Science, Tokyo Metropolitan Univ.	EXAFS study of metallofullerenes
93-G154	T. Kamiyama Faculty of Science, Hokkaido Univ.	EXAFS studies about the growth of Bi_2S_3 microcrystallites in a borate glass matrix
93-G155	Y. Nakamura Faculty of Science, Hokkaido Univ.	P-n transition and local structure in molten semiconductors As_2Te_3-Tl and As_2Te_3-Bi
93-G156	H. Kasatani Shizuoka Institute of Science and Technology	Polarized XAFS study of supercoductive phase transition in $La_{2-x}Sr_xCuO_4$
93-G157	S. Nakajima Faculty of Science, Univ. of Tokyo	Characterization of metallic elements unusually accumulated in marine animals
93-G158	T. Miyanaga Faculty of Science, Hirosaki Univ.	XAFS studies of magnetic Ni-Alloys
93-G159	T. Ohta Faculty of Science, Univ. of Tokyo	Electronic structure of organic conductor dmit salts by polarized XANES
93-G160	I. Watanabe Faculty of Science, Osaka Univ.	Analysis of deposited thin film by electron yield XAFS method
93-G161	A. Morikawa Faculty of Engineering, Tokyo Institute of Technology	Investigation of photo-induced structural change of Rh(I) vaska complex supported on porous vycol glass
93-G162	M. Anpo College of Engineering, Univ. of Osaka Prefecture	XAFS studies on highly active titanium oxide photocatalysts for CO_2 reduction
93-G163	Y. Okamoto Faculty of Engineering Science, Osaka Univ.	Structure of iron oxide clusters fabricated in zeolites
93-G164	Y. Iwasawa Faculty of Science, Univ. of Tokyo	EXAFS study on the structure of Mo_3 attached catalysts and its dynamic change in catalytic reaction conditions
93-G165	Y. Iwasawa Faculty of Science, Univ. of Tokyo	XAFS studies on the d-electron densities of supported Pt catalysts and the behavior of the adsorbed hydrogens
93-G166	I. Nakai Department of Chemistry, Univ. of Tsukuba	Development and application of X-ray atomic absorption spectroscopy

Proposal Number	Spokesperson	Title
93-G167	M. Ichikawa Catalysis Research Center, Hokkaido Univ.	EXAFS study of surface grafted bimetal oxide clusters and their selective catalytic reaction
93-G168	T. Tanaka Faculty of Engineering, Kyoto Univ.	Structure and electronic state of surface complexes of Eu and Yb grafted on oxide supports
93-G169	T. Tanaka Faculty of Engineering, Kyoto Univ.	XAFS analysis of local structure around Ca ions in ettringites
93-G170	S. Yoshida Faculty of Engineering, Kyoto Univ.	Structural analysis of surface species of the catalyst for fixation of carbon dioxide by means of XAFS
93-G171	K. Sakaue School of Science, Kwansei Gakuin Univ.	XAFS study of the local strain in Cu/Ni superlattices
93-G172	S. Emura Institute of Scientific and Industrial, Osaka Univ.	XAFS study of ferrocene and $(\eta^6\text{-}C_6H_6)(\eta^5\text{-}C_5H_5)$ iron (II) complexes
93-G173	S. Emura Institute of Scientific and Industrial, Osaka Univ.	XAFS study of copper complexes in photo degration of nyrol-6
93-G174	T. Mukoyama Institute for Chemical Research, Kyoto Univ.	Investigation of multielectron excitations in K, V, Br, and Mo
93-G175	S. Tsunashima School of Engineering, Nagoya Univ.	Study of structural anisotropy in amorphous TbFe multilayered films via EXAFS
93-G176	M. Sakurai Institute for Materials Research, Tohoku Univ.	XAFS studies on the role of Ti addition for nano-scale-fiber formation in Si-C fiber
93-G177	M. Sakurai Institute for Materials Research, Tohoku Univ.	Local structure change around Ti atom in Al-Ti and Al-Ti-O system powdered by mechanical milling
93-G178	S. Kashino Faculty of Science, Okayama Univ.	Local structure of Superconducting Na_2CsC_{60} by intercalation of ammonia
93-G179	S. Hosokawa Faculty of Science, Hiroshima Univ.	EXAFS study on the photodoping in amorphous chalcogenide semiconductors
93-G180	Y. Kuroda Faculty of Science, Okayama Univ.	Structural analysis of nanospace in solid materials
93-G181	W. Liu China Univ. of Science and Technology	EXAFS studies of metal/semiconductor multilayer

Proposal Number	Spokesperson	Title
93-G182	X. Cai Department of Chemistry, Peking Univ.	Isolation of dispersion phase EXAFS for oxide and salt catalysts
93-G185	Y. Takeda School of Engineering, Nagoya Univ.	Fluorescence EXAFS study on local structure of Fe/Cu multiple layer
93-G186	Y. Takeda School of Engineering, Nagoya Univ.	Fluorescence EXAFS study on local structure of Initial grown layer of heteroepitaxial semiconductor
93-G187	H. Yamaguchi Enactortechnical Laboratory	Local structure in $CuInSe_2$ studied by XAFS
93-G188	M. Izumi Tokyo Univ. of Mercantile Marine	Studies on molecular alignment of pentacene thin films doped with iodine
93-G189	H. Ishida College of Liberal Arts and Sciences, Okayama Univ.	EXAFS studies on the solid-solid phase transition (phase $\alpha' \Leftrightarrow \delta$) in CH_3NH_3I
93-G190	M. Sakurai Institute for Materials Research, Tohoku Univ.	XAFS study on the local structure around In in As_2S_3
93-G191	N. Kojima Faculty of Science, Kyoto Univ.	Study on XANES in the mixed valence compounds $CsAuX_3$ (X=Cl, Br, I) under high pressure
93-G192	T. Matsui School of Engineering, Nagoya Univ.	EXAFS study on local structure of fluoride oxides
93-G193	T. Ohta Faculty of Agriculture, Univ. of Tokyo	Analysis of mechanism of allosteric transition of L-lactate dehydrogenase from Bifidobacterium longum
93-G194	K. Hirotsu Faculty of Science, Osaka City Univ.	X-ray crystallographic analysis of chimeric aminotransfevases
93-G195	Y. Takeda School of Engineering, Nagoya Univ.	Structure determination at the sub-atomic level in semiconductor double heterostructures by X-ray CTR scattering
93-G196	I. Tanaka Faculty of Science, Hokkaido Univ.	Structure analysis of macrophage migration inhibitory factor
93-G197	I. Tanaka Faculty of Science, Hokkaido Univ.	Evaluation of laue data collection method of protein crystal
93-G198	Y. Kai Faculty of Engineering, Osaka Univ.	X-ray crystal structure analysis of metallobiomacromolecules

Proposal Number	Spokesperson	Title
93-G199	K. Hirotsu Faculty of Engineering, Osaka City Univ.	Analysis of reaction mechanism of aminotransferases
93-G200	A. Nakagawa Photon Factory, KEK	Diffraction data collection of protein crystals using long and short wavelength SR
93-G201	M. Kusunoki Institute for Protein Research, Osaka Univ.	X-ray crystal analysis of glucose dehydrogenase
93-G202	N. Tanaka Faculty of Bioscience and Biotechnology, Tokyo Institute of Technology	Structural studies on hydroxylamine oxidoreductase
93-G203	N. Sakabe Photon Factory, KEK	Evaluation and application studies of novel protein data collection system with newly constructed large size of IP reader
93-G204	W. A. Bridger Department of Biochemistry, Univ. of Alberta	The crystal structure of succinyl-CoA synthetase
93-G205	E. N. Baker Department of Chemistry and Biochemistry, Massey Univ.	Determination of the structures of hydrolytic enzymes and mammalian binding proteins by X-ray crystallography
93-G206	A. B. Edmundson Crystallography and Immunology, Harringron Cancer Center	Three-dimensional structures of Immunoglobulins
93-G207	A. Mondoragon Department of Biochemistry, Northwestern Univ.	Structural studies of type I DNA topoisomerases
93-G208	R. J. Fletterick Department of Biochemistry and Biophysics, UCSF	Collection of derivative data for the ligand binding domain of the thyroid hormone receptor
93-G209	D. Ollis Research school of Chemistry, Australian National Univ.	Crystallographic studies of alanine racemase
93-G210	T. Blundell Department of Crystallography, Birkbeck College, Univ. of London	Structure, function and engineering of proteinases
93-G211	J. L. Smith Department of Biological Science, Purdue Univ.	Measurement of diffraction data from crystals of glutamine amidotransferase enzymes
93-G212	R. Stevens Department of Chemistry, Univ. of California	Structural studies of botulinum toxin and botulinum toxin/ganglioside GT1B complex
93-G213	K. Nakamura Showa Univ.	Studies on the three-dimensional structure and reaction mechanism of ribonuclease Rh by time-resolved laue method

Proposal Number	Spokesperson	Title
93-G214	K. Fukuyama Faculty of Science, Osaka Univ.	X-ray crystallographic study of the intermediates of arthromycesramosus peroxidaes
93-G215	H. Morimoto Faculty of Engineering Science, Osaka Univ.	The application of time-resolved laue method to the conformation change of hemoglobin
93-G216	M. Sakata School of Engineering, Nagoya Univ.	Electron densities of hydrogen and boron in crystals
93-G217	Y. Katsube Institute for Protein Research, Osaka Univ.	Time resolved structure analysis of glutathione synthetase by laue method
93-G218	K. Hara Faculty of Engineering, Kyushu Univ.	Time resolved observation of heat- and pressure-treated egg white during gel-to-glasslike transition
93-G219	Y. Inoko Faculty of Engineering Science, Osaka Univ.	Anomalous small-angle scattering experiment of ferritin solution
93-G220	K. Kajiwara Faculty of Engineering and Design, Kyoto Institute of Technology	Biodegradation mechanism of poly (L-lactic acid)
93-G221	A. L. Fink Department of Chemistry & Biochemistry, UCSC	SAXS studies of hsp70 chaperones & compact intermediates of proteins
93-G223	H. Yoshida Faculty of Technology, Tokyo Metropolitan Univ.	Structure formation of polysaccharide-water systems
93-G224	N. Niimura Japan Atomic Energy Research Institute	The initial stage of DNA crystallization Process
93-G225	Y. Izumi Macromolecular Research Laboratory, Yamagata Univ.	Solution structure of calmodulin and expression of function
93-G226	Y. Izumi Macromolecular Research Laboratory, Yamagata Univ.	Dynamic mechanism of thermoreversible gelation of Gellan gum microbial polysaccharide
93-G227	N. Matsushima School of Allied Health Profession, Sapporo Medical College	Solution X-ray scattering of S100 proteins
93-G228	K. Akasaka Faculty of Science, Kobe Univ.	X-ray solution scattering studies on denatured structures of SSI and apomyoglobin
93-G229	M. Watanabe Jikei Univ. School of Medicine	Time-resolved X-ray diffraction study on vertebrate smooth muscles

Proposal Number	Spokesperson	Title
93-G230	H. Tanaka Teikyo Heisei College of Nursing	Time lag between the X-ray intensity change and tension development in muscle contraction
93-G231	T. Hamanaka Faculty of Engineering Science, Osaka Univ.	X-ray structure analysis of the crystalloid in the fire-fly squid photophore
93-G232	H. Sugi School of Medicine, Teikyo Univ.	Mechanism of contraction and relaxation of skeletal muscle as studied by using caged compounds
93-G233	A. Yokoya Japan Atomic Energy Research Institute	Characteristics of degradation of sulfur-containing amino acids in aqueous solution with sulfur K-shell photoabsorption
93-G235	Y. Furusawa National Institute of Radiological Sciences	DNA strand breaks by inner-shell X-ray absorption upon mammalian cells
93-G236	H. Mori School of Medicine, Tokai Univ.	Measurement of myocardial blood flows in small contiguous regions and visualization of small coronary arteiries by monochromatic synchrotron radiation evoked-X ray fluorescence spectrometry
93-G237	K. Shinohara Tokyo Metropolitan Institute of Medical Science	Biological application of x-ray holography
93-G238	T. Takeda Institute of Clinical Medicine, Univ. of Tsukuba	Development of magnified coronary angiography to demonstrate the micro-vessel structures
93-G239	T. Takeda Institute of Clinical Medicine, Univ. of Tsukuba	Development of fluorescence computed tomography for biomedical diagnosis
93-G240	K. Hyodo Photon Factory, KEK	Development of a coronary angiography monochromator system for clinical applications
93-G241	H. Mori School of Medicine, Tokoai Univ.	Visualization of small coronary arteries by monochromatic synchrotron radiation
93-G242	S. Hasegawa Univ. of Elector-Communications	Development of life size energy subtraction X-ray television system for coronary angiography
93-G243	T.C. Qui Kyoto Institute of Technology	Phase behavior and structure analysis of semi- and full-interpenetrating polymer networks obtained by photo-crosslink reactions
93-G244	Y. Izumi Macromolecular Research Laboratory, Yamagata Univ.	Dynamic mechanism of thermoreversible gelation of liquid-crystalline polymer
93-G245	M. Shibayama Kyoto Institute of Technology	Structure formation of network polymers in solutions
93-G246	T. Inoue Faculty of Engineering, Tokyo Institute of Technology	Time-resolved small-angle X-ray scattering studies on the crystallization in polymers

Proposal Number	Spokesperson	Title
93-G247	K. Dusek Institute of Macromolecular Chemistry	Structure and elasticity on inhomogenous polymer network
93-G248	T. Hashimoto Faculty of Engineering, Kyoto Univ.	Order-disorder transition and an ordered structure of a diblock copolymer
93-G249	K. Yamaoka Faculty of Science, Hiroshima Univ.	Development of X-ray small angle electric light scattering method
93-G250	K. Nishikawa Faculty of Education, Yokohama National Univ.	Study of mixing state of solutions with critical point
93-G251	K. Osamura Faculty of Engineering, Kyoto Univ.	Kinetics of phase decomposition with ordering in Al and Ni based alloys
93-G252	Y. Amemiya Photon Factory, KEK	Evaluation of the X-ray polarimeter and its application to measurements of optical activity
93-G253	S. Sasaki Research Lab. of Engineering Materials, Tokyo Institute of Technology	Distribution of ferrous and ferric ions in magnetite
93-G254	S. Sasaki Research Lab. of Engineering Materials, Tokyo Institute of Technology	Structure analysis of a-SiO_x thin-film by X-ray diffraction
93-G255	A. Iida Photon Factory, KEK	Research + development of wavelength dispersive X-ray fluorescence analysis
93-G256	M. Sakata School of Engineering, Nagoya Univ.	Detection of K- or L-electrons by the maximum entropy method
93-G257	Y. Sugishita Institute of Clinical Medicine, Univ. of Tsukuba	Measurement of myocardial heavy metals content in various heart diseases and its relation to cardiac function
93-G258	I. Nakai Department of Chemistry, Univ. of Tsukuba	Ecological study of the fish migration based on the X-ray fluorescence microprobe analysis of otoliths
93-G259	N. Haga Faculty of Science, Himeji Institute of Technology	Microbeam analysis of trace CL activators in carbonatites
93-G260	Y. Gohshi Faculty of Engineering, Univ. of Tokyo	XRF and X-ray excited optical luminescence coincidence measurements
93-G261	Y. Socjima Faculty of Science, Kyushu Univ.	DAFS of the superlattice diffraction from $PbZrO_3$

Proposal Number	Spokesperson	Title
93-G262	K. Honda National Institute of Materials and Chemical Research	X-ray diffraction on very small crystals of tetraalkylammonium-Au(dmit)$_2$
93-G263	K. Kikuchi Faculty of Science, Tokyo Metropolitan Univ.	Crystal structures of higher fullerenes
93-G264	N. Ishizawa Research Lab. of Engineering Materials, Tokyo Institute of Technology	Particle-size dependency on the axial ratio of tetragonal barium titanate micro crystals
93-G265	H. Kasatani Shizuoka Institute of Science and Technology	Study of the low temperature structure in solid C_{60}
93-G266	Y. Kashihara Japan Atomic Energy Research Institute	Development of the method for measuring CTR scattering from inclined surface
93-G267	I. Takahashi School of Engineering, Nagoya Univ.	Effects of electrical and magnetic properties on the structure of rare-earth alloy
93-G268	S. Nikolai Ioffe Physico-Technical-Institute, Academy of Sciences of Russia	Structural study of fluorite-hydrogen terminated Si(III) interface by X-ray CTR scattering technique
93-G269	Y. Waseda Institute for Advanced Materials Processing, Tohoku Univ.	Structural analysis of Zr-Y based amorphous alloys by means of anomalous X-ray scattering
93-G270	S. Minomura Okayama Univ. of Science	Pressure dependence of u-parameter in $AgGaS_2$
93-G271	K. Sugiyama Institute for Advanced Materials Processing, Tohoku Univ.	Structural analysis of ZrO_2-RE_2O_3 amorphous oxides by means of anomalous X-ray scattering
93-G272	T. Fukamachi Saitama Institute of Technology	Dynamical diffraction where the real part of X-ray polarizability is zero
93-G273	N. Kamijo Government Industrial Research Institute, Osaka	Experimental characterization of hard X-ray zone plate
93-G274	S. Nanao Institute of Industrial Science, Univ. of Tokyo	A structural analysis of F-type single quasicrystals by X ray anomalous scattering
93-G275	S. Urakawa Japan Atomic Energy Research Institute	Precise measurement of P-V-T relations of Au and Pt as a pressure scale
93-G276	Y. Chikaura Faculty of Engineering, Kyushu Institute of Technology	Instrumentation research on high resolution X-ray topography using X-ray zooming tube
93-G277	Y. Chikaura Faculty of Engineering, Kyushu Institute of Technology	Observation of thermal behaviour of microdefects in thinned silicon wafers by means of plane-wave SR topography

Proposal Number	Spokesperson	Title
93-G278	H. Kawata Photon Factory, KEK	X-ray topography by mean of X-ray magnetic Bragg scattering
93-G279	H. Kawata Photon Factory, KEK	Site-specific magnetic XANES by mean of a resonant magnetic Bragg scattering
93-G280	Y. Chikaura Faculty of Engineering, Kyushu Institute of Technology	Instrumentation research on SR microbeam scanning X-ray spectroscopy scattering topography
93-G281	K. Namikawa Tokyo Gakugei Univ.	Spectroscopic study of magnetic multilayer films by means of X-ray magnetic resonant scattering
93-G282	K. Sakaue School of Science, Kwansei Gakuin Univ.	Structural study of the Cu/Ni superlattices using anomalous scattering
93-G283	F. Marumo College of Humanities and Sciences, Nihon Univ.	Site preference of transition metal ions in diposide solid solutions
93-G284	K. Uchinokura Faculty of Engineering, Univ. of Tokyo	Structure of spin-peierls phase in a cuprate $CuGeO_3$
93-G285	T. Cho Institute of Physics, Univ. of Tsukuba	Characterization of semiconductor X-ray detectors designed by our new theory
93-G286	I. Nakai Department of Chemistry, Univ. of Tsukuba	Chemical state analyses of light elements on silicates, phosphates, and sulfide minerals by XANES spectra
93-G287	Y. Udagawa Research Ins. for Scientific Measurements, Tohoku Univ.	Structural study of low Z element by X-ray raman spectroscopy
93-G288	K. Itaya Faculty of Engineering, Tohoku Univ.	Structural analysis of electrode surfaces in electrolytic solution by synchrotron X-ray diffraction
93-G289	D. Creagh Physics Department, Univ. of College, UNSW	Magnetic ordering and structural studies in the truly two dimensional : manganese stearate
93-G290	F. Sato Japan Broadcasting Corporation (NHK)	Mechanism of crystallization process of semiconductors with X-ray irradiation
93-G291	K. Uosaki Faculty of Science, Hokkaido Univ.	Structural study of single crystal electrode/electrolyte interfaces by surface X-ray diffraction
93-G292	C. Kennard Department of Chemistry, Univ. of Queensland	The structure of langmuir-blodgett films with frequency doubling properties

Proposal Number	Spokesperson	Title
93-G293	H. Maruyama Faculty of Science, Okayama Univ.	XAS and MCD studies on (TM)Pt_3 (TM=Cr, Mn, Fe, Co) intermetallic compounds
93-G294	M. Ito Faculty of Science, Himeji Institute of Technology	Structural study of magnetic amorphous alloys by X-ray magnetic diffraction
93-G295	A. Onodera Faculty of Engineering Science, Osaka Univ.	Search for a phase transition in wurtzite-type BN at high pressure and temperature
93-G296	K. Yaoita National Institute for Research in Inorganic Materials	Development of an angle-dispersive diffraction measurement system using a radial slit under high pressure
93-G299	T. Akatsuka Faculty of Engineering, Yamagata Univ.	SR imaging with rotating monochromator
93-G301	T. Yamanaka College of General Education, Osaka Univ.	Pressure-induced amorphization of germanium pyroxenes and pyroxenoids
93-G302	H. Kihara Kansai Medical Univ.	Observation of circuits in air with submicron resolution by using X-ray zooming tube
93-G303	H. Maruyama Faculty of Science, Okayama Univ.	DAFS study on local structure of Fe ions in garnet and inverse spinel iron oxides
93-G304	D. Creagh Physics Department, College Univ., UNSW	High pressure studies of MgSiO3 (n% Al_2O_3)
93-G305	D. Creagh Physics Department, College Univ., UNSW	The use of the Australian national beamline in X ray diffraction & scattering experiments
93-G306	T. Matsushita Photon Factory, KEK	Grazing incidence X-ray diffraction study of structure of monolayers at the air/water interface : influence of ions in water
93-G307	H. Fukutani Institute of Physics, Univ. of Tsukuba	Surface electronic states of single-domain Ge(001)-(2×1) and -c(4×2) structures
93-G308	T. Hayaishi Institute of Applied Physics, Univ. of Tsukuba	Observation of post-collision interaction of rare gases using threshold Photoionization methods
93-G309	H. Kobayashi Research Center for Photoenergetics of Organic Materials, Osaka Univ.	Observation of the semiconductor band edge shift by applying bias voltage
93-G310	T. Mitsuishi Facility of Engineering, Utsunomiya Univ.	Core-level resonant potoemission of hevey rere-earth compounds

Proposal Number	Spokesperson	Title
93-G311	E. Shigemasa Photon Factory, KEK	Fixed-molecule photoelectron and Auger-electron angular distributions
93-G312	A. Yagishita Photon Factory, KEK	Studies of angular correlation between fragment-ions from inner-shell excited molecules
93-G313	S. Shin Institute of Solid State Physics, Univ. of Tokyo	Soft X-ray emission and photoemission of transition metal compounds
93-G314	K. Okuno Faculty of Science, Tokyo Metropolitan Univ.	Electron-correlation in inner-shell Photoionization of atoms
93-G315	M. Ukai Faculty of Science, Tokyo Institute of Technology	Dynamic spectroscopy of double excited states and correlation satellites of simple molecules
93-G316	T. Sasaki Japan Atomic Energy Research Institute	Resonant photoemission spectroscopy of TiO_2 and $SrTiO_3$ Surfaces implanted with low-energy ions
93-G317	N. Yamada Univ. of Elector-Communications	X-ray absorption spectroscopy of Y1-xPrxBa2Cu4O8 near oxygen K-absorption edge
93-G318	Y. Ouchi School of Science, Nagoya Univ.	XANES studies in the rubbing effect of polymer films for liquid crystal alignment
93-G319	K. Shinohara Tokyo Metropolitan Institute of Medical Science	Measurements of XANES for biomolecules
93-G320	H. Kimura Institute of Physical and Chemical Research	Evaluation of the polarization characteristics of VUV diffraction gratings
93-G321	T. Sekitani Photon Factory, KEK	Surface photochemical decomposition of organic acids and alcohols by core electron excitation
93-G322	H. Yanagihara Research Ins. for Scientific Measurements, Tohoku Univ.	Development and application of small d-spacing multilayer elements for soft X rays
93-G323	N. Yamaguchi Plasma Research Center, Univ. of Tsukuba	Calibration of soft X-ray spectrometers for plasma diagnostics
93-G324	K. Seki School of Science, Nagoya Univ.	Polarized soft X-ray absorption of well controlled evaporated films of dyes and other organics
93-G325	K. Akimoto Institute of Materials Science, Univ. of Tsukuba	Characterization of II-VI compound semiconductors

Proposal Number	Spokesperson	Title
93-G326	Y. Kitajima Photon Factory, KEK	Measurements of soft x-ray absorption spectra by fluorescence yield detection
93-G327	K. Ito Photon Factory, KEK	High-resolution absorption measurements O_2 Rydberg series
93-G328	S. Okano Faculty of Science, Tohoku Univ.	Absorption profile measur is using hydrogen/deuterium absorption cells at 121,566/121,533 nm
93-G329	N.Ueno Faculty of Engineering, Chiba Univ.	Sift specific photochemical decomposition of organic solids by core electron excitation
93-G330	A. Nishijima National Institute of Materials and Chemical Research	Study on high resolution XAFS and XPS using soft X-ray from undulator
93-G331	A. Yokoya Japan Atomic Energy Research Institute	Characteristics of degradation of biological molecules with inner-shell photoabsorption of carbon, nitrogen and oxygen
93-G332	T. Mizoguchi Faculty of Science, Gakushuin Univ.	Study of NEA surface of GaAs spin polarized photo-electron source
93-G333	A. Kakizaki Institute for Solid State Physics, Univ. of Tokyo	Photoelectron spectroscopy of single crystals of rare earth (R) compounds (RB_6)
93-G334	T. Kinoshita Institute for Solid State Physics, Univ. of Tokyo	Photoelectron spectroscopy of Ce/Si interface
93-G335	A. Fujimori Faculty of Science, Univ. of Tokyo	Spin-polarized photoemission of transition-metal chalcogenide itinerant ferromagnets
93-G336	A. Kakizaki Institute for Solid State Physics, Univ. of Tokyo	Surface ferromagnetism of non ferromagnetic transition metal
93-G337	A. Kakizaki Institute for Solid State Physics, Univ. of Tokyo	Angle resolved spin polarized photoemission spectroscopy of Ni single crystal
93-G338	T. Kinoshita Institute for Solid State Physics, Univ. of Tokyo	Low temperature measurements of the ferromagnetic materials by spin-polarized photoemission
93-G339	K. Ito Photon Factory, KEK	Measurements of the kinetic energy distributions and the angular distributions of dissociation fragments produced by the outer shell electron excitation of diatomic molecules
93-G340	T. Koide Photon Factory, KEK	Magnetic circular dichroism of 3d transition metal oxides and halides and of valence-fluctuated Ce compounds

Proposal Number	Spokesperson	Title
93-G341	A. Fujimori Faculty of Science, Univ. of Tokyo	Photoemission magnetic circular dicroism from ferromagnetic transition-metal compounds
93-G342	H. Miki Faculty of Science and Technology, Science Univ. of Tokyo	Chemisorption state of NO on Pt surfaces
93-G343	S. Imada Faculty of Engineering Science, Osaka Univ.	Magnetic circular dichroism in XAS and XPS of ferromagnets
93-G344	J. T. Bolin Department of Biological Science, Purdue Univ.	Measurement of high resolution diffraction data from crystals of nitrogenase and other metalloproteins
93-P002	T. Hamanaka Faculty of Engineering Science. Osaka Univ.	Structural study of biological substances by circulary polarized synchrotron radiation
93-P003	T. Hashimoto Faculty of Engineering, Kyoto Univ.	Order-disorder transition and an ordered structure of a diblock copolymer
93-P004	T. Hinoue Faculty of Science, Osaka Univ.	Examination on enhancement of X-ray phtopyroelectric signal *in vacuo*
93-P005	T. Yamasaki Himeji Institute of Technology	Structural study of decomposition of metal-hydrides during heating at high pressures
93-P006	K. Kato National Institute for Research in Inorganic Materials	Structure determination of $Pb_{11}Ge_3O_{17}$
93-P007	H. Kobayashi Research Center for Photoenergetics of Organic Materials, Osaka Univ.	Observation of the semiconductor band edge shift by applying bias voltage
93-P008	S. Shin Institute for Solid State Physics, Univ. of Tokyo	The study of the local structures in the perovskite-type protonic conductors
93-P009	Saito Faculty of Science Tohoku Univ.	Local Structure and superconductivity in $La_{2-y-x}Nd_ySr_xCuO_4$
93-P010	H. Yamada School of Engineering, Okayama Univ.	A role of the hydrogen network on the β-sheet of chicken lysozyme
93-P011	M. Imai Institute for solid state physics, Univ. of Tokyo	Structural formation during induction period of crystallization of polyethylene terephthalate
93-P012	K. Nakahigashi College of Integrated Arts and Science, Univ. of Osaka Prefecture	Electron density distribution in δ-Cr

Proposal Number	Spokesperson	Title
93-P013	A. Yasuda Earthquake Research Institute, Univ. of Tokyo	Viscosity measurement of silicate melt at high pressure
93-P014	M. Itoh Institute of Atomic Energy, Kyoto Univ.	Measurement of the coherence of soft X-ray undulator radiation by photon correlation spectroscopy
93-U001	H. Suematsu Faculty of Science Univ. of Tokyo	Study of crystal structure of endohedral fullerene La@C_{82}
93-U002	K. Kikuchi Faculty of Science Tokyo Metropolitan Univ.	The EXAFS study of LaC_{82}
93-Y001	K. Izumi NTT	Msaterials analysis, lithography and photo-reaction using SR
93-Y002	T. Kobayashi Cnetral Research Institute, Mitsui Toatsu Chemicals, Inc.	XAFS analysis of mixture of metalo phtalocyanine and other metal complexes
93-Y003	M. Miyao Center Research Laboratory, Hitachi Ltd.	BL-8A; Soft X-ray diffractometry, XPS. B; Silicon EXAFS experiments, total reflection measurement. C; Digital radiography, lithography, microprobe experiments, and micro X-ray diffractometry
93-Y004	M. Ohtsuki Fujitsu Laboratories Ltd.	Exposure tests by synchrotron radiation in BL-17A, BL-17B, and BL-17C
93-Y005	T. Onoda Mitsubishi Kasei Corpration	The structual analysis of Ni complexes by XAFS
93-Y006	Y. Goto Fundamental Research Lab., NEC Corp.	Soft-X ray lithography, photo-chemical reaction experiments and X-ray optics
93-Y007	K. Inaba Cosmo Research Institute	EXAFS study of Co(Ni)-Mo/Al_2O_3 desulphurization catalysts
93-Y008	M. Miyao Center Research Laboratory, Hitachi Ltd.	BL-8A; Soft X-ray diffractometry, XPS. B; Silicon EXAFS experiments, total reflection measurement. C; Digital radiography, lithography, microprobe experiments, and micro X-ray diffractometry
93-Y009	M. Ohtsuki Fujitsu Laboratories Ltd.	Exposure tests by synchrotron radiation in BL-17A, BL-17B, and BL-17C
93-Y010	Y. Goto Fundamental Research Lab., NEC Corp.	Soft-X ray lithography, photo-chemical reaction experiments adn X-ray optics
93-Y011	T. Onoda Mitsubishi Kasei Corpration	The structural analysis of Ru-Zn catalysts by XAFS
93-Y012	T. Kobayashi Cnetral Research Institute, Mitsui Toatsu Chemicals, Inc.	Characterization of Cu-Zn-Al catalysts by XAFS

Proposal Number	Spokesperson	Title
93-C001	Y. Ohishi Tsukuba Research Laboratory, Sumitomo Chemical Co., Ltd.	Small angle X-ray scattering study for dynamical structural change of polymers
93-C002	K. Akimoto Fundamental Research Lab., NEC Corp.	Characterization of semiconductor materials by high precision X-ray goniometer system
93-C003	S. Suzuki Tsukuba Research Center, Sanyo Electric Co., Ltd.	Microfabrication technique using synchrotron radiation
93-C004	Y. Takagi Nippon Steel Corp.	Dynamic observation of materials processing using synchrotron radiation
93-C005	A. Aoki Technical research Center, NKK Corp.	Structure analysis of materials bombarded with particle beams
93-C006	H. Nagata Nikon Corp.	Reflectivity measurement of Mo/Si multilayers
93-C007	K. Hayashi Nippon Steel Corp.	Quantitative materials evaluation by monochromatic X-ray CT using synchrotron radiation
93-C008	S. Yasuami ULSI Research Center, Toshiba Corp.	Characterization of semiconductor materials by means of X-ray diffraction and scattering
93-C009	S. Nakagawa Kawasaki Heavy Industries Ltd.	Developments of in-vacuum damping wigglers
93-C010	S. Kawado Research Center, Sony Corp.	Characterization of crystaldefects and surface states of semiconductor crystals
93-C011	T. Shima Development Center, Konika Corp.	Study on structure of photographic silver halide microcrystals using high resolution X-ray powder diffraction
93-C012	N. Ishikawa Petroleum Energy Center	EXAFS study on hydrodesulfurization catalysts for ultra low sulfur distillate
93-C013	S. Tani Power Reactor and Nuclear, Fuel Development Corp.	Research and development of an intense CW electron liner
93-C014	H. Hashimoto Toray Research Center	Development of gas-flow total electron yield detection system for XAFS measurement
93-C015	H. Ayato Fuji Photo Film Co., Ltd.	Local structure analysis of photographic silver halides
93-C016	M. Matsumoto Mechanical Research Lab., Hitachi Ltd.	Reduction of photodesorption with surface conditions of Practical materials

Proposal Number	Spokesperson	Title
93-C017	T. Arikado ULSI Research Center, Toshiba Corp.	Photo-induced processing of semiconductors using system synchrotron radiation
93-C018	Y. Oku Kawasaki Heavy Industries, Ltd.	Design of storage ring dedicated to medical applications
93-C019	M. Yamaguchi Toyama Co., Ltd.	Design study of beamline using super brilliant synchrotron radiation
93-C020	M. Nishiura Tigold Cop.	Surface properties of ceramic thin films
93-C021	J. Suzaki Denki Kagaku Kogyo Co. Ltd.	Structrural study of mulite under hgih pressure and high temperature
93-C022	Y. Tsutsui Sumitomo Heavy Industries, Ltd.	Basic study of photon storage ring

G : General
P : Preliminary
U : Urgent
Y : Approved for charged beam time.
C : Collaborations between the Photon Factory and institutes of private companies.

Injector Linac

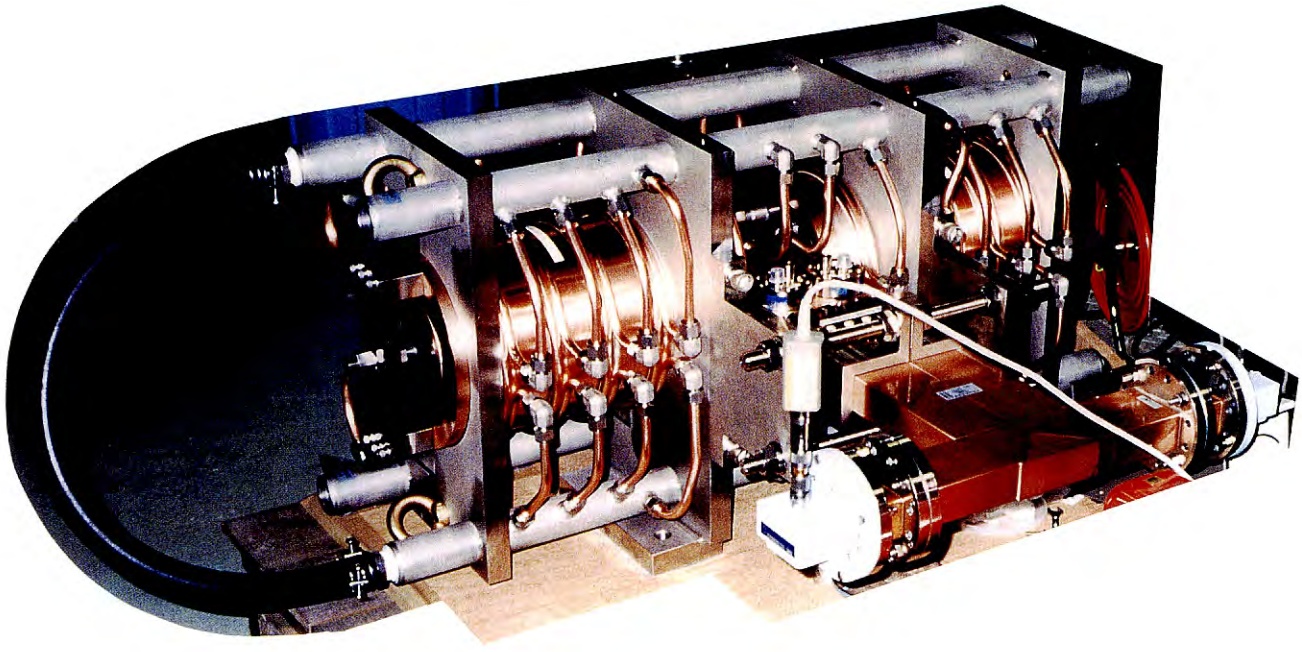

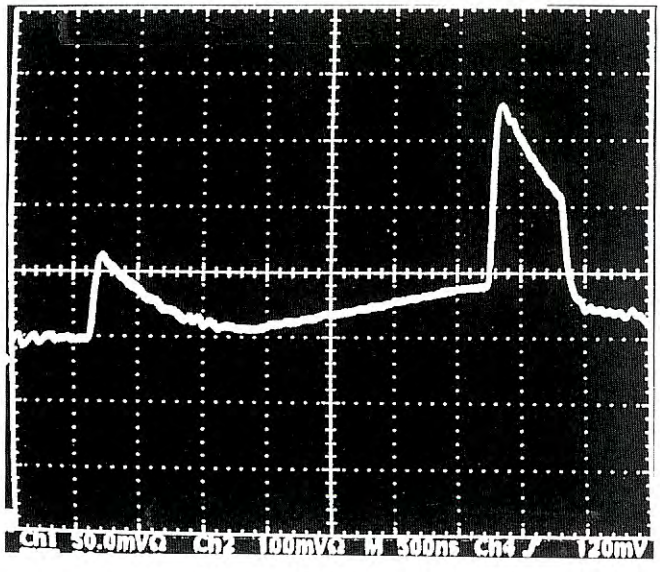

A SLED cavity (upper) and an output waveform from the SLED cavity (see section D).

CONTENTS

A. INTRODUCTION

The operation of the PF 2.5-GeV linac has been satisfactorily performed.

The minicomputers for the linac control system, which has been used more than ten years, have been replaced. The newly installed control system has started operation.

In the KEK B-Factory(KEKB) project, the beam energy of the electron and positron beams is to be increased from 2.5 GeV to 8 GeV and from 2.5 GeV to 3.5 GeV, respectively. The required positron beam intensity is 20-times as intense as the present one as well as a large upgrade in energy.

A single-bunch beam of both electrons and of positrons is to be injected in the KEKB project. The single-bunch beam from the upgraded linac should be injected into the KEKB rings with a time accuracy of better than 30 ps. In order to make efficient use of the present resources of the linac and of the TRISTAN ring, the operation frequency for the linac and the rings are to be fixed at the present one: 2856 MHz for the linac and 508.58±0.3 MHz for the rings, respectively. In order to synchronize these two large accelerators, a special master oscillator and a trigger system are required, and are thus being investigated.

These new demands require much R&D. R&D details concerning the energy upgrade, single-bunch beam acceleration, the vacuum system and the beam monitors are described in this issue.

The acceleration of high-current single-bunch beams has started to show how the wakefield affects the beam stability.

Research regarding the generation of an intense slow positron beam has progressed aiming at generating a slow positron beam with an intensity of $10^9 e^+$/sec.

B. OPERATION

During the period from October, 1992, to September, 1993, the linac has been stably operated with a total operation time of 5,120 hours and a high operation rate of 98.7%. The operation statistics for this period are listed in Table 1. There were no severe failures which took a comparatively long recovering time during this run.

The averaged fault rate with the averaged applied anode voltage during these eight years and the cumulative usage hours of klystrons are given in Table 2 and 3, respectively. The cumulative status of the klystrons up to the end of this term is summarized in Table 4.

Table 1. Operation and failure time during this period

	date	operation time (hrs)	failure time (hrs)	rate (%)
FY 1992	Sep. 28-Nov. 11	1039	34.1	96.7
	Nov. 17-Dec. 21	800	9.8	98.8
	Feb. 8-Mar. 29	1153.5	6.4	99.5
FY 1993	Apr. 5-May 1	618	4.5	99.3
	May 6-June 2	636	5.0	99.2
	June 7-July 14	874	5.1	99.4
total		5120.5	64.9	98.7

Table 2. Averaged fault rate and averaged applied voltage to klystrons.

Period	Fault rate (/day·tube)	Applied voltage (kV)	Total operation (tube·days)
1985/8-1986/7	1.0	238	5,600
1986/8-1987/7	1.0	239	7,740
1987/8-1988/7	1.0	240	9,990
1988/8-1989/7	0.6	241	10,510
1989/8-1990/7	0.3	244	10,690
1990/8-1991/7	0.2	246	10,750
1991/8-1992/7	0.1	248	10,140
1992/8-1993/7	0.1	247	10,010

Table 3. Cumulative usage hours of the klystrons during the past years.

Period	Total No.of tubes	Unused No.of tubes	Failed No.of tubes	Failed Mean age (hours)	Living No.of tubes	Living Av.op.time (hours)	MTBF (hours)
up to 1985/7	79	2	28	3,600	49	6,200	13,400
up to 1986/7	91	3	39	4,400	49	7,400	13,100
up to 1987/7	106	4	52	4,400	50	9,600	13,600
up to 1988/7	120	2	67	4,500	51	11,400	13,500
up to 1989/7	140	5	82	6,400	53	12,400	14,400
up to 1990/7	158	6	98	8,500	54	11,200	14,700
up to 1991/7	176	14	107	10,100	55	11,100	15,800
up to 1992/7	191	24	113	10,800	54	13,400	17,100
up to 1993/7	203	19	123	10,800	56	15,300	17,700

Table 4. Cumulative status of klystrons up to July 1993 corresponding to the year of production. Unused tubes are those which have never been used in the klystron gallery. STB(stand-by) tubes are those which have been used in the gallery and can be used there again.

Year of production	Cathode	Total No.of tubes	Unused No.of tubes	Living No.of tubes	(STB	Working) e-	e+	Av.op.time (hours)	Failed No.of tubes	(arcing	Causes window	others)	Mean age (hours)	Cumulative operation (tube-hours)	MTBF (hours)
1979	oxide	4	0	0	(0	0	0)	------	4	(2	1	1)	3,902	15,608	3,902
1980	oxide	20	0	1	(1	0	0)	3,657	19	(13	5	1)	9,050	175,606	9,242
1981	oxide	20	0	1	(1	0	0)	11,277	19	(11	2	6)	15,965	314,611	16,588
1982	oxide	9	0	1	(1	0	0)	2,120	8	(5	2	1)	10,054	82,549	10,317
1983	oxide	13	0	1	(1	0	0)	14,170	12	(6	2	4)	18,753	239,205	19,934
1984	oxide	13	1	0	(0	0	0)	------	12	(10	0	2)	9,950	119,401	9,950
1985	oxide	12	1	0	(0	0	0)	------	11	(7	0	4)	13,409	147,494	13,409
1986	oxide	15	0	1	(1	0	0)	11,568	14	(13	0	1)	3,524	60,910	4,351
1987	oxide	7	0	0	(0	0	0)	------	7	(5	1	1)	4,342	30,393	4,342
	total	113	2	5	(5	0	0)	8,558	106	(72	13	21)	10,783	1,185,777	11,187

Year of production	Cathode	Total No.of tubes	Unused No.of tubes	Living No.of tubes	(STB	Working) e-	e+	Av.op.time (hours)	Failed No.of tubes	(arcing	Causes window	others)	Mean age (hours)	Cumulative operation (tube-hours)	MTBF (hours)
1987	BI	7	0	5	(0	5	0)	27,857	2	(0	1	1)	16,748	172,782	86,391
1988	BI	20	1	15	(3	9	3)	20,393	4	(0	3	1)	12,814	357,153	89,288
1989	BI	18	1	11	(0	10	1)	19,194	6	(0	5	1)	10,525	274,284	45,714
1990	BI	18	6	9	(1	7	1)	12,568	3	(0	2	1)	8,902	139,817	4
1991	BI	15	8	5	(0	4	1)	4,106	2	(0	2	0)	2,843	26,216	1
1992	BI	12	6	6	(0	5	1)	3,652	0	(0	0	0)	-----	21,913	
	total	90	17	51	(4	40	7)	15,919	17	(0	13	4)	10,605	992,165	5
	total	203	19	56	(9	40	7)	15,262	123	(72	26	25)	10,758	2,177,942	1

C. PROGRESS AND IMPROVEMENTS

1. CONTROL SYSTEM

1.1 Replacement of Minicomputers for Linac Control

The PF 2.5-GeV linac was operated with the old control system, which comprised eight minicomputers (Mitsubishi MELCOM 70/30) and hundreds of microcomputers. Since Mitsubishi has discontinued support for the MELCOM 70/30 system, we decided to replace the minicomputers and their associated fiber-optic network (LOOP-I) with a new system. We are continuing to use microprocessor-based device controllers with low-level communication networks (LOOP-II, LOOP-III). This replacement was carried out in the summer shutdown of 1993, and the new system started operation in September, 1993.

The new control system comprises four components:

(a) A TCP/IP network used as a high-speed communication network, (b) Unix-based workstations used as resource servers, (c) VME-bus-based systems used as front-end stations, and (d) microprocessor-based device controllers and the low-level communication networks. The correspondence between the old and new control systems is given in Table 5. The hardware architecture of the new system is shown in Fig. 1.

Table 5. Correspondence between the old and the new control systems.

component	old system	new system
server (for console)	MELCOM 70/30 Realtime OS	Unix workstations Unix
network (response)	LOOP-I (5Mbps) 100 ms	TCP/IP(Ethernet) (10Mbps) 1-10 ms
front-end	MELCOM 70/30 CAMAC	Force CPU-40 68040,25MHz VME-bus
low-level net.	LOOP-II,LOOP-III	LOOP-II,LOOP-III
device controller	μprocessor-based	μprocessor-based

We currently use three Unix-based workstations. One (DECstation 5000, named peach) is used as a server to provide other workstations and VME systems with huge disks. The others (DECstation 5000 named maple, and disk-less DECstation 5000 named lime) are used for software development and VME systems (Force CPU-40, 68040) with the OS-9 operating system are used as new front-end systems. A VME system is placed in each subcontrol room, which is located every 80 meters along the linac. Low-level communication networks (LOOP-II and LOOP-III) are now connected to the VME system.

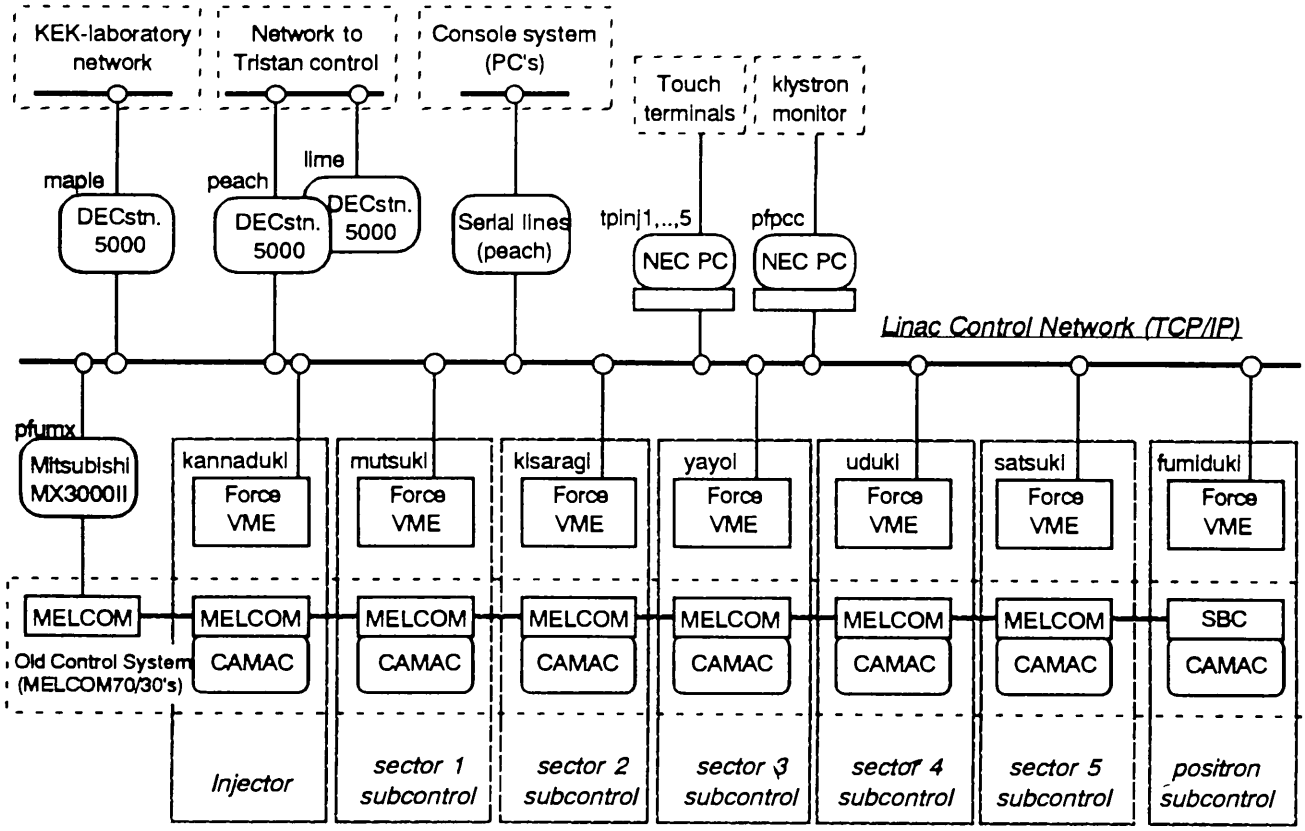

Fig.1

The new control system for the KEK Linac. Unix-based workstations are shown at the upper side of the Linac control network. Each VME-bus system is placed at each subcontrol room. The old control system (MELCOM 70/30 with CAMAC) is also shown. In addition, subsystems connected and networks for different purposes are shown at the top of the figure.

The sub-systems, such as the operator's console system (described in 1.2) and touch-terminal consoles, are connected with the new control system and are available as before.

The communication software of the new system relies on the TCP/IP socket library. This enables us to use several kinds of computers with different operating systems, including DOS and VMS, in a single control system. After a socket connection has been established, the communication throughput (round-trip) between an application process (at a DECstation) and a VME station is 8-10 ms. When the socket connection is closed every time, one round-trip requires 35-40 ms. The measured throughput is roughly one order higher than the old control system.

1.2 New Console System Scheme

As described in 1.1, we tried to replace the minicomputers and networks for the linac with UNIX, VME-OS/9 and TCP/IP. The operator's console of the linac control system has its own independent network segments for its purposes, and is connected to middle and lower-layer level computers through a gateway (FM-R70HD). This console segment was extended in the summer of 1993 to each subcontrol room where the minicomputer had been running. On this segment, personal computers (IBM-PC, 486/50 MHz, DOS/V) at each subcontrol room were set for about one year in order to back up the minicomputers or the new developing VME system when they experienced some problems. For the backup system, control programs were developed which were the same as those for the minicomputers in a short time using Quick BASIC and C on the Netware network system. The speed was improved to be more than that of the old real-time minicomputer system.

Recent PC's have a remarkable performance in speed, easy GUI (Graphical User Interface), and high cost/performance. The operator's console for the linac was upgraded using the Windows3.1-Japanese version and Visual-BASIC on the PCs (486/66 MHz, 64 MB). One of the pictures is shown below (Fig. 2).

The windows system is a type of standard display system that is easy to learn and Visual BASIC for Windows could improve the productivity of Window graphics programming in object-oriented programming (OOP) manners. Since the operator's console sometimes require multi-task operation on a network client, OS/2 and Windows NT have been tested, and undergoing installation on a high-performance CPU.

Plans to add a more powerful pentium and reliable server system (HD array and UPS) on the operators console segment are now proceeding; it will be completed by the middle of March, 1994. The OS will soon be upgraded to Netware 4.0 from 3.11 and 3.11J. Windows NT is also under testing as a network server for the console segment.

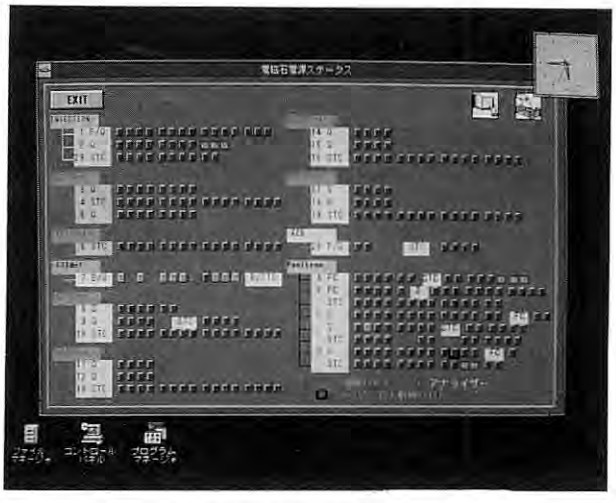

Fig. 2 Graphic display on the operators console

D. R&D REGARDING KEKB

1. ENERGY UPGRADE

1.1 High-Power RF Source

1.1.1 Reinforcement of the klystron modulator

Following a successful long-term test operation of the modified No. 4-6 klystron modulator, 8 main modulators out of a remaining total of 47 regular modulators were reinforced. The specifications are nearly the same as those for No. 4-6, except for abandoning a recirculation scheme.

1.1.2 Improvement of the 30-MW Klystron

An upgrading of the existing 30-MW klystrons, especially those of the low-gradient type, with a large curvature of the gun electrode and anode (PV3030A2) to reduce failures due to arcing in the gun region, is being pursued at KEK. A simulation analysis of the PV3030A2 using the FCI code has suggested the possibility that it can produce more than a 60-MW output power at a 350 kV beam voltage with reasonable efficiency by optimizing the profile of the focusing magnetic field.

A tentative test of the 30-MW klystron up to a beam voltage of 300 kV was carried out with a low-duty-rate in order to prevent the tube from any failures due to the high-voltage ceramic seal and an output window. At that level, a peak power of 47.3 MW with a reasonable efficiency of 44% was obtained. After obtaining this test result we replaced the high-voltage ceramic seal with a larger one in order to increase the insulating length (PV3030A3). A test of this improved klystron was performed up to a beam voltage of 310 kV; at this level a peak output power of 51.5 MW with an efficiency of 44% was obtained. The test results have shown that the maximum of the focusing magnetic field is about 1150 G. It exceeded the available maximum field of the permanent magnets presently used.

In a test of the higher duty rate, the temperature of the output window of the tube was measured; 22°C of the temperature rise was obtained at Po=46 MW in 4 μsec under 40 pps conditions. The temperature rise changed linearly to the average power, and the window worked normally up to that rating.

This window material is a high-density pure alumna of 99.7% (HA997) and has a very low tanδ value. Figure 3 shows the output characteristics of the 30-MW klystron. The results of the 60-MW tubes which were developed in Mitsubishi Co. and Toshiba Co. are also shown for a comparison.

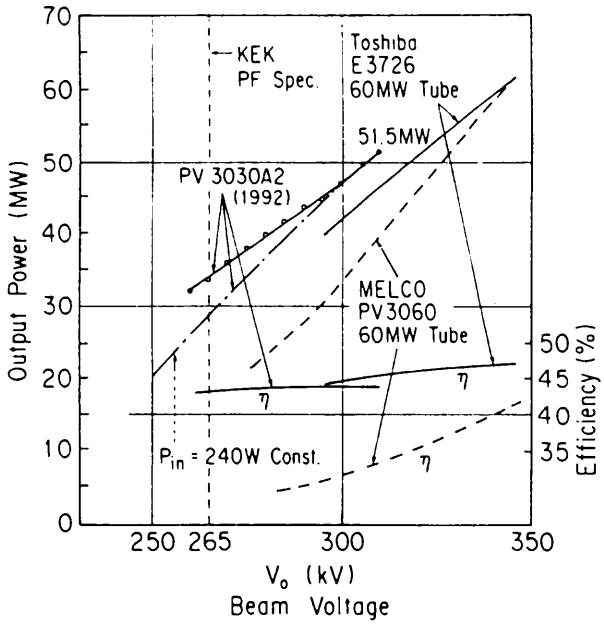

Fig. 3 Output characteristics of the PV3030A2 (PV3030A3) klystron and the 60 MW tubes.

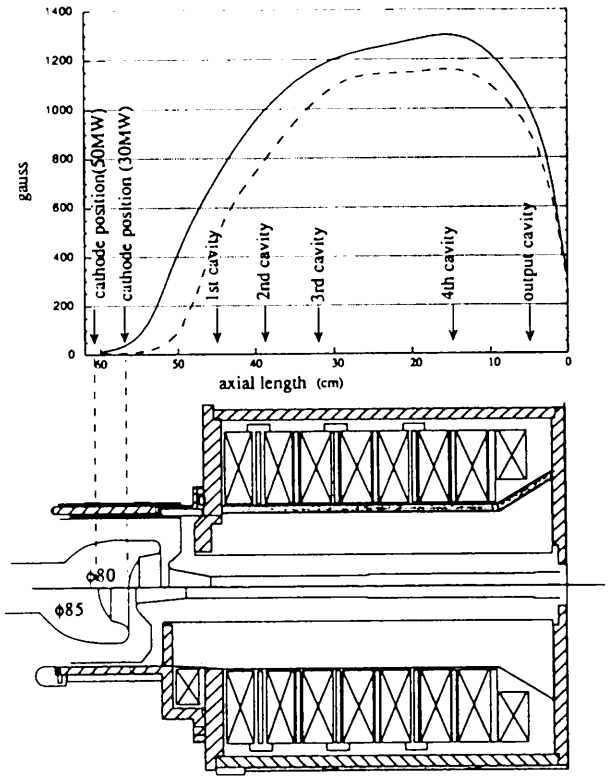

Fig. 4 Comparison between the 30 MW tube and the 50 MW tube, which was newly designed. The optimum magnetic field distributions are also shown.

1.1.3 Development of a 50-MW Klystron

The improvement in the PV3030A3 Klystron enables them to be applied to the KEKB project. In order to increase the reliability, a slight modification of the 30-MW tube was attempted. The design concepts were as follows: (1) The rf interaction region (i.e., parameters of cavities) was kept the same as those of the PV3030A3 (therefore, the same as the SLAC XK-5 tube). (2) The cathode diameter was enlarged from φ80 to φ85 in order to reduce the average pulse-current density from the cathode. (3) The high-voltage ceramic seal of the gun housing was enlarged so as to increase the capability to higher voltage applications. (4) The klystron dimension was determined while considering that the main part of the focusing electromagnet has a compatibility between the 30 MW tube and 50 MW tube if a slight change at the gun region of the tube is made. (5) The length from the anode to the 1st cavity was prolonged by 4 cm from the microwave considerations. (6) X-ray shielding was reinforced by making a large space between the collector and its outer spool.

A simulation of the FCI predicts a similar result with the performances of the PV3030A3 test. Figure 4 shows a comparison of cut-away views of the old and new tubes with an optimum magnetic field. Figure 5 shows a comparison of the outer dimensions of the PV3030A2, PV3030A3 and 50 MW tubes.

The focusing electromagnet was slightly changed in accordance with the design concept of (3) mentioned above. The inner-bore diameter was slightly enlarged, and an X-ray shield was moved to the outer side. These modifications enable the tube outer diameter to be enlarged. An auxiliary coil was replaced in a test of the 50 MW tube with the old-type iron cylinder, which was suitable for the 30 MW tube.

It is necessary to reinforce the existing pulse transformer, of which step-up ratio is 1:12. These pulse transformers are operated without any core reset bias. The cores can be reused only by supplying the core-reset bias current to the primary windings. We are slightly changing the winding of the primary and secondary so as to obtain a step-up ratio of 1:13.5. The insulating lengths of the pulse transformer have been redesigned in order to withstand over 310 kV during operation.

Pulse-transformer oil tanks can also be reused, since there has been no change in their overall size. However, they require extension adapter tanks (10 cm high) for mounting new klystrons with long gun insulators. All of the other parts, such as the feeder

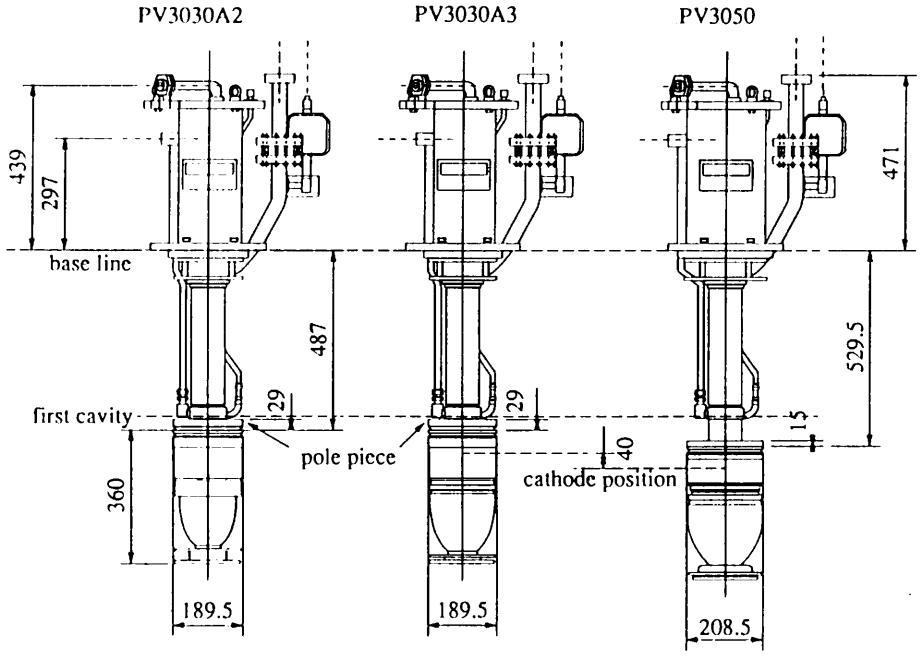

Fig. 5 Comparison of the outer view between PV3030A2, PV3030A3 and the 50 MW tube.

sockets, cooling pipes, klystron socket and heater transformer, and wave-form monitors, are also being reused as they are. The costs of these modifications are much less than if a new set of the assemblies were to be introduced.

1.2 High-Gradient Acceleration

1.2.1 High-Gradient Acceleration Test Using a Resonant Ring

In 1992, high-gradient acceleration tests were started for a future energy upgrade plan of the linac regarding the KEKB project; one of the main proposes was to check the upper limit of the feeding power to the existing accelerator sections. At first, this test was simply performed by feeding a maximum power from a klystron into one of the accelerator sections used in normal operation. In this test, it was proved that it can withstand the full power (~30 MW) corresponding to an accelerator gradient of ~20 MV/m. Since the autumn of 1992, the tests have further been continued in order to prove the performance at a level of ~30 MV/m, which is required for the KEKB project. These were carried out using a traveling-wave resonant ring and a SLED-type rf pulse compressor (also see the following section 1.2.2).

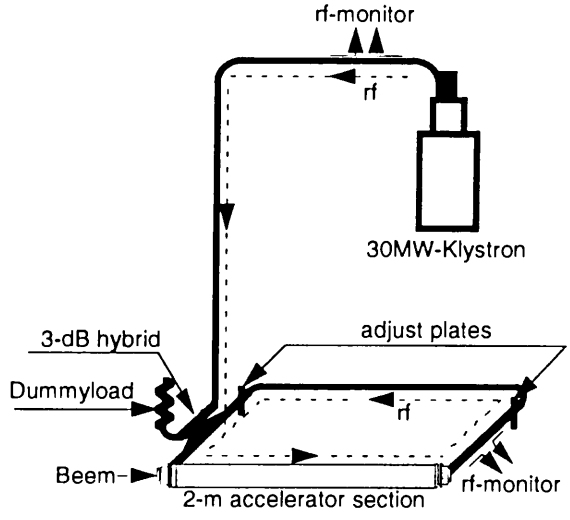

Fig. 6 Traveling-wave resonant ring with a 2-m accelerator section.

After the first stage ended, the rf-guide system of the NO.4-8 acceleration unit was changed so as to comprise a traveling-wave resonant ring with a 2-m accelerator section (Fig. 6). The rf phase length of the resonant ring was adjusted using short rf-guide plates. The rf processing was performed by gradually increasing the feeding power with 3.5 μs (width) and

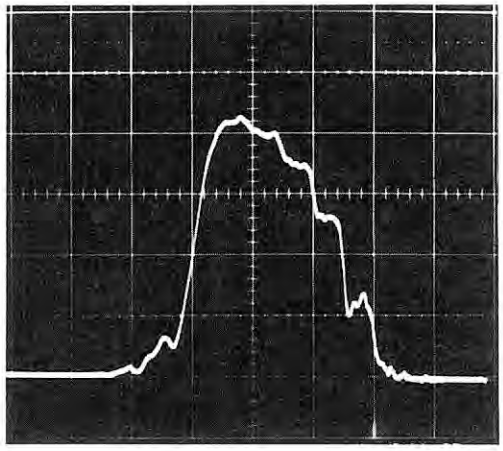

Fig. 7 Radio-frequency wave form building up in the section during a pulse.

Table 6. Results of a high-gradient acceleration test by a traveling-wave resonant ring with a 2-m accelerator section.

Acceleration energy	54.1MeV
Acceleration field	28.6 MV/m
Fed rf power	30 MW

25 pps (repetition) to the maximum (~30 MW); outgassing and electric breakdown due to an inexperienced high-gradient were overcome; this section eventually came to be operated stably. Figure 7 shows an rf waveform building up in the section during a pulse.

The result concerning the test are summarized in Table 6. The acceleration energy (54.1 MeV) was obtained based on the difference between the maximum and minimum beam energies measured at a 2.5-GeV energy analyzing station by changing the rf phase of the 4-8 unit. The energy gain was 28.6 MeV/m. This value is larger than the peak acceleration field to be used in the KEKB project.

1.2.2 High-Gradient Acceleration with SLED

A prototype SLED (SLAC Energy Doubler), developed by the JLC group, was installed in the No. 4-6 high-power rf source. A klystron modulator of this source had already been upgraded so as to generate a high-voltage pulse with a 4 μs-flat top up to 300 kV.

An independent klystron driver was also prepared for SLED operation, as illustrated in Fig. 8. The

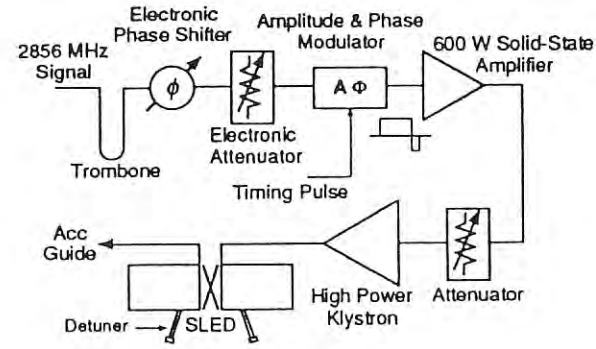

Fig. 8 4-6 SLED Test System.

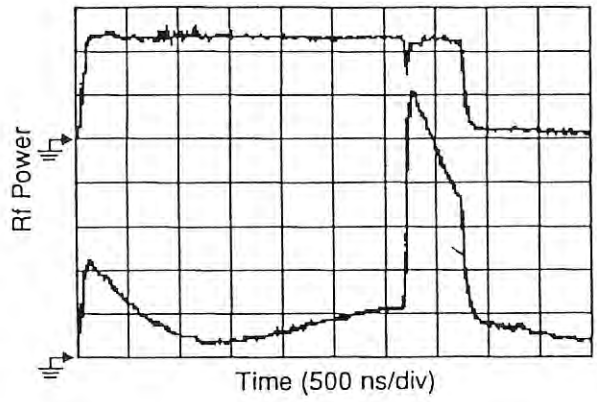

Fig. 9 Rf pulse wave forms monitored at the SLED output port. The upper one represents the wave form at 15 MW output when the SLED is disabled. The lower one is the case in which the SLED works. The vertical values are not proportional to the real rf power.

phase-&-amplitude modulator can inverse the rf phase with a short transient time (< 50 ns). The total rf-pulse width and the phase-inverse time were 3.7 μs and 0.5 μs, respectively. The solid-state amplifier feeds a 600 W rf pulse into a high-power klystron.

The SLED, itself, can be disabled by inserting detuning rods into the SLED cavities.

Rf-conditioning of the SLED system had been carefully carried out so as not to cause any serious problem; that is, big reflected rf waves which are caused by discharges in the SLED system, might break the rf windows mounted in a wave guide. Examples of the observed rf pulses are shown in Fig. 9.

The first beam acceleration test was carried out in March with a 30-MW klystron; an rf power of around

Table 7. Results of beam acceleration tests with SLED.

Es(kV)	Energy gain (MeV)	Accelerating field (MV/m)[3]	Energy multiplication[4]	Power (MW)[5]
31.5[1]	100±4	13.2±0.5	1.86±0.1	15±2
35.0[1]	130±4	17.2±0.5	1.90±0.1	24±2
37.5[2]	147±4	19.4±0.5	1.89±0.1	31±2

1) Data in this line were obtained with the 30 MW klystron.
2) Data in this line were obtained with the 46 MW klystron.
3) Averaged field strength in an acceleration guide.
4) The energy multiplication factor is defined as being the ratio of the two energy gains when the SLED is disabled/enabled.
5) The values of the rf power were calculated using the energy gains in the case of the SLED being disabled. Losses in a wave guide were taken into account.

25 MW was fed into the SLED. As the next step, in April the first 46-MW klystron replaced the previous one in order to obtain the specified energy gain (160 MeV/unit) required for the linac upgrade. A summary of the results is given in Table 7.

An rf power of more than 35 MW could not be fed into the SLED, because the rf conditioning had not yet been completed. Therefore, the examined energy gain could not reach the specified one (Table 7). However, the average value of the obtained energy multiplication factors is higher than the specified value (1.85).

A beam-acceleration test under full-power operation of the klystron will soon be carried out.

1.2.3 Developments of a new-type rf pulse compressor

We have started to develop a new-type rf pulse compressor utilizing a coaxial traveling-wave resonator. This method is similar to that used in the SLED-type pulse compressor at the point that it release a high peak power upon switching the rf phase during the pulse after storing the rf power in the cavity. The resonant mode of the new rf pulse compressor, however, is not a standing wave, as in the usual type cavity resonator including a SLED, but is a traveling-wave. The structure is simple (only one storage cavity and no 3-db coupler), and it is easy to tune the frequency. A schematic drawing of this new-type rf pulse compressor is shown in Fig. 10.

In the design of the cavity, it is necessary to find a resonant mode which is sufficiently far away from the

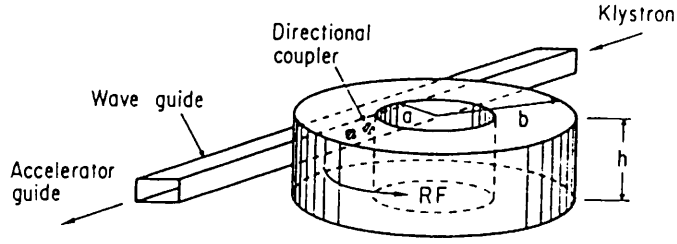

Fig. 10 Schematic drawing of a new-type rf pulse compressor using traveling-wave resonator.

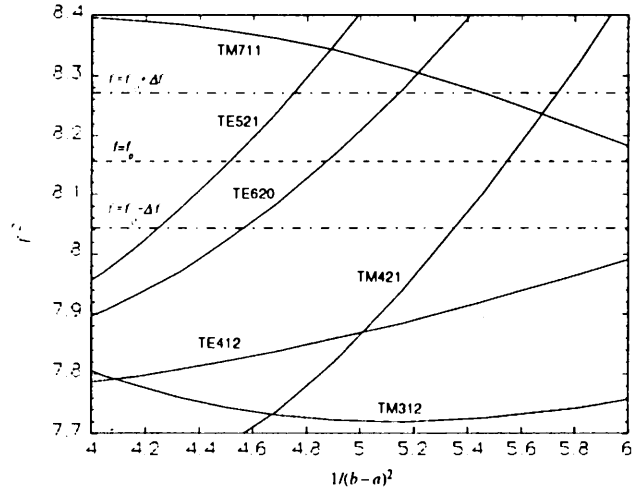

Fig. 11 Mode chart for TE_{620} at 2856 MHz. *a* is the inner radius; *b* is the outer radius; f_0=2856 MHz and Δf=20 MHz.

others, as well as to find such a mode with a sufficiently high Q value. The mode search was restricted to TE_{620} because of practical size limitations. The cavity dimensions (inner radius, outer radius and height) were surveyed under the condition described above. A mode chart for the dimensions which was finally determined is shown in Fig. 11. The separations of the parasitic modes are +31 and -53 MHz for the nearest two modes (TE_{521} and TE_{412}); these values are sufficiently large. The voltage multiplication factor in the cavity and the maximum electric field strength are 20.6 and 132 MV/m, respectively. The energy gain integrated along an accelerator guide is smaller than that of the SLED by 5%. As a directional coupler between the cavity and the waveguide, a two-hole coupler is used. The coupling is adjusted so as to give a maximum energy gain. A narrow-width waveguide is used to provide the same guided-wavelength at the irises for

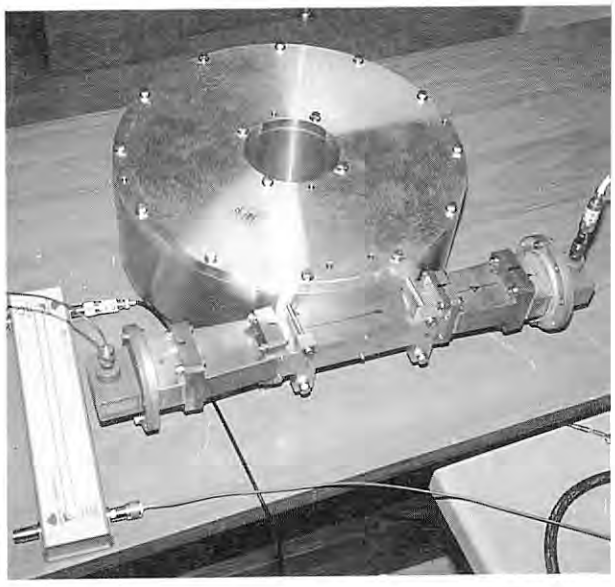

Fig. 12 Cold model of the traveling-wave resonator pulse compressor.

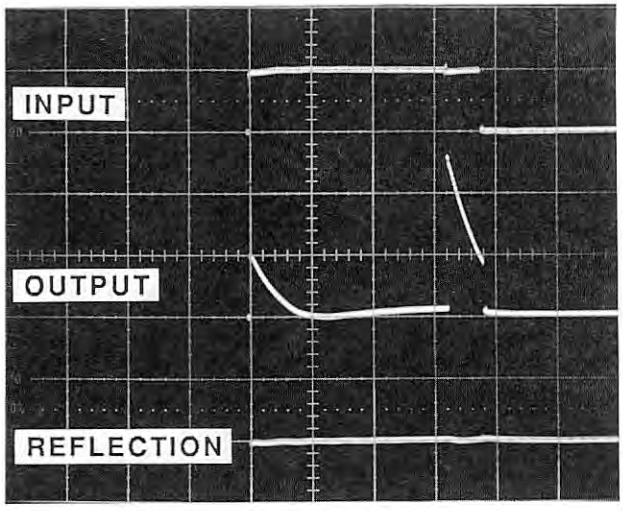

Fig. 13 Pulse response of the new-type rf pulse compressor, input (upper trace), output (center) and reflection. The pulse width and phase-switching time are 3.8 and 3.2 μs, respectively.

the waveguide and the cavity resonator (at most outside). Tapered waveguides are used between the narrow-width waveguide and ordinary ones. A photograph of the cold model (made of aluminum) is shown in Fig. 12. The measured pulse response is shown in Fig. 13. The power multiplication factor is 5.24. The precise tuning of the resonant frequency will be done by pushing a part of the outer side wall. According to the MAFIA calculation, pushing by 0.7 mm is necessary for a frequency change of 200 kHz. Detuning of the cavity for non-pulse compression mode operation can be performed by inserting two rods just in front of the irises.

A verification test of the tuner and building of a hot model are scheduled for the future.

2. SINGLE-BUNCH BEAM

2.1 Trigger System and Master Oscillator

The single-bunch beam accelerated in the linac should be injected into the ring rf buckets with an accuracy of better than 30 ps from the center. This specification will be satisfied when accelerating frequencies of both the linac and the ring are multiples of a common subharmonic, and are subsequently synchronized very well.

Additionally, the ring frequency should be 508.58±0.3 MHz in order to utilize the TRISTAN rf components; the linac frequency (2856 MHz) should have suitable subharmonics for bunching on the way of multiplication, near to 100 and 500MHz for example.

Starting from the above-mentioned boundary conditions, we found 10.38545 MHz to be the common subharmonic which is one 49th of 508.887 MHz and one 275th of 2856 MHz. The ring and the linac frequency are made by using 7*7 and 11*5*5 multiplication of 10.38545 MHz, respectively. Since the ring frequency is 0.307 MHz higher than that of TRISTAN and 114.24 MHz and 571.20 MHz are useful for subharmonics of the linac 2856 MHz, we can almost satisfy the above -mentioned boundary conditions. A block diagram of the trigger system is shown in Fig. 14

As for multibunch injection in a pulse in this scheme, we can inject only two bunches spaced from the other by 49 ring buckets (96ns) with the same timing accuracy, which comes at every 49 cycles of the ring frequency. The third bunch, 96 ns later, can not be stably accelerated in a narrow rf pulse obtained after rf pulse-multiplication, and may not be injected.

We have made an identical pair of 275-times multipliers of 10.38545 MHz and have been testing the phase difference stability of those 2856 MHz outputs from the same inputs under a temperature-regulated condition. In the preliminary results, the phase difference doesn't change by more than 2° under the condition of ±0.5°C temperature variation.

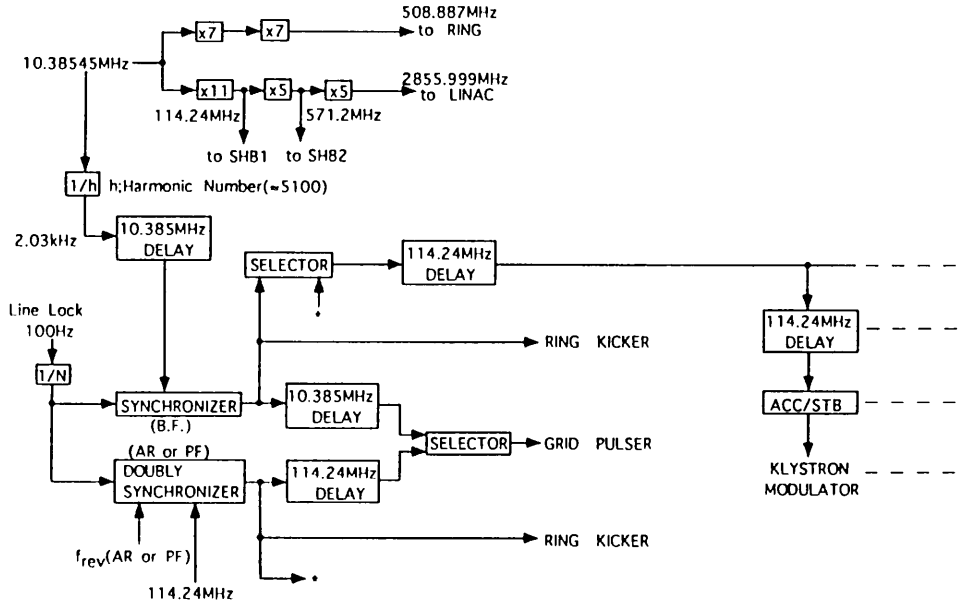

Fig. 14 Block diagram of the trigger system.

2.2 Single-Beam Acceleration

2.2.1 Beam-dynamics Simulation

The KEKB project requires S-band single-bunch beams of electrons and positrons for injection. The required intensities per pulse are more than 4×10^9 for positrons and 8×10^9 for electrons. To meet the requirement for positrons, it is necessary to accelerate an intense primary electron beam without degradation through a long section to the positron production target. It therefore became necessary to investigate any problems occurring with the intense beam acceleration. It should be fedback in order to upgrade the linac.

To obtain a single-bunched beam in the linac, a 476-MHz sub-harmonic buncher (SHB) was introduced, which was installed between the electron gun and the first prebuncher (Fig. 15). A simulation calculation using "PARMELA" predicts that a single bunch beam can be obtained if the beam-pulse duration is less than 1 ns. However a small satellite accompanies each side of the main bunch if the beam duration is not sufficiently short. Figure 16 shows a typical result of a simulation which was calculated for the rectangular beam of 1-ns and 10 A at the SHB-entrance.

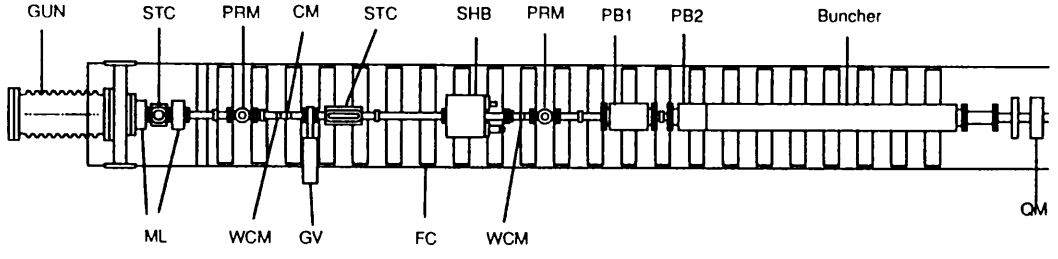

Fig. 15 Layout of the injection system with the 476-MHz SHB. GUN is an electron gun; STC, steering coils; ML, a magnetic lens; PRM, a profile monitor; WCM, a wall current monitor; CM, core monitor; GV, a gate valve; FC, a focusing coil; PB1, first prebuncher; PB2, second prebuncher; Buncher, a buncher with accelerating cavities.

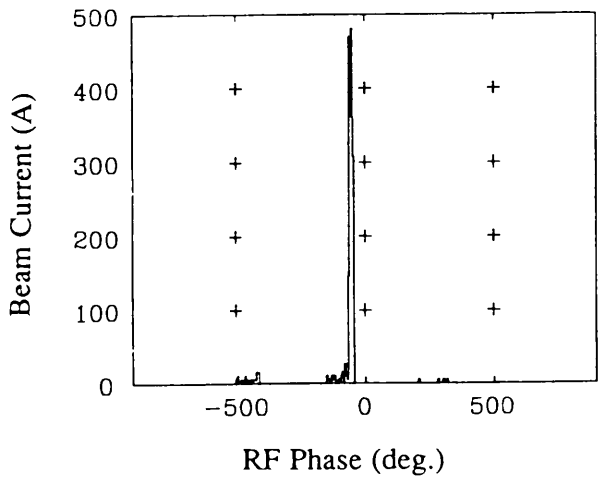

Fig. 16 Typical result of a bunch simulation at the buncher exit. It was calculated for a rectangular beam of 1-ns and 10 A at the SHB-entrance.

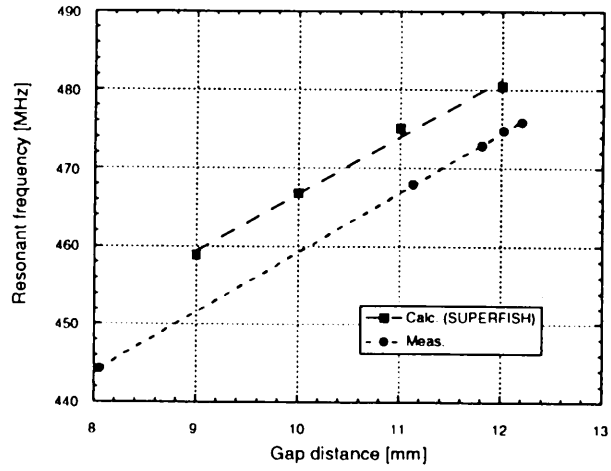

Fig. 18 Relation between the resonant frequency and the gap distance.

2.2.2 Sub-harmonic Buncher (SHB)

A new SHB cavity has been fabricated and installed at the injector of the PF 2.5-GeV electron linac for single-bunch operation. The frequency of the cavity has been selected to be 476 MHz because a power source already existed, and the existing cavity dimensions (designed by the staff of the University of Tokyo) were applicable. A cross-sectional view of the cavity is shown in Fig. 17. The rf coupler is isolated from the vacuum by using a ceramic window in order to enable us to adjust the coupling coefficient without breaking the vacuum. The accelerating-gap distance has been adjusted in order that the resonant frequency stays within the adjustable frequency range of the tuner (see Fig. 18). The frequency range of the tuner was 1.36 MHz. The measured rf characteristics of the cavity are as follows: the Q-value (unloaded) is 8361, the coupling coefficient is 1.22 and the shunt impedance is 0.98 MΩ. After rf conditioning of a few days, the input rf power reached the operational value (3.5 kW).

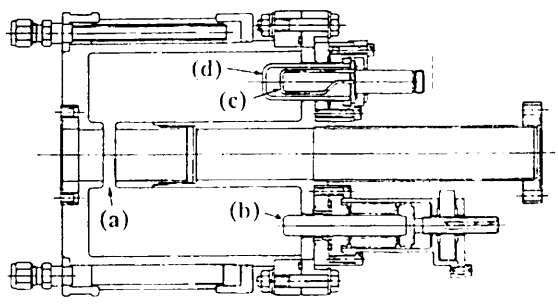

Fig. 17 New Sub-harmonic buncher: (a) acceleration gap, (b) tuner, (c) coupler, and (d) ceramic window.

2.2.3 First Acceleration Test Results

After installing the SHB, the single-bunch beam characteristics were measured, which were the bunch length, energy spectrum and transmission rates along the entire linac.

A bunch measurement was performed by means of a streak camera utilizing the transition radiation from the emitter at the end of the injection system (~ 45 MeV). As can be seen in a typical picture of the measurement (Fig. 19), a single bunch was obtained in the linac. Although it had small satellites, as predicted by the PARMELA simulation, this would not seriously affect the investigation of the intense single-bunch beam acceleration. Figure 20 shows a single-shot picture of a bunch containing 4×10^{10} electrons. The bunch length (FWHM) was measured to be 11 ps.

The energy spectrum of the beam was also measured at the end of the injection system. It is shown in Fig. 21. The momentum spread (FWHM) was 0.6%.

The transmission rates of the beam were measured along the entire linac at various beam intensities. Very preliminary results are shown in Fig. 22. The measurement was performed without any adjustment of the transport system, because of a lack of time.

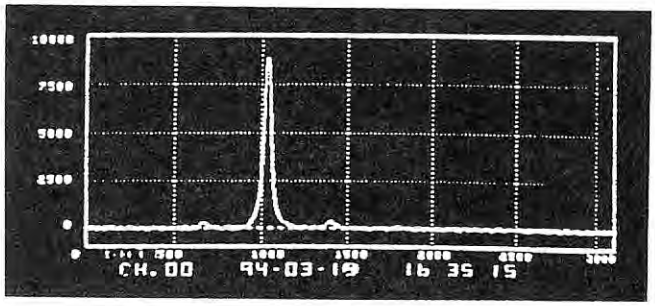

Fig. 19 Typical picture of a bunch measurement. Almost a single bunch was obtained. The beam charge is ~0.9 nC.

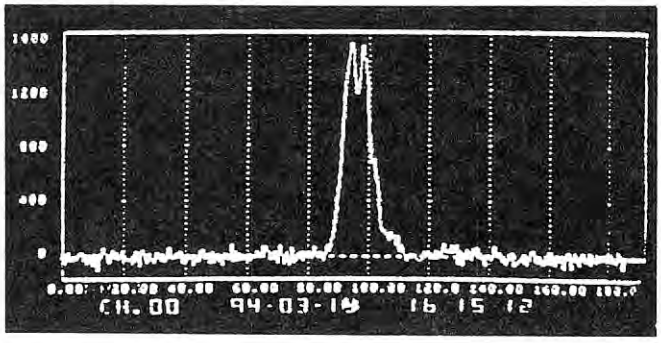

Fig. 20 Single-shot picture of bunch containing 4×10^{10} electrons. The bunch length is 11 ps (FWHM).

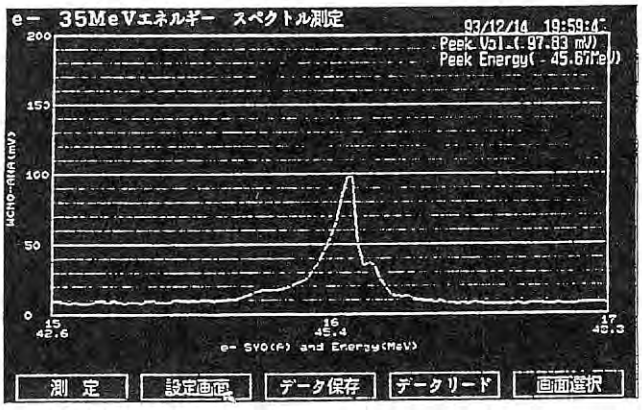

Fig. 21 Energy spectrum of a single-bunch beam. The momentum spread (FWHM) was 0.6 %.

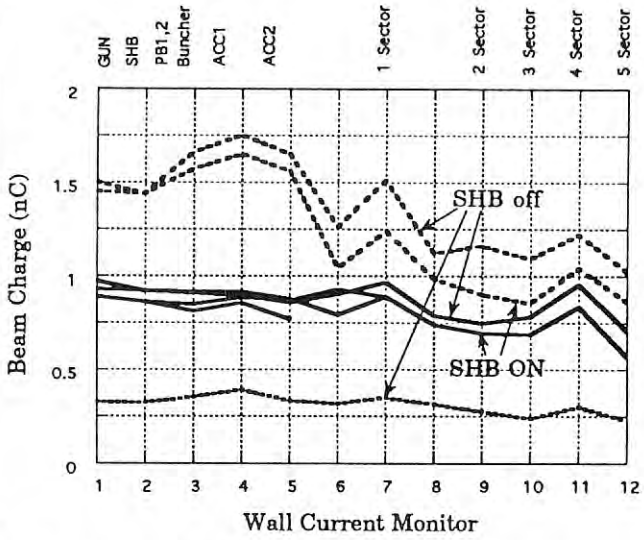

Fig. 22 Transmission rates measured along the entire linac

3. VACUUM SYSTEM

A regular accelerating unit in the linac has been evacuated with two sputter ion pumps (SIPs) having pumping speeds of 50 and 500 l/s, respectively. An abrupt pressure rise has often been observed near to the 50 l/s SIP, which is mounted on a rectangular waveguide through pumping slots (6 mm width). Discharges or arcing in the pump were possibly induced by higher-order harmonic components of the klystron output leaking through the slots, thus causing such an abrupt outgassing. Indeed, the installation of a net (3 mm mesh (SUS304)) in a SIP flange has been found to be remarkably effective for suppressing the discharge and, consequently, the outgassing. In this way, twenty units have been improved so far, and the SIPs have completely obtained stable functioning.

Also, the electrical breakdown phenomena of both the rf windows and the accelerator-column electrodes have been serious problems for linac operation. Since the future KEKB project at KEK will demand an rf power of 50 MW or more (~200 MW peak) for the 8-GeV linac, such a breakdown would become ever more serious.

In order to investigate the relationship between the vacuum condition and electrical breakdown phenomena, an analysis of the pressure distribution was carried out for a vacuum system comprising various conduit pipes, such as accelerator guides, waveguides and pumping pipes. Using a Green-function matrix, the pressure distribution was calculated for several cases of the pump configuration (Fig. 23). The results given in Fig. 24 indicate that the pressure near to the rf window can be reduced

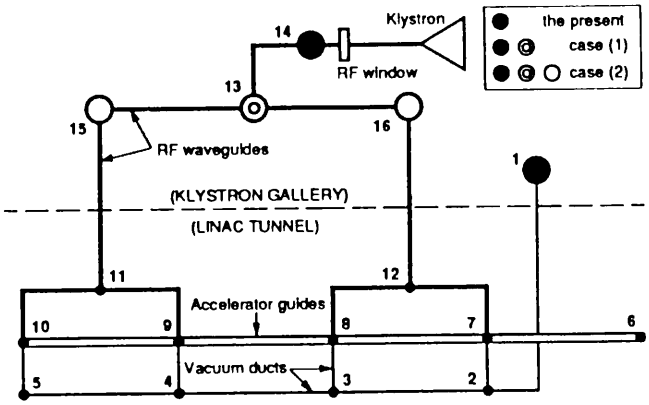

Fig. 23 Schematic diagram of the vacuum network in the accelerating unit. Two SIPs are presently installed at the 1-st and 14-th node.

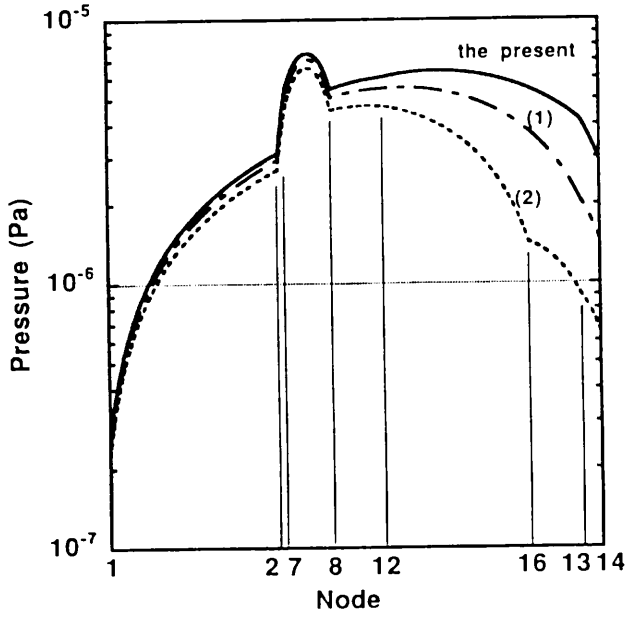

Fig. 24 Pressure distributions calculated for configurations of Fig. 23. The outgassing rate per unit surface area of every pipe is supposed to be 10^{-8} $Pa \cdot m^3/m^2 \cdot s$ in the calculation.

down to the order of 10^{-7} Pa only when three additional pumps having a pumping speed of 20 l/s are equipped.

Furthermore, additional SIPs, valves and gauges have been installed at accelerating unit (4-8); pressure measurements necessary to optimize the pump configuration will be carried out.

Based on recent research concerning rf windows, we have adopted brazed-sealed windows, which are of the same types as those used in SLAC 5045 klystrons, instead of shrink-sealed windows; 16 windows of this braze-type have so far been installed in the waveguide system. High-purity alumina ceramics (NTK; HA-997) are used in the window and a thin TiN film (~1.5 nm) is coated in order to suppress multipactoring.

Baking (115°C for 6 hours) of the waveguide system between the klystron and waveguide windows has been performed after replacing a klystron. The baking process showed a significant effect on the pumping duration required for a pressure on the order of 10^{-5} Pa. This possibly enables a reduction of the rf conditioning period.

4. BEAM MONITOR

4.1 Bunch and Profile Monitor Utilizing Optical Transition Radiation

An elaborate beam-monitoring system is indispensable in order to realize stable operation of the linac with high current beams for KEKB. In this connection, we have developed and installed several types of monitors since last year. Among them, we provided brief accommodation this year for a control system of the bunch and profile monitor utilizing optical transition radiation (OTR). The OTR monitor comprises a radiator of thin metal plate inserted into a beam line at an angle of 45 degrees, an optical-transport system, a CCD camera for beam-profile observations, and a streak camera system for bunch-shape measurements. Although the OTR, itself, has several good features for bunch and profile monitors, it should be associated with an adequate optical and control system; the sharp spatial directivity of the OTR requires a fine control of the optical components so as to obtain large intensity; the characteristics of fast time resolution necessitates a delicate trigger-delay control for the streak-camera system as well as the computer control of the streak-camera system, itself. Table 8 gives a list of control elements for the OTR monitor.

Since each component for the bunch-shape monitor has been designed independently, it's important to bring them together so that they comprise a single monitoring system. We tried to construct the system so as to associate the components with each other. The components were connected with a computer through ethernet, employing a terminal server and a GPIB-ethernet adapter (Fig. 25). The host computer communicates with them via the TCP/IP protocol. The software was designed so as to organize separate devices into a single control object. We also developed a graphical user interface on an X-window

in order to manipulate the system. We simplified the user interface by hiding unimportant information, so that operators may observe the beam structure easily (Fig. 26). This system will be used as a effective tool to study linac beams for KEKB. We also expect that the operators will utilize it during normal accelerator operation as a fundamental beam monitor.

Table 8. List of the control elements for the OTR monitor.

	Name	Control	Comments
Optical Components			
	Lens 1	RS-232C	1-DOF
	Lens 2	RS-232C	3-DOF
Streak-Camera System			
	Temporal Analyzer	GPIB	
	Remote Controller	RS-232C	
Trigger System			
	Delay 1	GPIB	Coarse(2ns)
	Delay 2	GPIB	Fine(30ps)

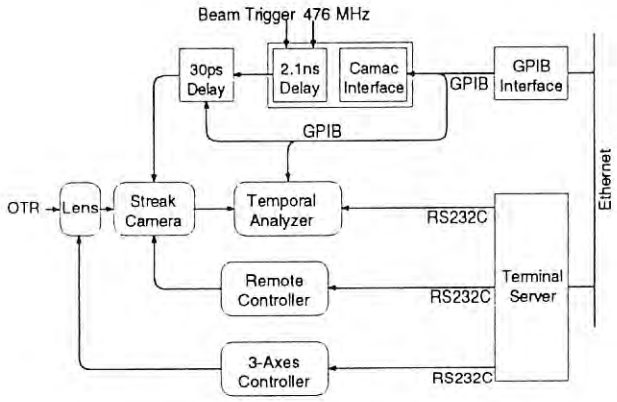

Fig. 25 Interface system for the streak-camera components.

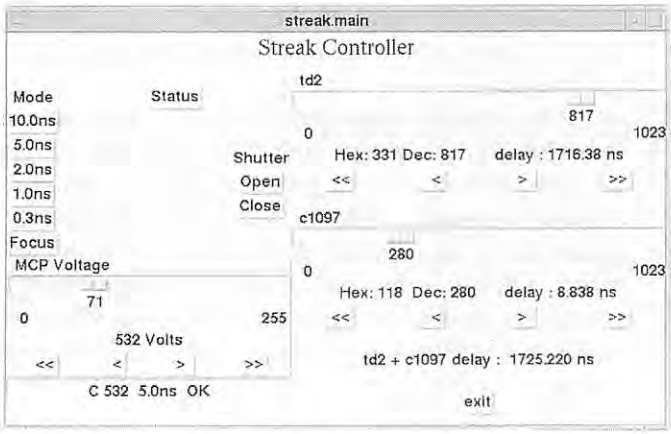

Fig. 26 One of the user interfaces used for streak-camera operation.

4.2 Beam-Position Monitor

A stripline-type beam-position monitor (BPM) is under development at the PF 2.5-GeV linac. This monitor will be installed in order to easily handle the orbit of a high-current electron beam (~10nC) generating a positron beam in the KEKB. The prototype BPM was tested by using a single-bunch electron beam at the NERL linac of the University of Tokyo.

4.2.1 Stripline-type BPM

During last year a wireline-type BPM was developed. However, this monitor has some difficulty in obtaining a good matching condition as the transmission line of a wire pickup, because of limited space in the BPM bore. The new prototype BPM is shown in Fig. 27. It is a conventional srtripline-type monitor made from stainless steel (SUS 304). The total length (250 mm), stripline length (130 mm) and stripline inner radius (20 mm) were chosen so that it could be installed into the present beam line of the PF 2.5-GeV linac. The four pickups are connected with 50Ω SMA vacuum feedthroughs. The opening angle

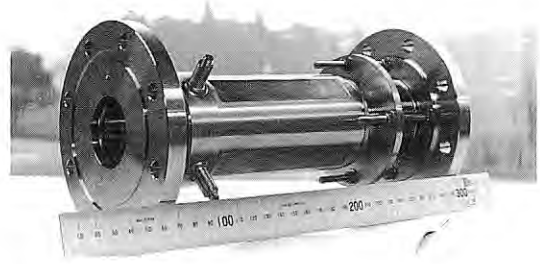

Fig. 27 Stripline-type BPM.

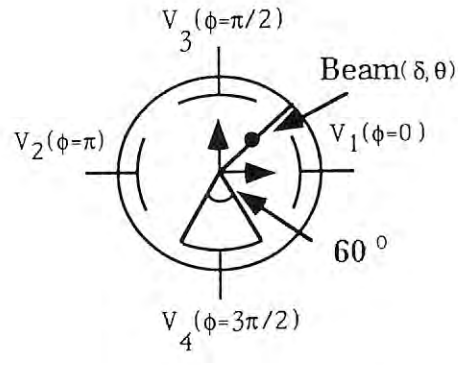

Fig. 28 Cross section of the stripline BPM.

of the electrode viewed from the center position of the BPM was chosen to be 60 degrees. The beam position (x, y) in the BPM can be calculated using the ratio Difference/Sum ($x=S_b\ (V_1-V_2)/(V_1+V_2)$, $y=S_b\ (V_3-V_4)/(V_3+V_4)$) of the signals coming from two pairs of the electrodes facing each other (Fig. 28).

4.2.2 Experimental Set-up and Procedure

A beam experiment of the BPM was carried out by using a single-bunch electron beam (E=35 MeV, I=0.27 nC/bunch, FWHM~10 ps). The experimental set-up is shown in Fig. 29. At the exit of the linac a slit (3 mmϕ) was inserted so as to ensure a small beam size. After the slit, a lead block with a hole (9 mmϕ) was placed so as to reduce any background showers from the slit. Following the lead block, two waveguide-type BPMs and the stripline-type BPM were installed on a precision micro-adjustable stage in order to change the position of the BPMs relative to the beam in the horizontal and vertical directions manually. Behind the BPMs, several lead blocks were inserted so as to reduce any backscattering of the beam from the carbon blocks used as a current monitor. A screen monitor was inserted after the lead blocks in order to monitor the beam profile. The profile was about 6 mm in diameter, measured by a radiation-color film at this point. The pickup signals were sent to the measurement room using 15 m coaxial cables (RG 223/U), and the pulse height was measured using an analog oscilloscope (Tektronix model 7104, BW=1GHz) and a digital sampling scope (HP 54120B, BW=50 GHz). The frequency spectrum was also measured by using a spectrum analyzer (ADVANTEST R4131D).

4.2.3 Experimental Results

The pulse height from each pickup was measured by changing the position of the BPM in the vertical and horizontal directions by using the micro-adjustable stage manually. A typical wave form measured by the digital sampling oscilloscope is shown in Fig. 30. The variation in the pickup voltages due to the horizontal displacement are shown in Fig. 31. Here, the output pulse height is defined as being the height of the first negative peak measured by the oscilloscope. The solid lines show the theoretical curves. The measurement includes about a 10% error due to the oscilloscope amplifier gain difference and the absolute position error relative to the beams. Figure 32 shows Difference/Sum curves measured by moving the BPM in the horizontal direction. The coupling strength (S_b) between the beam and the electrode is 13.9 mm at the center position, which can be calculated by using the slope of the

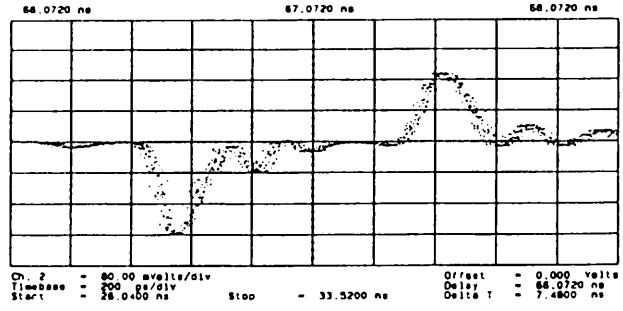

Fig. 30 Pickup pulse measured by the digital sampling oscilloscope.

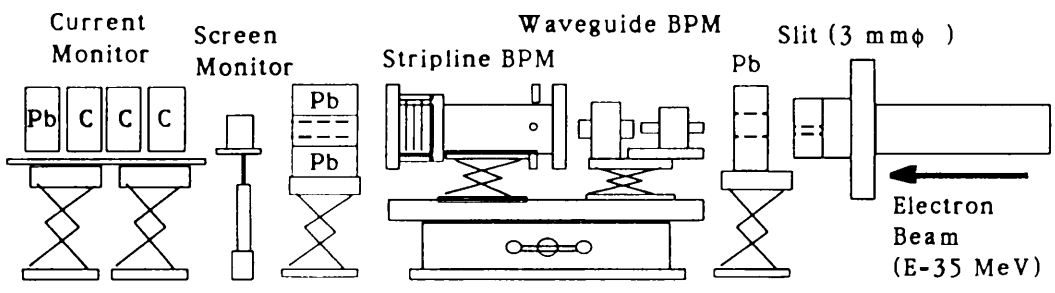

Fig. 29 Experimental Set-up.

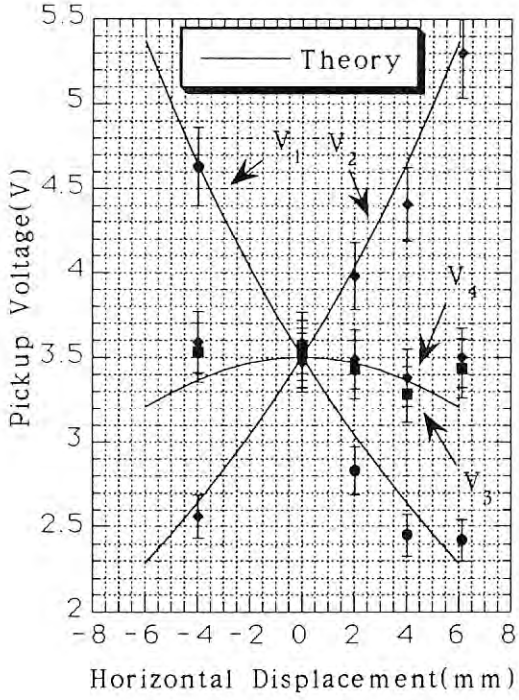

Fig. 31 Pickup voltages as a function of the horizontal displacement.

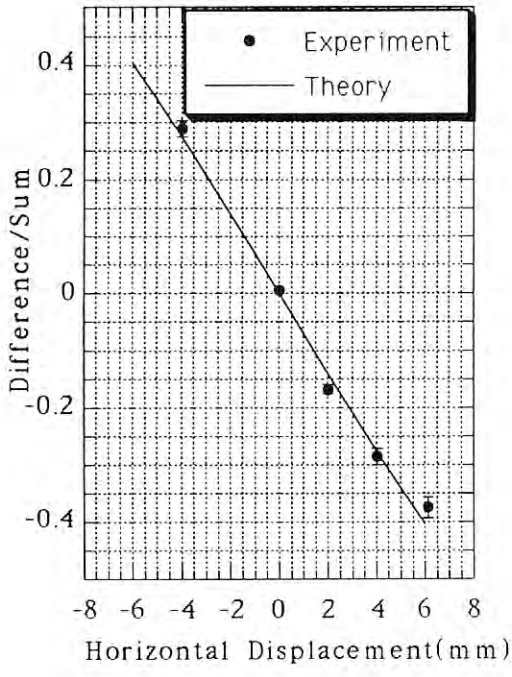

Fig. 32 A Difference/Sum as a function of the horizontal displacement.

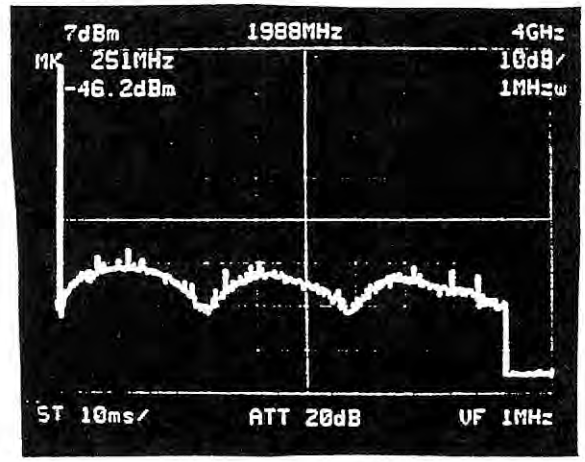

Fig. 33 Frequency spectrum of the pickup pulse.

Difference/Sum curve. The agreement between theory and the experiment is good within the errors. Figure 33 shows the frequency spectrum of the pickup pulse measured by the spectrum analyzer. The spectrum shows half-sine forms with some dips which depend on the length of the stripline. The first dip is at 1.17 GHz, and the second one is at 2.35 GHz. These frequencies agree well with the theoretical values. By this experiment the basic characteristics of the BPM were understood well. As the next stage, an analog part of the electronics and data-taking system using VME ADC modules are presently under development.

E. RESEARCH

1. SLOW POSITRON SOURCE

1.1 Overview

The KEK slow positron source is in the final stage of its construction, aiming to produce more than 10^9 e^+/s slow positrons utilizing the PF 2.5-GeV electron linac as its primary beam source. A slow positron beam, which is produced by bombarding a target assembly (a water-cooled tantalum rod of 5 radiation length and a moderator with multiple tungsten vanes) is directed by a 30 m beam transport system to an experimental area at the end of the klystron gallery through a 2.5 m thick radiation shield floor.

At the end of FY 1992, a high-voltage station capable of applying 60 kV was installed in the beam-

transport system in order to vary the energy of the positron beam dedicated to depth-profile measurements. Relevant coils at 90° bending sections along the beam transport line were also reinforced accordingly. A device controller, combining a personal computer and a programmable sequence controller through optical fiber, is adopted in order to control monitors and power supplies at the high-voltage station.

The brightness enhancement of the positron beam for positron reemission microscope experiments is also under consideration.

At a preliminary test with 2.0 GeV, a 10 W primary beam, a slow positron beam of 4×10^4 e^+/s was observed by detecting annihilation γ-rays at the end of the beam-transport line. Further improvements of up to 2×10^7 e^+/s will be easily achieved by using a 6 kW primary beam.

1.2 Control system for the positron-beam guide

We have several kinds of power supplies to be controlled on the positron-beam guide. They are operated individually by hand, except for devices in a high-voltage potential. Since part of the beam-guide is raised to a high voltage, we need to operate devices there from the ground-potential side.

A block diagram of the control system is shown in Fig. 34. All of the power supplies are installed in high-voltage racks together with a local controller which receives messages from a personal computer and controls devices. They are connected with an operator's console by an optical-fiber cable. A device-handling program was written on a personal computer using an object-oriented-programming method. 'Help' menus are available on the screen; no other operation manual is required.

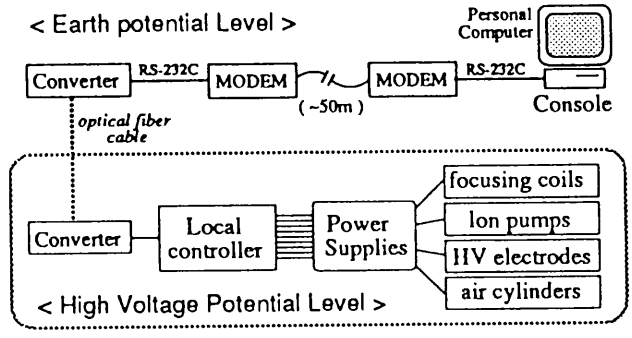

Fig. 34 Block diagram of the control system for devices located in a high voltage.

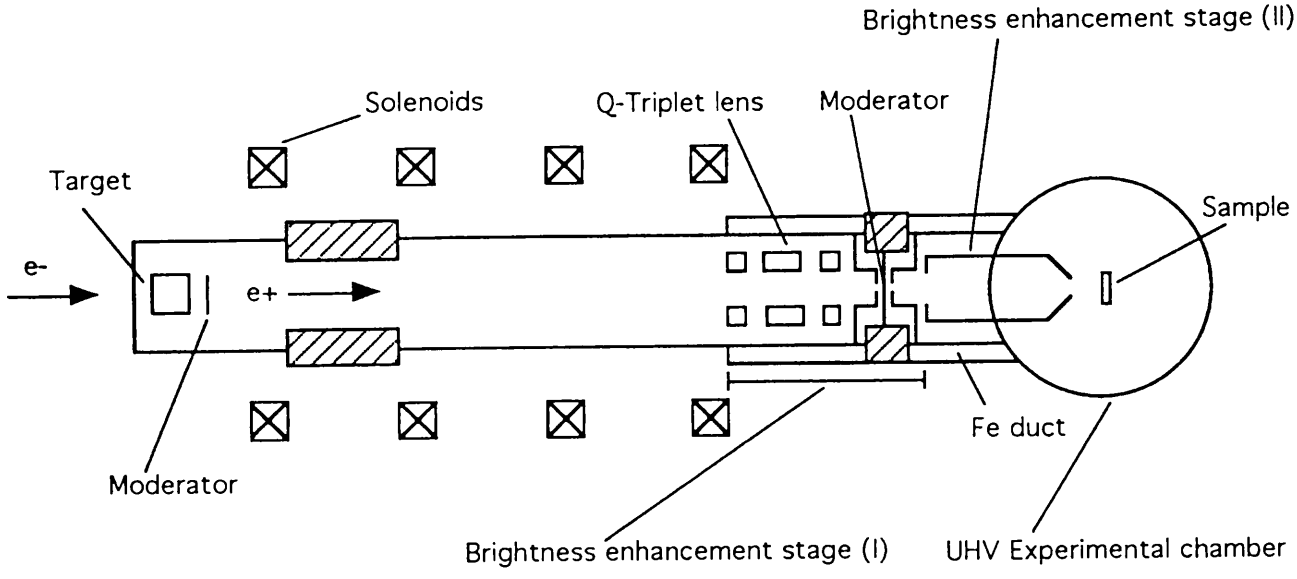

Fig. 35 Schematic layout of the slow-positron beam line. Electrostatic Q-triplet lens is installed at the end of the solenoidal magnet beam transport line. Focused slow-positrons (kinetic energy is up to 60 keV) will land on the moderator on a retarding electrode. From Q-triplet lens to the downstream, the slow-positron beam is transported in the electrostatic field.

1.3 Brightness Enhancement of Slow-positron Source (I) Transfer from Magnetic Transport to Electrostatic Transport

For material surface studies as well as depth-profile and other experiments, a so-called microbeam is a useful probe. In order to obtain a small spot-sized beam, collimation is widely used for electron or ion beams. We do not apply this method to the production of a slow-positron microbeam, because the intensity of the slow-positron beam produced by the PF 2.5-GeV electron linac is still weak compared with a conventional electron beam or ion beam. There does exist a novel method to produce a high-brightness positron beam. It is called positron re-emission from the surface. For almost all metals the positron work function is nearly zero, or negative. This means that positrons are much more easily emitted from the surface than are electrons. Once a positron having a large divergence angle enters some metal film, it diffuses to the counter side of the surface and emerges from the surface with a negligible divergence angle. These materials used for this purpose are called moderators. Figure 35 shows the schematic layout of this beam line. The end of the solenoidal magnetic beam transport, an electrostatic Q-triplet lens is installed so as to focus any slow positron onto a moderator on a retarding electrode. With this system, there is no need to pull up almost all of the transport duct. This is the brightness enhancement stage (I). This section is installed within iron duct so as to avoid the magnetic field. From the electrostatic Q-triplet lens to the sample holder, slow positrons are transported with only an electrostatic field. Between the retarding electrode and the sample, there will be one more stage. The design of this stage is now in progress.

Light Source

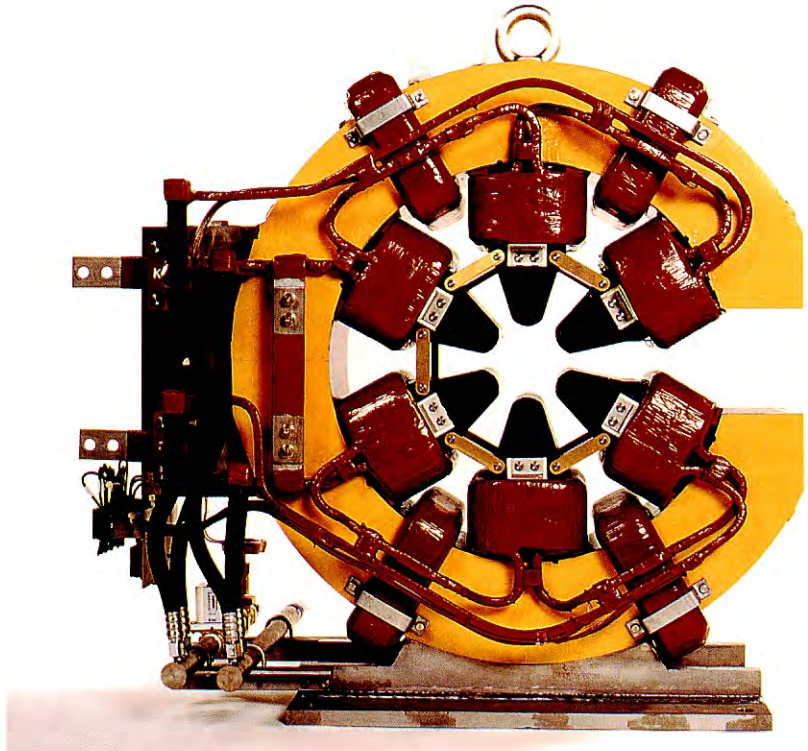

A Model Sextupole Magnet for the High Brilliance Configuration (see D.1)

CONTENTS

A. INTRODUCTION

During the scheduled shutdown last summer (from July 15 to September 30, 1993) one-sixth of the storage-ring chambers was vented to the atmosphere. A mirror for monitoring the beam profiles using visible light in BL21 was replaced by a new copper-made one. The old mirror had a distortion problem under high-current operation. Beam scrapers in the straight section (B04-05) were repaired, which had a heating problem under single-bunch operation in excess of a beam current of 50 mA. In beam channels BL01, 02, 13, and 20, vacuum components, such as large isolation valves, in bad condition were replaced by new ones.

On August 30 to September 3, 1993, an accelerator summer-school (OHO'93) was held at KEK. It has been held every summer from ten years ago; this year, the school featured especially synchrotron radiation. Young physicists of the Photon Factory gave lectures on basic subjects related to the beam orbits, emittances and beam instabilities of the electron-storage rings, the insertion devices and their synchrotron-radiation properties, as well as the optics of the beamlines

FEL research is underway at the PF storage ring in order to develop a coherent radiation source in the short-wavelength region. A gain measurement at 177-nm is our present goal. We are using BL02 where, at present, a 120-pole undulator is operating as the most popular insertion device at the Photon Factory. This undulator was replaced by an optical klystron in the summer of 1991. During routine user runs, the optical klystron is switched to the undulator mode. For an FEL-study, extra time is typically provided for 2-3 days, usually before or after long user runs. A movable VUV mirror for the FEL study was installed at BL02 in 1992. The mirror reflects 177-nm light emitted from the optical klystron down to the basement where a detection system is located. On December 7, 1992, a spectrum of spontaneous radiation from the optical klystron was observed at a beam energy of 0.75 GeV. During fiscal year 1993, many improvements were made on both the optical system and the detection system. The detection sensitivity of 177-nm light through the monochromater was increased by roughly 100 times by using a double-layered micro-channel plate. For gain measurements, we will use the 6th-harmonics of Nd-YAG laser light as an external source of 177-nm coherent light, which was successfully produced this fiscal year by using a nonlinear optical-crystal system. An optical pass used to lead the incident light from the laser source to the optical klystron was constructed. At present, transportation of the 177-nm light is under way. A precise matching on the incident light and circulating positron beams is required for both positioning and timing. Methods for adjustment are under investigation.

The spectral distribution of spontaneous emission results from interference of the radiation emitted by two undulators of the optical klystron. The spectrum has many sharp peaks around the central wavelength of 177 nm. The energy spread and angular spread of the beams broaden those peaks. This, of course, destroys the gain of the FEL; however, we are able to use this property for beam diagnostics. The impedance of the ring vacuum chambers destroys the beam quality; the bunch suffers increments in its length and spreads in beam energy. We are investigating how instabilities develop in the bunch by analyzing the spectrum of the spontaneous radiation of the optical klystron.

We have a program to upgrade the storage ring, which is to reduce the beam emittance by a factor of 5 and to increase the brilliance of the synchrotron radiation by approximately a factor of 10. Under this plan, we must add new quadrupole and sextupole magnets, each of which will have a small-bore radius of 40 mm (the present bore radius is 55 mm); their side yokes are open for the beamline ports. Since the bending magnets will not be changed, the source points and lines of the synchrotron light will also not be changed.

This program will take 3-4 years. Even during the construction phase, the time for user experiments in each fiscal year will not be cut very much. Construction will proceed simultaneously with that of the B-factory, which will build two storage rings, an 8-GeV electron ring and a 3.5-GeV positron ring. Beams will be injected into these rings directly from an 8-GeV linac and a 3.5-GeV linac, respectively. The present 2.5-GeV linac is to undergo a large change during these several years. Thus, the Photon Factory storage ring will inevitably operate with electron beams probably between 1995 and 1998. During those years the linac will undergo a large reconstruction phase. The low-emittance program of the PF storage ring will be completed in 1997, which will precede commissioning of the B-factory by one year. In fiscal years 1996 and 1997, the PF storage ring must undergo a long shutdown of approximately nine continuous months for the large construction of ring components. However, the cut in the user time during these fiscal years will be small, even in this phase. Commissioning of the new PF storage ring will be in Autumn of 1997.

A field measurement of a new quadrupole magnet for the low-emittance program was carried out during last summer (1993). Thirty-two quadrupole and

thirty-two sextupole magnets must be newly constructed. The vacuum systems must be significantly changed: sixteen chambers of the bending magnet sections with beam channel ports, sixteen ducts for straight sections and beam-position monitors and so on. Since new beam channels should be installed before the large construction phase, construction of the channels have to precede other things. The designs of the beam channels were almost finished this year. The RF-cavities should be replaced by improved ones in order to suppress any higher-order-mode resonances by using a damped structure.

B. SUMMARY OF STORAGE RING OPERATION

A summary of the operation times of the storage ring is given in Fig. 1. Table 1(a) gives the operation statistics for fiscal year 1992, and (b) those of between April 6 and December 20, 1993. The integrated beam current during each year and the percentage of time due to machine failures are given in Figs. 2(a) and 2(b), respectively. The injection intervals and average currents are given in Fig. 3. The initial stored current is 370 mA for user runs and the beam lifetime is 70-80 hours at 300 mA. The average stored current is about 320 mA during 24 hours of operation. During fiscal year 1992, 301.7 hours were provided for single-bunch users. In fiscal year 1993, the single-bunch time was 204.0 hours, as listed in Table 1. The initial current is 65 mA for single-bunch runs and the beam lifetime at 50 mA is 20-30 hours, which is limited mainly by the Touschek effect. Since the number of positrons in the neighboring buckets gradually increases during user runs, cleaning the beams in the neighboring buckets routinely takes place by

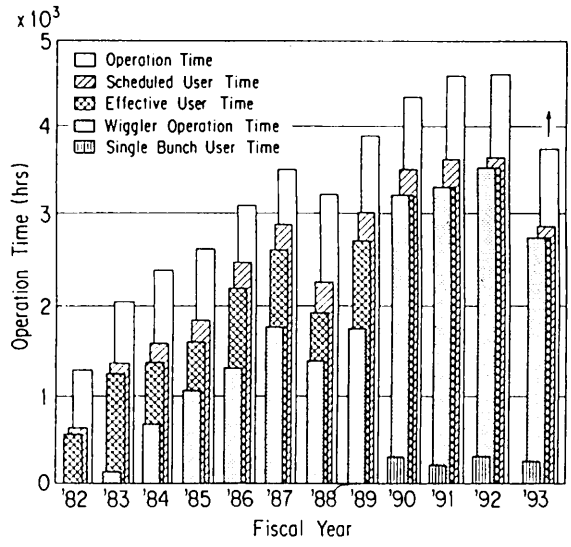

Fig. 1 Operation times of the storage ring.

Table 1(a). Statistics of the storage-ring operation during fiscal year 1992.

	Multi-bunch	Single-bunch	Total
Ring Operation Time (hours)	—	—	4616.0
Scheduled user time (hours)	3323.0	325.0	3648.0
Net user time T (hours)	3194.1	301.7	3495.8
Time used for injection (hours)	74.5	18.4	92.9
Integrated current in T (A·hours)	900.4	13.7	914.7
Average current in T (mA)	281.9	45.4	—
Number of injections	119	30	149
Interval between injections (hours)	16.1	10.1	—

Table 1(b). Statistics between April 6 and December 20,1993.

	Multi-bunch	Single-bunch	Total
Ring Operation Time (hours)	—	—	3756.0
Scheduled user time (hours)	2643.0	216.0	2859.0
Net user time T (hours)	2558.0	204.0	2762.0
Time used for injection (hours)	51.8	9.0	60.8
Integrated current in T (A·hours)	827.2	9.7	836.9
Average current in T (mA)	323.4	47.5	—
Number of injections	142	20	162
Interval between injections (hours)	18.0	10.2	—

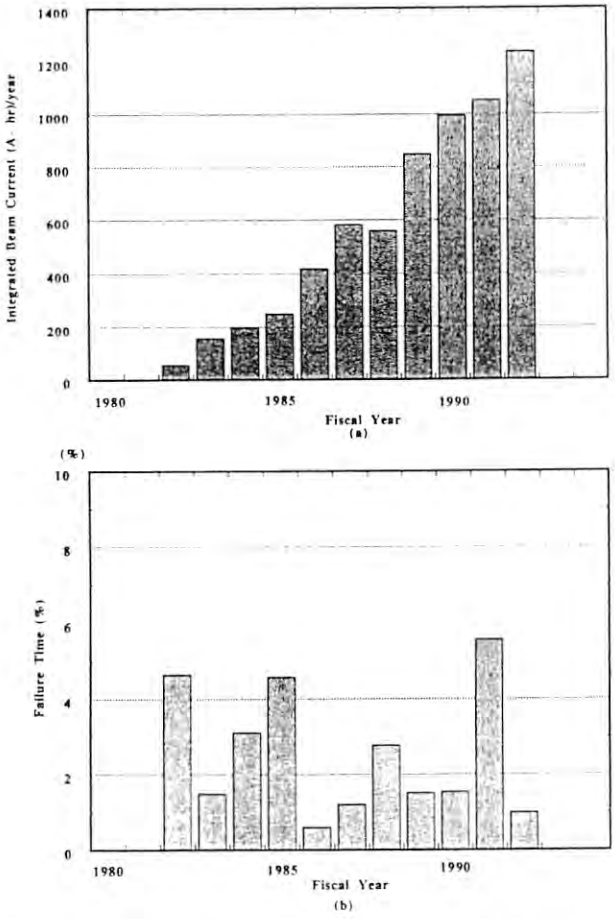

Fig. 2 (a) Integrated beam currents during each fiscal year. (b) Percentage of failure time of storage ring operation.

continuous running of the RF knock-out with the vertical scrapers at straight section B04-B05. A ratio of the satellite bunch to the main one is less than 10^{-6}. The ratio of better than 10^{-8} was achieved, which was measured with an avalanche-type photo-diode that is a high time-resolution X-ray detector.

Fig. 4 shows a plot of $I\tau$ (beam current × lifetime). This value is presently being kept at around 1400 A·min, which is very large.

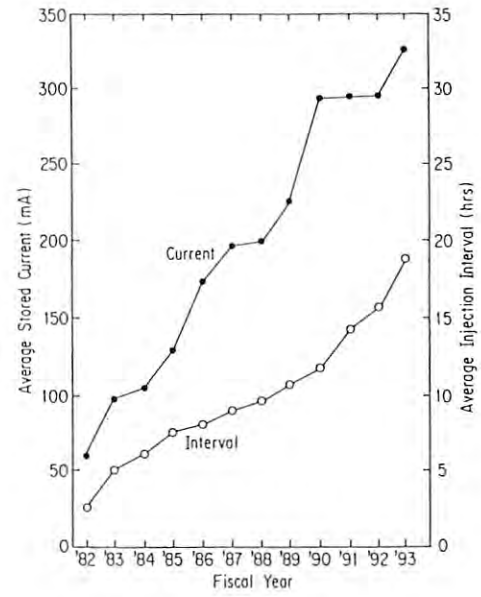

Fig. 3 Average stored currents and injection intervals.

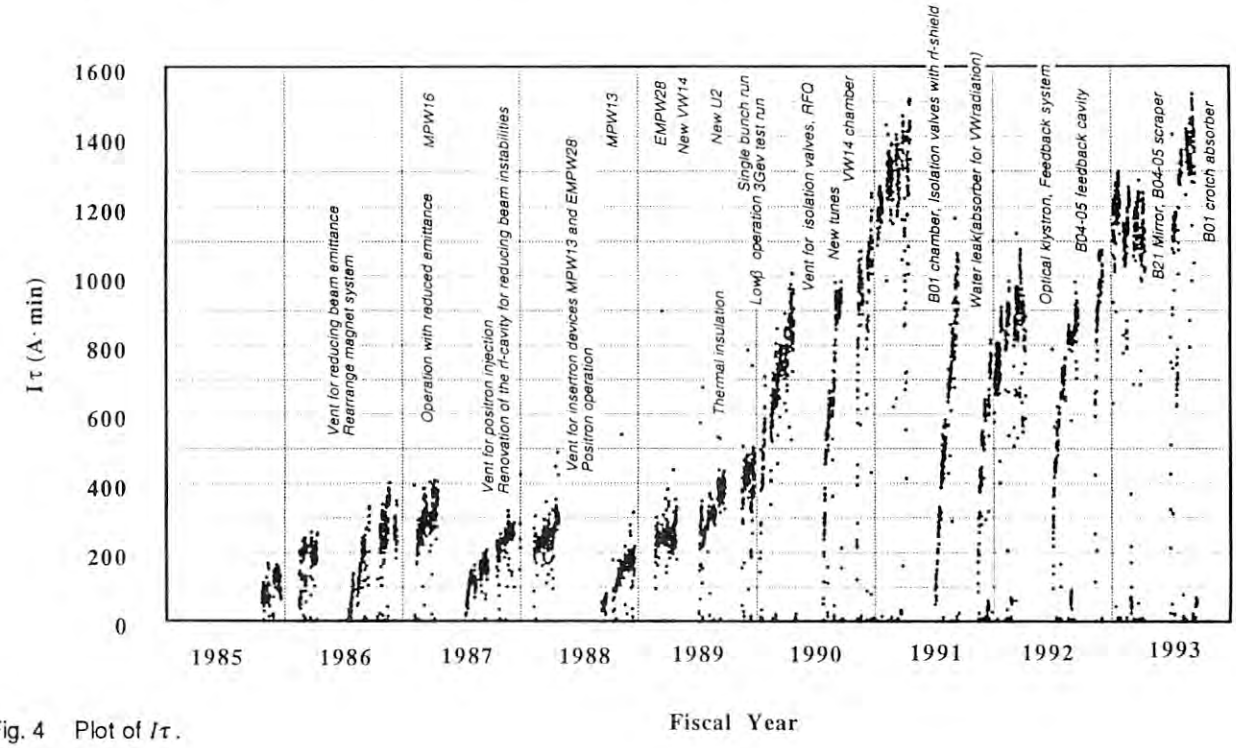

Fig. 4 Plot of $I\tau$.

C. IMPROVEMENTS AND DEVELOPMENTS

1. VACUUM

1.1 Interlock System for Cooling Water

To protect all vacuum components from heat-up due to SR irradiation, cooling water flows in the beam ducts and photon absorber masks exposed to SR. The cooling water must always be monitored, because the stoppage of flow in any water channel could cause serious trouble. There are a large number of conduit pipes in the ring, and each flow rate is different. The requirements that we considered for the flow-meter to be used in the ring are:

1) rated pressure is above 10 kg/cm^2,
2) reliable operation under 1 l/min of flow rate,
3) immune to electric noise,
4) compact and low cost, and
5) easy maintenance.

We selected a rotating magnet type of the flow-meter and made some modifications so as to improve the reliability. The flow-meter adopted in the ring is schematically shown in Fig. 5. There are 84 flow-meters in the ring, which should be monitored in the vacuum system. The AC output signal gained at each flow-meter is converted to a DC voltage. The DC signal is compared with a standard level which is adjusted to each ordinary flow rate. A circuit diagram of the amplifier is shown in Fig. 6. When any output signal voltage becomes under 70 % of its standard level, a failure signal is given to dump the stored beam.

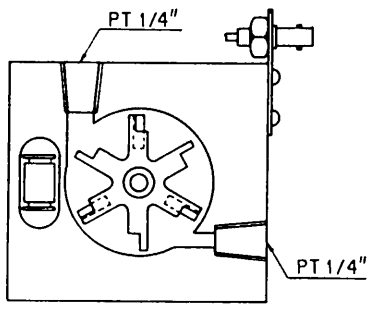

Fig. 5 Schematic drawing of the flow meter.

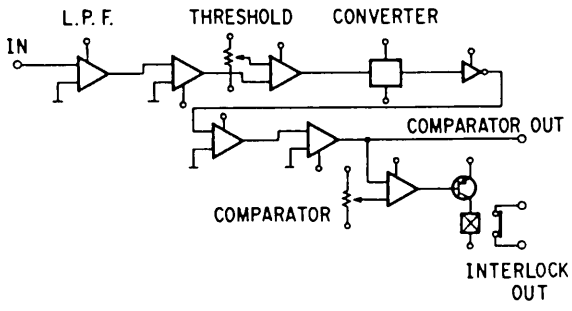

Fig. 6 Circuit diagram of the amplifier.

2. MONITOR

2.1 Installation of a Pinhole Tune Monitor

For measurement of the frequency dependence of the betatron amplitude, a pinhole tune monitor was installed on a branch of the visible light beam line for beam diagnostics.

The block diagram of the pinhole tune monitor is shown in Fig. 7. The betatron oscillation of a beam excited by a transverse kicker is detected with a pinhole and a photo multiplier tube (PMT). The existing RF-knockout (RF-KO) electrodes are used as a kicker for this purpose. Synchrotron radiation from a bending section is focused onto a pinhole with lenses, and is detected by the PMT. The kicker is driven by a burst wave from a sweep signal generator (SG). The output signal of the PMT is amplified with a current-input amplifier and its change corresponding to the amplitude of the oscillation is detected by a lock-in amplifier whose reference input signal is a square wave synchronized with the burst. The amplitude of the betatron oscillation is digitized, sent to a workstation and plotted as a function of the excitation frequency (Fig. 8). This system is also used for purifying the single bunch[1].

1) Photon Factory Activity Report 1992.

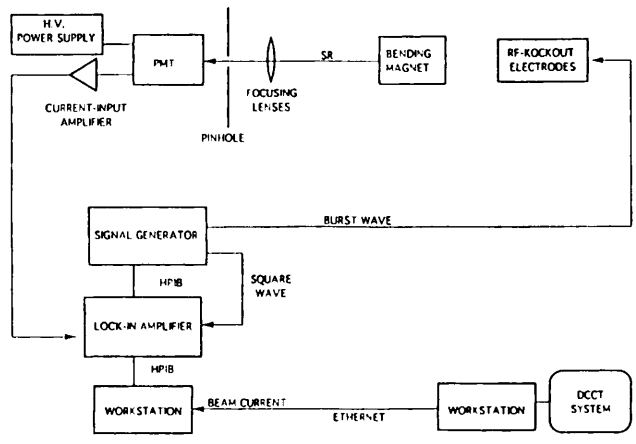

Fig. 7 Block diagram of the pinhole tune monitor.

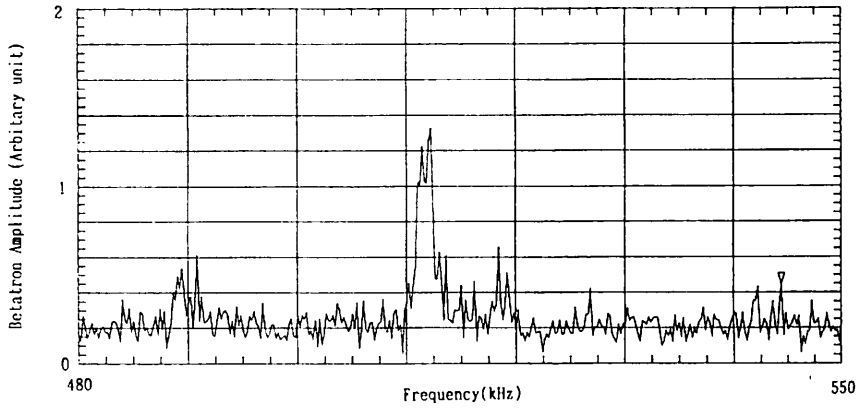

Fig. 8 Plot of the frequency dependence of the betatron amplitude.

2.2 Resolution and Stability of a Beam-Current Measurement

The stored beam current is measured using a DC current transformer manufactured by BERGOZ Co., France[1]. The PF ring is characterized by its long beam lifetime. The product of the current and the lifetime amounts to 1500 A·min. The lifetime is continuously recorded in order to monitor the operational condition of the accelerator. Since the beam-loss rate is very small, e.g. 1 μA per second, a resolution and stability of better than a few micro-amperes is required to estimate the beam lifetime accurately within a short period.

Under multi-bunch operation, a sufficient resolution and stability was accomplished. When an integration time of AD conversion was set at 20 ms, a resolution of 2 μA was deduced. The major factors that cause a zero drift of the DCCT are the external magnetic field and temperature change of the DCCT toroid. The magnetic drift was suppressed by magnetic shields of Mu-metal. The temperature-dependent drift was measured to be 8 μA/°C. Under multi-bunch operation, of which the initial current was 360 mA, the heating-up of the DCCT toroid was less than 4 °C. The zero drift due to the temperature variation was thus limited to within 30 μA.

Under single-bunch operation, the resolution was inferior to that under multi-bunch operation. When the initial stored current was 50 mA, the single-bunch beam caused a heating-up of the DCCT toroid up to 70 °C. A typical fluctuation observed in the DCCT signal under single-bunch operation is shown in Fig. 9. The characteristic time of the fluctuation was so long that an ordinary low-pass filter could not eliminate the fluctuation. The correlation between the rate of the temperature change and the power of the fluctuation was recognized. The faster the temperature changed, the harder the signal fluctuated. The origin of the fluctuation is attributable to unstable thermal strains induced in the DCCT toroid[2]. The heating-up of the toroid must be suppressed in order to improve the resolution under single-bunch operation.

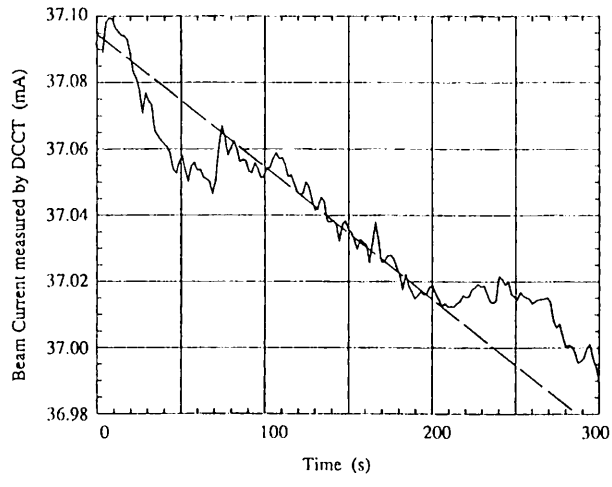

Fig. 9 Typical fluctuation in the DCCT signal observed under single-bunch operation. The broken line is a guide to the eye that represents a constant beam loss.

1) Photon Factory Activity Report #10 (1992) R-13.
2) T. Honda, Y. Sato and T. Katsura, *Proc. 9th Symposium on Accelerator Science and Technology*, Tsukuba, Japan, 1993, p345.

2.3 Improvement in the Photon Counting System

The photon counting system that was installed in BL-21 in order to measure the bunch time structure under the single-bunch condition has been improved to achieve a better time resolution. As shown in the Fig. 10, a new timing system was adopted to avoid any jitter due to the longitudinal dipole oscillation of the bunch; new focusing elements were installed in order to minimize any effects of undesirable light, such as stimulated radiation from the mirror or the glass of the view port, or stray light due to reflection by the inner wall of the beam pipe.

In the old system, the timing signal corresponding to a certain bunch was generated by a circuit in which the RF signal (500MHz) was divided by the harmonic number (312). However, the center of mass of a bunch oscillates around the stable phase of the RF, even under the single-bunch condition. A fast PIN photodiode and a constant-fraction discriminator were used in the new timing system to detect the bunch center more strictly. The rms timing error is negligible in the new system, as compared with the bunch length.

Since a "gross" longitudinal bunch shape obtained with a photon counting system is given by the convolution of the true-bunch time structure and the impulse response of the system, it is essential to make the response as fast as possible so as to obtain the "net" bunch shape precisely by the deconvolution method. The effect of the transit time spread (TTS) in the photomultiplier tube (PMT) and the discriminator on the response was discussed in the previous activity report. Any undesirable light might also affect the time response. New optical elements were set to feed the PIN photodiode and to reject spurious light. SR reflected by a beam splitter is focused on an iris with a lens and led to the photomultiplier tube without loss. On the other hand, since spurious light cannot be focused on the opening of the iris, the main part is rejected by the stop of the iris.

Preliminary experiments show that the time resolution has been greatly improved.

3. INSERTION DEVICE

3.1 Development of a High-Field Superconducting Wiggler

A superconducting wiggler with an extremely high field has been designed. The wiggler is expected to produce a maximum field strength of 10 T on the beam orbit. The critical energy of the synchrotron radiation shifts to 10-times larger than that produced by the bending magnet. The brilliances of the radiation are shown in Fig. 11[1]. The critical energies are 42 keV at a beam energy of 2.5 GeV and 60 keV at 3.0 GeV. If installed into the Tristan AR, it reaches 280 keV at 6.5 GeV. The high critical energy has possibilities to develop new types of applications of synchrotron radiation.

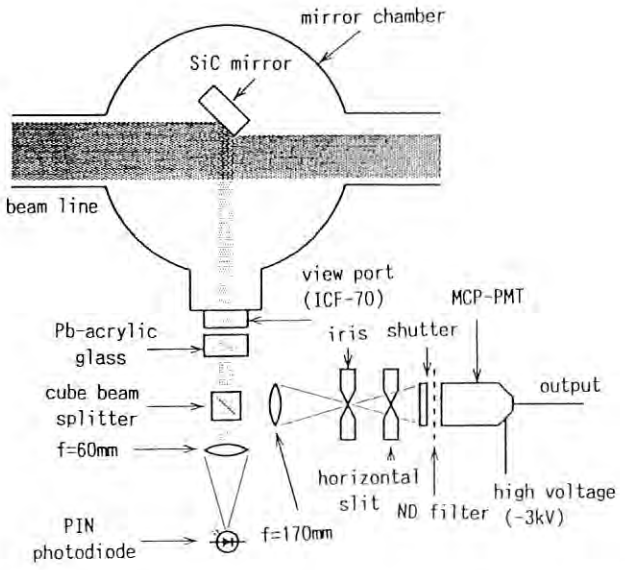

Fig. 10 Block diagram of the photon counting system with a new timing system and optical elements.

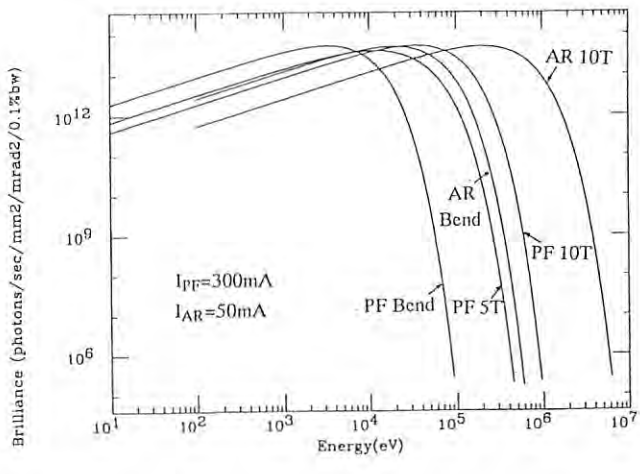

Fig. 11 Brilliances of the radiation from the 10T wiggler.

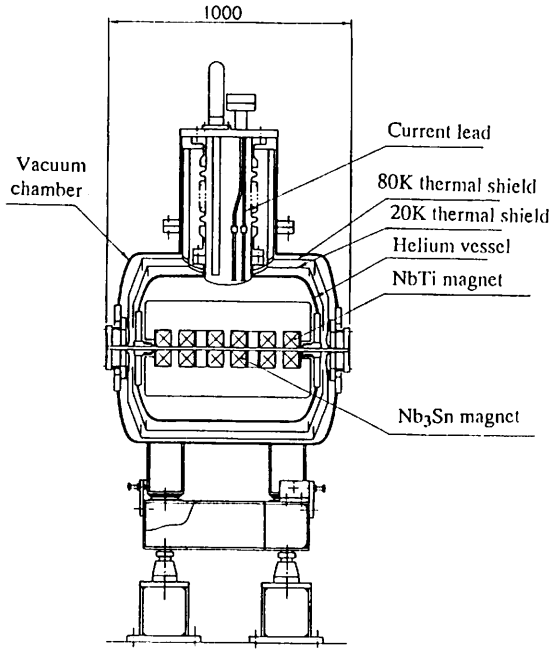

Fig. 12 Schematic design of the 10T superconducting wiggler.

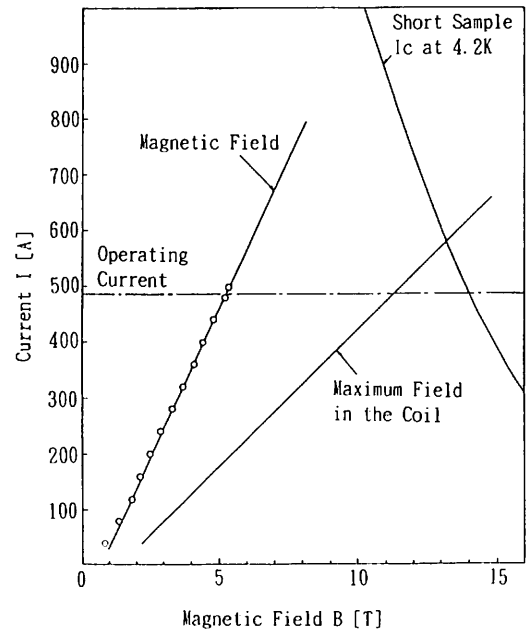

Fig. 13 Excitation curve of the Nb_3Sn coil.

A schematic design is shown in Fig. 12. The wiggler has 3 pairs of coils. The center pair produces a 10 T field on the beam orbit. The beam wiggles on the horizontal plane and radiates horizontally polarized photons. The wiggler currently in use at BL14 is a vertical type which allows for vertically polarized photons. The requirement is mainly due to technologies of instrumentation. The technologies now proceed and the requirement of vertical polarization is becoming not so essential. Thus, the horizontal type, which has advantages to produce a higher field strength, is proposed, i.e. it can have a narrower magnet gap than the vertical type.

To produce an extremely high field, Nb_3Sn is used for the superconducting material. Nb_3Sn has a much better performance than does the NbTi conventionally used, but is more difficult to deal with, since it is weak and brittle. A racetrack-shaped coil was wound in order to study the Nb_3Sn characteristics. Fig. 13 shows an excitation curve of the coil. The measured fields are plotted as circles, and are compared with the calculated and critical values. The field strength at a point 9.5 mm distant from the center of the pole face reached 5.3 T at an operating current of 492 A. That is equivalent to producing a field strength of about 10 T with a pair of magnets comprising the same type of racetrack magnet constructed in this study.

A phenomenon which we had never experienced was observed during the training of the coil. The magnet showed a progressive improvement in performance until it had experienced 11 quenches. However, after the 11-th quench, its performance became degraded, and could not be improved any more. It is considered that microcraking of the Nb_3Sn filament occurred under macrocracking caused by quenches, and that the critical current thus decreased. If it is so, this phenomenon would be a characteristic feature of Nb_3Sn resulting from its brittleness. Although this phenomenon seems to be serious, the coil keeps 80 % of the maximum performance. The next step is to construct a pair of coils and to produce a field strength of 10 T.

1) The spectra are calculated by using Kitamura's program.

D. RESEARCH

1. Design Study of a High-Brilliance Configuration

As a result of decade-long research and development, the performance of the PF ring has been steadily improved. In particular, the beam current, the beam lifetime and the beam stability have achieved the highest level in the world. However, because of its relatively higher beam emittance (130 nm-rad), the brilliance of the SR beam is lower by one or two orders of magnitude than those of third-generation rings. To compete with these rings in the next decade, a lower beam emittance is indispensable.

A design study[1] showed that a small beam emittance of 27 nm-rad could be achieved by doubling the number of quadrupoles and sextupoles in the FODO cells, without any changes in the bendings. The present and new optics are shown in Figs. 14 and 15. The beam parameters are summarized in Table 2. The emittance reduction will result in a ten-times higher brilliance of the SR beam from the existing insertion devices, as shown in Fig. 16. Since the small dynamic aperture due to the strong sextupole fields are considered to be an essential problem for successful operation, a careful orbit analysis is progressing. The beam lifetime is expected to be more than 40 hours in spite of the strong Touschek effect.

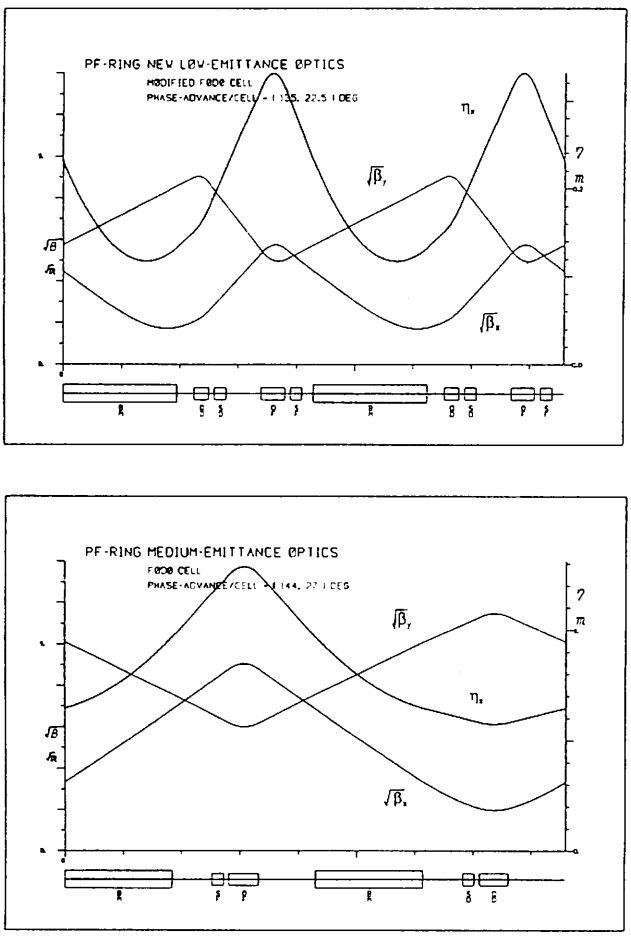

Fig. 14 Present (upper) and high-brilliance (lower) optics. A part of the FODO cells is shown

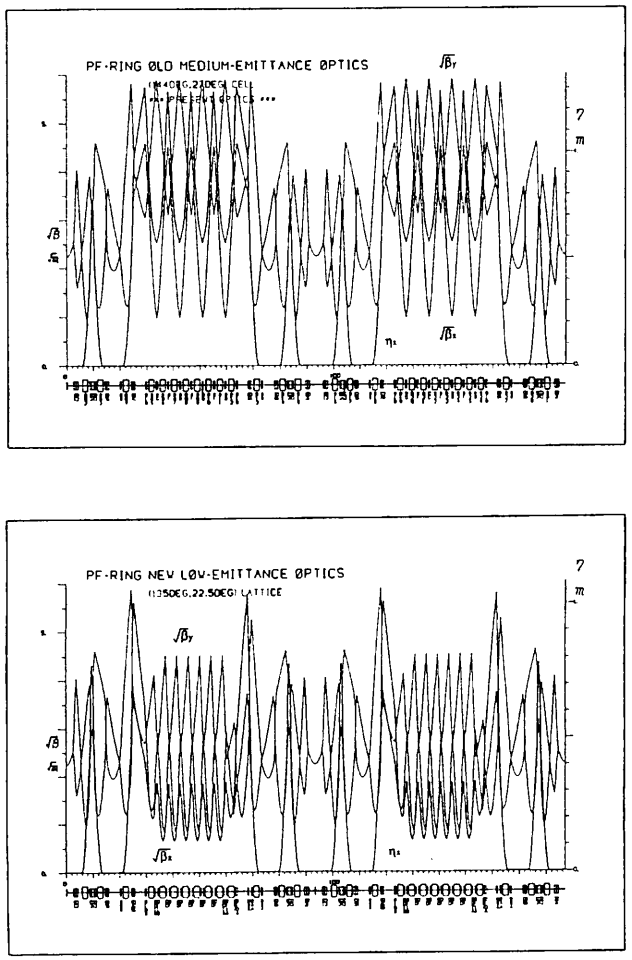

Fig. 15 Present (upper) and high-brilliance (lower) optics. One half of the ring is shown

Table 2. Beam parameters

	Present	High Brilliance
Emittance	130 nm-rad	27 nm-rad
Momentum Compact.	0.016	0.0043
Betatron Tune	(8.44,3.30)	(10.85,4.20)
Chromaticity	(-13.5,-9.0)	(-16.1,-13.3)

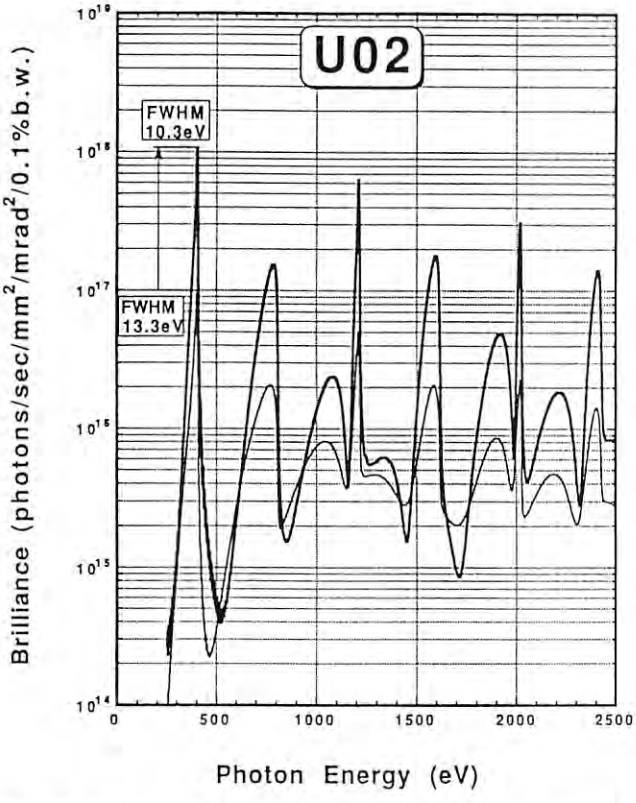

Fig. 16 Brilliance of the undulator (U#2) for the present (plain) and high brilliance (bold) optics.

Since much higher field gradients of the quadrupoles and sextupoles in the FODO cells will be required, reinforced magnets with small-bore radii were designed. They are of the Collins type, so as not to disturb the SR beam extraction to the existing beam lines. The model magnets were fabricated and the field measurements are progressing. Since the optical functions near to the injection point will be changed, the injection kickers should be reinforced, and are being developed. The vacuum duct in the FODO cells should be modified so as to be suitable for the smaller bore radii of the new magnets. The configuration of the vacuum components, the beam monitors and the front-ends of the SR beam channels have been carefully designed, considering the limited spaces allowed for them[2].

1) M. Katoh et al., "Design Study on a High Brilliance Lattice of the PF Storage Ring", Proc. of the 9th Symp. on Accel. Sci. and Tech., 1993
2) M. Katoh and Y. Hori (ed.), "Report of the Design Study on a High Brilliance Configuration of the PF Storage Ring", KEK Report 92-20 (in Japanese), 1993

2. Field Measurement of Model Magnets for a High-Brilliance Configuration

Two model magnets for a high-brilliance configuration[1] were newly constructed during this fiscal year. One is a defocusing quadrupole magnet; and the other is a sextupole. Since the magnets have to be set in a limited space, interference between the magnets and the SR beam ports is inevitable if the magnets are the same type as the existing ones. It is thus necessary to put a split space in the iron yoke so as to pass through synchrotron radiation. This means that the yoke structure obtains a geometric asymmetry, and a structural distortion of the iron yoke and a large shift of the magnetic center will thus be induced due to magnetic stress without any mechanical support. We therefore adopted a Collins-type magnet, for which the magnetic center does not move very much due to its geometric symmetry, and attached some non-magnetic supports at the opposite side to the split space of the yoke and among the magnetic poles. The model magnets were designed in consideration of the results obtained by a computer simulation. Fig. 17 shows

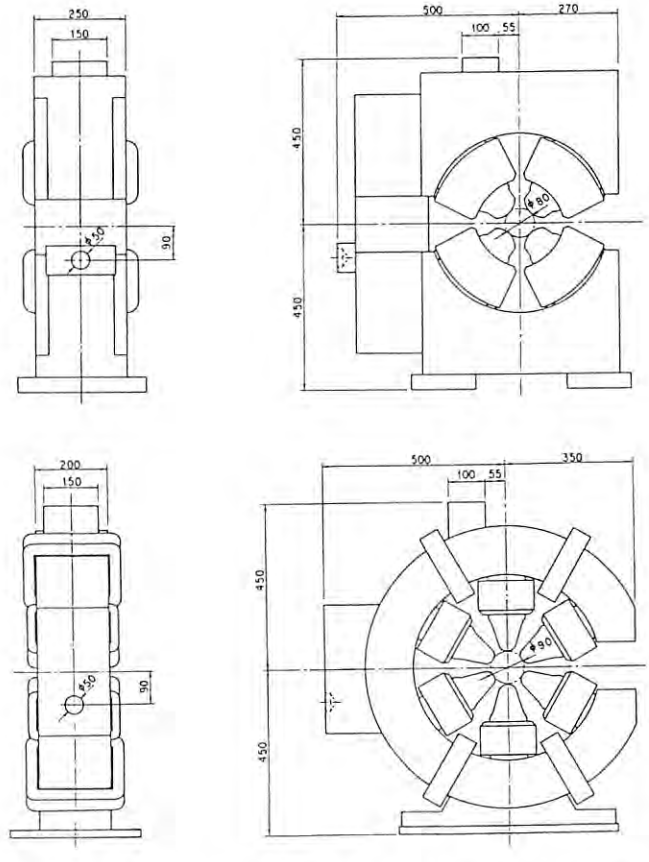

Fig. 17 Schematic view of the model magnets. (a) Quadrupole magnet, (b) Sextupole magnet.

schematic views of these magnets. The specifications are also tabulated in Table 3.

We first measured the field gradient of the quadrupole magnet by a search coil. Fig. 18 shows the distribution of the field gradient at several excitation currents. The horizontal axis represents the horizontal position; the zero means the geometric center of the magnets. The vertical axis indicates the relative value of the field gradient to that at the geometric center.

Table 3. Specifications of the model magnets

Magnets	Quadrupole (QD type)	Sextupole
Bore radius (mm)	40	45
Magnet length (m)	0.25	0.20
Max. field (T/m, T/m^2)	24	600
Max. Current (A)	900	400
Coil turn number/pole	19	17

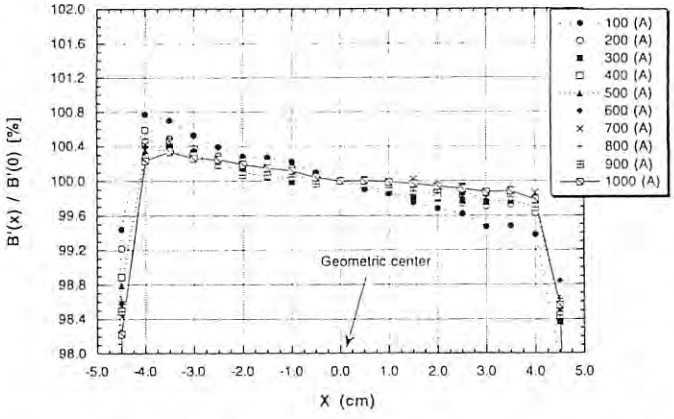

Fig. 18 Relative field-gradient distribution of the quadrupole magnet.

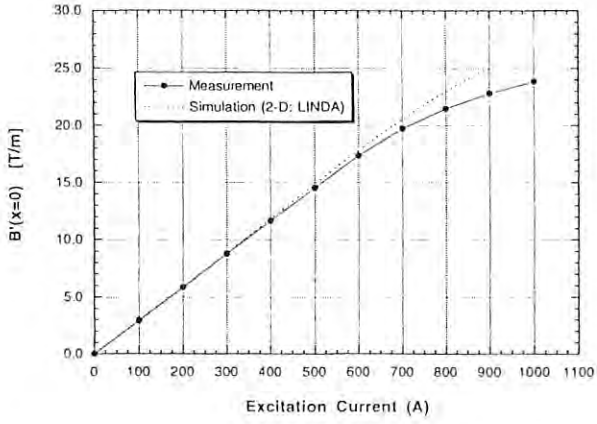

Fig. 19 Excitation curve of the quadrupole magnet.

Although a sextupole component appeared in the lower excitation current, the goodness of the distribution is acceptable. Fig. 19 shows the measured excitation curve together with the result simulated by a two-dimensional code (LINDA). The measured field was saturated earlier at a lower current than the simulated one. We guess that it is a three-dimensional effect due to the magnet length. The field gradient, however, is sufficiently satisfied for the most severe case of the optics. Another field measurement using a rotating coil is now progressing, and the sextupole magnet is also waiting for a measurement.

1) M. Katoh, A. Araki, Y. Kobayashi and Y. Hori, Proceedings of the 9-th Symposium on Accelerator Science and Technology, Aug. 1993

3. Test Construction of a Pulse-Forming-Line-Type Power Supply for the Kicker Magnet

A test model of a pulse-forming-line (PFL) type kicker magnet power supply was constructed and tested for full-aperture injection in the new low-emittance project of the PF ring. In the conventional PFL-type kicker power supply, the outer conductor of the pulse-forming line is normally grounded. The cathode of the thyratron tube thus obtain a high-voltage level in every excitation of the power supply. To insulate the driving circuit of the thyratron becomes harder when the charging voltage of the PFL goes beyond 60 kV. To avoid this problem, we have made

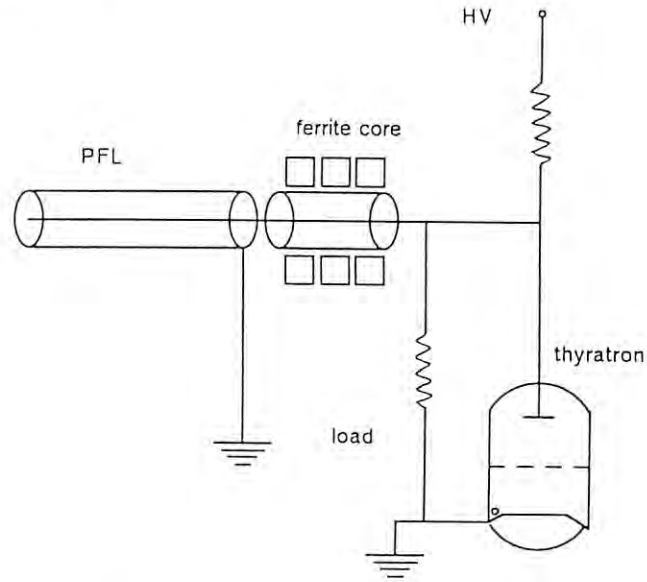

Fig. 20 Block diagram of the power supply.

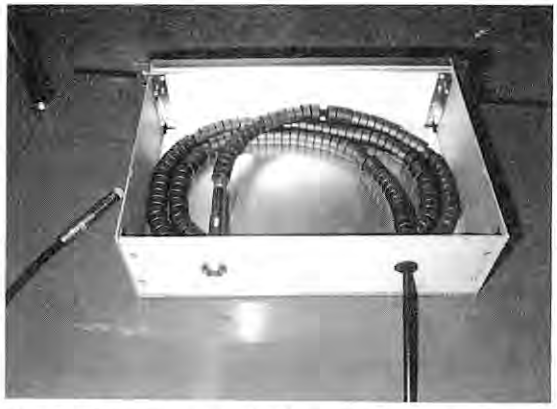

Fig. 21 Photograph of the ferrite core used to suppress the in-phase current.

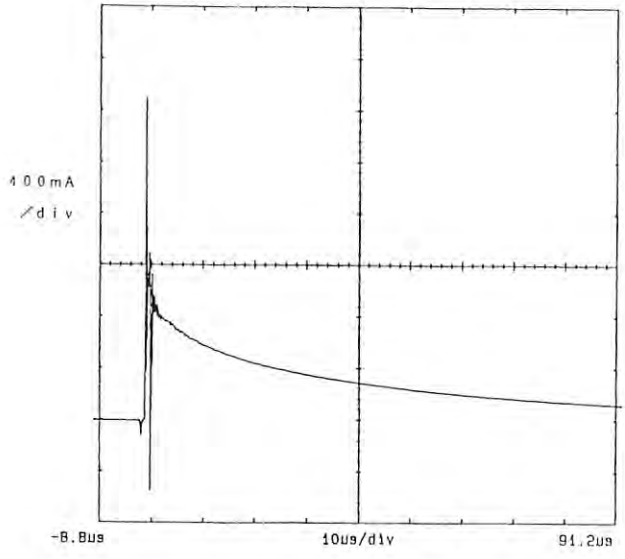

Fig. 22 Preliminary results of suppressing the in-phase current.

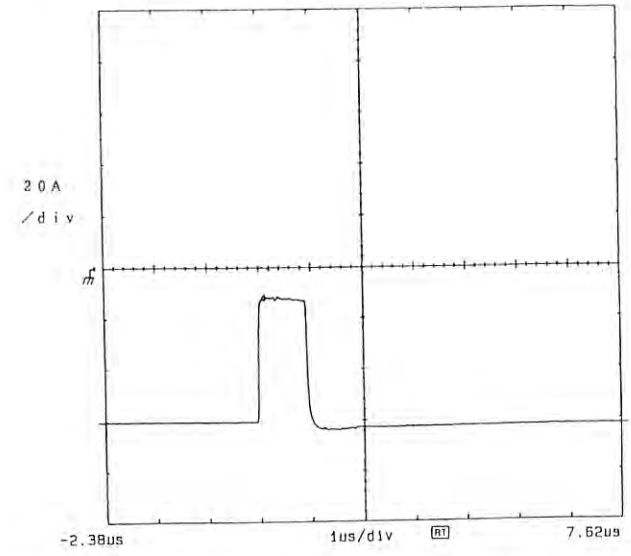

Fig. 23 Preliminary results of the output current

a new design of the power supply in which the cathode of the thyratron tube is ground. A block diagram of the power supply is shown in Fig. 20. In this design, an in-phase current appears from the both ground point of the outer conductor of the pulse-forming line and the cathode of the thyratron tube. The existence of in-phase current prevents current in the load magnet. To suppress the harmful in-phase current, we apply troidal ferrite cores between the grounded point of the outer conductor of PFL and output of the PFL (Fig. 20). A photograph of the ferrite core assembly is shown in Fig. 21. A result of suppressing the in-phase current is shown in Fig. 22. The in-phase current was suppressed by less than a few A by ferrite-core loading. A result of the pulse shape of the output current is shown in Fig. 23. A 50Ω resister was used as a laod. Suppression of the in-phase current by the use of a ferrite core causes an output current to the load.

4. Measurement of the Dynamic Aperture

In the PF-ring, because the strong octupole magnets were used to suppress the transverse coupled-bunch instabilities under multi-bunch operation, the dynamic aperture could be substantially reduced. Actually, we have observed that the beam lifetime and the injection rate were strongly dependent on the octupole magnetic strengths; this was qualitatively consistent with the result of a computer simulation[1]. However, since the beam lifetime and injection rate included other effects, it was difficult to obtain the quantitative size of the dynamic aperture. We thus measured the size of the dynamic aperture of the ring using a more direct method, and compared it with a computer simulation quantitatively.

In the last year, kicker magnets with a fast pulse width were installed into the ring. The specification of the kicker magnets is shown in Table 4. Since they can provide a stored beam with a large kick angle at some time, we can make the beam circulate with a large

Table 4. Specifications of the fast kicker magnets

Magnet Core Material	Ferrite
Coil Turn Number	2
Core Gap [H/V]	56/96 mm
Core Length	150 mm
Magnet Inductance [H/V]	2.2/1.1 μH
Maximum Charging Voltage	40 kV
Maximum Repetition Rate	0.5 Hz
Pulse Width [H/V]	425/335 nsec

amplitude. When the beam oscillation reaches the aperture limitation, the beam is lost from the ring. We can therefore evaluate the aperture by measuring the beam loss with increasing the oscillation amplitude. Here, we define the aperture as the amplitude where the beam current becomes half. The oscillation amplitude given by the kicker magnets is calibrated by the scraper.

The measurements were made at several excitation currents of the octupole magnets in the single-bunch positron mode. The initial stored current was fixed at 5 mA. Fig. 24 shows the oscillation amplitude with a half loss of the beam as a function of the octupole excitation currents in the horizontal direction. It also includes the result of a computer simulation. It is clearly understood that the aperture is physically determined without the octupole excitation. In fact, the effective physical aperture at the scraper is about 30 mm, which is predicted from that of the narrowest duct size in the ring (VW#14 duct). On the other hand, when the octupole magnets are excited, the aperture seems to be dynamically limited because of a remarkable dependence. As a result, the measurement almost agrees with the dynamic aperture predicted by a computer simulation.

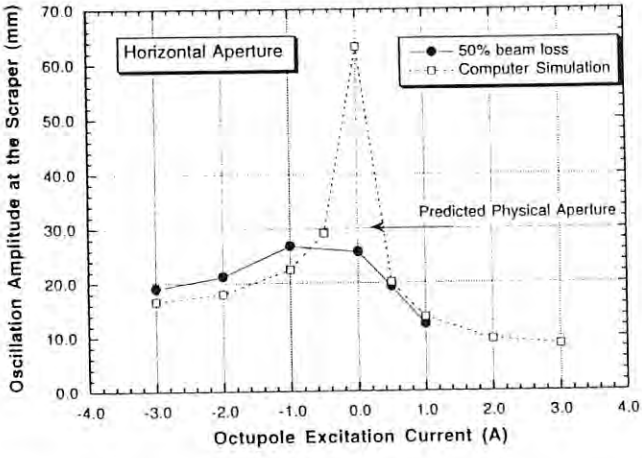

Fig. 24 Oscillation amplitude at the scraper as a function of the octupole excitation currents in the horizontal direction. The closed circles indicate the measured value and the open squares the results of a computer simulation.

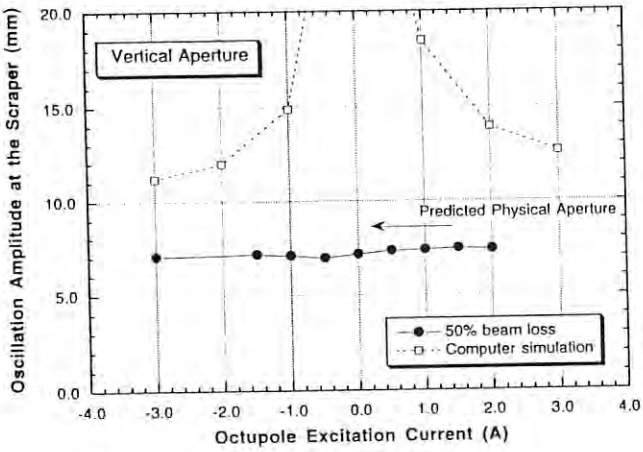

Fig. 25 Same as Fig. 24, but in the vertical direction.

Fig. 25 shows the measurement result for the vertical aperture. A remarkable octupole dependence is not observed. This suggests that the vertical aperture is always determined physically under this experimental condition, even if the octupole magnets are strongly excited. This result is consistent with the prediction of the computer simulation.

1) M. Katoh et al., "Dynamic Aperture of the Photon Factory Storage Ring", Particle Accelerators, Vol.28, p.17, 1990

5. Construction and Operation of the Longitudinal Feedback System

The longitudinal feedback system described in the previous report[1] has been constructed. The feedback system operates on up to four equally spaced bunches in order to suppress any longitudinal coupled-bunch instabilities under low-energy (0.75 GeV) operation for FEL experiments. A block diagram of the system is shown in Fig. 26. Phase oscillations of the bunches are detected independently, and their phases are shifted by 90° in order to obtain energy oscillation signals. The signals are combined into one signal which is used to correct the energy deviation by means of a feedback cavity. A detailed description of the system is given in ref. 2).

Fig. 27 shows the test result of the feedback at a beam energy of 2.5 GeV. In this experiment, the strong coherent oscillation of a bunch (Robinson instability) was deliberately excited by tuning one of the accelerating cavities, and the oscillation was damped by the feedback. Also, the feedback system was successfully operated at a beam energy of 0.75 GeV, and the longitudinal coupled-bunch instabilities were largely suppressed. As a result, a stored current of 40 mA in four bunches was achieved at 0.75 GeV. The feedback system is now routinely used under low-energy operation for the FEL experiments.

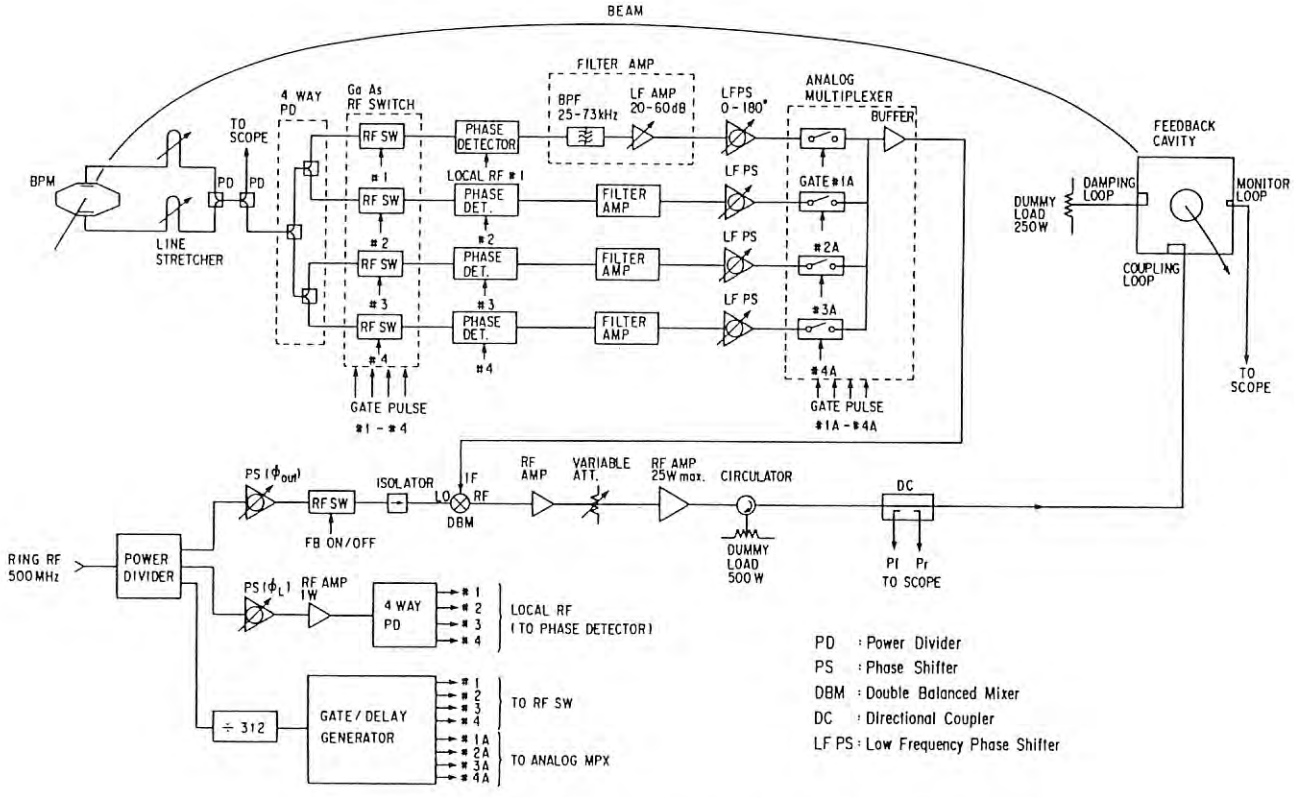

Fig. 26 Longitudinal feedback system for FEL operations with four bunches.

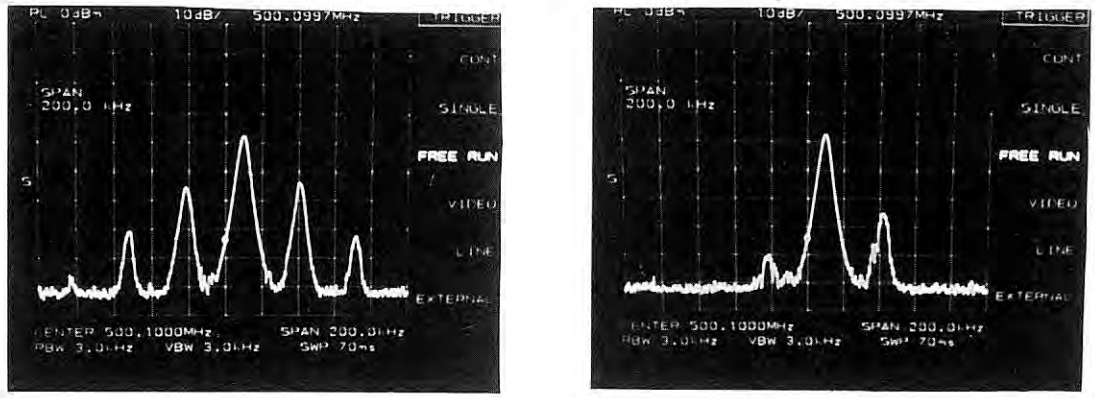

(a) Feedback off. (b) Feedback on.

Fig. 27 Effect of the longitudinal feedback. Spectra of a BPM signal without and with feedback. Beam energy, 2.5 GeV; beam current, 8.6 mA (in single bunch); abscissa, frequency (center 500.1 MHz, span 200 kHz); ordinate, spectrum (10 dB/div.).

Under routine multibunch and single-bunch operations, the body of the feedback cavity is removed from the ring and the ceramic gap is shielded by a cover. It was found that there is a large parasitic mode loss at the ceramic duct shielded by the cover. The temperature of the ceramics was raised up to 100 °C at a stored current of 70 mA in a single bunch. Some improvements are needed in the future. No problems were observed under routine multibunch runs of up to 360 mA.

1) Photon Factory Activity Report #10 (1992) p. R-5.
2) S. Sakanaka et al., KEK Preprint 93-54 (1993).

6. Photodesorption Yields of a Clean Z Test Duct

The outgassing characteristics of vacuum ducts under SR irradiation are very important for the ring vacuum system. The outgassing rate is evaluated by the photodesorption yield η [molecules/photon]; η depends on the material and surface treatment. To examine the characteristics of a stainless-steel "clean Z" for the UHV component, η was measured at a test beam port in the ring with the collaboration of NKK Co. The clean Z is a minimum carbon-content material developed and supplied by NKK Co. The experimental set-up is schematically shown in Fig. 28. The test duct is a cylindrical pipe with two gauge ports made of the clean Z. Its length is 800 mm and its diameter is 150 mm. The SR beam with 3 mrad of horizontal width incidents the test duct through a 22(hor.) x 10 (vert.) mm^2 rectangular orifice. Since the incident angle is 2.5 degree, the irradiated length is 500 mm. The incident photon flux is 2.9 x 10^{17} photons/s at 300 mA of the storage beam. The outgassing rate was measured by a through-put method using two BA gauges and a quadrupole mass filter. The experimental result is shown in Fig. 29, in which the x-axis is the total incident photon dose and y-axis is the η calculated from the total (nitrogen equivalent) and partial outgassing. Although η was very large at the beginning of the irradiation, every η decreased exponentially with the incident photon dose. The η of CO reached 2 x 10^{-6} at 1 x 10^{24} of the dose. The dose corresponds to 288 A·h of the ring operation time. This means that the above η-value can be achieved during 50 days of operation.

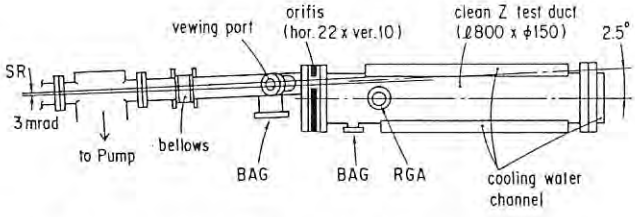

Fig. 28 Experimental set-up for the measurement of η.

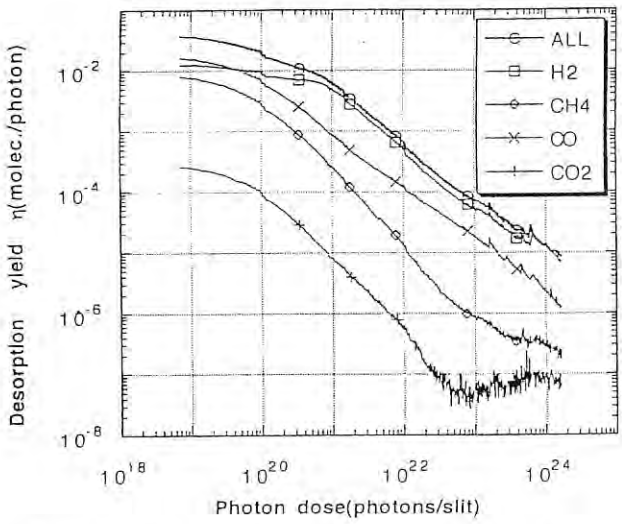

Fig. 29 Change in the η of the clean Z test duct with the total incident photon dose.

7. Observation of the TOK Spontaneous Emission

We measured the spontaneous emission from the transverse optical klystron (TOK) located in the straight section between B01 and B02. The TOK comprises two undulators (λ_u=9cm, N_u=19, K_{max}=5.9) and a dispersive section (N_d=90~200). The energy of the electron beam is lowered to 0.75 GeV so that the first harmonics from the TOK may be obtained at 177 nm with K=3.9.

The FEL gain is strongly affected by the modulation factor (*Fm*), which gives a characteristic oscillating structure in the TOK spectrum, and *Fm* depends mainly on the energy spread (σ_γ/γ) in the electron beam. We have therefore estimated *Fm* as well as the energy spread from the measured TOK spectra.

As shown in Fig. 30, the emission (λ_1=177nm) from the TOK is transported in the FEL beam line attached to beam line BL-2. Since the 1-m normal

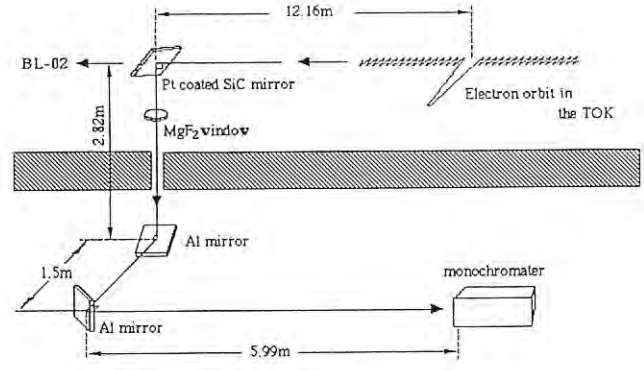

Fig. 30 Schematic layout of the FEL beam line.

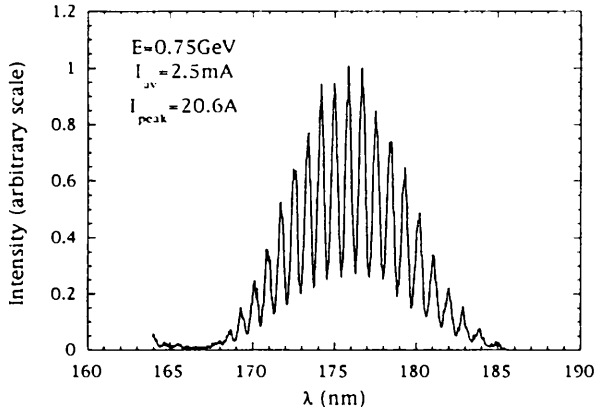

Fig. 31 Typical TOK spectrum obtained in single-bunch operation.

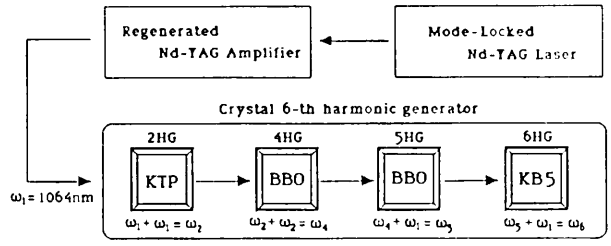

Fig. 32 Schematic diagram of the laser system for an FEL gain measurement.

incidence monochromater for the spectral measurements is located downstairs of the straight section, the TOK light is deflected vertically by a Pt-coated SiC mirror. MgF_2 is used for separating the FEL beam line (low vacuum) from the BL-2 line (ultrahigh vacuum). To detect emission in the vacuum ultraviolet region, an Au-coated MCP with a fluorescence plate and a photodiode array has been used. The spectral resolution is estimated to be 0.042 nm from the spatial resolution of the MCP.

Fig. 31 shows an example of the measured TOK spectra, which is thought to correspond to the highest FEL gain. From the spectral profile, F_m and σ_γ/γ are 0.58 and $3.8*10^{-4}$, respectively. Since the peak beam current is estimated to be 20.6 A, the FEL gain is expected to be 12.5 % with Nd=183.

To make an FEL gain measurement, external coherent radiation of 177.3 nm is necessary. The radiation has been generated by up-conversion using an Nd-YAG laser. The scheme of the conversion system is shown in Fig. 32. A nonlinear optical crystal system has been used with a mode-locked Nd-YAG and a regenerative amplifier. With the primary laser energy (30 mJ), an output pulse power of 177.3 nm is thought to exceed 100 kW. This VUV laser will be transported to the TOK for the FEL gain measurement.

E. 2.5 GeV LIGHT SOURCE SPECIFICATIONS

This section contains major specifications of the 2.5 GeV PF ring to provide quick and handy information for users and machine physicists.

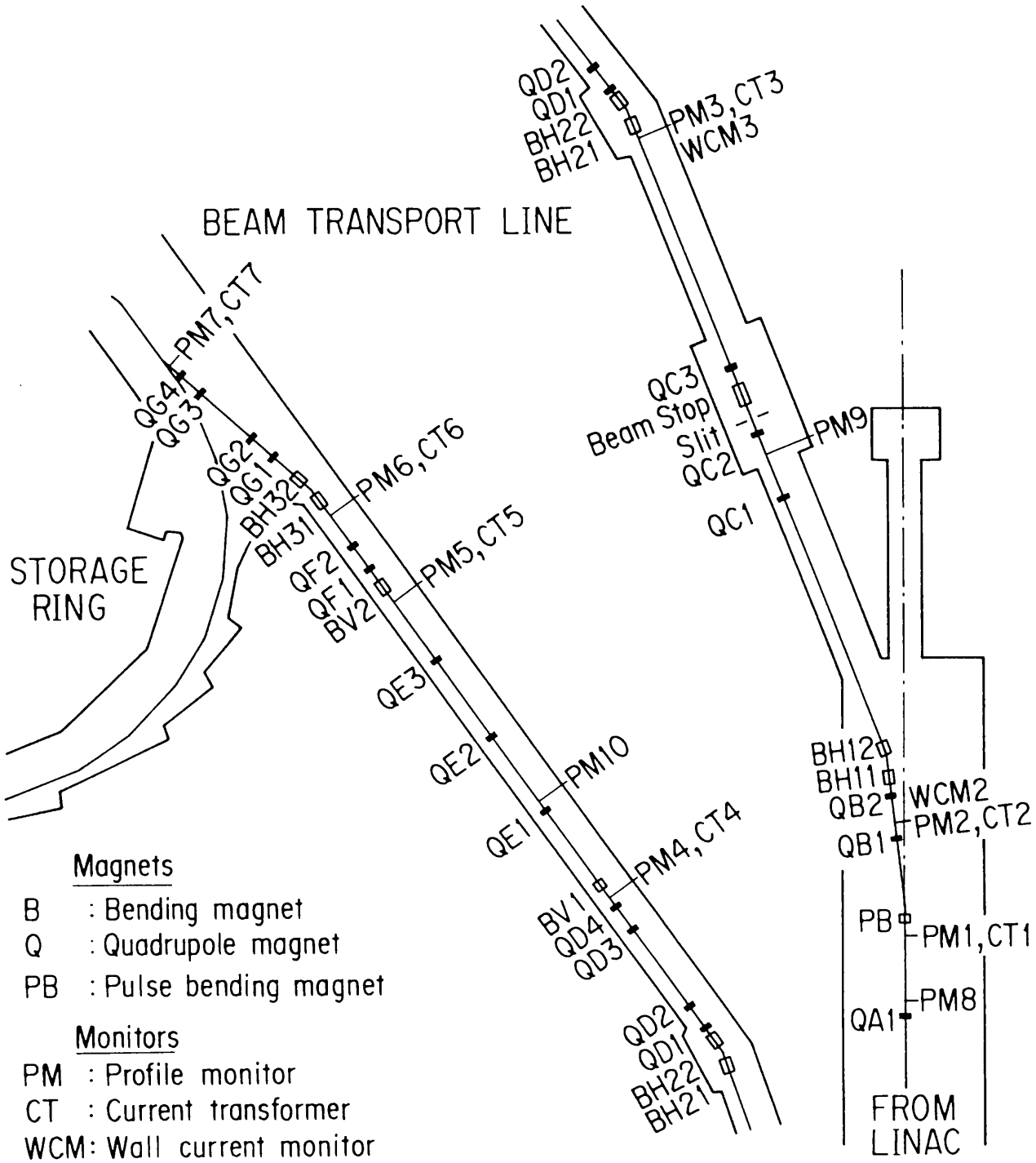

Fig. E-1. Beam transport line.

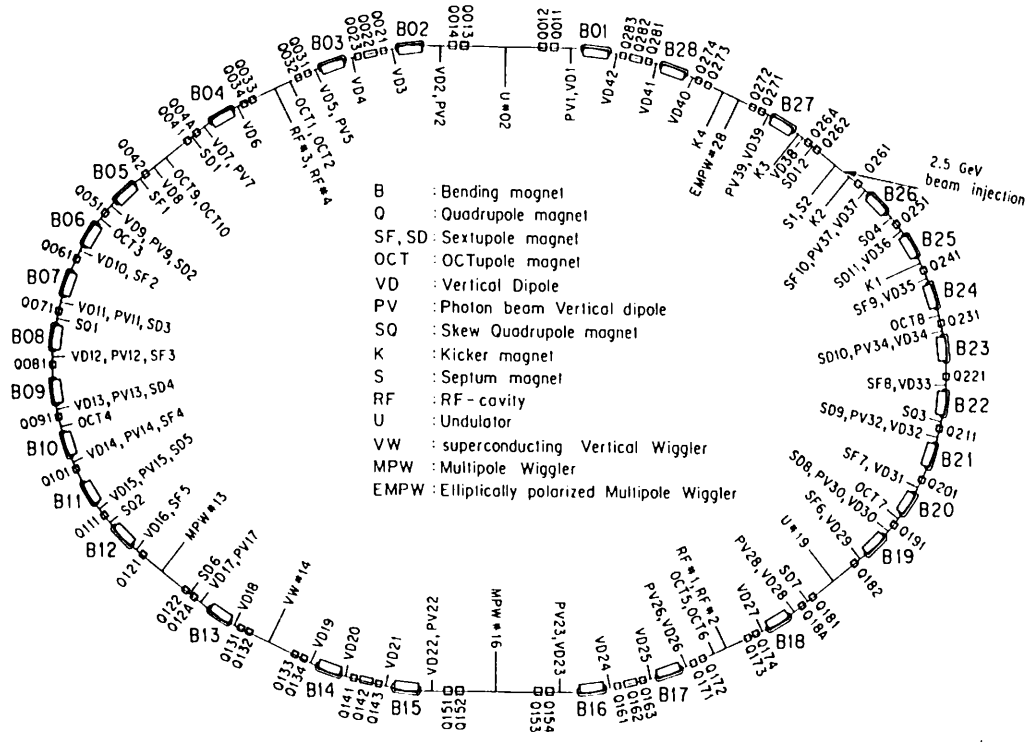

Fig. E-2. Ring lattice components.

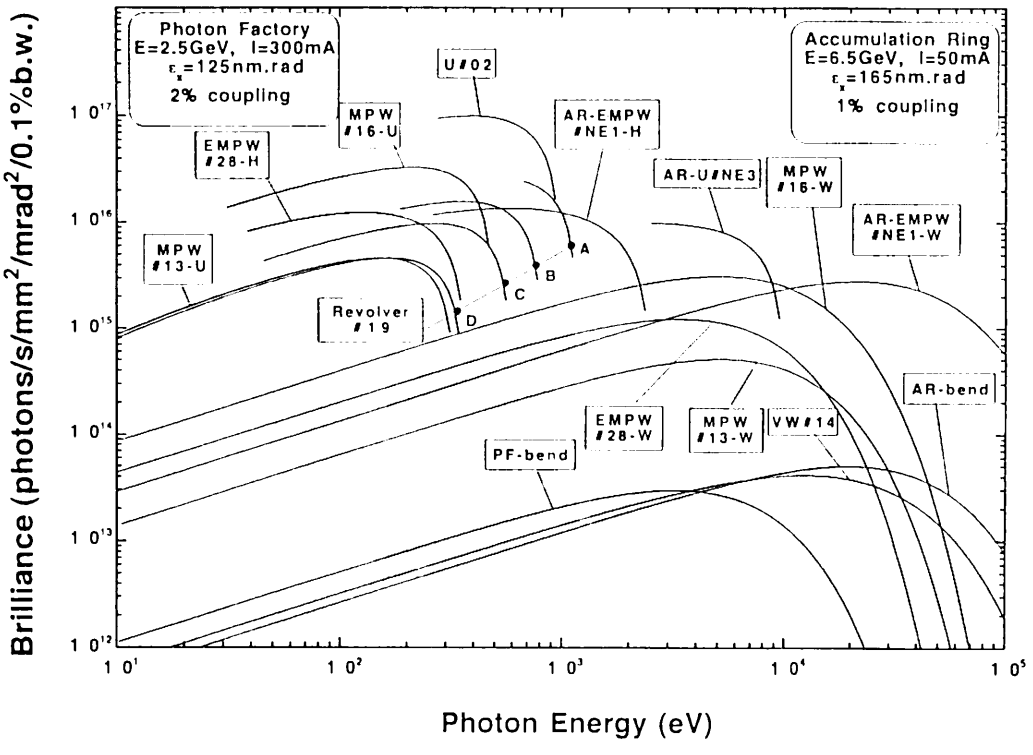

Fig. E-3. Synchrotron radiation spectra.
Brilliance of radiation vs. photon energy for the insertion devices (U#02, MPW#13, VW#14, MPW#16, Revolver#19 and EMPW#28) and the bending magnet (Bend) of the PF, and for the insertion device (EMPW#NE1) of the AR. The name of each source is assigned in Table D-4. Several insertion devices have both undulator and wiggler modes, which are denoted by U or W, respectively. The spectral curve of each undulator (or undulator mode of multipole wiggler) is a locus of the peak of the first harmonic within the allowable range of K-parameter. Spectra of Revolver#19 are shown for four kinds of period lengths.

Table E-4. Insertion Devices

Calculated spectral performances of the bend source and 6 insertion devices at the Photon Factory. E/I: beam energy and current, λ_u: period length, N: number of periods, L: length of undulator or wiggler, $G_v(G_x)$: minimum vertical (horizontal) gap height, $B_v(B_x)$: maximum vertical (horizontal) magnetic field, P: pure configuration, H: hybrid configuration, S.C.: superconducting magnet, $\sigma_{x,y}$: horizontal or vertical beam size, $\sigma_{x',y'}$: horizontal or vertical beam divergence, $K_h(K_v)$: horizontal(vertical) deflection parameter, $\varepsilon_1/\varepsilon_c$: photon energy of the first harmonic(critical energy in the case of bend source or wiggler), $\Delta\varepsilon/\varepsilon$: relative bandwidth, Pc: degree of circular polarization, $\mathcal{D}$: photon flux in unit solid angle (photons /s ·mrad^2 ·0.1%b.w.), $\mathcal{B}$: brilliance (photons /s ·mm^2 ·mrad^2 ·0.1%b.w.), P_T: total radiated power, $dP/d\Omega$: power in unit solid angle. Different operating modes of undulator and wiggler are denoted by -U and -W, respectively.

Name	E/I	λ_u	N	L	$G_v(G_x)$	$B_v(B_x)$	Type of	σ_x	σ_y	$\sigma_{x'}$	$\sigma_{y'}$	$K_h(K_v)$	$\varepsilon_1/\varepsilon_c$	$\Delta\varepsilon/\varepsilon$	$\mathcal{D}$	$\mathcal{B}$	P_T	$dP/d\Omega$
	GeV/mA	cm		m	cm	T	magnet	mm	mm	mrad	mrad		keV				kW	kW/mrad^2
Bend	2.5/300							0.74	0.26	0.38	0.037		4.0		3.5E13	2.9E13		0.060
U#02		6.0	60	3.6	2.8	0.4	H(NdFeB)	0.78	0.11	0.16	0.022	2.25	0.28	0.029	5.2E16	9.7E16	0.68	2.7
MPW#13-W -U		18.0	13	2.5	2.7	1.5	H(NdFeB)	1.66	0.17	0.15	0.019	25.0 2.0	6.2 0.108	0.086	9.7E14 5.7E15	4.9E14 3.2E15	6.7 .042	2.6 0.19
VW#14					5.0	5.0	S.C.	1.05	.096	0.16	0.025		20.8		2.2E13	3.4E13		0.18
MPW#16-W -U		12.0	26	3.1	1.9	1.5	H(NdFeB)	0.78	0.11	0.16	0.022	16.8 2.0	6.2 0.162	0.050	1.8E15 1.6E16	3.1E15 2.8E16	8.3 0.12	4.9 0.52
Revolver #19		5.0 7.2 10.0 16.4	46 32 23 14	2.3	3.0	0.28 0.41 0.53 0.62	H(NdFeB) H(NdFeB) H(NdFeB) P(NdFeB)	1.66	0.17	0.15	0.019	1.3 2.7 5.0 9.5	0.637 0.176 0.0436 0.0078	0.021 0.039 0.047 0.066	4.1E16 2.1E16 6.9E15 1.2E15	2.3E16 1.2E16 3.8E15 6.3E14	0.21 0.44 0.78 1.05	1.27 1.54 1.53 1.09
EMPW#28 -W -U		16.0	12	1.9	3(11)	1(0.2)	P(NdFeB)	1.05	.096	0.16	0.025	15(1) 1(1)	4.2(Pc=89%) .18(Pc=99%)	0.11	2.5E14 6.3E15	3.4E14 9.8E15	2.3 0.02	0.38 0.058

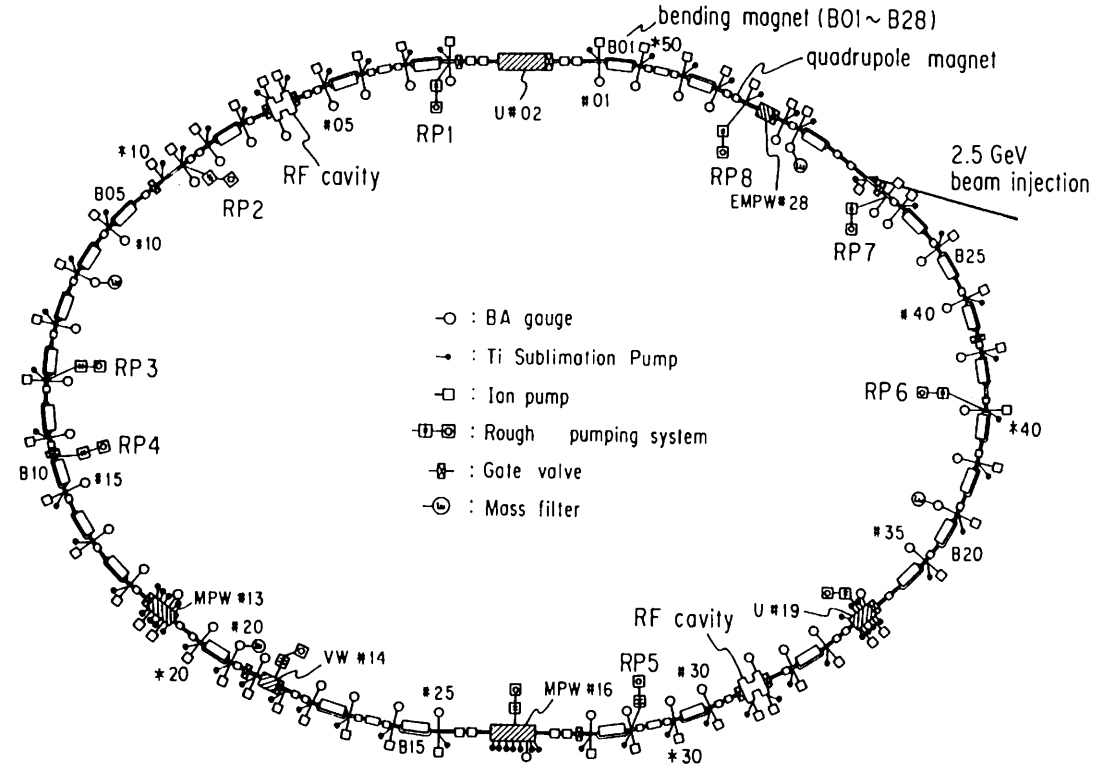

Fig. E-5. Vacuum system components.

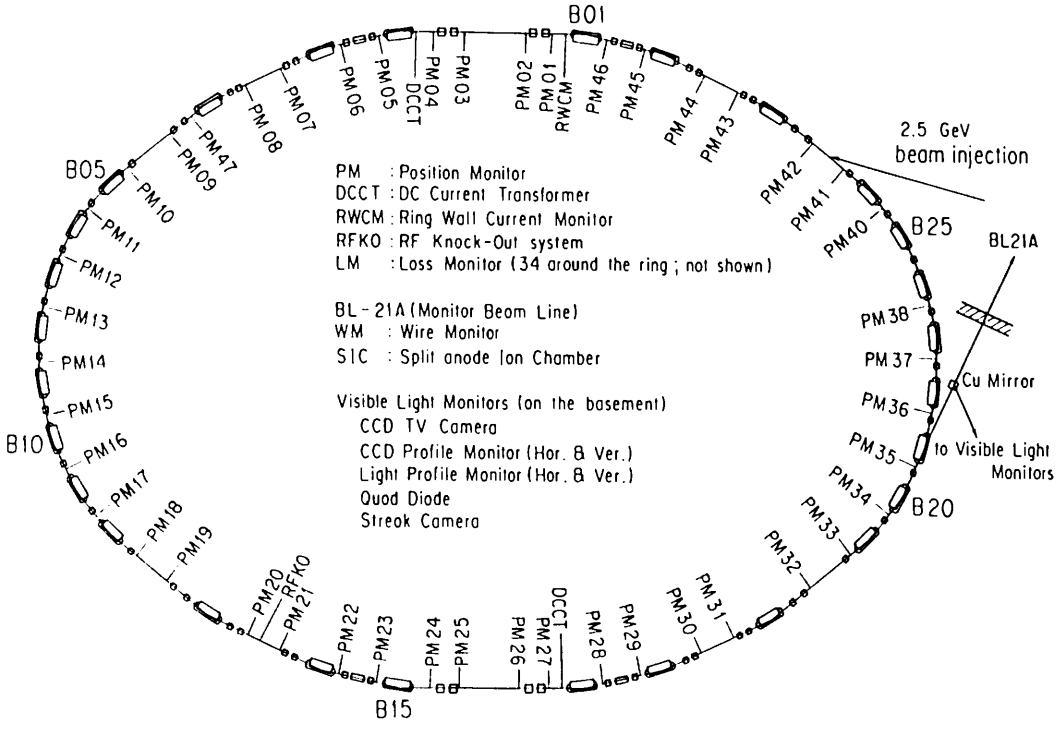

Fig. E-6. Beam monitors.

Table E-7. General parameters of the storage ring.

Energy	2.5 GeV	(0.75 GeV to 3 GeV)
Initial stored (multi-bunch) current	350 mA	(max 500 mA)
(single bunch)	60 mA	(max 104 mA)
Emittance	130nm·rad(horizontal) ~2nm·rad(vertical)	
Circumference	187m	(bending radius=8.66m)
RF frequency	500MHz	(harmonic number=312)
Injection	2.5GeV Linac	(positron/electron)
Beam lifetime	60 h (at 300 mA)	$I \cdot \tau \geq 18$ A·h (at ~250 mA ~ 350 mA)
Vacuum pressure	$\geq 3\times10^{-10}$ Torr (at 300mA) $P/I \sim 8\times10^{-10}$ Torr/A (at ~250 mA ~ 350 mA) $\sim 3\times10^{-11}$ Torr (at 0 mA)	
Insertion devices	Superconducting vertical wiggler 5T 60 period undulator K=1.78~0.1 26 period multipole wiggler/undulator 1.5T~0.04T Four way revolver type undulator 14 period multipole wiggler Elliptically polarized multipole wiggler	
SR channels	SR experiment 22 Beam diagnosis 3	

Table E-8. Beam parameters.

Horizontal tune ν_x	8.45
Vertical tune ν_y	3.30
Compaction factor α	0.015
Natural chromaticity ξ_x	-15.8
ξ_y	-8.6
Bunch length σ_z	1.5cm
Transverse damping time	7.8msec
Longitudinal damping time	3.9msec
Energy spread	7.3×10^{-4}
Radiation loss (without insertion devices)	400keV

Table E-9. Principal parameters of the accelerator system.

Magnet system

	number of magnets	number of power supplies
Bending	28	1
Quadrupole	58	12
Sextupole	22	2
Octupole	11	10
Skew quadrupole	4	4
Dodecapole	6	6
Vertical steering	42	42
Photon beam steering	20	20
Others		
Backleg winding of bending magnet	28	
Electric shunt for tune compensation	12	

RF system

Number of RF stations	4
Number of klystrons	4 (180kW/klystron)
Number of RF cavities	4 (single cell cavity)
Shunt impedance	32MΩ (four cavities)
Unloaded Q	39000
Total power dissipated in cavity wall	89kW
Total cavity gap voltage	1.7MV
Synchrotron frequency	37kHz

Vacuum system

main pumping system

pump	pumping speed	number
SIP (Sputter Ion Pump)	128 l/sec	54
DIP (Distributed Ion Pump)	150 l/sec	26
Ti sublimation	----------	71
NEG (Non-Evaporable Getter)	----------	2

total effective pumping speed = 2×10^4 l/sec (for CO)

Rough pumping system

	pumping speed	number
TMP (Turbo Molecular Pump)	300 l/sec	12

Measurement

	number
B-A gauge	48
mass filter	4
cold cathode gauge	16 (for baking)

Sector gate valve

	number
all metal with RF shield	5
all metal without RF shield	1
Viton seal with RF shield	10

Injection system

Septum magnet

name	Septum I (S1)	Septum II (S2)
core material	laminated silicon steel (passive type)	
length [mm]	1500	1000
maximum current [A]	6000	6000
deflection angle [degree]	7.0	5.0
pulse width [msec]	88	60

Kicker magnet

name	K1, K2, K3, K4
core material	ferrite (window frame type)
core length [mm]	300
maximum current [A]	3500
maximum deflection angle [mrad]	4.4
pulse width [msec]	5

Superconducting vertical wiggler

Maximum field strength on the beam orbit	5 Tesla
Magnet gap	66 mm
Magnet pole size (widthxhight)	40 mm × 260 mm
Number of magnetic poles	5 poles arranged every 200 mm
Rated exciting current	220 A at 5 Tesla
Superconducting wire	NbTi : Cu 1 : 1 size 1.70 × 0.85 mm^2
Cross section of coils	65 mm × 70 mm
Number of turn	2520
Liquid helium consumption in the permanent current mode	0.1 L/h
Damping rate of the permanent current	1.4×10^{-5}/h
Inductance	1.31 H/coil

FEL oscillator

1. General	
target wavelength	177 nm
FEL gain	18 %
cavity loss	12 %
net FEL gain	6 %
2. Storage ring	
beam energy	0.75 GeV
number of bunches	4
bunch length(2s)	60 psec
peak current	30 A
beam emittance	15 nm·rad
energy spread	3.5×10^{-4}
accelerating frequency(f_{rf})	500.1 MHz
3. Optical klystron	
periodic length	9 cm
number of periods	19+19
max. magnetic field	0.7 tesla
max. deflection parameter	5.9
optimum N_d	210
FEL gain	0.6 %/amp
4. Optical cavity	
type	Fabry Perot
cavity length	23.38 m
mirror 1(UHV Al)	R=92%
mirror 2(MgF_2 multilayer)	R=96%
cavity loss at 1770 Å	12 %
5. Laser system	
mode-lock YAG laser	
mode-lock frequency	83.35 MHz (= $f_{rf}/6$)
regenerative YAG amplifier	
repetition rate	50 Hz
pulse energy at 5320 Å	15 mJ
pulse duration	80 psec
Harmonic generation	
harmonic material	Xe or Cd vapor
max. pulse power	1 kW

Monitor system

I Orbiting Beam Monitors

PM(Position Monitor)	46
DCCT(Direct Current Current Transformer)	2
RFKO(Radio Frequency Knock-Out system	1
WCM(Wall Current Monitor)	1
Visible Light Monitor	
CCD TV Camera	1
CCD Profile Monitor (H &V)	1
Light Profile Monitor (H & V)	1
Quad Diode	1
Streak Camera	1
Photon Counting System	1

II Photon beam position monitors installed in beamlines of PF ring

Beamline	Source	Upstream	Downstream	Ver./Hor.
BL 2	U	DSPM	DSPM	V, H
BL 3A	B	SPM		V
BL 3C	B	SPM	SPM	V
BL 4C	B	SPM	SPM	V
BL 6B	B	SLIT		V
BL 6C	B	SLIT		V
BL 6C	B	SPM	SPM	V
BL 7C	B	SLIT	SPM	V
BL 10A	B	SIC		V
BL 10B	B	SLIT		V
BL 12A	B	WM	WM	V
BL 14C	SVW	SPM	SPM	H
BL 15A	B	SPM		V
BL 16	MPW	DSPM		V, H
BL 21	B	WM		V
BL 27	B	SPM		
BL 28	EMPW	Under constr.		

Note:
SPM : Split photoemission monitor
SIC : Split ion chamber
WM: Wire monitor
DSPM: Dual SPM for insertion device line
B: Bending magnet
U: Undulator
SVW: Superconducting vertical wiggler
MPW: Multipole wiggler
EMPW: Elliptical MPW

Control system

		number	memory
Control computers	FACOM S-3500	4	16 Mbyte
Library computer	FACOM M-780/10R	1	32 Mbyte
Computer network (type : optical token ring) number of nodes = 5 (max. 256)			

Table E-10. Beam size and divergence at source point.

location	σ_x [mm]	σ_y [mm]	σ'_x [mrad]	σ'_y [mrad]
B15&B01	0.34	0.16	0.41	0.033
B02&B16	0.60	0.13	0.38	0.033
B03&B17	0.43	0.22	0.32	0.018
B04&B18	0.52	0.18	0.29	0.045
B05&B19	1.26	0.21	0.39	0.037
B06&B20	0.85	0.25	0.38	0.037
B07&B21	1.26	0.21	0.39	0.037
B08&B22	0.85	0.25	0.38	0.037
B09&B23	1.26	0.21	0.39	0.037
B10&B24	0.85	0.25	0.38	0.037
B11&B25	1.26	0.21	0.39	0.037
B12&B26	0.85	0.25	0.38	0.037
B13&B27	0.44	0.23	0.31	0.045
B14&B28	0.50	0.20	0.30	0.018

Table E-11. Summary of Beamline (front-ends) in FY 1993.

Beamline	Affiliation	Source	Spectral range	Status
BL-1	NTT	bending magnet (B1)	VUV and soft X-ray	in operation
BL-2	KEK-PF	60-period permanent magnet undulator	Soft-X-ray	in operation
BL-3	KEK-PF	bending magnet (B2 & B3)	VUV and X-ray	in operation
BL-4	KEK-PF	bending magnet (B4)	X-ray	in operation
BL-5	KEK-PF	permanent magnet wiggler/undulator (under design)	-	under installation
BL-6	KEK-PF	bending magnet (B6)	X-ray	in operation
BL-7	University of Tokyo	bending magnet (B7)	VUV and X-ray	in operation
BL-8	Hitachi Ltd.	bending magnet (B8)	VUV and X-ray	in operation
BL-9	Nippon Electrical Co. (NEC)	bending magnet (B9)	VUV and X-ray	in operation
BL-10	KEK-PF	bending magnet (B10)	X-ray	in operation
BL-11	KEK-PF	bending magnet (B11)	VUV and soft X-ray	in operation
BL-12	KEK-PF	bending magnet (B12)	VUV and soft X-ray	in operation
BL-13	KEK-PF	27-pole wiggler	Soft and hard X-ray	in operation
BL-14	KEK-PF	superconducting vertical wiggler	Hard X-ray	in operation
BL-15	KEK-PF	bending magnet (B15)	X-ray	in operation
BL-16	KEK-PF	53-pole permanent magnet wiggler/undulator	Soft and hard X-ray	in operation
BL-17	Fujitsu Ltd.	bending magnet (B16 & B17)	VUV and X-ray	in operation
BL-18	ISSP and KEK-PF	bending magnet (B18)	VUV	in operation
BL-19	ISSP and KEK-PF	permanent magnet multi-undulator	VUV	in operation
BL-20	KEK-PF	bending magnet (B20)	VUV and X-ray	in operation
BL-21	KEK-PF	bending magnet (B21)	White, visible, and X-ray	in operation
BL-27	KEK-PF	bending magnet (B27)	Soft X-ray and X-ray	in operation
BL-28	KEK-PF	25-pole permanent magnet wiggler/undulator	Circularly polarized VUV and soft X-ray	in operation

Beamlines and Instrumentation

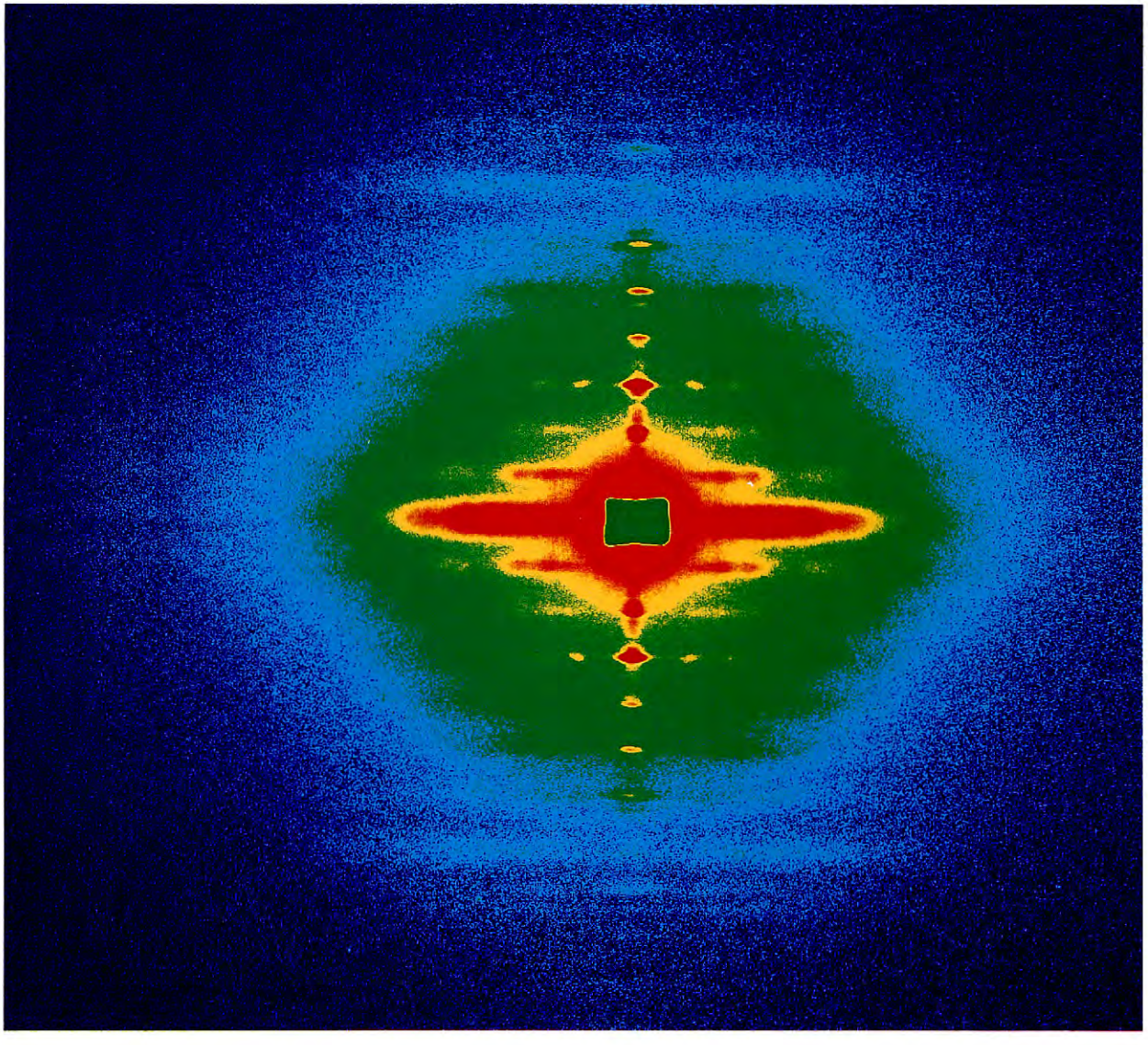

X-ray diffraction pattern from frog skeletal muscle which was obtained with a newly developed X-ray CCD detector at BL-15A. Exposure time: 15s. See the section of the Beamlines and Instrumentation division for more detail.

CONTENTS

A. INTRODUCTION

In 1993, the number of active proposals reached 630. Such a large number of proposals caused overscheduling on some of the beamlines. Furthermore, some of the proposed experiments require higher performance of the beamlines and related experimental facilities. To meet these demands, continuing efforts have been made in three areas: (1) construction and commissioning of new beamlines, (2) improvement of the existing beamlines and (3) development and introduction of new instruments at experimental stations.

Three new beamlines, (BL-18B, -20B and -28B) became fully operational in 1993 and have been opened to general users. BL-18B is equipped with a Weissenberg camera and a Laue camera, and is dedicatedly used for the protein crystallography experiments. BL-20B has been constructed under a collaborative program between the Australian National Beamline Consortium and the Photon Factory. Many Australian groups have already performed many kinds of X-ray experiments on this station. BL-28B is for circularly polarized X-rays in the 2 - 10 keV energy range .

We started the construction of BL-12C which will be dedicated to XAFS experiments. Upon completion of this station, the XAFS activities at BL-4C will be transferred to BL-12C. BL-4C will be dedicatedly used for diffraction/scattering experiments using a 6-circle diffractometer. Discussion is under way to upgrade BL-11, which is one of the oldest bending magnet VUV beamlines. A detailed design of the renewal of the beamline will be proposed by the fall of 1994.

Among various kinds of instrumental developments for X-ray experiments, much progress has been made in detector developments: (1) a readout system for large (800 mm x 400 mm) imaging plates to be used with the Weissenberg camera (2)an X-ray TV detector with a Be-windowed image intensifier and (3) an avalanche photodiode detector. An X-ray microbeam system and an ultra-low temperature diffractometer are also described.

For VUV experiments, two photoelectron spectrometers have been commissioned. One is installed in BL-27A under collaboration between JAERI and the PF and will be used to study of radioactive samples. The other is a new angle-resolved photoelectron spectrometer mainly used on BL-11D. We have also decided to introduce a high resolution electron spectrometer (SCIENTA SES 200), which will become available in mid 1994.

Completion of a new experimental preparation building having an area of 1000m^2 and starting the operation of a hot laboratory for handling radioisotopes are two major events to be mentioned as a part of our efforts to increase our capability for experimental support for users.

B. BEAMLINES

1. NEW BEAMLINES IN OPERATION

BL-18B Branch Beamline for Macro-molecular Crystallography

Performance tests of the beamline have almost been completed. The photon flux of the monochromatic beam was estimated for all monochromator crystals using an ionization chamber, and summarized in Fig. 1. The total power of a focused white X-ray beam, estimated using a calorimeter, was 260mW per 100mA. The beamline has been tentatively opened for domestic users from October, 1993. Data collection is performed using a Weissenberg camera for macromolecular crystallography (type-II), the prototype of a time-resolved Laue camera and the Fuji BAS2000 Imaging Plate scanner. The results of some experiments are in the Users' Reports section of this volume. Special Imaging Plates (IP) and a scanner have also been developed to allow more effective experiments using Weissenberg and Laue cameras at the station. The

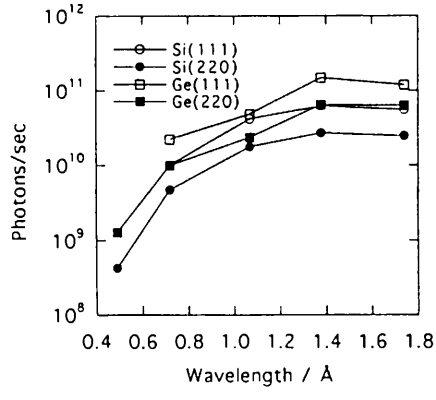

Fig.1 Intensity of the monochromatic beam at the sample position at 2.5GeV, 300mA. The acceptance angle of the first slit is about 0.2mrad (vertical) and 2.0mrad (horizontal). The focused beam size is about 0.4mm (vertical) and 1.2mm (horizontal).

dimensions of the new IP are 400mm×400mm and 400mm×800mm. The response of the scanner is shown in Fig.2. The nonlinearlity between the input X-ray photons and the measured intensity is quite negligible, from 1 to 1×10^5 photons per pixel.

The beamline will be opened for public use from April, 1994.

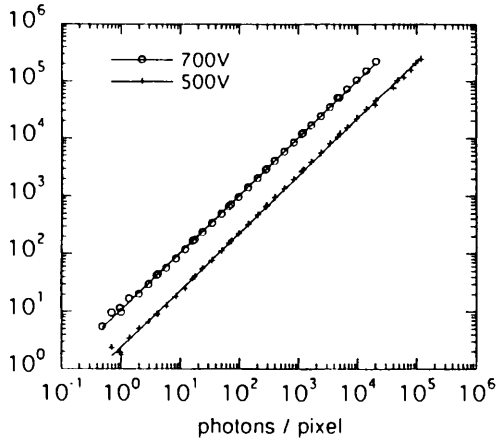

Fig.2 Response of the large IP scanner. The relative intensity output is the average over 50x50 pixels of uniform exposure level. The two plots represent the results obtained with different applied high voltages to the photomultiplier tube of the scanner.

BL-20B Australian National Beamline

Development and commissioning of the Australian National Beamline Facility (ANBF) continued at a steady pace throughout 1993. Several major milestones were passed, resulting in the facility being officially opened by the Australian Minister for Science and Small Business, The Hon. Mr. Chris Schacht, in October.

The first major addition to the beamline in 1993 was the installation in January of the Phase-I monochromator, consisting of a water-cooled Si(111) channel-cut crystal. The first monochromatic X-ray beam at BL-20B was obtained immediately after the winter shutdown. With the availability of monochromatic X-rays, it has become possible to carry out many more experiments at BL-20B, some of which are listed below.

The other major development at ANBF during 1993 was the installation of a multi-configuration diffractometer in the hutch at BL-20B in September. The diffractometer is a versatile, high-precision vacuum instrument capable of providing a large range of diffraction techniques with little compromise in performance in any given mode. The instrument has been optimized to facilitate the following types of experiments:

- High-speed (and time-resolved) powder diffraction using Imaging Plates (0.01° resolution)

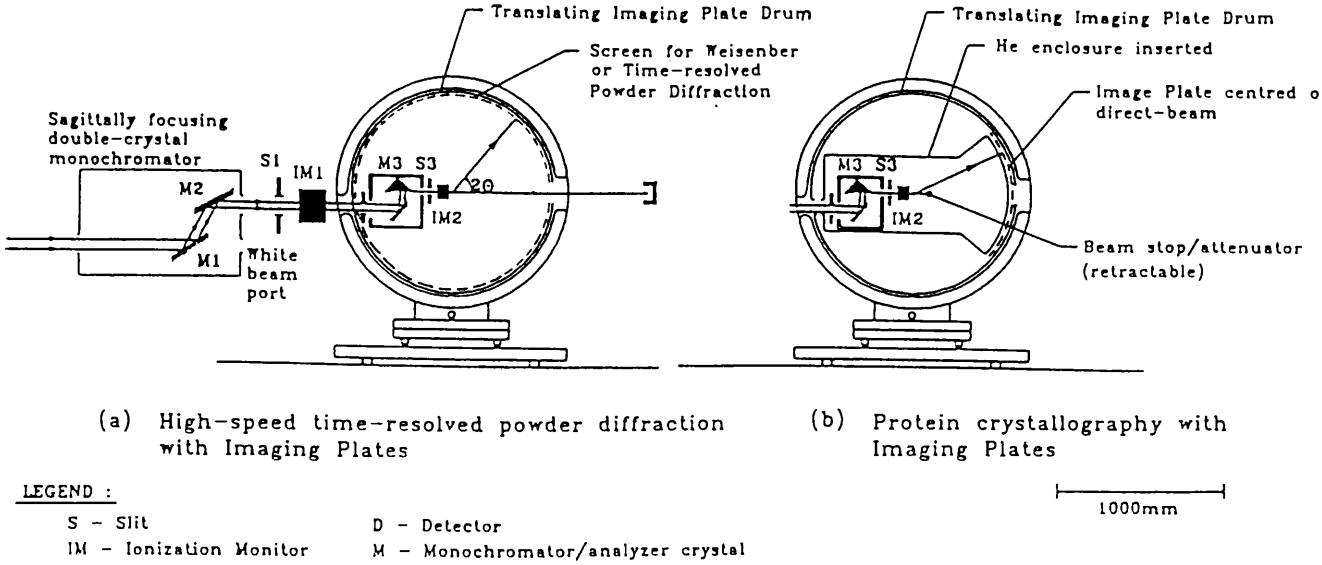

(a) High-speed time-resolved powder diffraction with Imaging Plates

(b) Protein crystallography with Imaging Plates

LEGEND :

S - Slit
IM - Ionization Monitor
D - Detector
M - Monochromator/analyzer crystal

Fig. 3 Two possible configurations of the multi-purpose diffractometer installed at the ANBF.

- High-resolution powder diffraction using a single-channel X-ray detector and an analyzer crystal
- Protein crystallography using Imaging Plates (Weissenberg geometry)
- Triple-axis diffraction and reflectometry
- Single-crystal diffraction with a scintillation detector or Imaging Plates.

Two possible configurations of the instrument are shown schematically in Fig. 3.

The experiments that have been carried out at ANBF during 1993 bear testimony of the multi-purpose nature of the beamline. These include transmission XAFS and XANES studies on organometallic catalysts and SYNROC components, X-ray diffraction micro-tomography (providing more element-specific information than dose the conventional CT), triple-axis reflectometry on mechano-chemically polished Si wafers, and high-resolution powder diffraction on standard samples.

The only major component of the beamline still under construction is the Phase-II monochromator, which will feature sagittal focusing and a fixed exit-beam height. The new monochromator will be interchangeable with the present model and will be brought to Japan in the spring of 1994. It is expected that the beamline will enter the full-operation mode following the summer shutdown in 1994.

BL-28B Beamline for Circularly Polarized X-rays

In the Photon Factory, there are two insertion devices used to generate intense circularly polarized synchrotron radiation, EMPW#28 and EMPW#NE1. Both devices complement each other regarding the radiated energy range. Beamlines NE1A2 (6 ~ 100 keV), NE1B (240 ~ 1500 eV) and 28A (5 ~ 300 eV) were already commissioned in 1991. Using EMPW#28 in the multipole wiggler mode, we can obtain intense circularly polarized X-rays in the energy range between NE1A2 and NE1B.

Designing of BL-28B for experiments using EMPW#28 in the multipole wiggler mode was started in the spring of 1991. The designed specifications are as follows;

EMPW#28: K_x=1.0, K_y=15.0
Acceptance: 4.0 mrad(H) × 0.2mrad(V)
Pre-Mirror: 18.8 m from source point
  16 mrad reflection
  Pt-coated Si, Ni-coated Si
  Bent cylinder for
    horizontal focusing and
    vertical focusing or collimating
  Indirect water cooling
Double-crystal monochromator:
  29.0 m from source point
  Fixed exit beam position
  Several kinds of crystals
  Indirect water cooling
Post-Mirror:
  30.5 m from source point
  16 mrad reflection
  Pt- and Ni-coated SiO_2
  Bent plane for vertical focusing
Focusing Point:
  34.5 m from source point.

The design and construction of this beamline were carried out from the spring of 1991 to February of 1993. On February 15, 1993, photon beams were successfully transported into the experimental hutch. Adjustments of the optical components and some performance checks of the beamline were carried out. The obtained specifications at the focusing point in the present stage are as follows;

Focusing Size: 2.4 mm(H) × 0.3 mm(V)
Photon Flux: ~ 3×10^{10}(photons/sec at 9 keV)
Energy Resolution: ~ 2 eV at 6.3 keV
Degree of Circular Polarization:
  0.46 at 8.3 keV,
  0.41 at 7.7 keV,
  0.30 at 6.5 keV.

All of the above data were taken using a Pt-coated pre-mirror, Si(220) monochromator crystals and a Pt-coated post-mirror.

The main purpose of this beamline is to use circularly polarized X-rays. Magnetic XANES and EXAFS studies have already been started. This beamline has another possibility of high heat-load studies. According to calculations, white X-ray beams whose heat power is about 1 kW will be applied at the above-mentioned focus area. Preparation of a high heat-load study is now progressing.

2. BEAMLINES UNDER CONSTRUCTION AND PLANNING

BL-11 Renewal of the Beamline

BL-11 has played an important role in carrying out solid-state and surface sciences since the early stage of the Photon Factory operation. BL-11 consists of four branch beamlines equipped with a grasshopper monochromator (11A), a double-crystal monochromator (11B), a 1-m Seya-Namioka monochromator (11C), and a constant-deviation monochromator (11D). Many remarkable experimental investigations have already been made using these branch beamlines. However, in the last few years, the monochromators of BL-11 have not always met the users' requirements from the viewpoint of photon intensity and resolving power. It is quite natural for experimental demand to grow with scientific development. This situation has made us decide to upgrade beamline 11. We plan to totally replace BL-11A and 11D with new monochromators, and to improve the focusing optics of BL-11B and 11C. For BL-11A and 11D, a high-resolving power will be achieved by adopting monochromators with concave gratings having relatively large radii. A high flux will be realized with new focusing optics upstream of the monochromators, where the heat load to the first mirrors is important.

BL-12C A New XAFS Beamline

A new XAFS beamline is to be constructed during the summer shutdown of 1994 at BL12C, which is now being used for photochemical reaction experiments.[1] The layout of the new beamline is shown in Fig. 4. The new beamline consists of a double-crystal monochromator and a focusing mirror system, which realizes 2:1 focusing. The horizontal acceptance of the beamline is 2 mrad. The main purpose of the optics is to realize a small beam size and a fixed beam position during the measurement of an XAFS spectrum. The small beam size (less than 1mm square) is useful for XAFS measurements of newly developed materials, whose quantity is generally limited, such as metallofullerenes. The fixed-beam position is essential for experiments with secondary analyzer systems, such as XEOL experiments.

The first optical element is a double-crystal monochromator, which is placed after beryllium windows. The fixed exit-beam position from it is realized by using two cams, as are commonly used in the Photon Factory.[2] However, special care is taken to minimize any nonlinearity or backlash. For example, the crystal holders and their position aligners are made as light as possible by eliminating any unessential freedoms and motors, while keeping sufficient maintaining rigidness. Si(311) or Si(111) crystals will be used according to the required energy range.

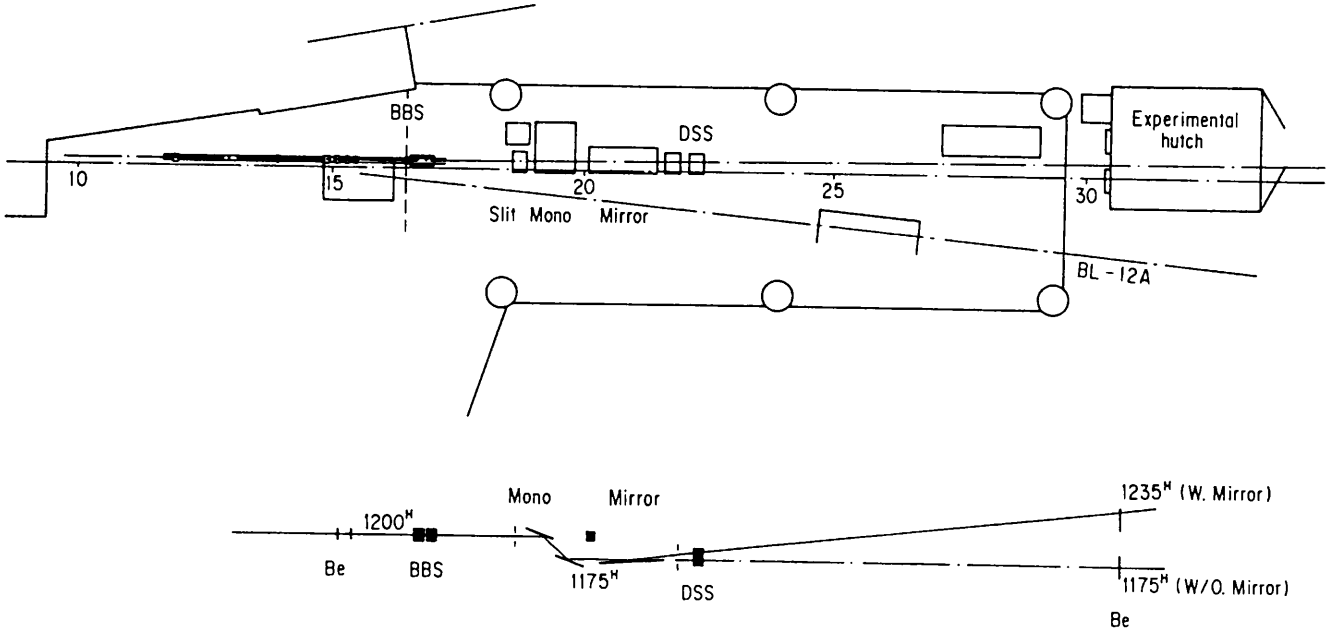

Fig. 4 Layout of the New BL-12C.

A one-meter long rhodium-coated silicon mirror accepts the monochromatic beam and realizes a 2:1 focus at the sample position by bending it. The mirror is free from any absorption edges within the commonly used energy region, and reflects X-rays up to 23 keV. The mirror gets out of the path of X-ray beam when X-rays of higher energy are required.

The beamline is to be opened for public use during 1995.

1) PF Activity Report #6, I-11 (1989).
2) T.Matsushita, T.Ishikawa and H.Oyanagi, Nucl. Instrum. Methods, **A246**, 377 (1986).

3. IMPROVEMENT OF BEAMLINES

BL-1B and 1C Restoration of the Stations

The construction of BL-1 (NTT beam line) started in 1982 under a joint-research contract between NTT and PF. Research activities involving surface analysis (BL-1A), X-ray lithography (BL-1B), and photochemical reactions (BL-1C) have been proceeding since 1983. BL-1B comprises a bending SiC plane mirror of glancing angle 1 deg. and a Be window (25μm in thickness) at the downstream end of the line. BL-1C comprises a bending SiC toroidal mirror of glancing angle 3 deg., a differential evacuation system, and a PGM monochrometer.

(1) X-ray Lithography at BL-1B

From 1983 to 1992, research concerning X-ray proximity lithography has been carried out at BL-1B. At first, by using proximity lithography technology, a 0.2μm LSI pattern was successfully performed in 1984. Based on this success, developmental research on the thermal expansion of photo-masks (1985-86), and cooperative research with PF on SR-induced gas desorption (1987-89), and characterization on photo-resist materials aiming at nano-meter order resolution for future devices (1989-92) followed.

In 1987, a sub-beam line 1B' was branched by using a bending mirror having a glancing angle of 3 deg. at a point 20 m distanct from the light source point. BL-1B' was a windowless beam line aiming at research for X-ray projection lithography and at reflectivity measurements of multi-layer mirrors in the longer wavelength region. During that year, NTT succeeded in projection lithography in the soft X-ray region for the first time.

By 1988, NTT completed its own SR ring at the NTT Atsugi R&D Center, Kanagawa, Japan, which was specially designed to be optimized for X-ray lithography on the basis of the experimental results obtained at BL-1B. At present, 0.2μm-class LSI fabrication is actively being promoted by using the NTT ring

(2) Photochemical Reaction Study at BL-1C

SR-excited semiconductor processes, such as surface etching, film growth, and material modification, have continuously been studied in BL-1C. From 1985 to 1986, NTT reported on challenging experimental results involving SR-excited semiconductor processes: photo-chemical etching of silicon and silicon dioxide surfaces, and photo-chemical vapor deposition of silicon nitride films.

From 1989 to 1990, an ultra-high vacuum reaction system for SR-excited gas-source molecular beam epitaxy was constructed. SR-excited silicon epitaxial growth was successful for the first time, and SR-excited direct evaporation of silicon dioxide without using etching gas was achieved in 1990. Based on these new phenomena, several SR-excited surface processes, such as surface cleaning, silicon selective-area growth, atomic-layer epitaxy, and material modification were developed.

For the further development of these research activities, NTT has constructed its own SR facility, and beam lines for projection lithography and photo-chemical reaction are under construction in this facility. Accordingly, these activities will be transferred to the new facility. By the end of fiscal year 1993, sub-branch beam line 1B' and the reaction gas-supplying and -exhausting system at BL-1C were removed. In April of 1994, BL-1B and BL-1C will be opend for public use. BL-1A will be successively used for cooperative research under the contract between NTT and PF until 1996.

BL-2A Installation of a Focusing Mirror

In order to increase the available photon flux at the sample position, a pin-hole aperture of 1mm in diameter has been replaced by a V-slit at 15.1m from the center of the undulator, and a cylindrical mirror for horizontal focusing has been installed downstream of the crystal monochromator.

The horizontal opening of the V-slit is variable from 1mm to 8mm, so that the maximum acceptance should be about 0.5mrad. The vertical acceptance is fixed by a mask of 1mm opening. This slit system is assembled in a vacuum chamber whose position can

be adjusted to the center of the undulator radiation with a two-axis stage.

To reduce the increased heat load to the first crystal of the monochromator, a 1μm-thick graphite foil has been installed as an absorber of intense low-energy harmonics of the undulator radiation.

The cylindrical mirror is placed at 27.4m from the source point where only monochromatized beams are illuminated. It is 300-mm long and made of fused-quartz coated with nickel so that the X-rays in a vertical size of 3mm with an energy under 5.5keV should be reflected upwards at an incident angle of 10mrad. With a three-axis adjusting mechanism, we can precisely set the vertical position and angles of the incidence and rotation in the mirror plane.

In a performance test using the Si(111) two-crystal monochromator, we could obtain about 5-times as many photons as before without any sacrifice of the energy resolution (E/ΔE>5000) in a 2mm × 2mm spot at a focal point 1600mm downstream from the mirror center. The typical intensity was measured by monitoring the drain current from a nickel plate in the normal-incidence geometry as around 1×10^{-9}A at the peak energies of the undulator harmonics under 4keV. In the higher energy region, the available photon flux gradually decreases because of the radiation spectrum of the undulator source and the reduced reflectivity of the mirror with a certain surface roughness. As a resulting merit of the mirror, higher order diffraction of the crystal monochromator is almost completely suppressed, which used to be necessarily eliminated by the detuning of two crystals in the experiments, such as X-ray absorption measurements. The high flux in the small spot is expected to be quite useful in various experiments, such as X-ray fluorescent emission spectroscopy and high-resolution photoelectron spectroscopy.

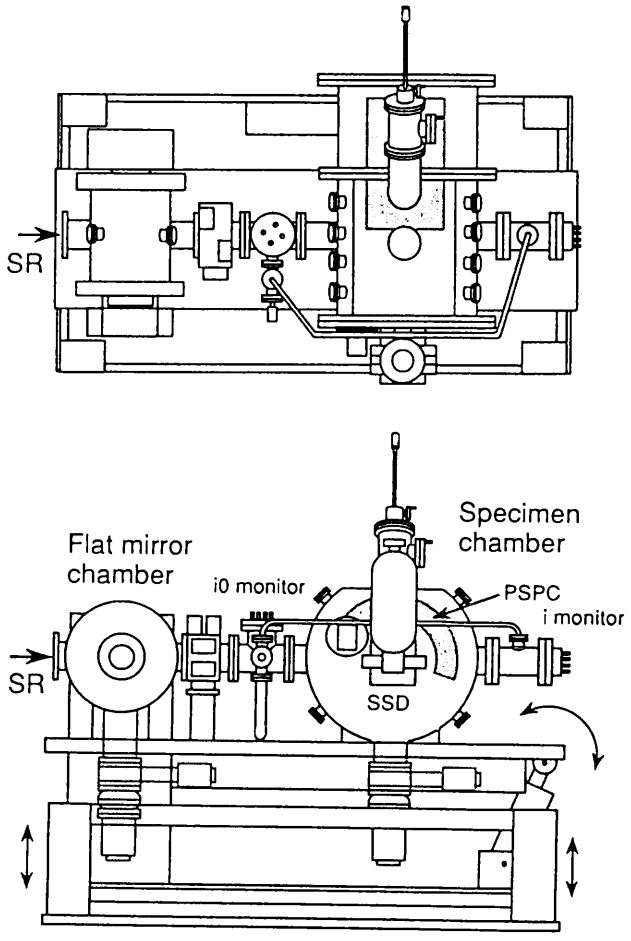

Fig. 5 Side and top views of the X-ray measurement system.

BL-8B New Measurement System

A new measurement system has been installed at BL-8B to obtain X-ray diffraction, absorption and fluorescent yield spectra. (Fig. 5.) The system has a six-axis goniometer and five detectors in a high-vacuum environment to reveal the surface and interfacial structures of electronic materials.

The beamline was developed for XAFS studies of amorphous materials involving Si compounds. Therefore, all of the optics were installed in a high-vacuum condition of 10^{-6} Pa in order to decrease any X-ray absorption and scattering by windows and the beam-path. An incident X-ray beam was monochromatized by a double-crystal monochromator with InSb(111) and Si(311). The monochromator provides X-rays from 1.7 to 20 keV in energy with an energy resolution (E/ΔE) of about 5000. A bent cylindrical mirror was installed downstream from the monochromator to focus the X-ray beam. A flat mirror was used to reduce the harmonics. An SR beam with a size of 25.0 (H) × 1.0 (V) mm upstream from the monochromator was focused to a size of 2.5 (H) × 0.7 (V) mm at the sample position.

Three kinds of X-ray detectors are placed in the system. The incident and transmitted beams are measured by ionization chambers. Fluorescent X-rays are measured by two solid state detectors (SSD) with three Si(Li) crystals. A position-sensitive proportional counter (PSPC) is used for diffraction studies. The ionization chambers and PSPC have been specially developed for installation in a high-vacuum condition.

The goniometer has six axes (ω, φ, χ, x, y and X).

The ω, ϕ, and χ axes of the Eulerian cradle system are used to set the sample orientation. An x-y stage is placed normal to the ϕ-axis and the X stage is used to move the goniometer to the sample-changing position. As the axes are driven by stepping motors and AC servo-motors installed in the chamber, and the base pressure is 1×10^{-5} Pa, surface studies which require ultra-high vacuum conditions, such as surface reconstructions, cannot be performed. However, analyses of interfaces and absorptions on a surface can be studied using a goniometer, which enables a precise setting of the sample orientation.

BL-13C Improvement of Optical Elements

In 1993, some of the optical elements of the BL-13C[1] were improved. The mechanically ruled grating (750 gl/mm) was exchanged with a new one with fewer scratches and fouling materials. The mechanical system of both the entrance and exit slits was modified so that even opening could be achieved without any fluctuation of the vertical center.

Figure 6 shows the spectrum of undulator radiation with an undulator gap of 160 mm (K=1.68) recorded by gold mesh (80% transmission), when the energy resolution is estimated at c.a. 400 meV at 400 eV. A high-resolution photoionization spectrum of gas-phase nitrogen is shown in Fig. 7. The monochromator resolution at 400 eV is calculated at 62 meV by a curve-fitting analysis, assuming a Lorenzian natural width of 128 meV for each band. The details are described in users report "91-030".

1) N. Matsubayashi, H. Shimada, K. Tanaka, T. Sato, Y. Yoshimura, and A. Nishijima, Rev. Sci. Instrum., 63, 1363 (1992).

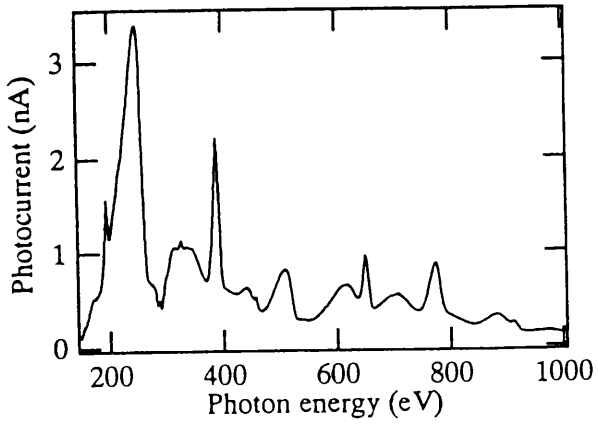

Fig. 6 Spectrum of undulator radiation at BL-13C.

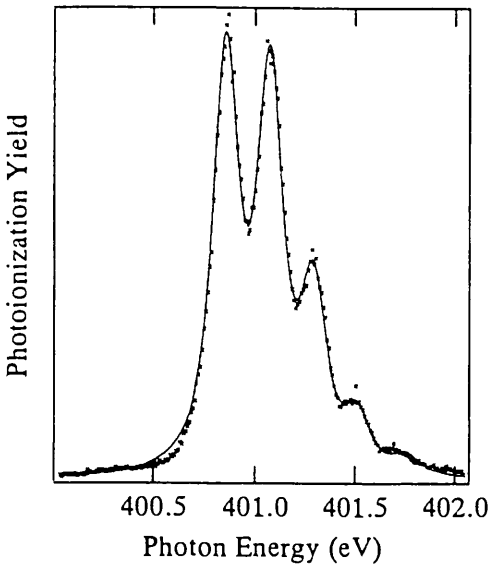

Fig. 7 Photoionization at the N 1s->π^* resonance in gas-phase N_2 .

C. NEW INSTRUMENTATION

Photoelectron Spectrometer at BL-27A

A new photoelectron spectrometer was installed at beamline BL-27A. The sample position in the analyzer chamber of the spectrometer is located at about 32 m distance from the source point in the bending magnet of the storage ring. The apparatus houses two kinds of electron analyzers. One is a 50-mm hemispherical analyzer for angle-resolved photoemission spectroscopy; the other is a double-focusing hemispherical analyzer for versatile use. The latter employs a system of high retarding-ratio which permits high-resolution operation in the high kinetic-energy region. The electron-lens systems were specially designed for analyses of electron energy ranging from 0 to 6 keV. A sample under a pressure in the 2×10^{-8} - 2×10^{-6} Pa range can be linearly heated from 80 to 1050 K using a single manipulator. It will be used for analyses of the electronic states of radioactive materials as well. The spectrometer was used to check the monochromaticity of a double-crystal monochromator employing the InSb(111) plane of BL-27A. Figure 8(a) shows a photoelectron spectrum of the $4f_{5/2,7/2}$ region of an Au plate excited with 1913.6 eV photons. The full width at half maximum (FWHM) of the $4f_{7/2}$ line was determined to be 1.2 eV. Figure 8(b) shows the photon-energy

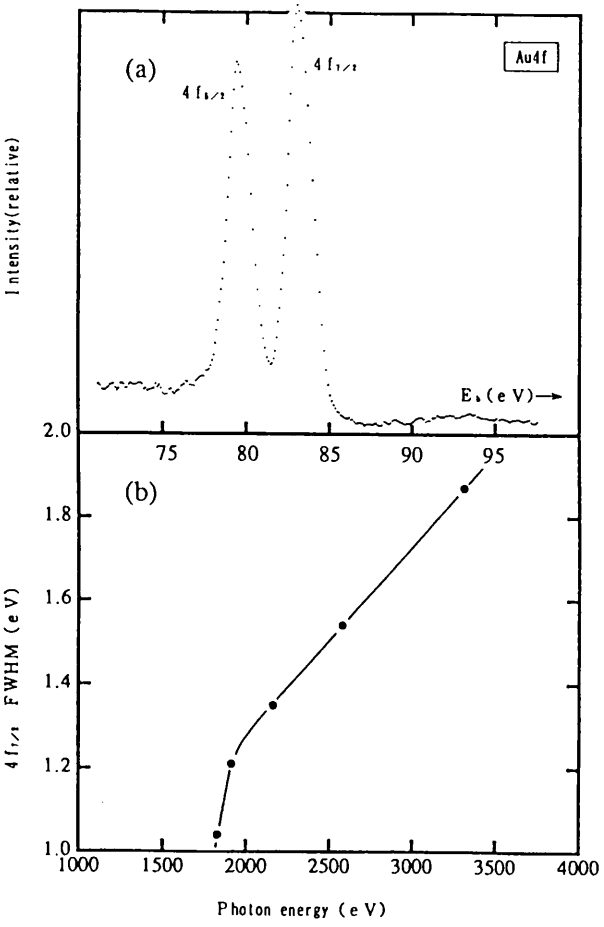

Fig. 8 Photoelectron spectrum of Au4f$_{5/2,7/2}$ of Au excited with 1913.6eV photons (a) and FWHM of the 4f$_{7/2}$ line (b).

dependence of the FWHM of the Au 4f$_{7/2}$ line. From the data obtained it seems that the monochromaticity of the SR beam at BL-27A (1.8 keV - 6 keV) is quite sufficient for photoemission experiments.

Versatile Multi-Circle Diffractometer at BL-27B

A multipurpose diffractometer has been installed at BL-27B, which was constructed in a JAERI-PF cooperation. It is to be used in the field of materials science, especially concerning actinide and other radioactive samples. This system was designed by JAERI based on the conventional 6-circle diffractometer of the vertical type. The following new features were considered so as that techniques of diffuse-scattering measurements could be ideally developed:

a) Fully remote control: Computer-controlled motors (33) and solenoids (2) are employed.
b) High-speed operation: The drive speeds of the circles are more than 3 degree/sec.
c) Additional circles for wide applicability: i) a $\chi_{2\theta}$ that allows the detector to climb longitudinally from the equatorial plane of the Ewald sphere, ii) a χ_{α} to rotate the analyzer system about the diffracted beam direction, iii) an α to rotate a entire body of goniometer around the vertical axis, and iv) a Z_{ϕ} to actuate the ϕ sample table along the ϕ-axis.
d) Environmental conditions on sample: i) Low and ii) high temperatures, iii) high pressure, iv)vacuum, v)magnetic field, etc.
e) Exchangeability of detectors: i) Scintillation detector and ii) Peltier-cooled Si(Li) SSD, which can be combined with iii) crystal analyzers of Si(111), Ge(111) and HOPG, iv) PSDs and v) Imaging Plate and Polaroid cameras.
f) Upstream optical table for incident-beam processing, as well as radiation-biology and XAFS studies.

The entire system comprises five blocks, as shown in Fig. 9. The main parts in the diffractometer system are a goniometer and its table, which include the following components:

a) Crystal orienter: This is equipped with three circles, (ω, χ and ϕ) and *a new Z_{ϕ} stage.*
b) Diffracted beam optical system: This is installed on a detector stage, which revolves with the 2θ arm and moves on *a new longitudinal arc of $\chi_{2\theta}$.* A fine collimator stand, slits, ionization chamber, analyzer and detector are set on it.
c) Goniometer table: This has three actuators to lift up, incline and rotate the goniometer. The wide-angle rotation is made by *a new α turn-table.*

The ϕ table was designed so as to be able to accommodate several kinds of stages to control the sample environment. Experiments can be performed by fully remote control from outside of the hutch.

The system will be widely applied to various kinds of experiments, which might be classified from the viewpoint of design, as follows:

a) Sample states: i) Single-, ii) poly-, and iii) powdered-crystals, iv) amorphous states, v) liquid, etc.
b) Sample environments considered: i) High and ii) Low temperatures, iii) high pressure, iv) high

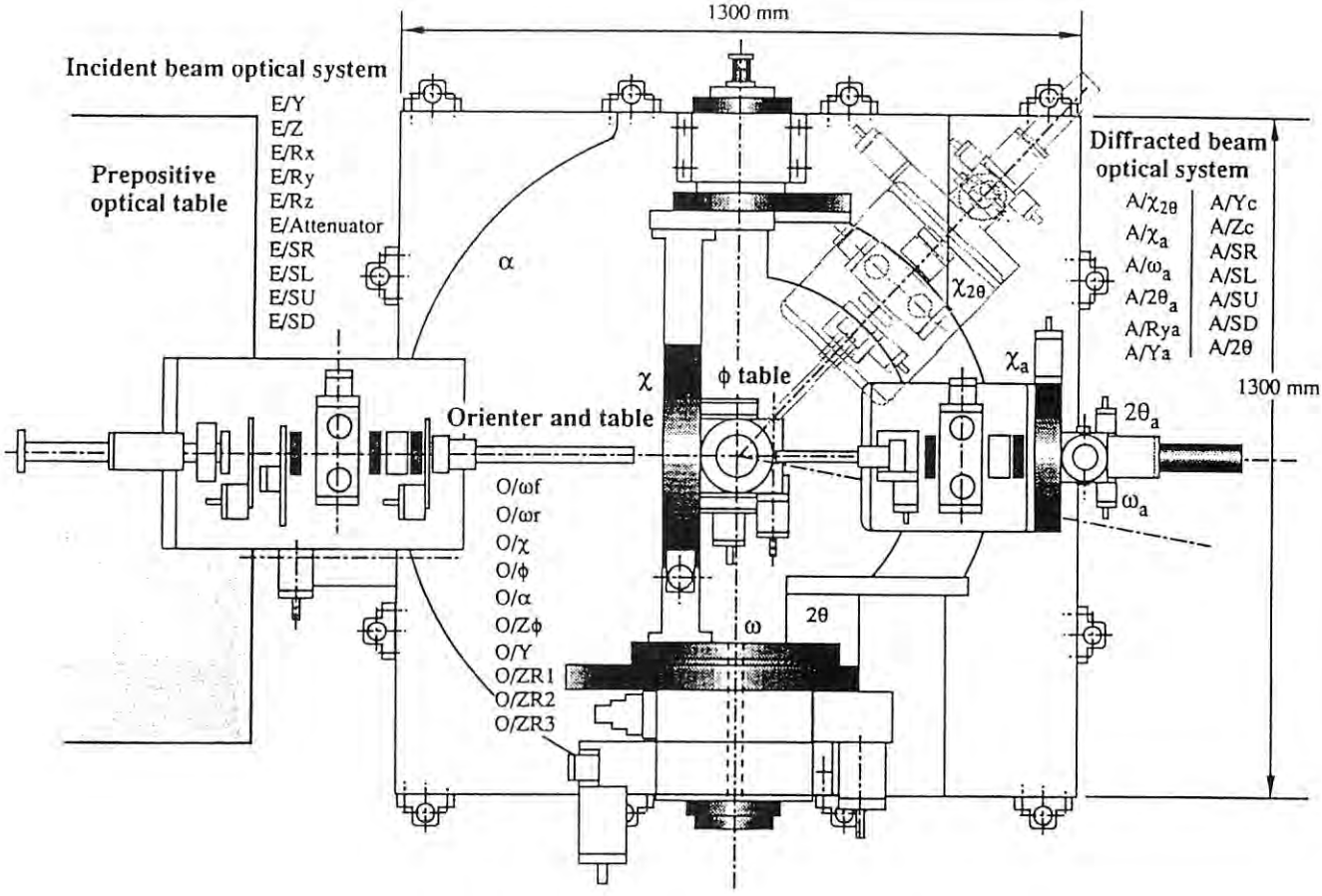

Fig. 9 9-circle diffractometer (top view).

vacuum and v) magnetic field.

c) Scattering techniques: i) Bragg-intensity collection, ii) diffuse-scattering measurements, iii) high-resolution measurements (in energy and angle), iv) polarization analysis, etc.

New Apparatus for Angle-Resolved Photoelectron Spectroscopy

A new apparatus has been designed and constructed for angle-resolved ultraviolet photoelectron spectroscopy, which will be used to determine the characteristics of bulk and surface electronic states. The apparatus consists of an analysis chamber and a sample-preparation chamber. The analysis chamber is made of μ-metal, the same as that of the ADES500 system (VG) widely used for surface analysis. It is equipped with a hemispherical electron-energy analyzer of 50 mm mean radius (HA45 (VSW)) mounted on a two-axis goniometer. The energy resolving power (E/ΔE) and angle resolution are presently 100 and 1°, respectively. Another hemispherical analyzer of 100 mm radius (VG100AX (VG)) has been prepared for Auger spectroscopy. If necessary, it is also available for angle-integrated photoemission measurements after some rearrangement. The measurement systems of these are controlled by an IBM-AT-compatible microcomputer. The chamber is also equipped with a ion-gun (ANELVA), RHEED optics (Vieetech) and LEED optics (PHI) for both sample preparation and characterization. Several sample manipulators with a liquid-N_2 or liquid-He cooling system are prepared for proper use. They are typical VG products for common use among similar equipment. The sample-preparation chamber is presently a small and simple manifold, considering rapid evacuation and simple operation. It can be provided with combinations of a cleavage system, K-cells, evaporation guns and

sample-transfer mechanisms, as the occasion demands.

The analysis chamber is evacuated by a 1500 *l/s* turbomolecular pump and the sample-preparation chamber by a 500 *l/s* pump. The exhaust of both pumps is also evacuated by a 150 *l/s* turbomolecular pump, which is used for rough evacuation during the start-up. The resulting base pressure is less than 2×10^{-9} Pa. Each section of the apparatus is separated by automatic valves and is always monitored by a combination gauges covering the entire vacuum region. The vacuum system is controlled by a systematic controller with a vacuum interlock to realize simple operation.

High-Resolution Photoemission Instrument

Photoemission experiments are intensively performed at the general-purpose beam lines of BL-2B, BL-11D, BL-19A and so on, besides BL-1(NTT) and BL-7(Univ. Tokyo). Resonance photoemissions are being carried out these days by many groups in the core excitation region. The feasible resolution was, however, limited to about 0.5 eV at around 500 eV in order to realize a good S/N ratio. In the region below 100 eV, a resolution of better than 80 meV is realized. In both cases, the resolution is not limited by the photon monochromator, but is limited by the electron analyzer. The higher energy resolution is expected to provide much more abundant information concerning the electronic states. The installation of a high-resolution electron analyzer is thus proposed in cooperation with outside user, and is being funded for two fiscal years (1993 and 1994).

The system consists of a SCIENTA SES 200 electron analyzer and a High-Tran UHV183-IS-102 He-flow-type cryostat. Two-dimensional detection by use of a CCD camera can considerably shorten the integration time for reliable measurements. High-resolution photoemission measurements are only limited by the monochromator and are expected to give a total resolution of better than 10 meV for low-photon-energy UPS in the valence band and the Fermi-level region. Core-level resonance photo-emission can be easily sutdied with a total resolution of 100 meV at 500eV. The analyzer system will not be fixed at some particular BL, but will be movable to other beam lines, such as BL-2B, BL-3B and BL-20A.

The system is schematically shown in Figs. 10(a) and 10(b). The analyzer axis is set at 65 degrees from the incident light. The sample-mounted on the cold finger of the cryostat (not shown in the figure) is

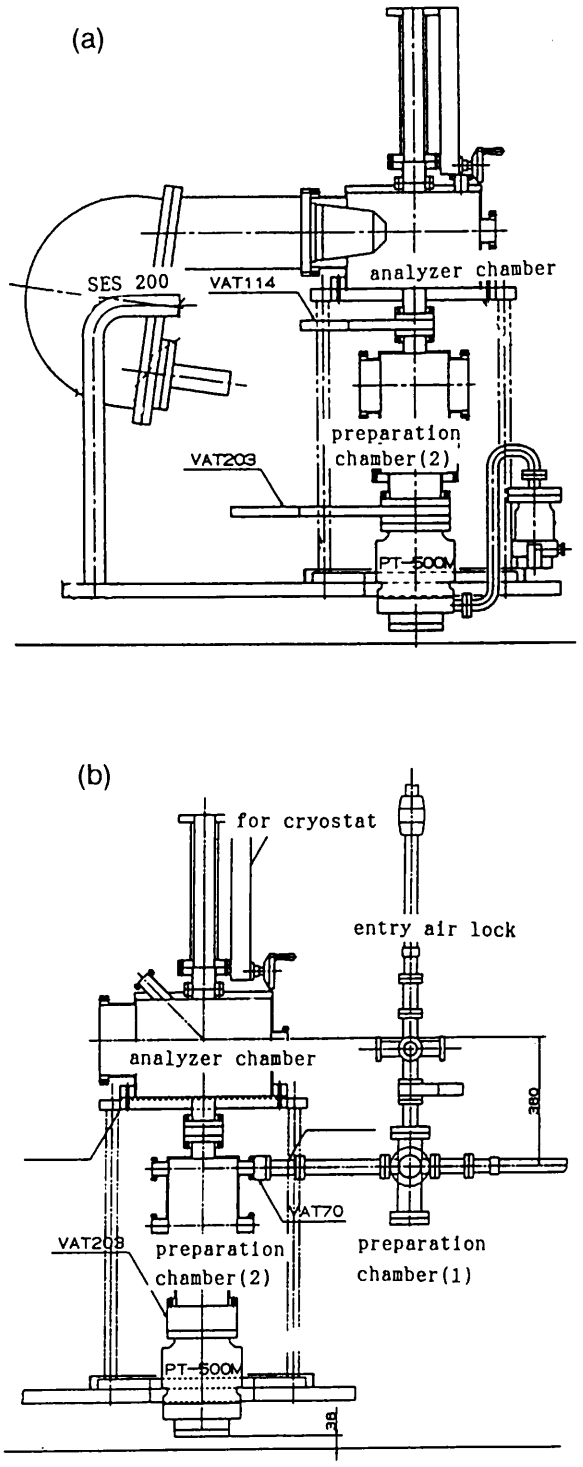

Fig. 10 Side view (a) and front view (b) of the high resolution photoemission spectrometer.

treated (cleaned) in the sample-preparation chamber (2) just below the analyzer chamber. The sample-preparation chamber (2) is evacuated by tandem turbomolecular pumps (TMP) of 500 *l/s* and 150 *l/s*, and the analyzer chamber is pumped by both a sputter ion pump and a 1500 *l/s* TMP backed by a 150 *l/s* TMP. The sample is introduced through an entry air lock system to a sample treatmen, such as filing-or the ion sputtering will be done before further treatment in the preparation chamber (2).

X-Ray Microbeam System for Chemical and Structural Analyses

A new X-ray microprobe system based on Kirkpatrick-Baez optics has been constructed and opened to users at BL-4A. The experimental arrangement is schematically shown in Fig. 11. Radiation from a bending-magnet source is used. Two types of monochromators, a constant-exit Si (111) double-crystal monochromator (DXM) and a synthetic multilayer monochromator (SMM), are equipped to meet the demands for various applications. The DXM system is suitable for high-energy-resolution measurements, such as XAFS, while the SMM system is good for highly sensitive measurements of trace elements and X-ray diffraction studies.

The elliptical Kirkpatrick-Baez system was designed so as to compromise the beam size (spatial resolution) and the photon flux (sensitivity). Elliptical mirrors were fabricated from Pt-coated fused quartz. The glancing angle is 5.3 mrad; as a result, the available highest energy is 15.6 keV. The beam size at the sample is about 5 × 5 μm and the photon flux is of the order of 10^8-10^{10} and 10^7-10^8 photons/s/300 mA for the multilayer and double-crystal monochromators, respectively.

The sample is mounted on *X-Z* translation stages and a θ-rotation stage driven by stepping motors. A *in-situ* high-magnification optical microscope in combination with a TV system is used to determine the analyzing position; it is also used to set the sample at the X-ray focal position using its focal depth.

The present X-ray microbeam system has been used for the following application fields: 1) Trace element analysis using fluorescence X-rays; distributions of trace elements in biological and geological samples are obtained (see Fig.12). 2) XAFS measurements over a small region and chemical-state imaging. 3) Surface characterization using the grazing-exit condition (3-dimensional surface analysis). 4) X-ray diffraction experiments over a small region .

Detailed descriptions of the X-ray microbeam system and its applications to various research fields have been published elsewhere.[1] Another X-ray microbeam by a simple slit system is also available at

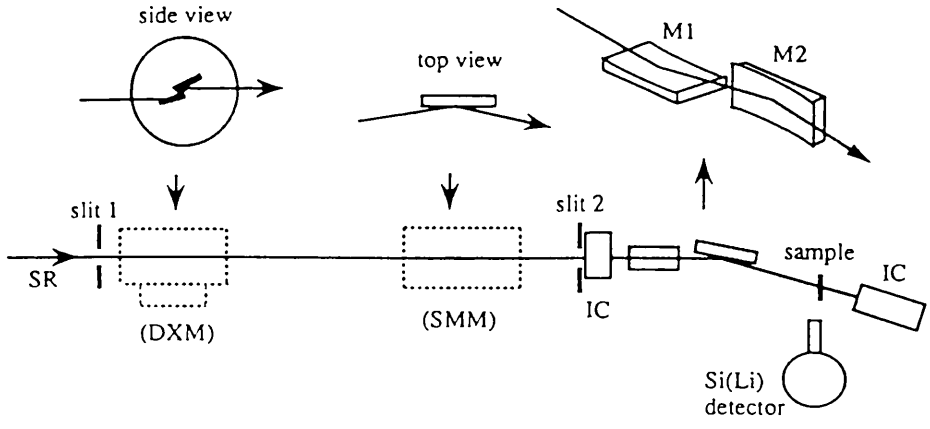

Fig.11 Experimental arrangement of the synchrotron X-ray microbeam. M1 and M2 are focusing mirrors. IC is the ionization chamber.

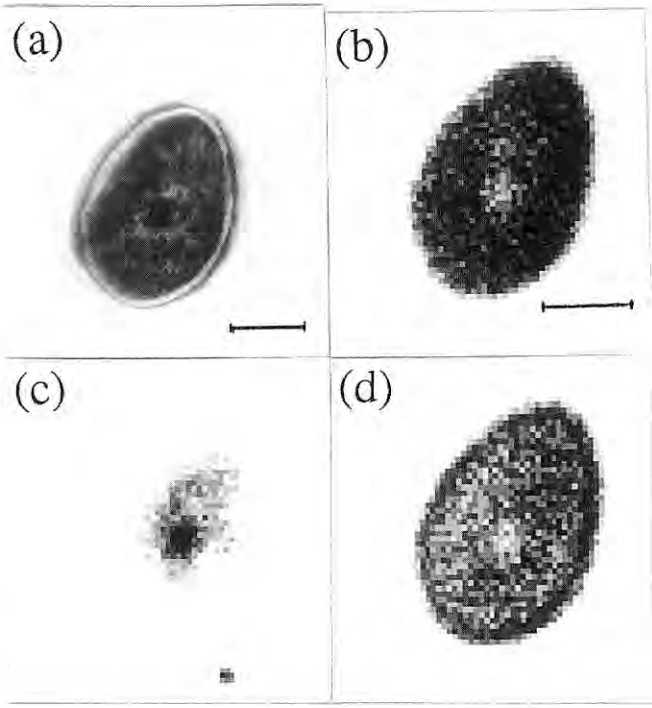

Fig.12 Optical micrograph (a) and fluorescent X-ray intensity distributions from the cross section of a hair shaft. (b) S, (c) Ca and (d) Zn. Scale marks are 50 μm. The incident X-ray energy was 11.5 keV.

BL-4A. The practical beam size is more than 3 μm with continuum X-rays.

1) A. Iida and T. Noma, Nucl. Instrum. and Methods, B82(1993)129 and also see PF Activity Report #10 (1993) and this report.

Ultra-Low-Temperature Diffractometer Based on a ^{3}He-^{4}He Dilution Refrigerator Used for Synchrotron Radiation X-ray topography of Solid Helium

The direct observation of variations in the crystal structure at ultra-low temperatures plays very important roles in gaining a better understanding of the mechanism of the phase transformation and stability of the phase as a ground state. For these purposes, two sets of ^{3}He-^{4}He dilution refrigerators with a top-loading facility were installed at BL-3C2 and BL-6C1. The former is used exclusively for taking topographs from quantum crystals of solid ^{3}He and ^{4}He for studies of lattice defects. The latter refrigerator is used for X-ray diffraction studies of crystalline solids.

The sample cell prepared for X-ray topographs of a helium single crystal should fulfill the following requirements:

(1) It can resist up to at least 10 MPa below 4 K.
(2) Incident and scattered X-ray beams can pass through with moderate attenuation.
(3) A capillary tube of helium inflow and a thermometer should be fitted.
(4) The goniometric adjustment of the crystal position and orientation should be feasible to take Laue patterns.

The helium single crystal was patiently prepared by *in situ* crystal growth at the time of each experiment by a trial-and-error method. Thus, a goniometric adjustment of the orientation of the *in situ* grown crystal to the incident X-rays is indispensable both to assign the Laue spots to the Miller indices and to take topographs only after choosing the spots. Generally, moderately large ω, χ and ϕ rotations of the sample should be required in this case. Only the ω and χ rotation mechanism of the sample cell with a limit of $\pm 20°$ in each were established by modifying the top loading facility in the dilution refrigerators at BL-3C2, as shown in Fig. 13 .

In Fig 13, both ends of cylindrical sample cells made of Be ① were sealed by stainless-steel (SUS304) flanges (② and ③) with a thin In wire sealant, which were screwed to the outer cylindrical jacket ④ of SUS304. OFHC Cu rods (⑦ and ⑧) with a capillary in each center are the axis of the χ rotation of the sample cell, which are held by an Al supporter (⑤ and ⑥) with a surface treatment of Tufram[1] and a brass flange ⑭. Each of the two capillaries is used as an inlet of squeezed helium ⑱ and four lead wires ⑲ of the Matsushita carbon thermometer (50 Ω, 1/8 W)

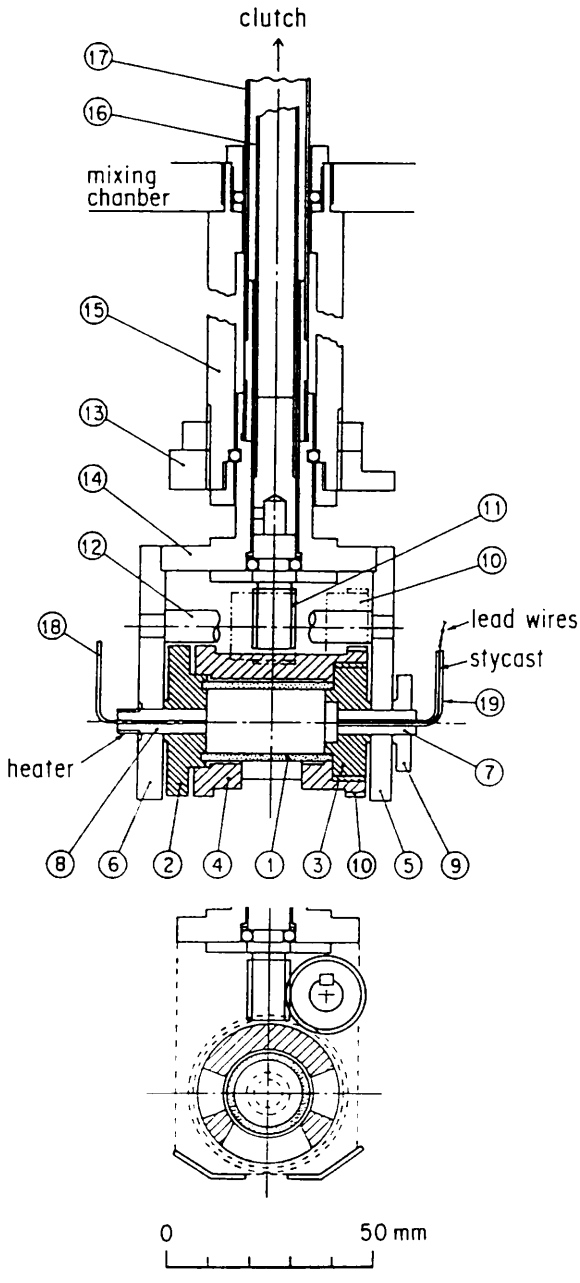

Fig 13 Sample cell with a mechanism of the ω- and χ-circle goniometer The ω-axis is vertical and the χ -axis is parallel to the cylinder-axis of the sample cell.

The jacket ④ has three windows that are similar in shape to a frustum of a right pyramid, which were used for the incident X-rays, the forward scattering ($2\theta_B \approx 0°$) and the downward one ($2\theta_B \approx 90°$). It has a flat gear ⑩ at one side for χ rotation. All of the sample cells are suspended by a thick heat-conduction pipe of OFHC Cu ⑮, which is tightened through a heat conduction plate ⑬ to a thermal-contact plug ⑨ by Cu mesh for ensuring heat conduction, considering the poor thermal conduction of the thrust bearings of the χ ⑯ and ω ⑰ rotation mechanism. Both driver tubes are separable by an occlusion clutch between the 1 K pot and the still.

Recently, typical examples of topographs indicating an annealing effect of solid helium, which might be understood in terms of a quantum tunneling effect, have been observed. The disappearance of downward diffraction Laue spots ($2\theta_B = 90$) was understood based on the temperature factor and others as being a peculiarity of quantum solid helium.

1) The "Tufram" is the registered trademark by ULVAC Co. of Japan. All of the gears used at low temperatures are treated with Tufram processing in the surface, in which Al or Al alloys are coated by Teflon after anodic oxidization. It was developed by Dr. Charles P Covino of General MagnaPlate Co. of USA in 1964.

X-ray TV Detector with a Be-Windowed Image Intensifier

An X-ray TV detector utilizing a beryllium(Be)-windowed X-ray Image Intensifier (I.I.) has been developed for diffraction experiments, especially for time-resolved measurements (Fig. 14). It consists of i) a Be-windowed X-ray I.I., ii) an optical-lens coupling, iii) an image sensor, such as a cooled CCD or a TV-scanning-rate CCD, and iv) data storage which includes an analog-to-digital converter. The Be-windowed X-ray I.I. was developed by HAMAMATSU PHOTONICS K.K. on the basis of accumulated technologies for aluminum-windowed X-ray I.I.s for medical use. It has an aperture of 150 mm$^{\phi}$ with a 1-mm thick Be window. A CsI:Na phosphor of 150 μm thickness is attached directly onto the inner surface of the Be window. The CsI:Na crystals were made in a columnar shape along the direction normal to the phosphor surface so that any undesired light scattering within the phosphor in the lateral direction is minimized. A bi-alkali (RbCsSb) photo-cathode is evaporated onto the inner surface of the CsI:Na phosphor. Incident X-rays are efficiently transmitted through the Be window (80% for 8-keV X-rays), and are converted to visible photons by the phosphor, resulting in photoelectrons with the photo cathode. The photoelectrons are accelerated with an energy of 30 keV so as to produce an intensified visible image on an output phosphor of (Zn, Cd)S:Ag. The intensified image is then viewed through the optical lens by the CCD image sensor. Compared with the prototype X-ray TV,[1] in which a visible-light I.I. is used in combination with a phosphor screen, the photon gain has been increased by about 10 times; further, the incident aperture was increased from 100 mm$^{\phi}$ to 150 mm$^{\phi}$. As a result, as many as 550 visible photons per an 8 keV photon are incident to the CCD. This value is much larger than the noise level of a cooled CCD (about 60 ~ 70 incident visible photons), and is sufficiently large to employ a CCD camera which works at a normal TV-scanning rate. This enables us to record time-resolved diffraction patterns at a rate of 30 frames per second with its background noise quantum-limited. The dynamic range of the Be-windowed X-ray I.I. is about 4 orders of magnitude. The X-ray TV detector has a non-uniformity of response, and any image distortion is corrected by software. This TV detector is being used for small-angle X-ray scattering and X-ray diffraction under high pressure. This project was carried out in collaboration with R & D on Area Detectors for SPring-8.

1) PF Activity Report #9, I-12 (1991).

Fig. 14 Front view of the X-ray TV detector, which utilizes a beryllium-windowed (1 mm thick) X-ray image intensifier.

Bunch-Purity Measurements With an Avalanche Photodiode Detector

Recently, the pulsed-time structure of synchrotron radiation is often used for timing experiments in a single-bunch run of a storage ring. The bunch purity, defined as the ratio of the counts for peaks caused by the impurity bunches to those for a peak caused by the main bunch, is needed to be kept sufficiently low, so as not to interfere with the time structure produced by the beam from the main bunch. It has thus become important to develop a monitor which can be used to measure the bunch purity to better than than 10^{-6}.

The avalanche photodiode (APD) detector, developed as a new timing detector for X-rays, has been applied to measuring the bunch purity. The APD detector detects X-rays directly without a scintillator, and is operated in the linear mode so as to obtain a fast pulse for good timing performance. Figure 15 shows the detector system for bunch-purity measurements at the Photon Factory ring. The APD device used in the present detector (S5343) is a silicon planar epitaxial-type developed by Hamamatsu Photonics K. K.. The diameter of its sensitive area is 1 mm, and the detection thickness is about 10 μm. The fast amplifier, which has a gain of 100, outputs a fast pulse for one X-ray photon detected and the time resolution (FWHM) by the detector system is 100 ps. A fast analog-to-digital converter, a successive approximation type with a fixed dead time of 800 ns, is useful for observing the time structure with a high count-rate up to 500 kcps.

Bunch-purity measurements with the APD detector system were carried out at BL-14A during a single-bunch run on March 27, 1993. The measured time spectra with the APD detector are shown in Figs. 16(a), (b) and (c); each measurement was started at 3, 5 and 9 hours after positron injection into the ring, respectively. Each measuring time was 1000 s. In Fig. 16 (a), the highest peak at t=0 was produced by X-rays emitted from positrons in the main RF bucket. It can be seen that the peak profile consists of a Gaussian peak and a tail, of which the width at 10^{-5} maximum is only 1.4 ns. The tail width, defined as the time width of the observed peak subtracted by the width of the fitted Gaussian peak, is 0.5 ns at 10^{-5} maximum. The small peak at t=2 ns was generated by X-rays emitted from the residual positrons in the second bucket. The count of the second peak decreases with increasing time; no other peaks of impurities can be seen in Fig. 2, because the bunch purification was severely executed during the run with a horizontal scraper and with the RF-knockout method. The background events cannot be seen entirely in each spectrum due to low-noise performance of the APD detector. The values of the bunch purity are thus obtained as the ratio of the counts for the total measured region, except for the main peak, to those of the main peak; 1.9×10^{-6}, 3.1×10^{-8}, and 6.1×10^{-9} are the values at three, five and nine hours after injection, respectively.

After the experiments described above, an APD detector was installed at BL-21 as a bunch-purity monitor which can be used to measure high purity on the order of 10^{-9}. The APD monitor, irradiated by a white beam (0.2x0.2mm), has been successfully operated in single-bunch runs for users.

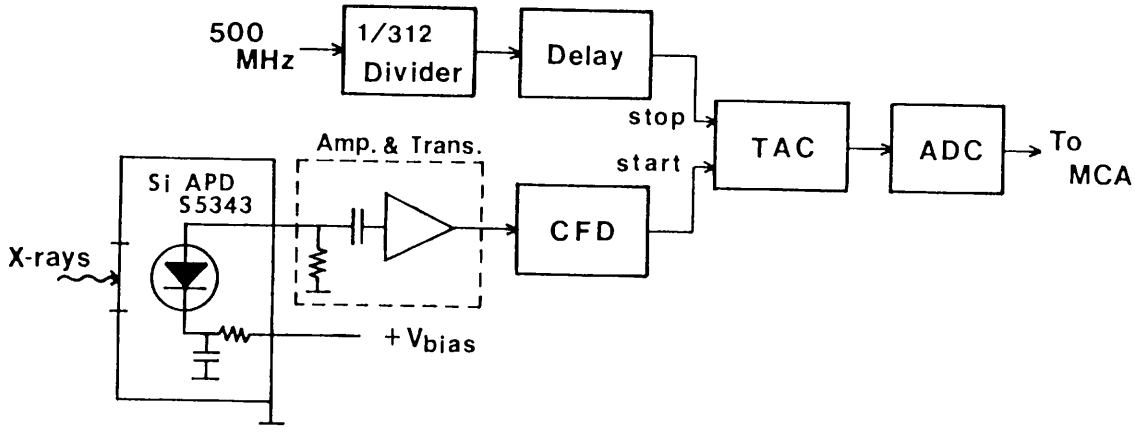

Fig. 15 Block diagram of the APD detector system for bunch purity measurements.

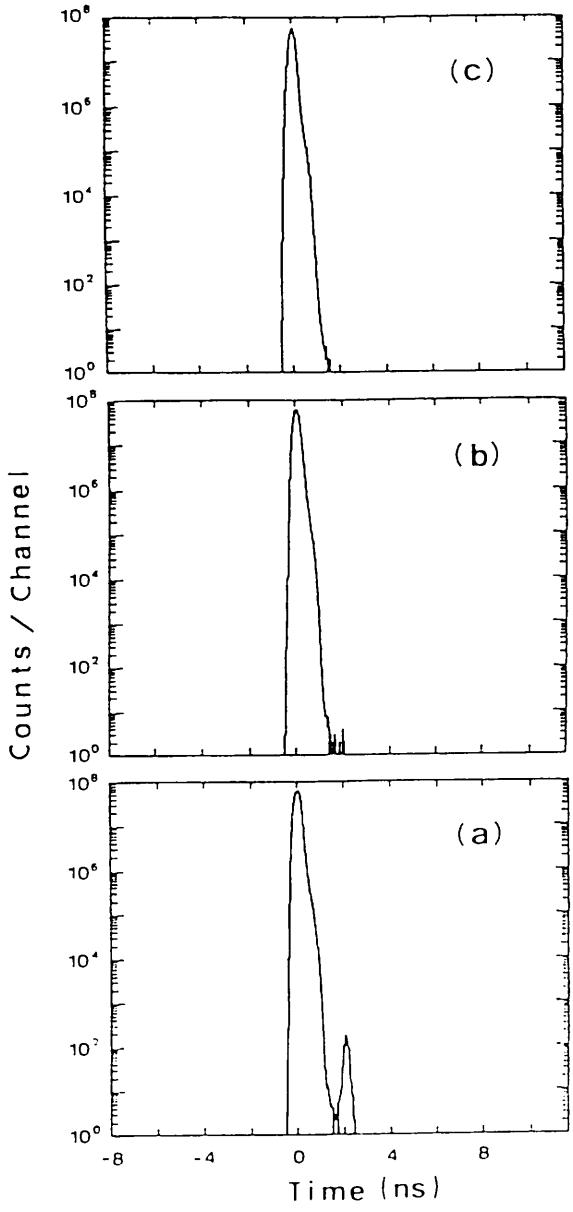

Fig. 16 Time structure of a single-bunch run on March 27, 1993, observed (a) three hours, (b) five hours and (c) nine hours after injection. The measuring time was 1000s for each spectrum.

Improvement of Double-Crystal Monochromators for XAFS experiments.

The percentage of higher order reflections can be controlled by slightly detuning (e.g. 2 arcsec) two crystals when a double-crystal monochromator is used. A piezoelectric translator is commonly used for this purpose, because it is suited for smooth and fine positional adjustments. However, it suffers serious drift as well as hysterisis after its length is changed. Owing to the drift, it was not easy to maintain a certain parallelism between two crystals for a long period; it was also difficult to adjust it at each energy point while measuring the XAFS spectra.

Recently, a piezo translator (PZT) fabricated with a position sensor can be easily obtained at a reasonable price. A PZT (PI P-251) was replaced by one with a position sensor (PI P-841.20) and a controller (PI P-862) at BL-7C. The controller continuously adjusts the voltage so as to keep the expansion of the PZT constant. A similar improvement was also made at BL-6B. By doing so, the intensity stability of monochromatic X-ray beam resulted in a great improvement. In order to test the stability, the parallelism of two crystals was changed from a half-maximum position to another half-maximum position on a rocking curve of Si(111) at 9 keV. Although the intensity changed by ca. 10% within 10 minutes without a sensor, it was constant when a new system was used. A fast-tune adjusting system is realized with the help of this new PZT system, which saves the time required for tune adjustments in the high energy region with crystals of higher indices.

Hot Laboratory for the Use of Radioisotopes as samples

After complicated procedures, and eventually obtaining permission to use radioisotopes, a hot laboratory for using radioisotopes began to operate, which includes the BL-27 area and adjacent sample preparation rooms for biological and biochemical experiments in the experimental hall. The layout of the hot laboratory is shown in Fig. 17. Two ways to use isotopes are expected. First, of isotopes are to be used as tracers, which is very popular in biological studies. Four β-emitting isotopes (^{3}H, ^{14}C, ^{32}P, ^{35}S) can be used to label some specific molecules; the consequences of these molecules after being irradiated with monochromatic synchrotron X-rays will be studied. The use radioisotopes as tracers will

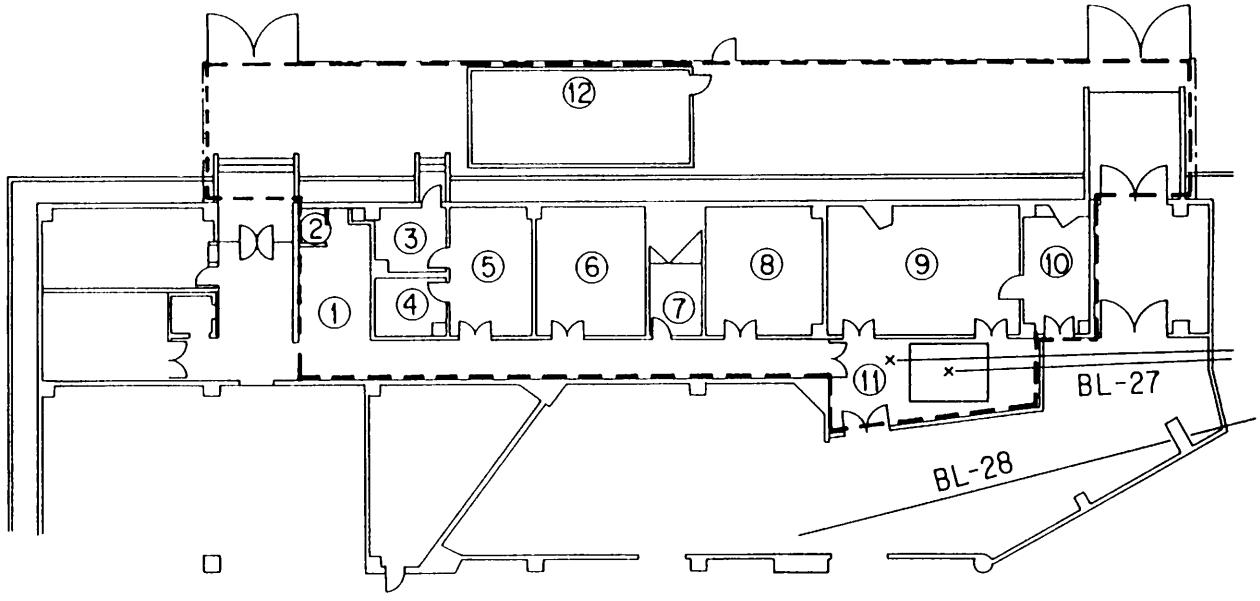

Fig. 17 Layout of the hot laboratory.
1. Gate monitor, 2. Shower for de-contamination, 3, 4, 5. Radioisotope treatment rooms, 6. Culture room for mammalian cells, 7. Radioisotope storage room, 8. Culture room for microorganisms, 9. Analysis room, 10, Radioisotope measurement room, 11. Experimental stations of BL-27, 12. Sewer storage tanks.

accelerate the progress of synchrotron-radiation biophysics, since it will lower the detection limit of molecules. In the second usage, samples containing radioisotopes are to be analyzed either by X-ray diffraction, by X-ray photoelectron spectroscopy or by X-ray absorption spectroscopy, without any further physical or chemical treatment of samples. More than 100 nuclei can be used. Structure analyses of neutron-activated or particle beam-bombarded materials as well as samples including actinide elements (U or Th) will be extensively carried out.

New Experimental Building

A rapid increase in the number of beamlines and experimental instruments gave rise to a serious problem: the lack of working space in the main experimental hall of the 2.5 GeV ring building. In order to solve this problem, plans for a new experimental building were proposed to the government in 1988. The plans were partly approved in January 1992. The construction of a building was started in April 1992, and was completed in March, 1993.

The new building (see Fig. 18) is located beside the Photon Factory office building, with a total floor space of 1190 m^2, including a main experimental hall (504 m^2) and a two-storied office-area (336 m^2). This newly constructed experimental hall can be used for preliminary experiments as well as for assembling and repairing various kinds of instruments.

D. SUMMARY OF EXPERIMENTAL STATION AND BEAMLINE OPTICS

Table 1 summaraizes the experimental stations in operation with the names of the contact persons. The basic characters of X-ray beamlines are listed in Table 2, and the types of monochromators for VUV and soft X-ray beamlines are listed in Table 3. Figure 18 is the latest plan view of the SR laboratory area of the PF experimental hall schematically showing the arrangement of the experimental stations now in operation or under construction.

Table 1. List of Experimental Stations

Experimental Station	Contact person
BL-1 [NTT]	
A Solid surface analysis	M. Oshima
B X-ray lithography	H. Kinoshita
C Photochemical reaction	Y. Utsumi
BL-2 (Undulator)	
A Soft X-ray spectroscopy	Y. Kitajima
B1 Soft X-ray microscopy	A. Yagishita
B2 Soft X-ray spectroscopy	A. Yagishita
BL-3	
A X-ray diffraction and scattering	T. Matsushita
B VUV and soft X-ray spectroscopy	E. Shigemasa
C1 X-ray diffraction	T. Matsushita
C2 X-ray topography in milli-Kelvin region (for solid helium)	T. Nakajima
BL-4	
A Trace element analysis, X-ray microprobe	A. Iida
B Liquid/melt structure analysis, powder diffraction, micro-crystal structure analysis	K. Ohsumi
C X-ray diffuse scattering, fluorescent EXAFS	S. Kishimoto
BL-6	
A Macromolecular crystallography by Weissenberg camera	A. Nakagawa
B X-ray spectroscopy and diffraction	M. Nomura
C1 X-ray diffraction at low temperatures	T. Nakajima
C2 Accurate lattice spacing measurement	M. Ando
BL-7 [The Research Center for Spectrochemistry, The Univ. of Tokyo]	
A Soft X-ray photoelectron spectroscopy	H. Namba
B Surface photochemical reaction and angle resolved photoelectron spectroscopy [PF]	H. Namba
C X-ray spectroscopy and diffraction	M. Nomura
BL-8 [Hitachi]	
A Soft X-ray spectroscopy	Y. Hirai
B EXAFS	A. Nakano
C1 X-ray lithography	M. Itou
C2 X-ray tomography and digital radiography	K. Usami
BL-9 [NEC]	
A X-ray lithography	K. Suzuki
B Photochemical reaction	I. Nishiyama
C EXAFS and X-ray topography/diffraction	J. Mizuki
BL-10	
A X-ray diffraction/scattering, crystal structure analysis	M. Tanaka
B XAFS	N. Usami
C Small-angle X-ray scattering of enzymes, surface diffraction	K. Kobayashi
BL-11	
A Soft X-ray spectroscopy	A. Yagishita
B Surface EXAFS, soft X-ray spectroscopy	Y. Kitajima
C VUV spectroscopy (solid state)	H. Kato
D Angle-resolved photoelectron spectroscopy	H. Kato

Experimental Station	Contact person
BL-12	
A Soft X-ray spectroscopy (under construction)	K. Tanaka
B VUV high-resolution spectroscopy	K. Ito
C Photochemical reaction	K. Tanaka
BL-13 (Multipole wiggler/Undulator) [Research team for advanced materials*]	
A Accurate lattice parameter measurement	K. Nakayama
B1 Surface-sensitive XAFS, X-ray diffraction	H. Oyanagi
B2 High pressure & high temperature X-ray diffraction	O. Shimomura
C Soft X-ray photoemission spectroscopy and XAFS	H. Shimada
BL-14 (Vertical wiggler)	
A Crystal structure analysis, EXAFS	S. Kishimoto
B High-precision X-ray optics	K. Hirano & A. Iida
C General purpose (X-rays)	N. Watanabe
BL-15	
A Small-angle X-ray scattering of muscle and alloys	Y. Amemiya
B White X-ray topography and X-ray magnetic bragg scattering	H. Kawata
C High-resolution X-ray diffraction	K. Hirano & A. Iida
BL-16 (Multipole wiggler/Undulator)	
A General purpose (X-rays)	K. Takeshita
U Soft X-ray spectroscopy	H. Kato
BL-17 [Fujitsu]	
A Characterization of crystals	S. Komiya
B Photochemical vapor deposition	S. Komiya
C X-ray lithography	S. Komiya
BL-18 [The Institute for Solid State Physics, The Univ. of Tokyo]	
A Angle-resolved photoelectron spectroscopy of surfaces and interfaces [PF]	A. Kakizaki
B Macromolecular crystallography (Weissenberg and Laue)	N. Watanabe
BL-19 (Revolver undulator) [The Institute for Solid State Physics, The Univ. of Tokyo]	
A Spin-polarized photoelectron spectroscopy	A. Kakizaki
B Photoelectron spectroscopy at various temperatures	A. Kakizaki
BL-20 [PF]	
A VUV spectroscopy [Australia]	K. Ito
B White and monochromatic beam general purpose X-ray station	G. Foran
BL-21 [Light Source Division]	
Beam position monitoring	T. Katsura
BL-27 (Beamline for experiments using radioisotopes, under construction)	
A Radiation biology, Soft X-ray photoelectron spectroscopy	K. Kobayashi
B Radiation biology, X-ray diffuse scattering	K. Kobayashi
BL-28 (Multipole wiggler/Undulator)	
A VUV and soft X-ray spectroscopy with circularly polarized undulator radiation	T. Miyahara
B Spectroscopy and scattering with polarized X-rays	T. Iwazumi

* National Laboratory of Metrology, National Institute of Researches in Inorganic Materials, Electrotechnical Laboratory, National Institute of Materials and Chemical Research, The Institute of Physics and Chemical Research

Table 2. X-Ray Beamline Optics

Branch Beam Line	Acceptance Horiz. (mrad)	Beam Size (H × V)	Photon Flux at Sample Position	Type of Monochromator	Energy Resolution $(\Delta E/E)\times10^{-4}$	Photon Energy (keV)	Mirror
BL-3A	4	100 × 5 4 × 0.1		Double Crystal Si(111) Sagittal Focusing	~ 2	4 ~ 25	Collimating and Focusing Mirrors (Fused Quartz)
BL-3C1/C2	2	20 × 4		None		4 ~ 30	None
BL-4A	6	50 × 4 4 × 1		Double Crystal Sagittal Focusing	~ 2	4 ~ 20	None
BL-4B	4.5	50 × 5		Double Crystal Si(111)	~ 2	4 ~ 35	None
BL-4C	4	4 × 1		Double Crystal Si(111) Sagittal Focusing	~ 2	4 ~ 20	None
BL-6A	4	2.5 × 1		Bent Si(111) (a = 0, 6.0°, 7.8°, 9.5°, 11.4°, 13.7°, 16.5°)		5 ~ 25	Bent Plane Fused Quartz
BL-6B	4	8 × 1		Double Crystal Si(220), Si(111), Si(311) Sagittal Focusing with Si(111)	~ 2	4 ~ 25 (4 ~ 13)	None
BL-6C1	4	37 × 5		None		8 ~ 30	
BL-6C2	0.5	5 × 5		Channel-Cut Si (111)	7.5	8 ~ 12	None
BL-7C	4	8 × 1	1×10^{10}/6mm^2 (8 keV, 300 mA) (1×10^{11} when focused)	Double Crystal Si (111) Sagittal Focusing	~ 2	4 ~ 20 (4 ~ 13)	Double Mirror Fused Quartz Focusing
BL-8C1/C2	5	50 × 5	2×10^6/mA·mm^2 at 10 keV with Si (111)	Channel-Cut Si(220), Si(111), Si(400)	~ 2	5 ~ 40	None
BL-9A	5	25 × 25				1.2 ~ 3.1	SiC
BL-9C	5	150 × 5		Double Crystal Si(111) Sagittal Focusing	~ 2	5 ~ 25	None
BL-10A	1	10 × 3		Si(111), Si(220) Ge(111), InSb(111) Quartz(100), PG(002) Curved Si(111) (α ~ 4°, 8°)	50 ~ 5	5 ~ 25	None
BL-10B	2	8 × 1	1×10^9/7mm^2 (10 keV, 300 mA)	Channel-Cut Si(311)	1	6 ~ 30	None
BL-10C	4	6 × 1.5	~ 10^{10}/9mm^2 (8 keV, 100 mA)	Double Crystal Si(111)	2	4 ~ 10	Bent Cylinder

Branch Beam Line	Acceptance Horiz. (mrad)	Beam Size (H × V)	Photon Flux at Sample Position	Type of Monochromator	Energy Resolution $(\Delta E/E)\times10^{-4}$	Photon Energy (keV)	Mirror
BL-13A	1			Double Crystal Si(220)	~ 0.1	4 ~ 30	None
BL-13B1/B2	4	4 × 1		Double Crystal Si(111), Si(220) Sagittal Focusing	~ 2	4 ~ 30	Bent plane Fused Quartz
BL-14A	1.28 (Vertical)	5 × 38		Double Crystal Si (111) Si (311) Si (553)	2	5.1 ~ 19.1 9.9 ~ 35.6 22.7 ~ 84.5	Bent Cylinder for Vertical Forcusing, Pt-coated Fused Quartz
BL-14B	2.2	5 × 30		Double Crystal Si(111),Si(220),Si(311)	2	5.2 ~ 57	None
BL-14C	1.3	10 × 40		Double Crystal Si(111), Si(220)	2	5.5 ~ 69	None
BL-15A	2	0.7 × 0.8 at focus	9×10^{10}/6mm^2 (8.0 keV, 150 mA)	Bent Crystal Ge(111) (α = 8.0°)	~ 10	5.6 ~ 12.4	Bent Plane, Fused Quartz
BL-15B	0.14	5 × 5		None		3.5 ~ 34	None
BL-15C	2	60 × 6		Double Crystal Si(111)		4 ~ 30	None
BL-16A	4	4 × 1		Double Crystal Si(111) Sagittal Focusing	~ 2	4 ~ 35	
BL-17A	4	100 × 10		Double Crystal Si(111)	~ 2	5 ~ 13	None
BL-17C	1	20 × 5		None		2	Quartz (plane)
BL-18B	2	1.2 × 0.4	1.1×10^{10} (12.4 keV, 300 mA) Si(111)	Double Crystal Si (111) Si (220) Ge (111) Ge (220)	~ 2	6 ~ 30	Bent Cylinder Fused Quartz, Pt-coated
BL-20B	2	26 × 3		Channel Cut Si (111)	~ 2	4 ~ 25	None
BL-27B	4	100 × 10		Double Crystal Si (111)	~ 2	4 ~ 20	None
BL-28B	4 × 0.2	2.4 × 0.3	3×10^{10} (9 Kev, 300 mA) Si (220) Pc ~ 0.5	Double Crystal Si (111) Si (220) InSb (111)	3 (at 6.3 keV)	2 ~ 10	Pre-mirror Bent Cylinder Si Pt- & Ni-coated Post-mirror Bent Plane Fused Quartz Pt- & Ni-coated

Table 3. VUV and Soft X-ray Monochromators

Branch Beamline	Acceptance Horiz./Vert. (mrad)	Type of Monochromator	Grating Grove density (l/mm)	Photon Energy (eV)	Beam Size (mm)	Typical Resolution ($\lambda/\Delta\lambda$)	Reference
BL-7B (RCS)	6 4	1m Seya-Namioka	1200 2400	5 ~ 50	1 × 1	1000	1
BL-11C	4.8 3	1m Seya-Namioka	1200	4 ~ 35	~1 ϕ	1000	2
BL-12B	5 3.6	6.65 m Off-Plane Eagle	1200 4800	5 ~ 30	——	2.5×10^5	3,4
BL-20A	28 5	3m Normal Incidence	1200 2400	5 ~ 40	2 × 1	3×10^4	----
BL-1A (NTT)	4 0.5	Grating/Crystal	1200 2400	50 ~ 900	4 × 1	500	5
BL-1B' (NTT)	1.2 4	Plane Grating	600 1200 2400	10 ~ 500	5 × 1	200	----
BL-1C' (NTT)	2 4	Plane Grating	600 1200	15 ~ 300	----	100	----
BL-2B2 Undulator	K = 0.55 ~ 2.2 λ_u = 6 cm	10 m Grazing Incidence α = 89°	1200 2400	250 ~ 1600	< 0.2 ϕ	500 ~ 5000	6, 7, 8
BL-3B	10 2	Grazing Incidence R = 24 m $\alpha+\beta$ = 165°	200 600 1800	10 ~ 280	< 2 ϕ	200 ~ 3000	9, 10
BL-7A (RCS)	6 1	Plane Grating	1200 2400	10 ~ 1000	2 × 1	500	11
BL-8A (Hitachi)	0.5 1	Varied-space Plane Grating	800 2400	40 ~ 1800	5 × 1	1000	12
BL-11A	1 0.5	2 m Grazing Incidence α = 88° Grasshopper Mark VII	600 1200 2400	40 ~ 1000	< 1 ϕ	200 ~ 2000	13
BL-11D	1.5 2	Grazing Incidence R = 2 m $\alpha+\beta$ = 154°	600 1200 2400	20 ~ 150	1.5 ϕ	100 ~ 1500	14
BL-12C'	5 1	Plane Grating	1200	50 ~ 800	1 × 1	100	----
BL-13C Undulator	K = 0.3 ~ 4.2 λ_u = 18 cm	Grazing Incidence R = 50 m $\alpha+\beta$ = 173.2°	750	140 ~ 1000	5 × 1	1000 ~ 6000	15
BL-16U Undulator	K = 0.5 ~ 5.75 λ_u = 12 cm	2 m Grazing Incidence α = 87°	1200 2400	40 ~ 600	----	1400 ~ 2500	16, 17
BL-18A (ISSP)	2 2	Grazing Incidence R = 3 m $\alpha+\beta$ = 160° R = 6.65 m $\alpha+\beta$ = 167.5°	300 600 1200 500	7 ~ 150	< 1 ϕ	1000 ~ 2000	18

Branch Beamline	Acceptance Horiz./Vert. (mrad)	Type of Monochromator	Grating Grove density (l/mm)	Photon Energy (eV)	Beam Size (mm)	Typical Resolution ($\lambda/\Delta\lambda$)	Reference
BL-19A Revolver Undulator (ISSP)	K = 1.0 ~ 9.0 λ_u = 16.4 cm	Grazing Incidence R = 2 m α+β = 160° R= 4 m α+β = 170°	600 1200 600 1200	12 ~ 250	< 0.7 φ	1000	19, 20
BL-19B Revolver Undulator (ISSP)	K = 0.5 ~ 1.25 λ_u = 5 cm K = 0.5 ~ 2.5 λ_u = 7.2 cm K = 1.0 ~ 5.0 λ_u = 10 cm	Varied-space Plane Grating	800 2400	10 ~ 1200	< 0.5 φ	1500	20
BL-28A Undulator	K_x ≃ 0.5 ~ 3 Ky ≃ 0.5 ~ 0.75 λ_u = 16 cm	Grazig Incedence R = 2 m α+β = 160° R = 4 m α+β = 170°	600 1200 600 1200	15 ~ 250	< 0.5 φ	1000	21
BL-1A (NTT)	4 0.5	Grating/Crystal InSb (111) Si (111)	----	1800 ~ 4000	4 × 1	2000	5
BL-2A Undulator	K = 0.5 ~ 2.2 λ_u = 6 cm	Double Crystal InSb (111) Si (111)	----	1760 ~ 5000	2 φ	5000	7, 22
BL-8B (Hitachi)	3 0.5	Double Crystal InSb (111) Si (311)	----	1700 ~ 14000	1.9 × 0.5	5000	----
BL-11B	4 0.6	Double Crystal InSb (111)	----	1760 ~ 3650	8 × 1	2000	23, 24
BL-27A	5 0.5	Double Crystal InSb (111)	----	1800 ~ 6000		2000	----
BL-1B (NTT)	1.2 4	Plane Mirror	----	----	5 × 1	----	----
BL-1C (NTT)	2 4	Toroidal Mirror	----	----	3 × 5	----	25
BL-2B1 Undulator	K = 0.55 ~ 2.2 λ_u = 6 cm	Zone Plate	----	400 ~ 830	~ 0.01φ	50	26, 27, 28
BL-9A (NEC)	5 0.3	Oscillating Mirror	----	----	----	----	29
BL-9B (NEC)	10	Plane + Toroidal Mirrors	----	----	15 × 20	----	29
BL-12C	5 1	Toroidal + Multilayer Mirrors	Rh - Si 21 Layers Rh - C 21 Layers	80 ~ 103 89 ~ 124	2 × 1	12 15	30
BL-17B (Fujitsu)	8 1	Toroidal Mirror	----	----	10 × 1	----	----

References

1. H. Namba et al., Rev. Sci. Instrum. **60**, 1917 (1989).
2. Photon Factory Activity Report 1982/1983, V-15 (1984).
3. K. Ito et. al., Appl. Opt. **25**, 837 (1986).
4. K. Ito et al., Appl. Opt. **28**, 1813 (1989).
5. T. Kawamura et al., Rev. Sci. Instrum. **60**, 1928 (1989).
6. H. Maezawa et al., Nucl. Instrum. and Meth. A**246**, 310 (1986).
7. H. Maezawa et al., Rev. Sci. Instrum. **60**, 1889 (1989).
8. A. Yagishita et al., Rev. Sci. Instrum. **63**, 1351 (1992).
9. A. Yagishita et al., KEK Preprint 90-132 (1990).
10. S. Masui, et al., Rev. Sci. Instrum. **63**, 1330 (1992).
11. H. Namba et al., Rev. Sci. Instrum. **60**, 1909 (1989).
12. M. Itou et al., Appl. Opt. **28**, 146 (1989).
13. M. Yanagihara et al., KEK Report 84-17 (1984).
14. T. Miyahara et al,. Jpn. J. Appl. Phys. **24**, 293 (1985).
15. M. Matsubayashi et al., Rev. Sci. Instrum. **63**, 1363 (1992).
16. Y. Muramatsu and H. Maezawa, Rev. Sci. Instrum. **60**, 2078 (1989).
17. Y. Muramatsu et al., Rev. Sci. Instrum. **63**, 1305 (1992).
18. S. Suzuki et al., Activity Report of SRL-ISSP 60 (1989).
19. A. Kakizaki et al., Rev. Sci. Instrum. **63**, 1289 (1992).
20. A. Kakizaki et al., Rev. Sci. Instrum. **60**, 367 (1989).
21. Y. Kagoshima et al.,Rev. Sci. Instrum. **63**, 1289 (1992).
22. Y. Kitajima et al., Rev. Sci. Instrum. **63**, 886 (1992).
23. T. Ohta et al., Nucl. Instrum. and Meth. A**246**, 373 (1986).
24. M. Funabashi et al., Rev. Sci. Instrum. **60**, 1983 (1989).
25. T. Urisu et al., Rev. Sci. Instrum. **60**, 2157 (1989).
26. Y. Kagoshima et al., Jpn. J. Appl. Phys. **29**, L 172 (1989).
27. Y. Kagoshima et al., Rev. Sci. Instrum. **60**, 2448 (1989).
28. Y. Kagoshima et al., Rev. Sci. Instrum. **63**, 605 (1992).
29. Photon Factory Activity Report 1988 # 6, I-13 (1989).
30. Photon Factory Activity Report 1988 # 6, I-11 (1989).

放射光実験施設配置図

Plan View of the Photon Factory

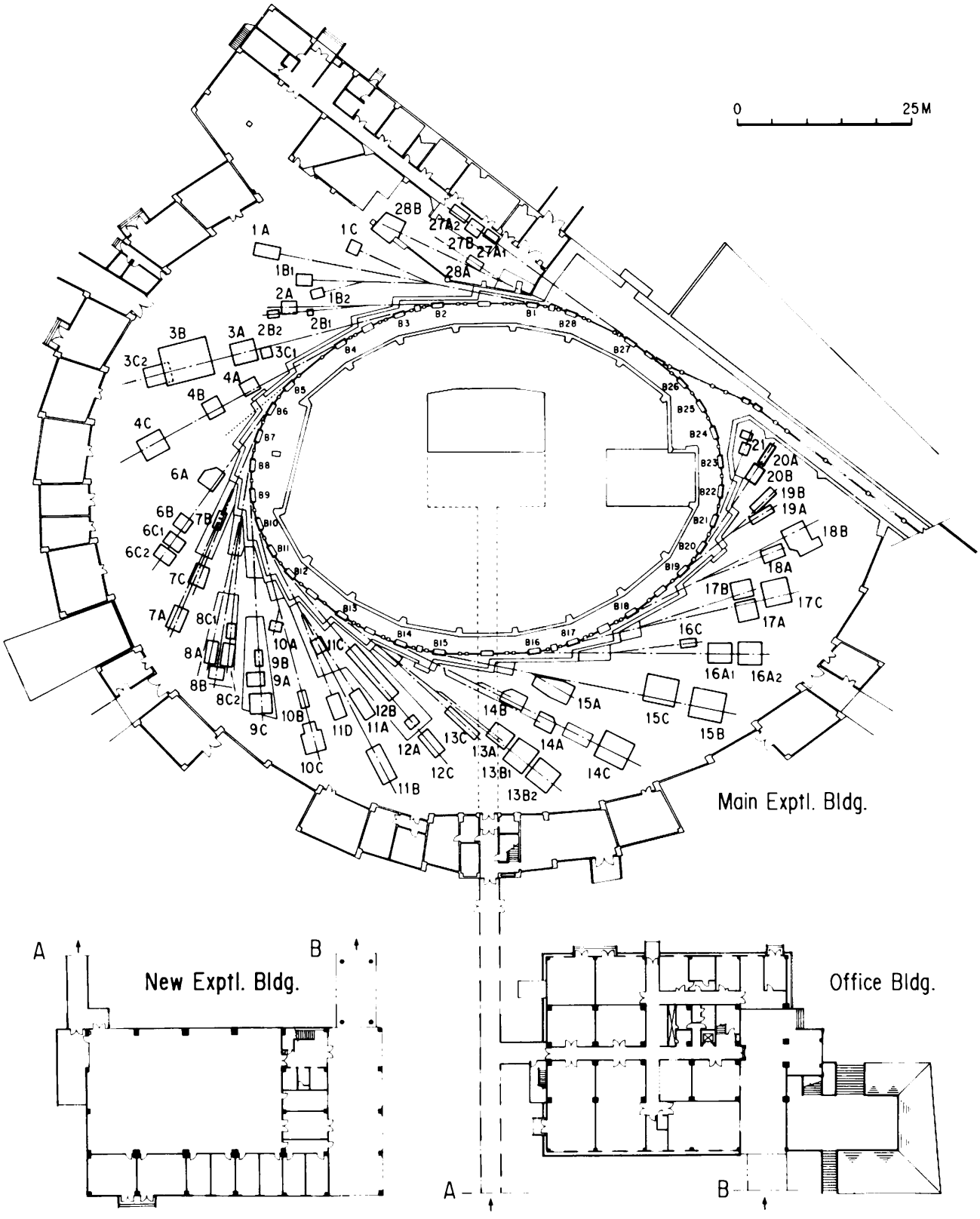

The Synchrotron Radiation Facility at the TRISTAN Accumulation Ring

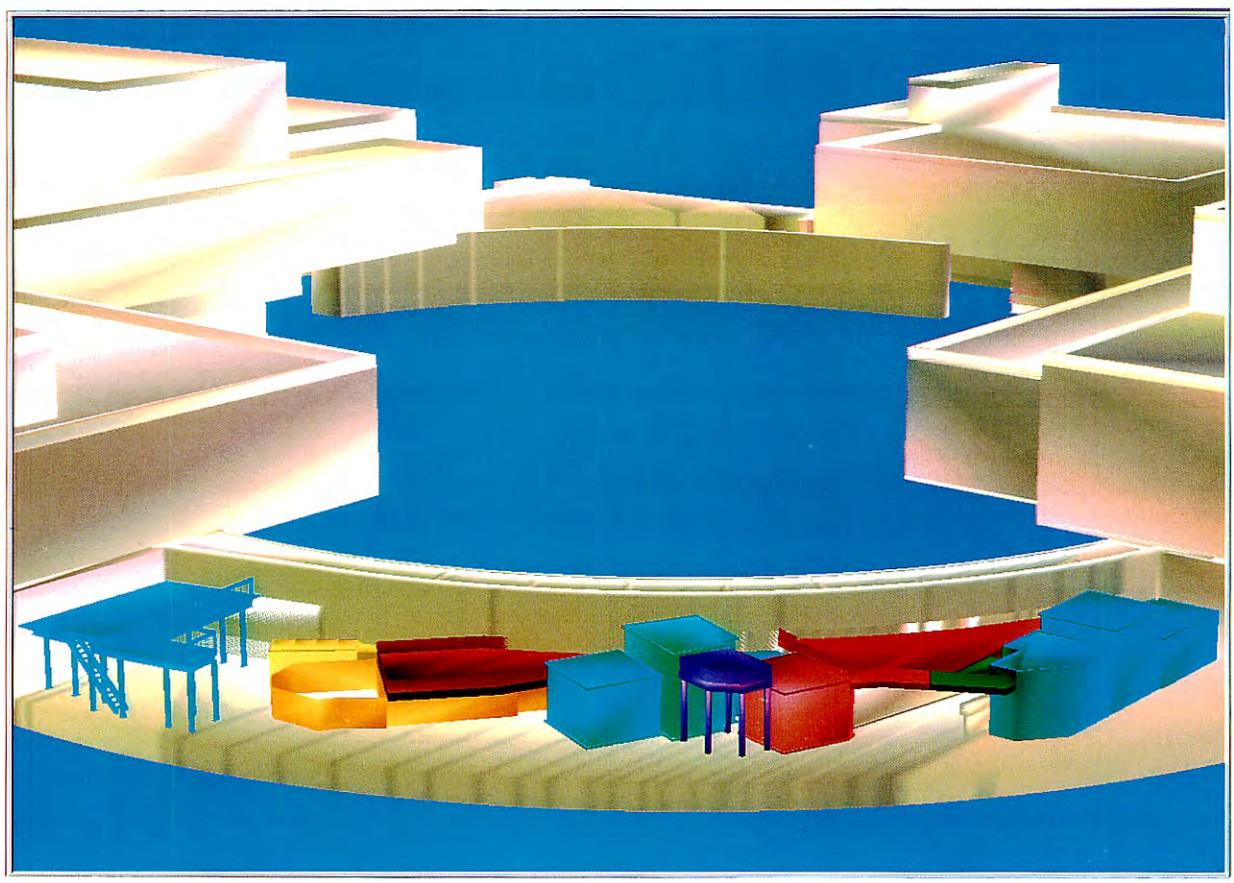

A computer sketch of the AR experimental hall where SR beamlines are located. From right to left a light blue hutch corresponds to NE1, purple to NE3, green and light blue to NE5 and yellow to NE9.

You can jump to the article by clicking its title.

CONTENTS

A. INTRODUCTION

TRISTAN Accumulation Ring (AR) has been used successfully as a high energy photon source since 1984.

Since the AR was designed to have function as a booster ring for the TRISTAN Main Ring (MR), its acceleration energy can be varied between 2.5GeV to 8GeV on request from SR users. It has been usually operated at 6.5 GeV for SR experiments and at 5.8 GeV for coronary angiography experiment.

The possibility of a status change of the TRISTAN Accumulation Ring (AR) as a booster ring to a dedicated ring for synchrotron-radiation sciences has been presented by the Director General. After an opportunity to discuss with the matter during the 10th anniversary commemoration symposium hold in December, 1992 at KEK, a group dedicated to a survey of the sciences using SR from the AR was formed in July 1993. Its members are listed in Table 1. A subpanel on machine modifications was also formed and its members are listed in Table 2.

Table 1. Member list of a group for survey of the sciences using SR from the AR.

Nasu, Keiichiro*	PF *chair
Ando, Masami	PF
Hieda, Kotaro	Rikkyo University
Ishii, Takehiko	ISSP
Iwasaki, Hiroshi	PF
Kamada, Susumu	PF
Kawata, Hiroshi	PF
Kikuta, Seishi	University of Tokyo
Kitamura, Hideo	PF
Kobayakawa, Hisashi	PF
Matsushita, Tadashi	PF
Miyahara, Tsuneaki	PF
Ohta, Toshiaki	University of Tokyo
Sato, Isamu	PF
Shimomura, Osamu	PF
Shiotani, Nobuhiro	Tokyo University of Fisheries

Table 2. Member list of a subpanel on machine modifications.

Kamada, Susumu*	PF *chair
Fukuma, Hitoshi	TRISTAN Accelerator
Hori, Yoichiro	PF
Isawa, Masaaki	PF
Kato, Masahiro	PF
Kitamura, Hideo	PF
Kobayakawa, Hisashi	PF
Kobayashi, Yukinori	PF
Omi, Kazunori	PF
Yamamoto, Shigeru	PF

Discussions have just started as to whether we should keep the current situation, or to modify the machine to be an advanced x-ray source, which means an approximately 4-GeV machine, or low -energy machine oriented towards VUV science, or even a very low-energy machine, such as for an FEL source. That committee is now reviewing what was done so far and what could be done in the near future at the AR. A subpanel on assessing of the utilization of SR at the AR was also formed, and its main members are listed in Table 3

Table 3. Member list of a subpanel assessing of the utilization of SR.

Nasu, Keiichiro*	PF *chair
Ando, Masami	PF
Hyodo, Kazuyuki	PF
Iwazumi, Toshiaki	PF
Kagoshima, Yasushi	PF
Kanazawa, Kenichi	TRISTAN Accelerator
Kawata, Hiroshi	PF
Kikegawa, Takumi	PF
Sugiyama, Hiroshi	PF
Zhang, Xiaowei	PF

The names of the persons who have been involved in the synchrotron radiation project at the AR in the period between October 1992 and September 1993 are listed in Table 10.

B. OPERATION OF THE TRISTAN ACCUMULATION RING FOR SR EXPERIMENTS

The TRISTAN accumulation ring(AR) is a booster synchrotron of the TRISTAN main ring (MR). In the interval between the beam filling in MR, the AR is operated as an electron storage ring for SR experiments. The typical period of a fill is about 2 hours. Table 4 shows the parameters of the AR. Table 5 summarizes the operation statistics of the AR during this year.

In SR operation during this last year, a curious beam intensity oscillation was observed at the SR beam line. It seems that the beam size was oscillating with a period of a few seconds. The mechanism of the oscillation has not yet been understood in detail; however, it was found that it could be avoided by changing the RF voltage. Now the RF cavities are operated with Vc=15MV at 6.5 GeV.

Table 4. General parameters of the TRISTAN AR.

Energy	6.5 GeV
Number of bunch	1
Stored current	40mA
Beam life time	4-5 hr.
Natural emittance	293 nm rad
Circumference	377 m
RF frequency	508.6 MHz
Bending radius	23.2 m
Energy loss per turn	6.66 MeV
Damping time	
horizontal	2.5 ms
vertical	2.5 ms
longitudinal	1.2 ms
Natural bunch length	18.6 mm
Momentum compaction factor	0.0129
Natural chromaticity	
horizontal	-14.3
vertical	-13.1

Table 5. Operation statistics of the TRISTAN AR.

AR machine study & tuning	209.0 hr.
MR machine study & injection	550.0
User time for SR research	3808.5
Machine failure	251.5
Others	120.0
Total	4939.0

C. BEAMLINES AND INSTRUMENTATION

1. Strong Pulsed Magnetic Field at BL-NE1A2

Experiments concerning magnetic scattering and absorption have been extensively carried out using circularly polarized synchrotron-radiation x-rays. For these experiments, an external magnetic field is essential to alternatively magnetize a sample is the opposite direction. We encountered a technical problem, as to how to magnetize a hard magnetic sample. A practical small electromagnet is applicable only for soft magnetic samples; a superconducting magnet, although it is effective for hard magnetic samples, requires a long time to reverse the large magnetic field. We are trying to overcome the problem by using a pulsed magnetic field. Our idea is as follows: if the sample comprises hard magnetic materials, a strong magnetic field is necessary only to change the magnetization direction, because the sample maintains its magnetization by a large remanence. The pulse magnet under preparation has a current duration of 1 ms with a wave form of a half-sinusoidal wave. The maximum field is 16 T with a maximum frequency of 1 Hz. Figure 1 shows a schematic diagram of the magnet. The details of the magnet are described in this activity report.

In addition to the application of the pulse magnet to technical problems, it would be interesting to investigate field-induced magnetic transitions, such as metamagnetic transitions. For instance, the field dependence of the magnetization of a specific atom will be measured by means of magnetic x-ray absorption spectroscopy around the absorption edge. This technique will be useful for examining the such magnetization processes as magnetostriction or magnetic aftereffects. Continuously, we intend to make an effort to improve the pulse magnet for a higher magnetic field.

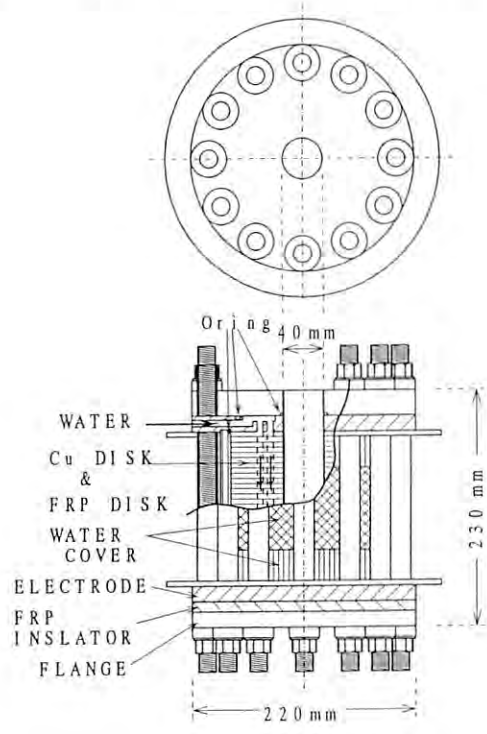

Fig.1 Schematic diagram of the pulsed magnet.

2. Spectral Resolution of a Vertical Dispersion 10m Grazing-Incidence Monochromator of BL-NE1B

The elliptical multiple wiggler (EMPW#NE1) provides circularly polarized soft x-rays with a photon energy ranging from 250 eV to 1500 eV.

One of the branch beamlines, NE1B, is equipped with a vertical dispersion grazing-incidence grating monochromator, approximately 43m apart from the EMPW#NE1. The monochromator is of the inverse Vodar type with two interchangeable gratings having a groove density of 1200 *lines/mm* and 2400 *lines/mm*. The radius of curvature of the gratings is 10.31 m. The details of the beamline have been described elsewhere [1], and are schematically shown in Fig.2.

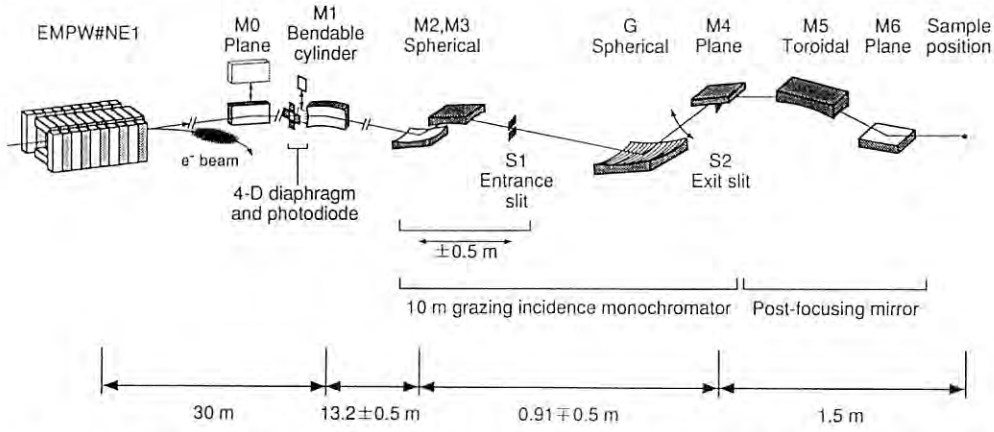

Fig.2 Schematic optical arrangement of the NE1B. It has two pre-mirrors: M0 (plane, water-cooled, SiC, platinum coated, θ_i=1.5°) and M1 (variably bendable cylindrical, ρ=485 mm, SiO_2, platinum coated, θ_i=1.5 °).

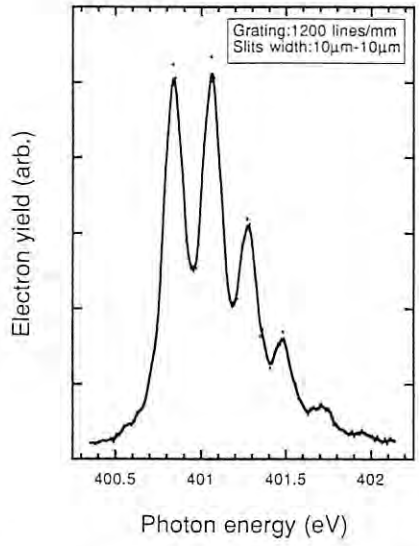

Fig.3 Absorption spectrum of the $N_{1s}\rightarrow 1\pi_g^*$ transitions of N_2 in the gas phase obtained with a vertical dispersion 10 m grazing-incidence monochromator of the NE1B.

In order to evaluate the spectral resolution of the monochromator, the well-known K-edge absorption spectrum of N_2 in the gas phase has been measured. The photon energy for the $N_{1s} \rightarrow 1\pi_g^*$ transitions is about 400 eV. Figure 3 shows the absorption spectrum measured with a grating having a groove density of 1200 *lines/mm* and 10μm-10μm slit openings. At least five vibration structures can be clearly observed. Compared with the results obtained at other facilities, the achieved energy resolution may be around 80 meV ($E/\Delta E$~5000), which is in good agreement with the value estimated by ray-tracing. Therefore, the result given in Fig.3 has almost achieved the designed resolution. From the photoelectron yield of the I_0 monitor, the photon flux under the above resolution was evaluated to be about 5×10^8 photons/s.

1) Photon Factory Activity Report **#9,** S-10(1991)

3. Development of a Soft X-ray Microscope Using Monochromatized Undulator Radiation - R & D on the Microscope with Future SR Sources

There are two major approaches in x-ray microscopy: one is imaging; and the other is scanning microscope.[1] The former directly produces a magnified image of a specimen by using an x-ray lens. Its spatial resolution is determined by the numerical aperture of the objective. The latter produces a small x-ray spot as a probe by using an x-ray lens and mechanically scanning the specimen two-dimensionally through the probe. Its spatial resolution is determined by only the spot size. The major merit of the former is direct magnification, which makes real-time

observations of "moving" specimens possible, while that of the latter is the minimized radiation dose.

An imaging soft x-ray microscope has been under development in the NE1B, presently aiming at real-time observations as well as microscopic applications of circular polarization in the future. A zone plate is used as the objective, because it has the highest spatial resolution in the soft x-ray region at present. The zone plate used is fabricated as part of collaboration between LBL and IBM.

In zone plate microscopes, monochromatic illumination is required because of the strong chromatic aberration of the zone plate. The Göttingen group employs a linear monochromator which consists of a large condenser zone plate (CZP) and a pinhole.[2] Since its spectral resolution($\Delta E/E$) is given by $2d/D$, where D and d are the diameter of CZP and a pinhole,[2] respectively, a large field of illumination on CZP is needed for high spectral resolution. Therefore, the linear monochromator matches synchrotron radiation possessing a relatively large angular divergence, such as that from the bending magnets, while the linear monochromator does not necessarily match synchrotron radiation possessing small angular divergence such as that from undulators in the low emittance ring. High power density of the undulators impinging onto CZP is also a severe problem. These suggest that another means for monochromatization must be introduced in the zone plate microscope using undulator radiation in the low-emittance ring.

Based on the above consideration, we have constructed a new microscope at the NE1B equipped with a grazing-incidence grating monochromator. Test patterns and some dry specimens have been successfully observed using this new microscope, of which picture is shown in Fig.4. The details concerning the results are reported in users' reports of this book by J. Wang *et al.* (PAC No.93G126).

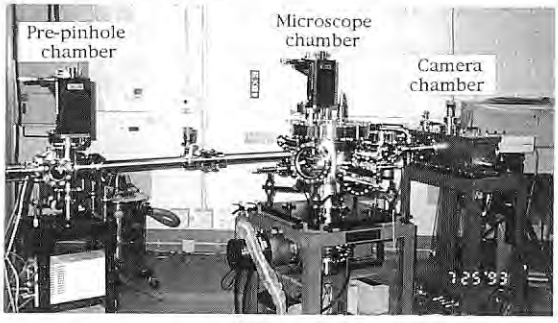

Fig.4 Photograph of the soft x-ray microscope apparatus constructed in at NE1B.

1) J. Kirz and H. Rarback, Rev. Sci. Instrum. **56**(1985)1.
2) B. Niemann, D. Rudolph and G. Schmahl, Nucl. Instrum. Meth. **208**(1983)367.

4. Energy Scan Test of the BL-NE3 Monochromator Using an X-ray Tube

In 1993, a new monochromator (Fig.5) was built at undulator beamline NE3. The linkage of two separate silicon crystals in the monochromator was constrained by the computer control software. The accuracy of the mechanical assembly was reported in the last Photon Factory activity report; the results of a quick energy scan are reported here.

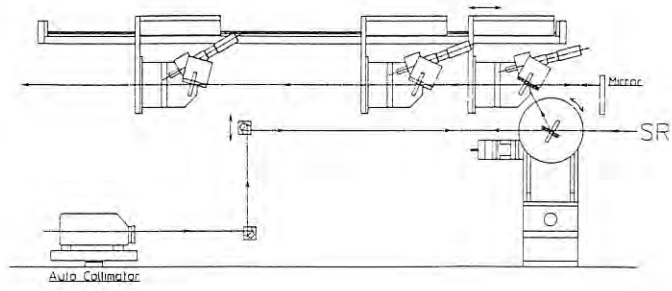

Fig.5 Scheme of the double-crystal monochromator. The first crystal chamber have a liquid nitrogen cooling system.

The rotation of the second crystal was designed to be driven by a linear actuator and a piezo-electric drive (Fig.6). The second crystal will be kept parallel to the first crystal within 2 arc seconds continuously, even during energy scan. The scan test using an x-ray tube of a molybdenum target is shown in Fig.7. The scan speed of the Bragg angle was 2 degrees per minute. The characteristic x-rays of Mo $K\alpha_1$, $K\alpha_2$, $K\beta_{1,3}$ and $K\beta_2$ are clearly seen on a chart paper.

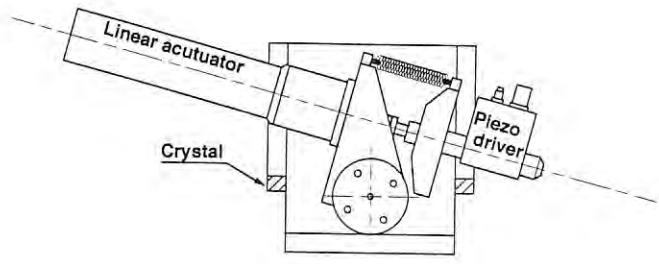

Fig.6 Detail of the second-crystal driving system.

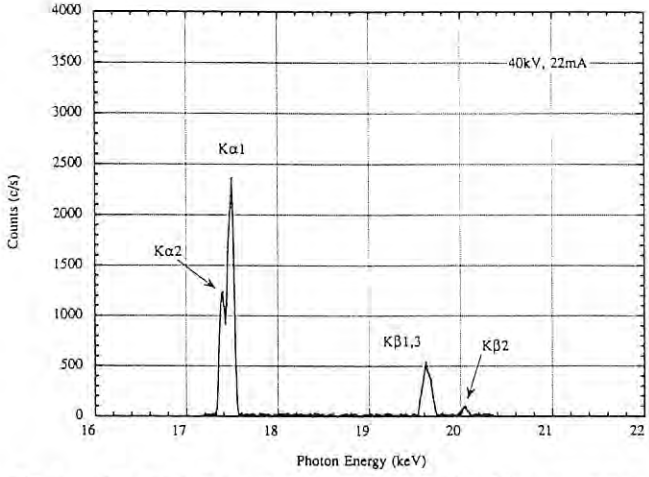

Fig.7 Result of a quick energy scan of the Mo x-ray tube with a Si(111) monochromator.

There happened a discharge trouble with the autocollimator built in a monochromator vessel filled with atmospheric-pressure of helium. The He-Ne laser tube in the autocollimator that monitors the laser beams available from two parallel silicon crystals requires a high-voltage power supply for population inversion pumping. In the He filled vessel, the breakdown voltage is much lower than in the air; thus the laser system can not emit lights. The autocollimator will be moved from inside the vessel to outside next year.

5. New Building for Experimental Preparation at the AR

The design of preparation rooms for experiments is in progress. A budget for rooms having a size of approximately 260m^2 has been approved. This space is naturally needed to encourage science at the AR area, because it is somewhat distant from the Photon Factory area. Nevertheless, it has taken almost six years for the approval. Since the AR lattice has four-fold symmetry, and only one arc corresponding to North East is used for SR utilization, one could consider an extension of other buildings; this will be associated with the main discussion on how to use this facility when it becomes a dedicated one.

Along with extensions of the beamlines and experimental stations, two container houses were build in December, 1991, just outside the experimental hall, to make up for a shortage of office space for both staff and users. In spite of this extension of space, since the activities as well as members concerned have been increasing rapidly, our demand for more space has been growing stronger year by year. To meet this demand, the Plant Engineering Department decided in Summer, 1993 to build a new building having an area of 260 m^2 near to the experimental hall (Fig.8).

Construction of the new building will be completed by the end of March, 1994. It is mainly for setting up the instruments and preparing samples as well as for R & D on SR science in the development at the AR. Figure 9 shows full views: south, north, east and west side views. It is a 30 m-long, 9.2 m-wide and 4.5 m-high construction with porch facing the south. Figure 10 shows its plan. It has eight rooms: from the west, room #1, a vacuum apparatus room; room #2, a crystal-cutting room; room #3, a rotating anode x-ray generator and an optical equipment room; room #4, a laser optics room; room #5, a data-analysis room; room #6, a sample-preparation room; room #7, a darkroom and; room #8, a stockroom.

Room #3, which will be used for off-line experiments on x-ray optics, is equipped with a hydro-thermostatic system, because the d-spacing of crystals is very sensitive to variation in the temperature and humidity. The any controllable fluctuation of the temperature is designed to be within $28\pm1^\circ$ C in the summer and $23\pm1^\circ$ C in the winter; -that of the humidity is within $50\pm5\%$. A rotating anode x-ray generator (type RU-300HFS of Rigaku Ltd.) will be installed there. In room #2, a slicing machine for crystal cutting (type ASM-3G of Okamoto Machine Tool Works Ltd.) will be installed, which will enable reseachers to make monochromators with individual specifications. Room #4 can be a large darkroom using blackout curtains. We have a plan to introduce a laser plasma x-ray source to this room, so that off-line soft x-ray experiments can be performed. In Room #5, a rack for the computer network system will be placed. Room #6 will be used for the sample preparation of angiography, x-ray microscopy and other experiments. There is a sink at the end of a corridor for the convenience of taking "coffee breaks" during experiments. There are two large doors: one, at the west side, is for carrying in/out apparatus from/to the experimental hall; and another, between rooms #1 and #3, is for separating room #3 hygro-thermally from room #1, as well as for carrying in/out equipment. Rooms #1, #2 and #3 are equipped with an H-beam hanging from the ceiling for a chainblock, so that heavy instruments can easily be manageable.

The new building will result in much convenience during experiments. Nevertheless, the

space available for this March will not necessarily be sufficient; thus in the near future a similar space will be needed.

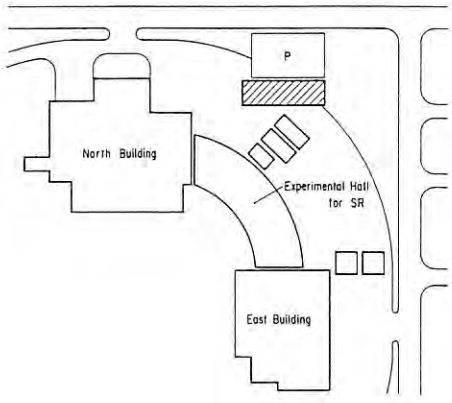

Fig.8 Site of the AR where the new building is to be built.

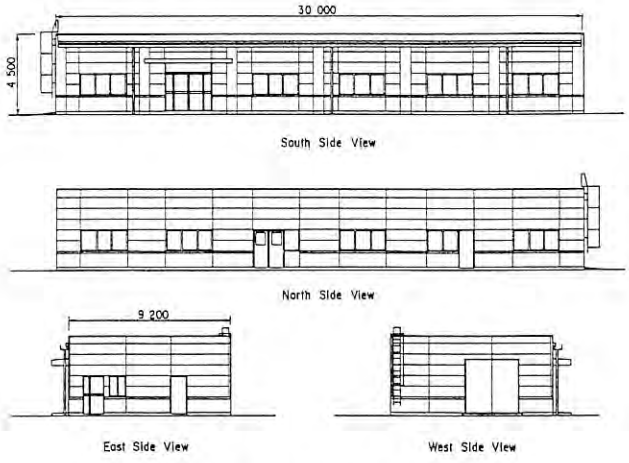

Fig.9 Full views of the new building.

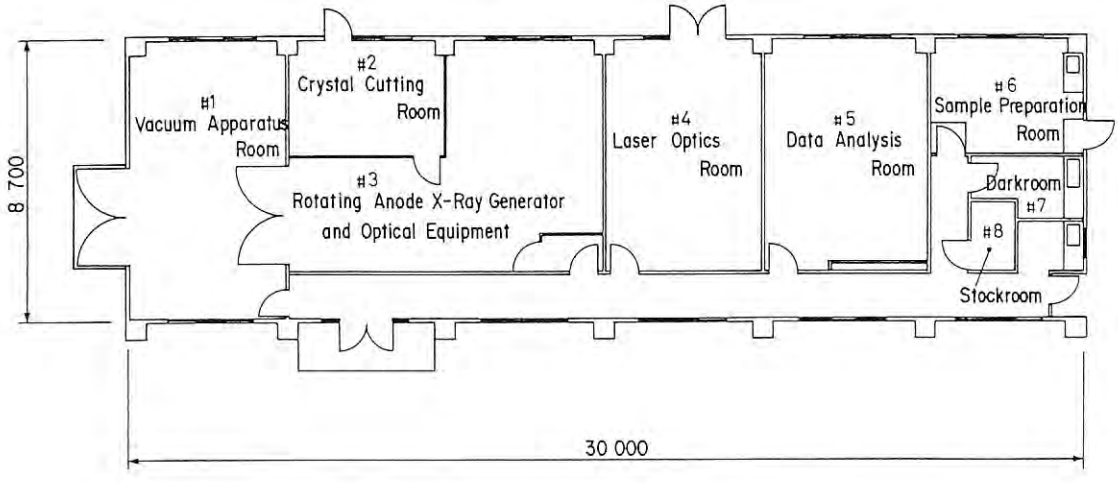

Fig.10 Plan showing the room arrangement.

D.NEW RESULTS OF EXPERIMENTS AND DESIGN STUDY

1. Magnetic Birefringence of Time-Dependent Nuclear Forward Scattering from an α-^{57}Fe Foil Using Synchrotron Radiation

Mössbauer spectroscopy, Mössbauer optics and its applications using SR have been vigorously studied at BL-NE3 in the AR for three years [1]. Important results concerning these experiments include the measurement of time spectra that are profiles of nuclear forward scattering (NFS) in a time domain. Here, we describe the magnetic birefringence of time-dependent NFS from an α-^{57}Fe foil.

Figure 11 shows the x-ray optics for measuring the time spectrum at BL-NE3.

We used third-harmonic radiation from undulator #NE3. It was adjusted on the resonant energy of 14.4 keV for ^{57}Fe. This radiation was completely polarized linearly in the horizontal plane. At this time, the AR was operated at 6.5 GeV with a current of 20 ~ 30 mA. Two Si 10 6 4 asymmetric channel-cut monochromators were employed to reduce non-resonant photons by narrowing down the diffracted energy width to about 5 meV.

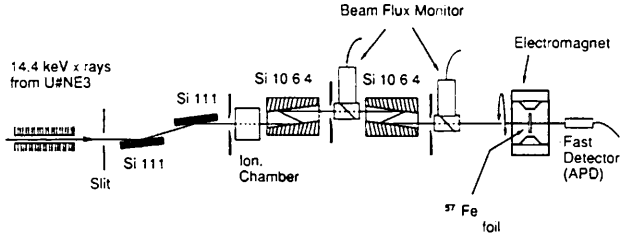

Fig.11 The experimental arrangement at the Voigt arrangement. At the Faraday arrangement, we used the same arrangement except a magnet.

The reduction of non-resonant photons improved the ratio of noise to signal, and protected the detector against saturating. The incident intensity to the first channel-cut monochromator was monitored by an ionization chamber. The diffracted intensity of each channel-cut monochromator was observed by a beam flux monitor, which detects scattering from Kapton foil by means of a NaI scintillation detector. Each channel-cut monochromator is finally adjusted by using of nuclear Bragg scattering of enriched α-$^{57}Fe_2O_3$ 7 7 7.

A well-monochromated beam was focused perpendicularly into the face of an enriched α-^{57}Fe foil as a sample. A magnetic field was applied to the foil perpendicular and parallel to the incident beam. These perpendicular and parallel arrangements correspond to the Voigt arrangement and the Faraday arrangement, respectively. We applied a magnetic field of about 0.05 ~ 0.5 T using an electromagnet in the Voigt arrangement and about 1 ~ 7 T by a superconducting magnet in the Faraday arrangement. In the Voigt arrangement, the direction of magnetic field is rotated on the beam.

An avalanche photo diode (APD) was used as a fast detector. The signals from APD were processed by a time-to-analog converter (TAC), an analog-to -digital converter (ADC) and a multichannel analyzer (MCA). We used the injection timing signal at the AR as a stop signal for the TAC. The received signals comprise two components: a prompt and a slow component. The slow signals mean NFS and the prompt signals as well as others. At this time, the rate of the slow component was 30 ~ 40 cps in the Voigt arrangement, and 10 ~ 20 cps in the Faraday arrangement. The total intensity into the APD detector is suppressed to less than about 700 kcps to prevent the detector from saturating and discounting the slow component. Prompt signals from the detector were removed to avoid TAC and ADC from overflowing.

Figure 12 shows the time spectra in the Voigt arrangement with an external magnetic field of 0.5 T.

The closed circles indicate the experimental data; 10^{-1} counts on the longitudinal logarithm axis means 0 counts for experimental data. The angle between the magnetic field (h^S) of incident x-rays and the external magnetic field (u_Z) was varied by 0°, 45° and 90°. This angle is expressed in term of $h^S \wedge u_Z$. The beat pattern of these spectra changes with a change in the angle of $h^S \wedge u_Z$.

The six transitions of $\Delta m=0, \pm 1$ that are labeled A ~ F in Fig. 13, are allowed in α-^{57}Fe. Here, "m" is the magnetic quantum number.

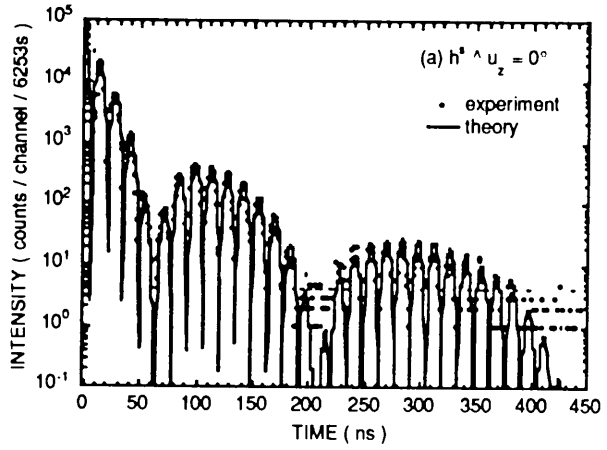

(a)

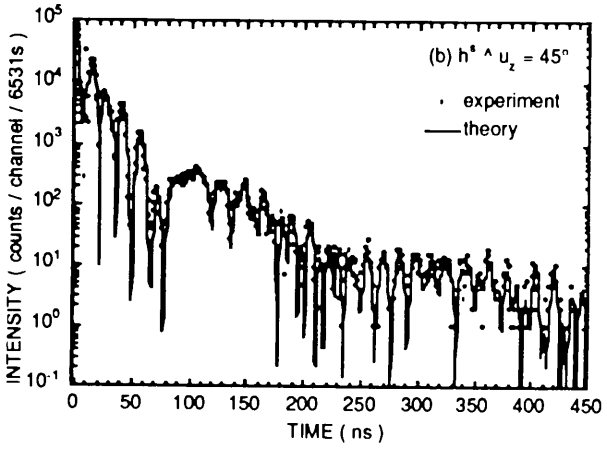

(b)

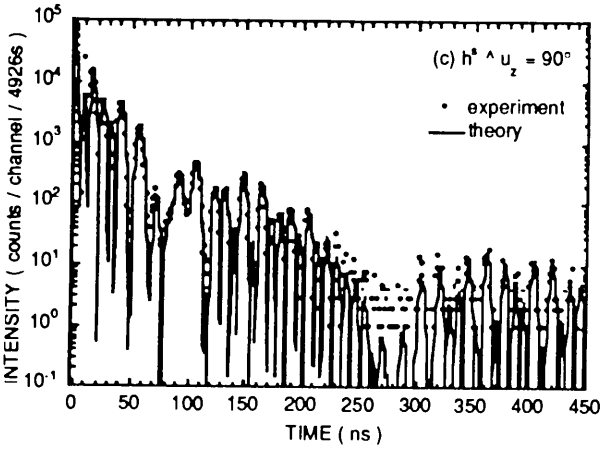

(c)

Fig.12 The time spectra at the Voigt arrangement. (a) $h^S \wedge u_Z = 0°$, (b) $h^S \wedge u_Z = 45°$, (c) $h^S \wedge u_Z = 90°$. Strength of external magnetic field was 0.50 T. The closed circles show experimental data and the solid lines show theoretical calculations. 10^{-1} counts on the longitudinal logarithm axis means 0 counts for experimental data.

When $h^S \wedge u_Z = 0°$, only two transitions of $\Delta m=0$ (labeled B and E in Fig. 13) contribute to the scattering. The simple beat pattern shown in Fig. 12(a) with a period of about 14.2 ns is caused by to the energy difference of two transitions. This beat pattern is called the quantum beat. The oscillating envelop of each peak of the quantum beat is caused by a resonant absorption thickness effect.

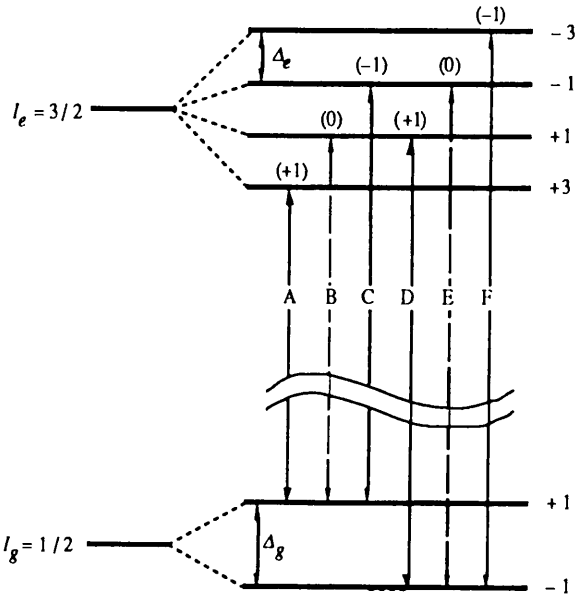

Fig.13 Schematic diagram of the ground and the first excited states of ^{57}Fe nuclear. (a) The degenerate condition. (b) The condition in which nuclear Zeeman splitting occur by internal magnetic field. Here, "m" is magnetic quantum number. The condition of ^{57}Fe nuclear in α-^{57}Fe is correspond to condition (b).

When $h^S \wedge u_Z = 90°$, only four transitions of $\Delta m=\pm 1$ that (labeled A, C, D and F in Fig. 13) contribute to the scattering. The quantum beat is more complex than the $h^S \wedge u_Z = 0°$ condition, as shown in Fig. 12(c). Oscillation of the envelope due to a thickness effect also occurred under this condition. Figure 12(b) shows the time spectra at $h^S \wedge u_Z = 45°$. In this case, all six transition components of both $\Delta m=0$ and $\Delta m=\pm 1$ contribute to the scattering.

Theoretical curves were fitted to these time spectra. The theoretical curves were calculated by a fast Fourier transformation of the nuclear resonant scattering cross-section as a function of energy. As a result, the fitted curves are indicated by the solid line in Fig. 12. The derived parameters for Fig. 12 (a) were as follows: internal magnetic field, –32.5 T [as a result, energy splitting of transition lines (ΔE) has been 2.91×10^{-7} eV]; Lamb-Mössbauer factor, 0.867;thickness of α-^{57}Fe foil, 1.43 mg ^{57}Fe / cm^2 [with correction of cross-section for a difference of

degeneracy of nuclear state]. The other parameters were general values using ordinary Mössbauer spectroscopy. The parameters for Fig. 12 (b), (c) were the same values as those for Fig. 12 (a).

Figure 14 shows the time spectra in the Faraday arrangement with an external magnetic field of 4.61 T (•) and 7.27 T (Δ). 10^{-1} counts on the longitudinal logarithm axis means 0 counts for the experimental data. The beat pattern of these spectra changes with a change in the strength of the magnetic field.

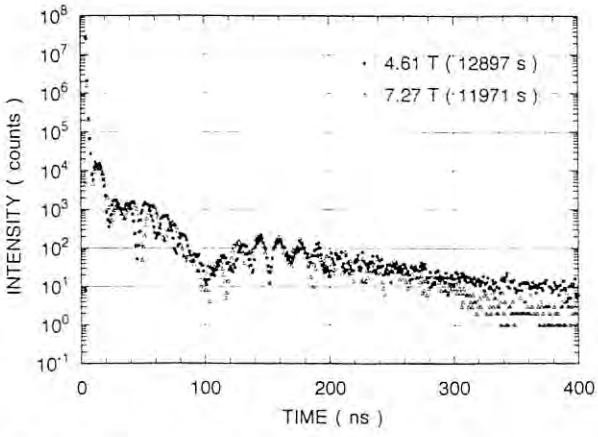

Fig.14 The time spectra at the Faraday arrangement. Strength of external magnetic field was 4.61 T (•) and 7.27 T (Δ). 10^{-1} counts on the longitudinal logarithm axis means 0 counts.

1) S. Kikuta et al. ICAME'91, Nanjing, to be published in the Hyperfine Interactions.

2. Intravenous Coronary Angiography Using Monochromatic x-rays

A two-dimensional imaging system for intravenous coronary angiography with a large-size monochromatic SR beam have been developed by using asymmetrical reflection from a silicon crystal and a two dimensional image acquisition system (an image-intensifier(II)-TV system).[1)]

An animal experiment was performed at above the iodine K-edge energy, 33.17keV+150eV. The monochromatic beam size available was 70mm by 70mm using a Si(311) crystal with α=5.0 degrees. The acceleration energy of the AR for the experiment was 5.8 GeV in order to reduce the contamination of the third higher harmonics photons from the silicon crystal. The stored current of the AR was about 35mA.

Five dogs, weighing from 12 to 15kg were anesthetized with sodium pentobarbital at a rate of 30mg/kg. A seven inch long Courand catheter was inserted into the femoral vein and contrast material(Urografin(76%)), an amount of 7ml, was injected into the right atrium by using an auto-injector at the speed of 10ml/s. X-ray images were obtained by a two-dimensional imaging system (II:TOSHIBA RTP9211G, TV:SONY XC-77) at the left or the right anterior oblique position. Those images were recorded on a video tape and digitized by an A/D converter(NEXUS 68000) on an off-line basis.

Two-dimensional, time-sequential and real-time images showing the flow of blood with contrast material in aorta, left ventricle and coronary arteries were obtained. Figure 15 shows one of those images. Left ventricle, left and right coronary arteries with its stenosis region are clearly distinguished. Possibility of this imaging system for clinical applications was successfully demonstrated.

Fig.15 Image of the dog's chest region. Left and right coronary arteries with its stenosis region are cleanly distinguished.

1) K. Hyodo, K. Nishimura, and M. Ando: Handbook on Synchrotron Radiation Vol. 4 55.(eds. S. Ebashi, M. Koch, and E. Rubenstein) Elsevier Science Publisher, Amsterdam (1991).

3. Conceptual Design Study on a Compact Electron Storage Ring System Dedicated to Coronary Angiography

The K-edge subtraction method is effective for coronary angiography by peripheral venous injection.[1)2)3)] We designed a compact storage ring system dedicated to coronary angiography using a two-dimensional imaging system. This design was undertaken through a collabration between PF, KEK and Kawasaki Heavy Industry Cop..

Requirements for SR

a. Photon flux

A high intensity of monochromatic x-rays at 33keV is required for the K-edge subtraction method using iodine as the contrast material. The photon flux density of x-rays at 33keV should be more than 10^{10}photons/mm^2/sec on the front surface of the patient's body with the following conditions: patient's body thickness (water equivalent) of 150mm, pixel size of a digital image of 0.3x0.3mm^2 and exposure time per one image of 2msec. If the 33keV photon flux density is 10^{10}photons/mm^2/sec in front of the patient's body, it decreases to 5.5×10^7 photons/mm^2/sec after passing through it. The photon flux to one pixel in a digital image, Ip is 10^4 photons/pixel/exp.time. thus, the signal-to-noise ratio (S/N) is Ip/ Ip = 100.

b. Exposure area

The x-ray exposure area should be larger than 150x150mm^2 in order to cover the entire images of coronary arteries using a two-dimensional imaging system. Therefore, the total photon flux in front of the patient's body should be more than 2.25×10^{14}photons/sec. Supposing a monochromator diffraction efficiency of 60%[5], the total photon flux in front of the monochromator should be more than 3.8×10^{14} photons/sec.

c. The third higher harmonics

On the other hand, the third higher harmonics (99keV) diffracted by a Si crystal monochromator also enters the imaging system.[3] Therefore, the photon flux density due to that should be less than 3% of the photon density at 33keV in order to avoid any deterioration of the image contrast.

Radiation Source

Wiggler magnets are suitable for meeting these three requirements. The spectral photon flux from a wiggler magnet is given by the following equation: [4]

$$N(\varepsilon) = C_n E\theta I N_w \Delta\varepsilon/\varepsilon S(X), \qquad (1)$$

where $C_n=4\times10^{11}$GeV^{-1}mrad^{-1}mA^{-1}sec^{-1}(1%BW)$^{-1}$, E is the beam energy in GeV, θ the angle of the radiation one in mrad, I the beam current in mA, Nw the pole number of the wiggler magnet, and $\Delta\varepsilon/\varepsilon$ the spectral band width in % and S(X) a mathematical function defined by

$$S(X) = \frac{9\sqrt{3}}{8\pi} \cdot X \cdot \int_X^\infty K_{5/3}(z)dz, \qquad (2)$$

with $K_{5/3}$ being a modified Bessel Function. The radiation spectrum given by S(X) with $X=\varepsilon/\varepsilon_{crit}$ is characterized by the critical photon energy given by

$$\varepsilon_{crit} = C_C E^2 B, \qquad (3)$$

where $C_C = 6.64\times10^{-7}$GeV^{-1}Tesla^{-1}, and B is the field strength of the wiggler magnet in Tesla. In order to obtain a horizontal photon beam width of 150mm at a distance of 12.5m from the radiation source, the horizontal angle of the radiation cone should be greater than 12mrad. A spectral band width of 0.3% at 33keV is produced using a lapped silicon monochromator.[5] A wiggler magnet whose pole number is 3(1 Main, 2 Sub) is easy to make because it has the simplest form. The supposed beam current is 800mA; this seems to be feasible with a little development of the storage ring. In Figure 16 the available 33keV photon flux from a wiggler (as derived from Eq.(1)) is shown for a parameter of different electron beam energies, as a function of the maximum wiggler magnetic field. On the broken line, the rate of the third higher harmonics photon flux relative to 33keV flux is 3%. [4]

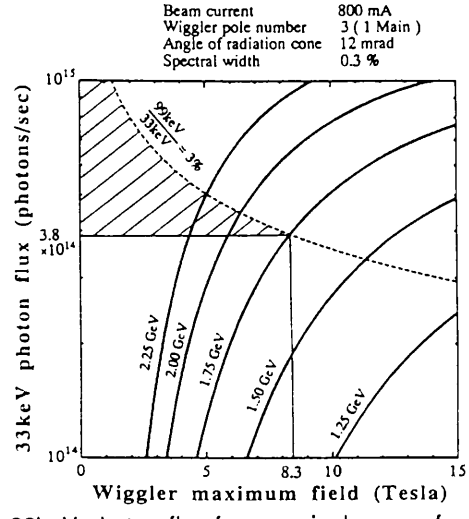

Fig.16 33keV photon flux from a wiggler as a function of the maximum field strength of the wiggler(the shaded portion is the acceptable area).

In the upper region of the broken line, the ratio of the third higher harmonics is more than 3%. Since the photon flux of the third higher harmonics must be less than 3%, when compared to that at 33keV, and a 33keV flux of 3.8×10^{14}photons/sec is desired, the acceptable area is in the shaded portion

of Fig.16. Thus, as the best choice, of a beam energy of 1.75GeV and a maximum wiggler magnetic field of 8.3Tesla have been adopted, because the lower is the electron beam energy, the shorter is the diameter of an electron storage ring.

Storage Ring

The lattice of our storage ring is the Chasman-Green type in order to avoid an excess increase in the emittance; it was chosen due to it's ability to control the dispersion function at the insertion point of the wigglers.

The machine design parameters are shown in Table 6. Low-energy injection is adopted so that the injector (linac) can be compact. At the time of injection, the wigglers are excited proportional to the magnetic field strength of the bending magnets, because there is a great difference in the betatron tunes between when wigglers are excited and when they are not excited.

Table 6. Machine design parameters.

Beam energy , E	
Operating	1.75GeV
Injection	250MeV
Beam current ,I	800mA
Lattice structure	Chasman - Green
Number of superperiods	2
Harmonic number , h	101
Circumference	60.6 m
RF system parameters	
Frequency	500 MHz
Voltage , V	1.5 MV
Momentum compaction factor	0.040567
Betatron tunes	
Horizontal	3.24
Vertical	2.32
Natural emittance	
at 1.75 GeV	4.5 x 10-7 m . rad
at 250 MeV	9.2 x 10-9 m . rad
SR energy loss per turn at 1.75 GeV	339.4 KeV
Wiggler parameters	
Peak field	8.3 Tesla
Pole number	3 (1 Main , 2 Sub)
SR critical energy	
Bending magnet	3.0 KeV
Wiggler	17.0 KeV

The lattice functions through one superperiod are shown in Fig.17. The design code MAGIC[6] has been used to calculate the machine parameters and lattice functions; the design code ZAP[7] has also been used to study the intrabeam scattering in order to estimate the emittance at the time of low-energy injection. Figure 18 shows the lattice of the compact ring.

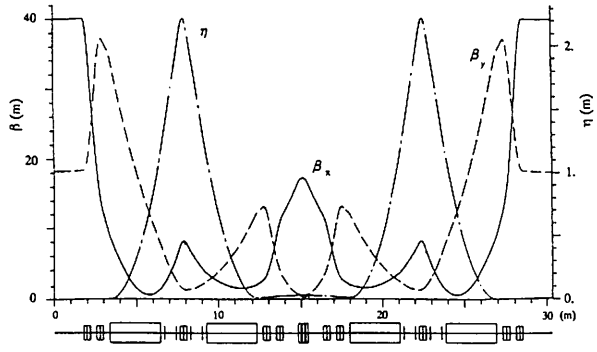

Fig.17 Lattice functions through one superperiod.

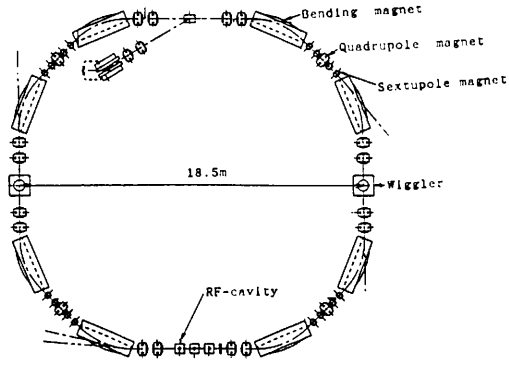

Fig.18 Lattice of the compact ring.

Layout Plan of a Facility

A layout plan of an SR facility dedicated to coronary angiography using the storage ring described above is shown in Fig.19.

A linac is placed on the underground level, in order to accommodate three other experiment rooms. SR angiography rooms, x-ray control rooms, medical treatment rooms etc. are 50cm higher than the ground floor level, because the diffracted x-rays by a Si(311) single crystal monochromator go upward at an angle of about 13 degree. Radiation shields and pillars in the underground level are placed at the same location relative to those on the ground level in order to support the structure on the ground.

The system is feasible, needing little development to store a high electron beam current of more than 800mA and to give a high magnetic field of more than 8Tesla. A photon flux density of 10^{10}-10^{11}photons/mm^2/sec on the front surface of the patient's body after expansion of the photon beam to 150x150mm^2 is possible. An electron beam energy of 1.5-2.0GeV and a magnetic field of the wiggler magnet of 5-10Tesla are suitable for coronary angiography, because of the limitation of the third higher harmonics. Therefore, if a much higher photon flux density is desired, the

development of storage of a high beam current of more than 1A or a multipole wiggler whose pole number is more than 15 is needed.

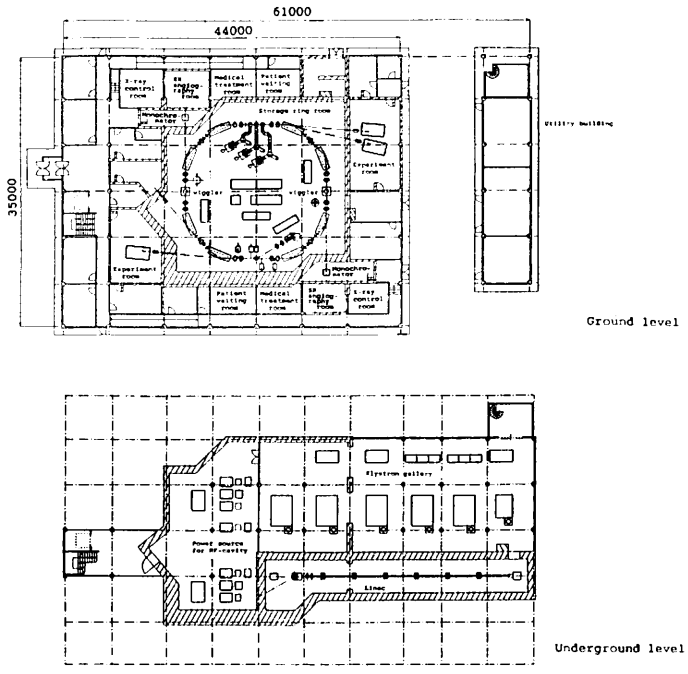

Fig.19 Layout plan of an SR facility dedicated to coronary angiography.

1) K. Hyodo, K. Nishimura, and M. Ando: Handbook on Synchrotron Radiation Vol. **4** 55 (eds. S. Ebashi, M. Koch, and E. Rubenstein) Elsevier Science Publisher, Amsterdam (1991).
2) E. Rubenstein, R. Hofstadter, H. D. Zeman, A. C. Thompson, J. N. Otis, G. S. Brown, J. C. Giacomini, H. J. Gordon, R. S. Kernoff, D. C. Harrison, and W. Thomlinson: Proc. Natl. Acad. Sci. USA **83** (1986)9724.
3) A. Akisada, M. Ando, K. Hyodo, S. Hasegawa, K. Konishi, K. Nishimura, A. Maruhashi, F.Toyofuku, A. Suwa, and K. Kohra: Nucl. Instr. and Meth. **A246**(1986)713.
4) H. Wiedemann: Italian Physical Society Conference Proceedings, Vol. **10**(1988)299.
5) H. Shiwaku, K. Hyodo, and M. Ando: Japanese Journal of Applied Physics, **30**,(1991)L2065.
6) A. S. King, M. J. Lee, and W. W. Lee: SLAC Report No. **183** (Aug. 1975).
7) M. S. Zisman, S. Chattopadhyay, and J. J. Bisognano: ZAP User's Manual LBL (1986)21270.

E. FUTURE PLAN AT THE TRISTAN AR

1. AR as a Light Source

The KEK B-factory is a high-luminosity electron-positron collider to be constructed in the

TRISTAN MR tunnel after the shut-down of the present TRISTAN MR operation. According to the plan, electron and positron beams will be supplied to the KEK B-factory directoly from the upgraded linac. Therefore, the accumulation ring (AR), which currently works as a MR injector as well as a light -source machine, could be converted to a dedicated synchrotron light source after completion of the linac upgrade.

To investigate the possibility of an AR conversion into a dedicated synchrotron-light source, a subpanel on machine modifications was organized upon the recommendation by the AR committee in July, 1993.

Circumstances concerning the AR Conversion

The following are thought to be the boundary conditions for the AR conversion into a dedicated synchrotron light source.

The AR conversion will become possible only after completing the KEK B-factory construction, which is currently foreseen to be in 1998.

A new light-source machine must fit the existing AR tunnel in order to avoid an excessive increase in civil-engineering costs

It is desirable for the AR conversion to take full advantage of spin-off from the machine development for the B-factory. From the view point of improved beam characteristics, of much interested are some machine components of the B-factory now under development: an rf cavity without harmful impedance, a vacuum chamber useful under a heavy radiation load and a beam-position monitor of high precision with a high repetition rate.

Relationship among Machine Parameters

In planning for the AR conversion, many issues must be taken into consideration. Figure 20 schematically shows the mutual relationship among many machine items related to the AR conversion. In an ideal design, all of these items must be well optimized to satisfy scientific requirements to the AR converted into a dedicated synchrotron light source.

For instance, the relationship between the beam emittance and the beam energy is given in Fig. 21. From the view point of beam emittance, the AR can be converted into an ordinary machine as an x-ray source and prominent one as a VUV/soft x-ray source, if design work considers the respective beam energy.

Brief Summary

The procedure for considering about the AR conversion as a dedicated synchrotron light source is just beginning. Now, active interplay is greatly expected between planning of machine conversion and surveying future prospect for scientific research at the AR.

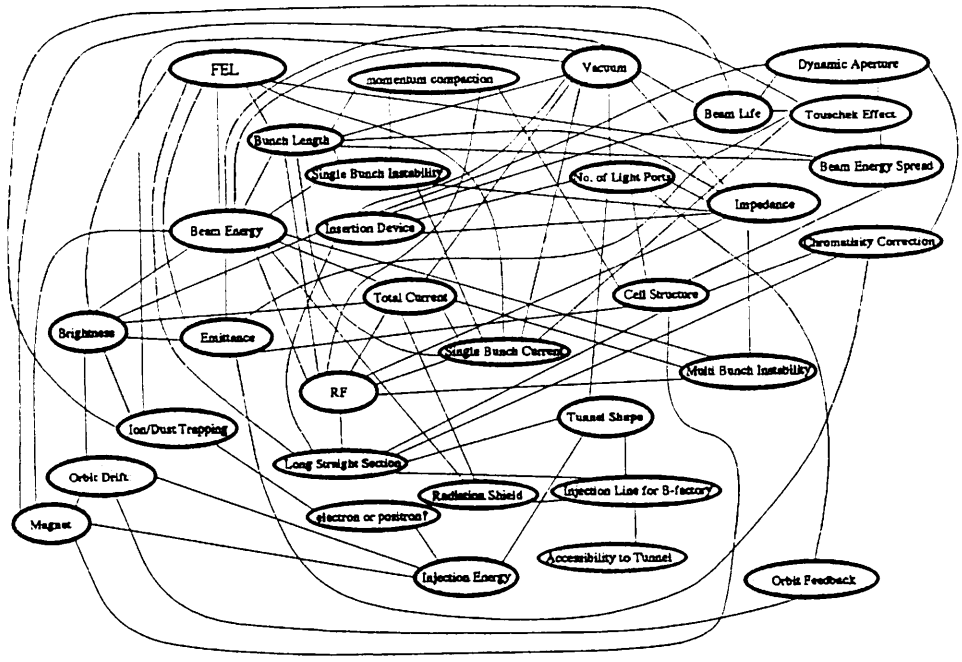

Fig. 20 Graph showing the mutual relationship among the machine items for a dedicated synchrotron light source based in the AR tunnel.

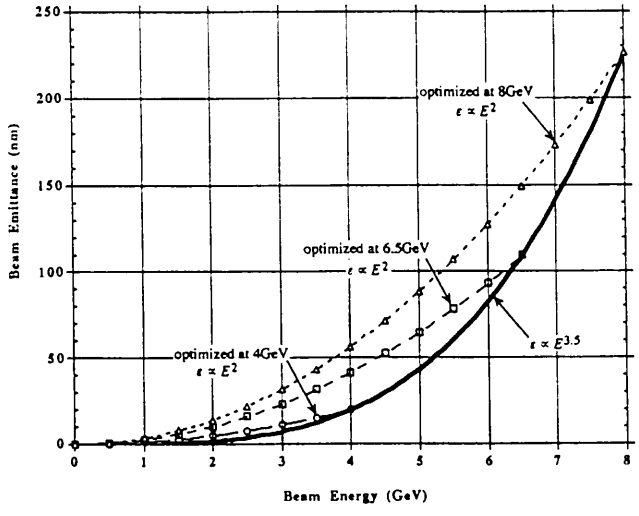

Fig. 21 Relationship between the attainable minimum beam emittance and the beam energy, where design is optimized.

2. Experiments using SR from the AR

A subpanel assessing of the utilization of SR was also held in Sep. 7, 1993. In the meeting, not only in-house staffs of the Photon Factory, but several users from other institutions, also participated and earnestly discussed this problem.

After these discussions, the following seven themes were proposed.

1. Coincident measurements of Compton scattering with recoiled electrons
2. Site-selective photon-chemical reactions at the surfaces of molecular crystals excited by soft x-rays
3. K-edge subtraction for coronary angiography
4. X-ray studies of materials under high pressures and temperatures
5. Circular dichroism in the soft x-ray region
6. Generation of extremely monochromatic X-rays
7. Soft x-ray lasers and nonlinear x-ray optics

F. SPECIFICATIONS OF THE TRISTAN ACCUMULATION RING

This section summarizes principal parameters of a bend source and insertion devices and their calculated spectral performance.

Table 7. Calculated spectral performance of the bend source and insertion devices at the TRISTAN Accumulation Ring. E/I: beam energy and current, λ_u: period length, N: number of periods, L: length of undulator or wiggler, G_y (G_x): minimum vertical (horizontal) gap, B_y (B_x): maximum vertical (horizontal) magnetic field, P: pure configuration, H: hybrid configuration, $\sigma_{x,y}$: horizontal and vertical beam size, $\sigma_{x',y'}$: horizontal and vertical beam divergence, K_y (K_x): horizontal (vertical) deflection parameter, $\varepsilon_1/\varepsilon_c$: photon energy of the first harmonic (critical energy in the case of bend source or wiggler), $\Delta\varepsilon/\varepsilon$: relative bandwidth, Pc: degree of circular polarization, D: photon flux in a unit solid angle (photons /s · mrad^2 · 0.1%b.w.), B: brilliance (photons/s · mm^2 · mrad^2 · 0.1%b.w.), P_T: total radiated power, dP/d Ω: power in a unit solid angle. Different operation modes of a helical undulator and a wiggler are denoted by -H and -W, respectively.

Name	Bend-NE5,NE9	EMPW#NE1 -W	-H	U#NE3	
E/I GeV/mA	6.5/50	6.5/50		6.5/50	
λ_u cm		16.0		4.0	
N		21		90	
L m		3.4		3.6	
G_y (G_x)		3 (11)		1.0	
B_y (B_x)		1 (0.2)		0.83	
Type of magnet		P (NdFeB)		P (NdFeB)	
σ_x mm	0.8	1.14		1.24	
σ_y mm	0.15	0.079		0.121	
$\sigma_{x'}$ mrad	0.45	0.14		1.24	
$\sigma_{y'}$ mrad	0.023	0.021		0.018	
K_y (K_x)		15 (1)	1 (1)	1.5	3.1
$\varepsilon_1/\varepsilon_c$ keV	26.3	28 (Pc=83%)	1.2 (Pc=97%)	4.68	
$\Delta\varepsilon/\varepsilon$			0.12	0.064	
D	3.5×10^{13}	5.3×10^{14}	5.4×10^{15}	1.4×10^{16}	
B	4.7×10^{13}	8.8×10^{14}	9.5×10^{15}	1.5×10^{16}	
P_T kW		4.5	0.04	0.78	3.3
dP/d Ω kW/mrad^2	0.38	5.6	0.49	8.95	35

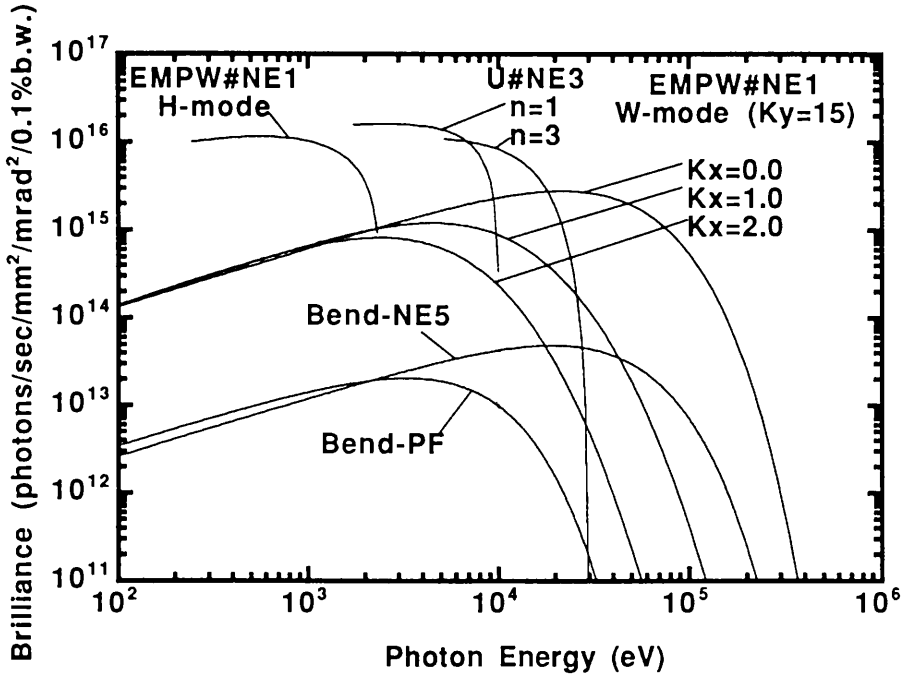

Fig. 22 Synchrotron radiation spectra.
Brilliance of radiation vs. photon energy for the insertion devices (EMPW#NE1 and U#NE3) and the bending magnet (Bend-NE5,NE9) of the AR. The name of each source is assigned in Table 7. EMPW#NE1 has both a helical undulator and a wiggler modes, which are denoted by H or W, respectively. The spectral curve of each undulator (or a helical undulator mode of EMPW) is a locus of the peak of the harmonics within the allowable range of K-parameter.

G. SPECIFICATIONS OF EXPERIMENTAL STATIONS

This section summarizes the experimental stations (Table 8) and the beamline optics (Table 9). Figure 23 shows a plan view of the experimental hall of the Accumulation Ring (AR).

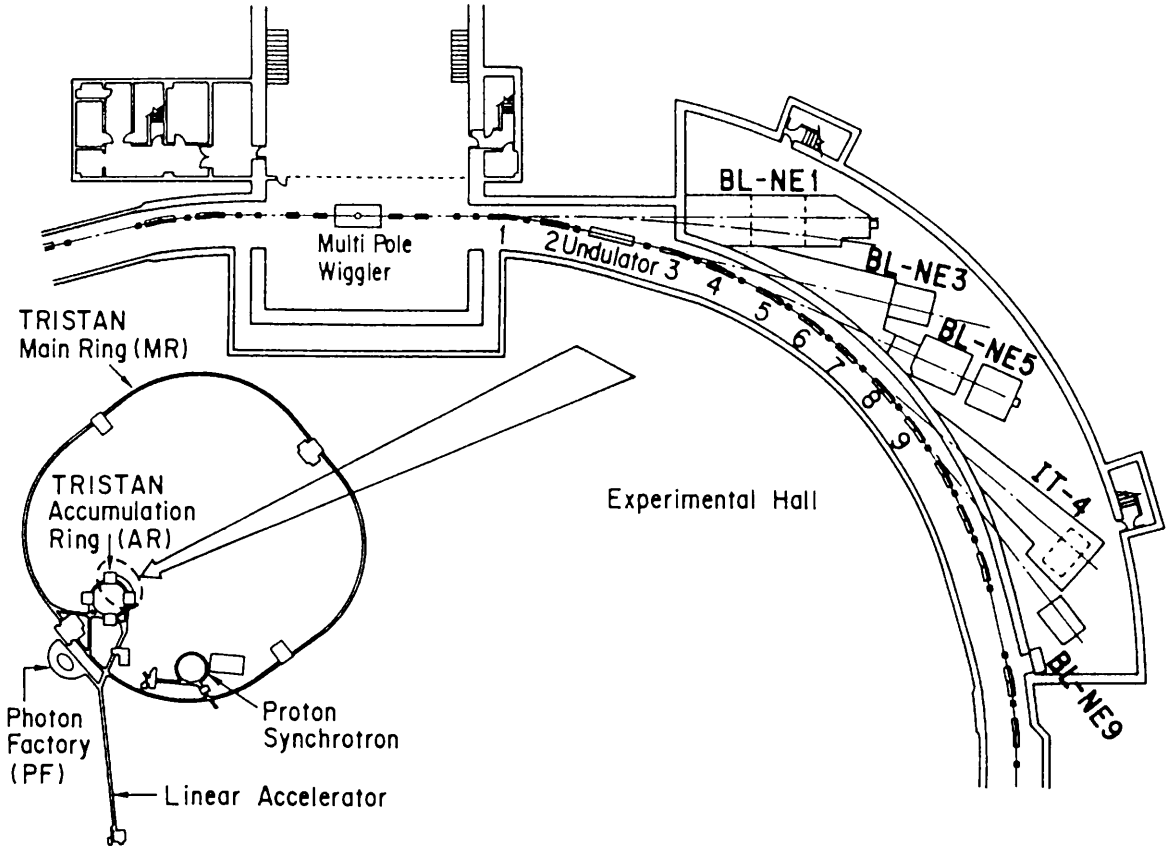

Fig.23 Plan view of the experimental hall of the TRISTAN Accumulation Ring (AR)

Table 8 List of Experimental Stations

Experimental station		Source	Typical Experiments
BL-NE1		EMPW#NE1	
	A1		High resolution Compton and magnetic Compton scattering
	A2		Spectroscopy and scattering with circularly polarized x-rays
	B		Spectroscopy and microscopy with circularly polarized soft x-rays
BL-NE3		Undulator#NE3	
	A1		Nuclear resonant scattering
	A2		Surface and interface diffraction
BL-NE5		Bending-NE4	
	A		Angiography and x-ray computed tomography
	C		High pressure and high temperature x-ray diffraction
BL-NE9		Bending-NE8	
	A		In design
	B		Vacuum science and technology

Table 9. List of Beamline Optics.

Experimental Station	Horizontal Angular Acceptance (mrad)	Typical Beam Size (hor.×ver.) (mm^2)	Photon Flux at Sample Position (mm^2/s/mA)	Monochromator System	Energy Resolution ($\Delta E/E$)	Energy Range (keV)
NE1-A1	2	8×3	1×10^{10} (60.0keV)	Double Bent Crystal Si(111)	1.5×10^{-3}	40~70
NE1-A2	2	80×4		Double Crystal Si(111)	2×10^{-4}	6~28
		3×4		Sagital Focusing Si(111)		
		3×0.5		Sagital Focusing + Bent Mirror		
NE1-B	~0.2 [0.02(ver.)]	~0.8×0.2	Slits:10μm-10μm ~3×10^{9} (400eV)	10m Grazing Incedence Grating	~2.5×10^{-4}	0.25~1.8
			Slits:50μm-50μm ~1×10^{11}(400eV)	(1200 or 2400*lines*/mm) β=89°	~2×10^{-3}	
NE-3A1	0.3	15×2	1×10^{3}	Double Crystal	1×10^{-4}	5~25
A2	[0.03(ver.)]		(14.4keV)	Si(111) with fine monochromator of Si	5×10^{-7}	
				with Single Crystal $^{57}Fe_2O_3$(777)	1×10^{-11}	
NE5-A	10	150×8	5×10^{8} (33.2keV)	Asymmetrically Cut Single Crystal Si(311) (α=4°~6°)	6×10^{-3}	20~40
NE5-C	3	60×5		Double Crystal Si(111)	1×10^{-4}	30~100
NE9-A	5			not fixed		
NE9-B	10	10×3		white beam	none	none

H. LIST OF STAFFS AND STUDENTS INVOLVED AT THE AR

Table 10. List of staffs and students involved at the AR between October 1992 and September 1993.

in-house staff

TRISTAN accelerator group

Fukuma, Hitoshi	machine operation and responsible for orbit development
Kuroda, Shigeru	machine operation and responsible for orbit development
Takeda, Shigeru	machine operation and facility concerns
Yosioka, Masakazu	responsible for machine operation schedule

Insertion device EMPW#NE1, UNDULATOR#NE3

Kitamura, Hideo
Shioya, Tatsuro
Yamamoto, Shigeru

Beamline interlock

Ito, Kenji
Kosuge, Takashi
Saitoh, Yuuki

Experimental station

Ando, Masami	NE9A
Hyodo, Kazuyuki	NE5A
Iwazumi, Toshiaki	NE1A2
Kagoshima, Yasushi	NE1B
Kanazawa, Kenichi	NE9B
Kawata,Hiroshi	NE1A1
Kikegawa, Takumi	NE5C
Miyahara, Tsuneaki	NE1B
Sugiyama, Hiroshi	NE3A2
Zhang, Xaowei	NE3A1

visiting staff from universities

Kikuta, Seishi	University of Tokyo	Mossbauer experiments
Namikawa, Kazumichi	Tokyo Gakugei University	Parametric scattering

visiting staff from industries

Yamaguchi, Masayuki	Toyama	Development of a high heat load monochromator
Oku, Yasunari	Kawasaki Heavy Industries	Design study on a compact ring for angiography

PhD student GUAS

Chen, Juhua	Structure analysis of Bi under high pressure at BL-NE5C
Mochizuki, Tetsuro	Development of optical components and a novel monochromator for a highly brilliant undulator at BL-NE3A1
Ota, Nobuhiko	Study of outgasing from aluminum surface layer induced by synchrotron radiation at BL-NE9B
Park, Serng-Yerl	Study of magnetic circular dichroism at BL-NE1B
Wang, Jidong	Development of soft x-ray zone-plate microscope utilizing polarized SR at BL-NE1B
Zhao, Jiyong	Development of Mossbauer photon production, its x-ray optics and Its application at BL-NE3A1

PhD students entrusted off home

Shoda, Mitsuhiro (Tokyo Science University)	Evaluation of a Ta grazing incidence antireflection mirror for Mossbauer photon production at BL-NE3A1

The Tristan Super Light Facility

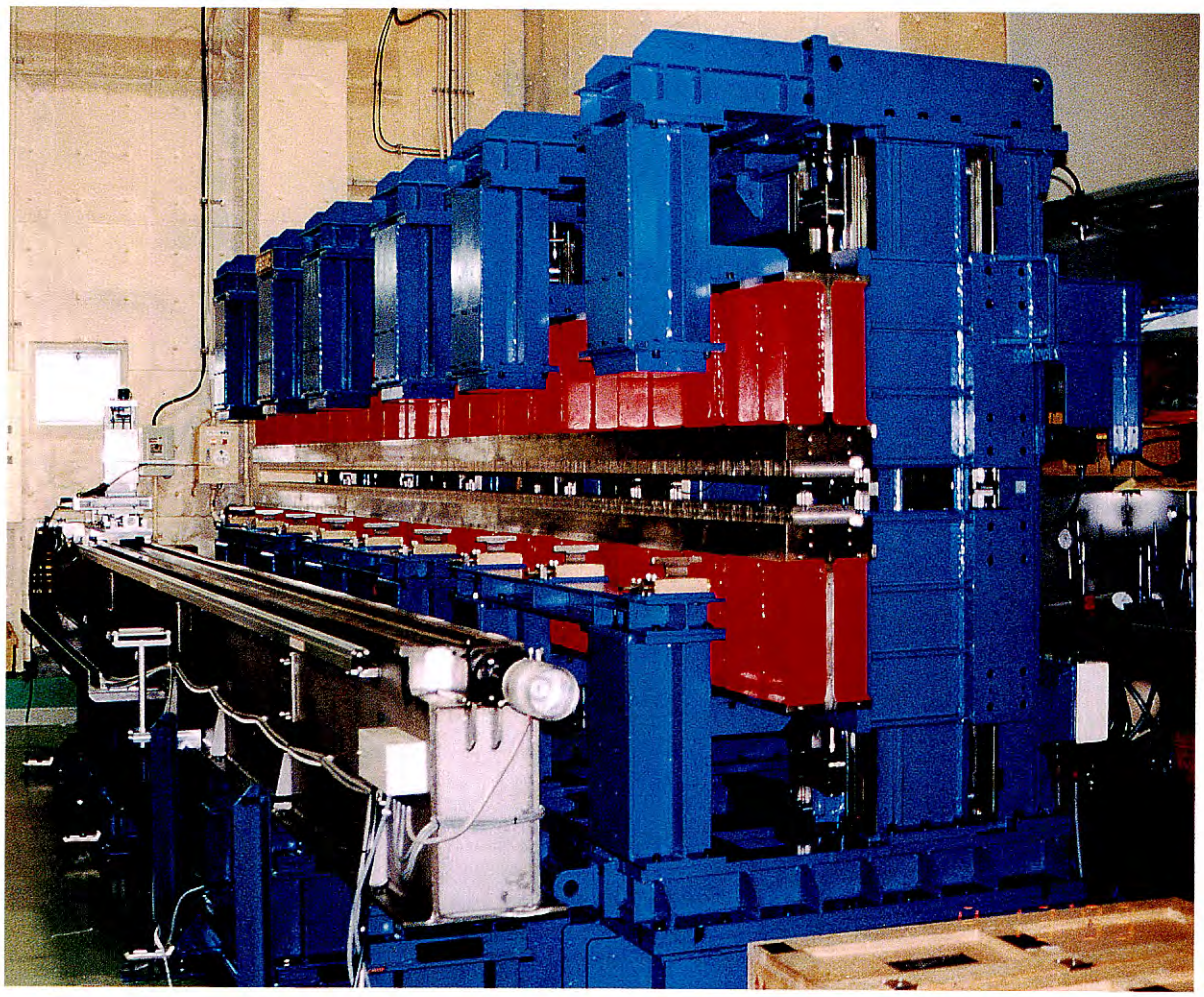

A super-brilliant-x-ray undulator, XU#MR0 under magnetic adjustment, which will be a light source for a feasibility study of SR experiments using the Tristan Main Ring.

You can jump to the article by clicking its title.

CONTENTS

A. INTRODUCTION

In December, 1992, the Photon Factory held a commemorating symposium for the 10th anniversary since the first extraction of synchrotron radiation at the PF ring in March, 1982. During the last moment of the meeting a session dedicated to future plans was held in which the TSLF (TRISTAN Super Light Facility) project was described in detail.

In January, 1993, a design report called the "TRISTAN Super Light Facility -- a Conceptual Design Report 1992 --" (KEK Progress Report 92-1, December, 1992) was published and distributed all over the world. Its chapters comprise the following:

preface (Hirotaka Sugawara)
chapter 1 What is leading to a Tristan Super Light Facility (Masami Ando)
chapter 2 Conversion Plan of Tristan to a Light Source (Susumu Kamada, Kazuhito Ohmi, Norio Nakamura, Hitoshi Fukuma, Shogo Sakanaka, Masaaki Isawa, Masanori Kobayashi, Toshihiro Mimashi, Tomotaro Katsura)
chapter 3 Basic Design of Insertion Devices for the Project (Shigeru Yamamoto)
chapter 4 Coherent X-ray Sources (Hideo Kitamura)
chapter 5 Beamline and Experimental Hall (Hiroshi Sugiyama, Makoto Urasawa, Yutaka Nakabayashi, Hideo Hirayama, Shuichi Ban, Hiroo Kato, Xiaowei Zhang, Tatsuo Arie, Yoshihiko Harada, and Yoshiyuki Amemiya)
chapter 6 Instrumentations and Experiments (Tsuneaki Miyahara, Tetsuya Ishikawa, Kazumichi Namikawa, Vladimir Belyakov, Seishi Kikuta, Kazumasa Ohsumi, Toshio Takahashi, Koichi Akimoto, Sadao Aoki, Yoshio Suzuki, Yasushi Kagoshima, Katsuzo Wakabayashi, and Naoto Yagi)
This report is available from the KEK library.

However, approximately at the beginning of 1993 the financial situation around the TSLF project was becoming worse while the high-energy physics community was becoming better. That the latter should use the current tunnel for the B-factory project seemed an almost unique chance to survive. Upon receipt of this news with astonishment among the synchrotron radiation-society, the outside users together with the outside members of the MR committee, which is chaired by Prof. Kikuta Seishi, has made a decision to address their wish to Mrs. Moriyama Mayumi, the Minister of the Monbusho (Ministry of Education, Science and Culture). That document was completed to pass to her together with the consent of over 200 strong supporters in May, 1993.

In April, 1993, a subcommittee dedicated to accelerator science in the Monbusho (hitherto called the accelerator science subcommittee) prepared a report that the Monbusho should promote a B-factory project at KEK, and then it is very difficult to recommend a conversion programme of the MR (TRISTAN Main Ring) into a super-light source.

This report was discussed and approved as a conclusion of that subcommittee's associated general assembly, which was held in July, 1993. As a result, it was reported without delay to the Monbusho. Both the general assembly and its subcommittee are organized for and under the sponsorship of the Monbusho. This report resulted in the fact that the budgetary requirement for the B-factory was executed by the high-energy physics community immediately after that decision, while the TSLF project therefore not; this procedure occurred in about July, 1993.

The TSLF and the MR committee therefore had to change their plan to a very realistic one, so that only one beamline for a feasibility study should be constructed just before starting the conversion of the Main Ring into a B-factory ring in the beginning of 1996. The design of a test beamline was initiated by Sugiyama with the help of Xia.

The construction of a prototype undulator by Yamamoto, comprising three units, has been completed. It was delivered in at the end of March, 1993. An in-vacuum version was not adopted in order to economize the manpower necessary for installing and commissioning. Nevertheless, its design was performed so that the 1st harmonic can provide photons at around 14.4 keV under an acceleration energy of 10 GeV.

In order to utilize this extremely brilliant light source effectively, the development of heat-tolerant x-ray optics against the super power-density of the light must simultaneously progress. A newly designed double-crystal monochromator in which its first Si crystal will be cooled by liquid nitrogen from its backside in a helium gas chamber has been commissioned by Zhang. A cooling test is underway.

Proper monitoring of the undulator light will also be one of the key technologies for controlling the orbit. The development of this technique must therefore be carried out. A prototype monitor using a wire made of graphite of designating the

beam location with an accuracy of one micron is being fabricated by Zhang and Xia.

The following are the names of the persons who have been involved in the TSLF project during the period between October, 1992 and September, 1993.

in-house staff:
Ando, Masami (TSLF)
Kamada, Susumu (TSLF)
Ohsumi, Kazumasa (TSLF)
Sugiyama, Hiroshi (TSLF)
Yamamoto, Shigeru (TSLF)
visiting staff from universities:
Kikuta, Seishi (University of Tokyo)
Namikawa, Kazumichi (Tokyo Gakugei University)
visiting engineer from abroad:
Xia, Shaojian (Institute of High Energy Physics, China)

The members of the Committee dedicated to the TSLF project in the period from October 1992 until September 1993 are as follows:
Ando, Masami(PF)
Hatano, Yoshihiko (Tokyo Institute of Technology)
Iwasaki, Hiroshi (PF)
Hieda, Kotaro (Rikkyo University also called as St.Paul's University)
Kikuta, Seishi* (University of Tokyo) *chair
Kimura, Yoshitaka (TRISTAN Accelerator Department)
Kobayakawa, Hisashi (PF)
Matsushita, Tadashi (PF)
Ohta, Toshiaki (University of Tokyo)
Sato, Isamu (PF)
Sato, Shigeru (Tohoku University)
Shiotani, Nobuhiro (Tokyo University of Fisheries).

B. TRISTAN MR AS A VERY LOW-EMITTANCE MACHINE

To study the feasibility of the TRISTAN MR as a synchrotron light source, beam experiments are scheduled for the latter half of 1995 at the TRISTAN MR. In converting the TRISTAN MR to a low-emittance light source for the sake of this feasibility study, the time and budget available are tightly limited. The following describes the conversion plan of the TRISTAN MR for the feasibility study, which will meet both the minimum requirements as a light source and the imposed limitations. Table 1 summarizes the beam parameters of the TRISTAN MR as a synchrotron light source for this feasibility study.

Table 1. Beam parameters for a feasibility study of the MR as a synchrotron light source.

			units
beam energy	10		GeV
normal cell phase(H/V)	90°/90°		
momentum compaction	7.2×10^{-4}		
accelerating voltage	36		MV
wiggler magnets	OFF	ON	
energy loss in a turn	3.8	6.5	MeV
energy spread in a beam	0.59	1.1	$\times10^{-3}$
natural bunch length	4.5	8.5	mm
natural emittance	7.0	5.1	nm

1. LATTICE MODIFICATION FOR THE INSTALLATION OF AN INSERTION DEVICE

As shown in Fig.1, a magnet free-space 6.5m long has been prepared for the installation of an insertion device. It is created by replacing two normal bending magnets (5.86m long each) with two short bending magnets (1.5m long each). The momentum dispersion falls to zero in this free space, so that the beam size remains small in the insertion device.

Some magnets along the passage of light are to be reversed in the orbit plane to make room for a light beam channel.

2. LOW-EMITTANCE OPTICS AND DAMPING WIGGLERS

The phase advance of the betatron oscillation is to be increased to 90° in both the horizontal and vertical directions in each FODO-type normal cell. This will reduce the beam emittance by a factor of three compared to the present optics of the 60° normal cell.

In the present optics for the collider operation, the momentum dispersion is large in the symmetry region where the wiggler magnets are installed so as to enhance the beam emittance. The present optics are used for relaxing the beam-beam interaction during beam injection and acceleration. For the light-source operation, the momentum dispersion is to vanish there, so that the wigglers will work as emittance-damping wigglers, and thus cut the beam emittance by 30%. Another advantage of the

wiggler excitation is to stabilize the beam oscillation against any instabilities, since the radiation damping rate is enhanced.

3. RF CAVITIES

The beam energy is to be below 10GeV for the feasibility study. On the other hand, the present RF system can afford beams above 30GeV.

For attaining a stable beam at a certain intensity, it is a key issue to remove any unnecessary RF cavities that may cause bunch-coupled instabilities. At least, the cavities must be removed from the straight section next to the insertion device, where the momentum dispersion does not vanish, because of the dispersion-free space for the insertion device.

4. NON-INTERLEAVED SEXTUPOLE SCHEME FOR A CHROMATICITY CORRECTION

The particle tracking shows a small safety margin for a dynamic aperture of the lattice for the feasibility study when the chromaticity is corrected by the conventional ways.

Greatly improved results are obtained by the "Non-Interleaved Sextupole Scheme" in which all of the sextupoles are arranged in pairs of the same strength. A partner sextupoles is located to the other with 180°-betatron phase difference in both the horizontal and vertical directions without being interleaved by other sextupole pairs. In this scheme, a geometric aberration caused by one sextupole is automatically canceled by the partner sextupole. A beam test of this chromaticity correction scheme will be conducted in the autumn of 1993.

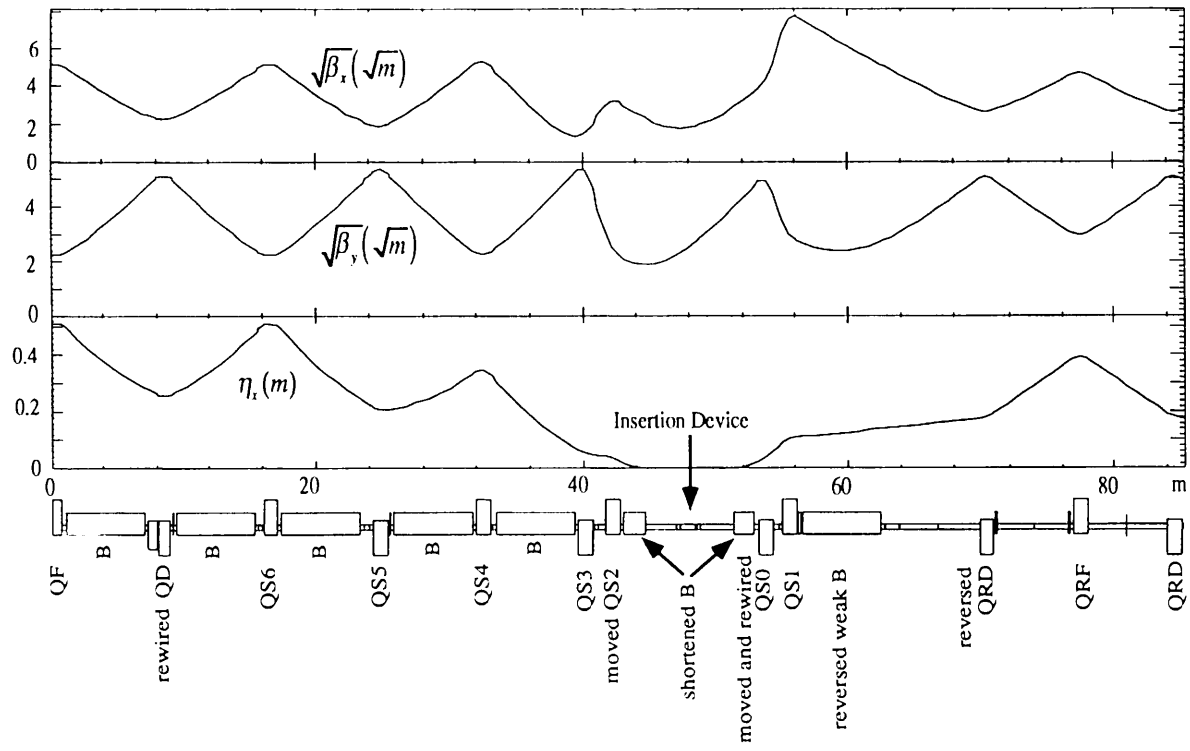

Fig. 1 Lattice modification for installing the insertion device. The optics parameters are also given.

C. SUPER-BRILLIANT X-RAY UNDULATOR

R&D studies on the insertion devices for the Tristan Super-Light Facility (TSLF) have been successively carried out from last year by constructing a standardized unit undulator, which is called XU#MR0. The TSLF is characterized by extremely brilliant radiation and coherent radiation produced by the low-emittance beam in the undulators and free-electron lasers (FEL's). When we optimize the MR for synchrotron-radiation experiments, three of four 200-m long straight sections of the present MR will be used for

installing the undulators. Each straight section is bent slightly outward for extracting light beams to form a 200-m arc, and is divided into two long (70 m) sections and two short (6m) ones; the 70-m and 6-m sections in the upper-stream half of the arc is to be used. The reason that we adopted the scheme of a standardized unit undulator for constructing the undulators for the TSLF, is the feasibility and convenience which are obtained by this scheme.[1,2] Since the total length of the undulators required for the TSLF amounts to 400m, it is not very practical to design and construct such undulators using a device-by-device policy, from both the view-points of design and construction costs as well as from that of man-power for commissioning and operation. In the construction of the XU#MR0, we have tried to explore and solve various mechanical problems, including thermal expansion and alignment issues, which will arise in the actual construction of standardized undulators for the TSLF.

1. MAGNETIC FIELD OF THE XU#MR0

The basic parameters of the XU#MR0 are given in Table 2. Three unit undulators are placed very precisely on a rigid common frame to form a 5.4-m undulator, as shown in Fig.2. We adopted a pure-type configuration of NdFeB magnets: the number of periods (N) is 120, the period length (λ_u) is 4.5cm, the remanent field (Br) is 12.8kG, and the coercivity (iHc) is 17kOe. These magnets are arranged in an out-of-vacuum scheme.

Table 2. Parameters of XU#MR0.

Magnetic structure	Pure configuration
Magnetic material	NdFeB (NEOMAX41H)
Period length	λ_u=4.5cm
Number of periods	120 [=3×(40/unit undulator)]
Magnet length	5.4m [=3×(1.8m/unit undulator)]
Maximum B	B=2.64kG
Maximum K	K=1.11
Minimum gap	3cm
Maximum aperture	2.5cm

The magnetic field of the XU#MR0 is optimized so that the orbit of an electron in the XU#MR0 is close to an ideal sinusoidal curve. For this purpose, the kick-angle of the electron at each magnetic pole is adjusted on the basis of a precise magnetic measurement using a Hall generator and a precise three-axes translation stage. At a coarse stage of the adjustment, magnets at a pole having a larger kick-angle (usually higher field strength) were exchanged with those at another pole having a smaller one (lower strength). For a fine adjustment, disk-shaped magnet chips were used in order to decrease the scatter of the kick-angles at the individual poles. Each holder which mounts the magnet block has halls in which these chips are embedded

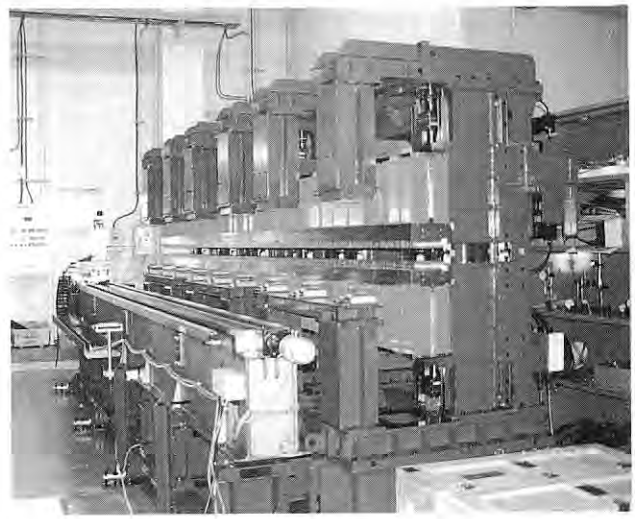

Fig. 2. Photograph of the XU#MR0.

Figure 3 shows a result of the field optimization in terms of the electron orbit. As a criterion in the field optimization, we used the following conditions concerning the deflection angle (θ_{defl}) and the effective amplitude (δ) of the envelope of the electron orbit in order to obtain a good transverse coherence of the radiation:

$$\theta_{defl} \leq \sigma_r' = \sqrt{\frac{\lambda}{N\lambda_u}},$$

$$\delta \leq \sigma_r = \frac{\sqrt{\lambda N \lambda_u}}{4\pi}.$$

Here, σ_r' is the divergence angle of the undulator radiation having a wavelength of λ, from a single electron. σ_r is the corresponding size of the radiation in the case of a diffraction limit. We adopted a value of σ_r' = 4 μrad as the critical deflection angle, and one of σ_r = 1.8μm as the critical amplitude, since we designed the XU#MR0 so that its first harmonic could be tuned at 14.4keV (0.86A in terms of λ). As can be seen from Fig.3, the optimization was performed fairly successfully,

and the deflections of the envelope become less than 0.2μrad and the amplitude less than 1μm.

The dependency of the peak magnetic field on the magnet gaps from 25 to 200mm is shown in Fig.4. The minimum gap (30mm) gives a maximum value of the K-parameter of K=1.11; whereas 14.4-keV radiation is obtained when K=0.97 with a 10-GeV operation of the MR.

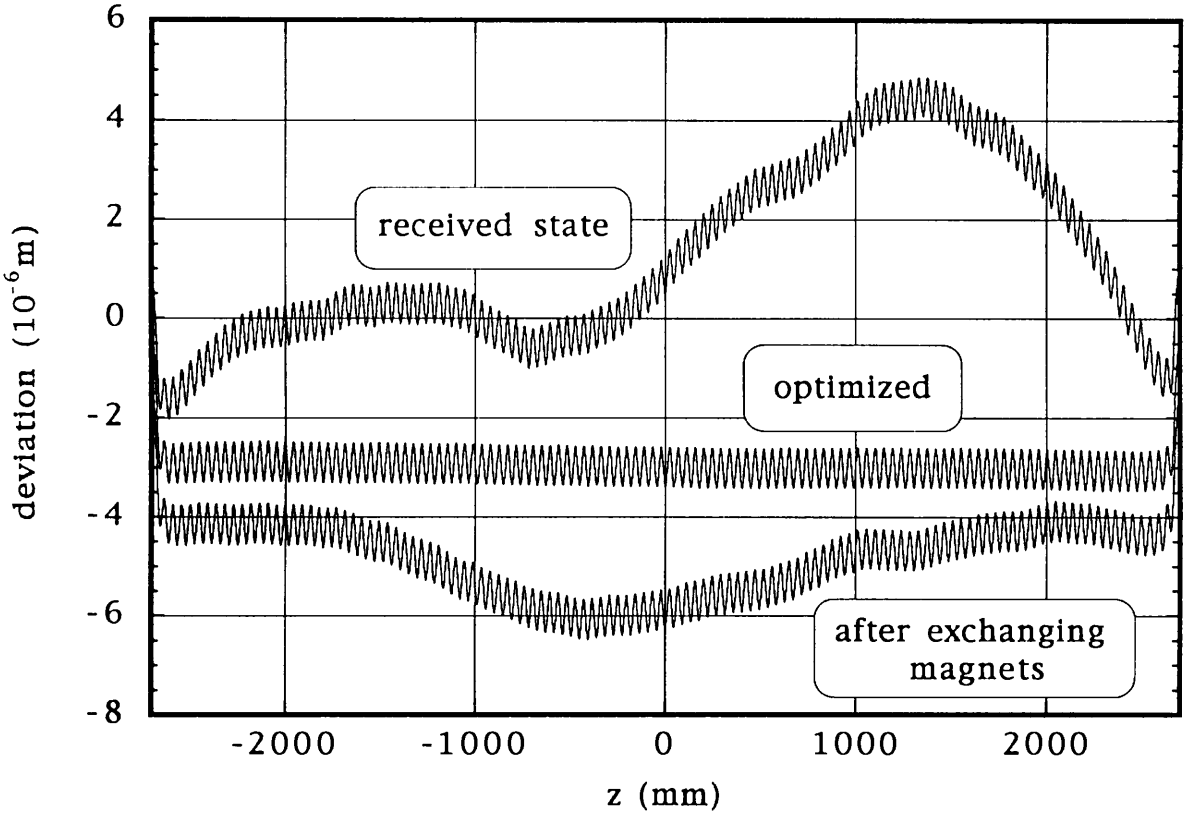

Fig. 3. Electron orbit in the XU#MR0. Orbit after optimization is compared with a received state.

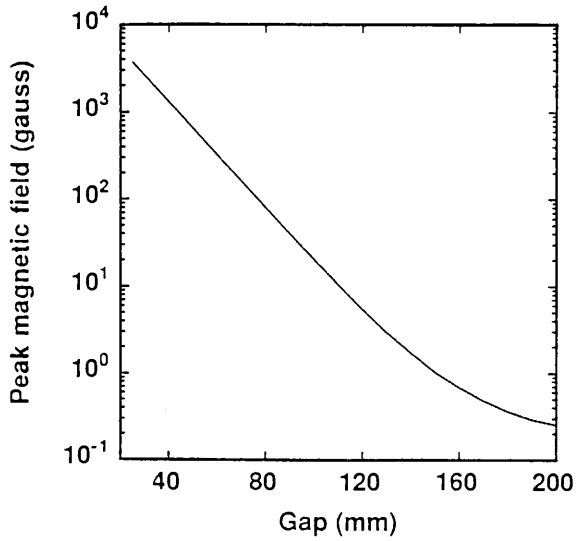

Fig. 4. Peak magnetic field versus magnet gap relation of the XU#MR0.

2. XU#MR0 AS A PRACTICAL SOURCE FOR A FEASIBILITY STUDY USING THE MR

As described in Chapter A, we will have an opportunity to carry out some feasibility experiments for the TSLF in the autumn of 1995. The XU#MR0 will be used as a practical source of super-brilliant x-rays. Although a conversion of the MR for this feasibility study is not complete, compared to the original conversion plan for the TSLF, we can reach a beam emittance of 5nm·rad, owing to a minimum, but adequate, modification of the MR lattice (see Chapter B). We have already reissued a slim version of the common frame of the XU#MR0, and reassembled three unit undulators on it. This modification of the undulator frame is required, since the beam-path height of the installation point available in the present conversion of the MR differs from that planned in an original TSLF.

Table 3. Characteristics of radiation from the XU#MR0: E=10GeV, I=10mA, ε=5nm·rad.

σ_x (mm)	146
σ_y (mm)	17
$\sigma_{x'}$ (mrad)	35
$\sigma_{y'}$ (mrad)	9
K	0.97
B (kG)	2.3
ε_1 (keV)	14.4
σ_r (mm)	1.8
$\sigma_{r'}$ (mrad)	4.0
Brilliance*	1.0×10^{18}
Angular flux Density**	4.8×10^{16}

* : (photons/s/mm^2/mrad^2/0.1% bandwidth)
** : (photons/s/mrad^2/0.1% bandwidth)

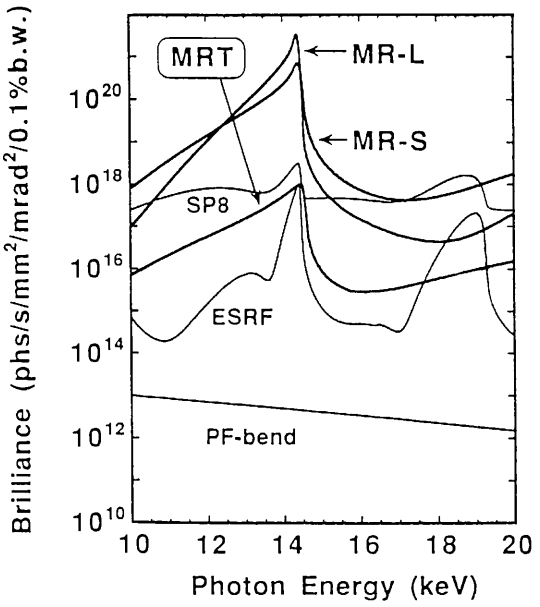

Fig. 5. Comparison of the brilliance of the TSLF and other SR facilities. MRT stands for the brilliance obtained from the XU#MR0 in the MR lattice for the feasibility study (see Chapter B; 10GeV). MR-L and -S, respectively, denote those obtained from the long and the short undulators planned in the original TSLF (10GeV). SP8 (Nishi-harima, Japan; 8GeV) and ESRF (Grenoble, France; 6GeV) denote those from third generation SR facilities. It should be noted that the brilliance for our feasibility study is obtained at 10mA, whereas those from other facilities including the original TSLF are obtained at 100mA.

A calculation shows that the XU#MR0 is able to produce quasi-monochromatic x-rays as the first harmonic with a brilliance of 1.0×10^{18} [photons/s/mm^2/mrad^2/0.1% bandwidth] in the case of K=0.97 at 14.4keV, when the MR is operated at 10GeV and 10mA. The characteristics of the radiation are given in Table 3. The spectrum obtained in the feasibility study is compared with other SR facilities, including the original TSLF plan, in Fig.5.

References

1) The Tristan Super Light Facility; Conceptual Design Report 1992, KEK Progress Report No. 92-1 (1993).
2) Yamamoto, S., R&D studies for a new insertion devices for the project, Photon Factory Activity Report 1992, S-7.

D. BEAMLINE AND EXPERIMENTAL STATION

1. SIMULATED CONSTRUCTION OF THE TSLF USING A COMPUTER-AIDED DESIGNING SYSTEM

We have adopted and have been using a 3-dimensional (3D) computer-aided design (CAD) system in order to design a TSLF which comprises accelerators, beamlines which include insertion devices, buildings and others.

The software of this CAD system, which is called MEDUSA (Computer-vision Corporation), comprises three modules: a 2-dimensional (2D) drafting module, a 3D model-constructing module and a management module for assembling 3D models (the Assembly-manager). An engineering work station of the system is a Sun SPARC station 10 GS (Sun Microsystems, Inc.) having 200-MB memories, 4-GB harddisks, a printer, a plotter for A0 paper and a color hard-copy machine. The present system, especially the Assembly-manager, enables us to easily treat a large assembly comprising several thousands 3D models, as in our case of the TSLF.

The useful points of the present system are as follows:

1) Since the redrawing of plans is very easy and fast, we can effectively examine various versions of the designs. We have tried seven different plans, some of which were made for a feasibility study; more than two hundred drawings were made in these last two years.

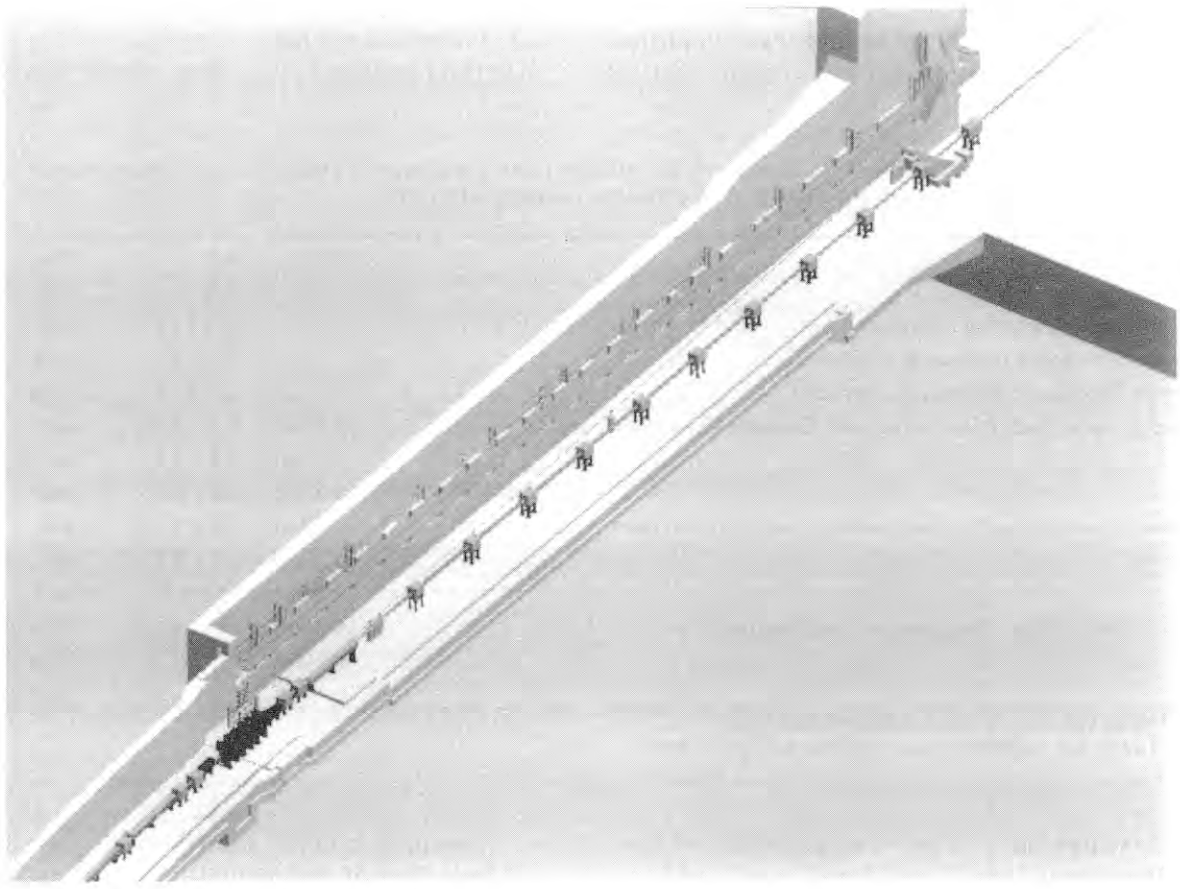

Fig. 6. Bird's eye view of beamline BL-BW-TL sketched as yellow components. The other components in different colors are as follows. The MR tunnel and the Tsukuba experimental hall (partially cut out) are colored in light gray and pink, the MR in light blue, the undulator (XU#MR0) in dark blue, and the cable racks and the pipes of the cooling water in light brown.

2) We can check the 3-dimensional interference of the designed components concerning the TSLF in detail.
3) We can obtain cross-sectional and projection views on any plane.
4) We can obtain a visual comprehension of the alignment of the components in the TSLF.

In the practical design processes, we must check any spatial interference or geometrical restrictions between newly designed components and the old ones which already exist, such as the MR, itself, the MR tunnel, the experimental halls, etc. In other words, we have made simulations of the TSLF construction on the 3D-CAD system. For this purpose, we have constructed various CAD-assemblies of the Tristan experimental halls, the MR tunnels, the newly designed halls for undulator radiation experiments, the accelerator components (the bending magnets, the quadrupole magnets and the RF-cavities, etc.), the undulator XU#MR0, the cable racks, the pipes of the cooling water and test beamline BL-BW-TL. As an example of such a simulation, Fig. 6 shows a bird's eye view of beamline BL-BW-TL

2. DESIGN AND CONSTRUCTION FOR A FEASIBILITY STUDY

As mentioned in section A, a feasibility study for SR experiments using the MR as a super-brilliant x-ray source should be the most important task. Here, we describe the design of the test beamline (BL-BW-TL) that is to be constructed for a feasibility study of the SR experiments. It will be installed in the north-west-side tunnel of the Tsukuba experimental hall, as shown in Fig.7 as a plane view. In this beamline, super-brilliant radiation from electrons which pass through the x-ray undulator (XU#MR0) is used. The main features of this beamline are as follows:

1) It was designed for super-brilliant radiation in the x-ray region having a high heat load.
2) The structure of the beamline was simplified, since the time allotted for construction and SR experiments is limited.
3) The beam-path line is kicked down to the SR experimental station, which is located 4.5m lower than the MR.
4) The beamline is very long; almost 100 m.

Table 4 Characteristics of undulator radiation from the XU#MR0 with a maximum K value (K = 1.07) when the MR is operated at 10GeV with a current of 100mA and an emittance coupling ratio of 1%.

Total Power		2.2	kW
Power Density		222	kW/mrad^2
Source Size (horizontal / vertical)*		292 / 35	μm
Beam Divergence (horizontal / vertical)*,**		71 / 19	μrad
Power Divergence (horizontal / vertical)*		127 / 74	μrad
Beam Size at Each Position from the Emission Point (horizontal / vertical)*,**	(at 17m)	1.5 / 0.36	mm
	(at 50m)	3.8 / 1.0	mm
	(at 85m)	6.3 / 1.7	mm
Power Size at Each Position from the Emission Point (horizontal / vertical)*	(at 17m)	2.5 / 1.3	mm
	(at 50m)	6.7 / 3.8	mm
	(at 85m)	11 / 6.4	mm
Power Flux at Each Position from the Emission Point	(at 17m)	768	W/mm^2
	(at 50m)	89	W/mm^2
	(at 85m)	31	W/mm^2

*: These values are twice standard deviations.
**: These are values for the first harmonic (13.4 keV).

2.1 Arrangement and Components of the Beamline

The beamline is divided into three main parts: 1) the upstream part (located about 17m from the emission point), which consists of a water-cooled shutter, a γ-ray shutter and other parts; 2) the middle part (at about 50m), which consists of a beam-position monitor and a water-cooled mask; and 3) the downstream part (at about 85m), which consists of water-cooled slits, beryllium windows and other parts. Ports for vacuum pumps are distributed appropriately along the entire beamline. Table 4 gives the radiation characteristics from the x-ray undulator (XU#MR0) when it has a maximum K value of 1.07; the MR is operated at 10GeV with a current of 100mA and an emittance coupling ratio of 1%. As design parameters for the highest heat-load condition, we used the values of 10GeV for the MR's operation energy and 100mA for the beam current. The important characteristics of the beamline structure are given below:

a) We use beam ducts (35mm in diameter) which are connected by ICF70 flanges, since the beam size is very small (Table 4).
b) In order to curtail the number of vacuum pumps, we obtained the optimum design of the pumping-power distribution based on a principle of differential pumping, and obtained an optimum pressure distribution: 10^{-9} Torr at the most upstream point of the beamline and 10^{-7} Torr at the most downstream point. This design is based on a simulation of the pressure distribution using a simplified beamline model of the BL-BW-TL.
c) We need to align the beamline with an accuracy of less than ±1mm throughout. For this purpose, we can use the quadrupole magnets of the MR as targets for this alignment, since the beamline is placed along the long straight section of the MR within about 2m, as shown in Fig.7.
d) A manual gate valve is the most upper-stream component of the beamline. It is placed at a point 15.5m from the emission point.
e) In order to monitor the light beam position, graphite-wire beam position monitors (BPM) are installed at each front of the three main divisions of the beamline mentioned above; they are placed at 17m, 49m and 84m from the emission point, respectively. The development of this type of BPM is in progress in the BL-NE3 in the AR.

f) Water-cooled masks are placed on 17m and 49m from the emission point after the first and second BPM's, respectively.
g) A water-cooled shutter and a γ-ray shutter are placed after the first water-cooled mask at 17.5m and 19m, respectively. Only a single set of these shutters is used, unlike the usual cases in which two sets are used as spares.
h) A fast closing valve (FCV) is installed between the water-cooled shutter and the γ-ray shutter. This is to protect the vacuum of the MR against any accidental leak at the lower reaches of the beamline. To protect the valve plate of the FCV against high heat-load radiation from the XU#MR0, we must put a thermal protective object which closes faster than the FCV, or turn off the power of the RF cavity when the FCV is closed.
i) Water-cooled X-Y slits are installed at 85m in order to remove any excess heat load for downstream devices.
j) Graphite absorbers are placed at 86.5m so as to reduce the heat load for beryllium windows which are placed at 85.5m for vacuum isolation between the MR and the downstream devices

2.2 Experimental Station

Whereas the MR, itself, is located at the third basement, a room which can be used as an SR experimental station is located at the fourth basement (the north-west and external side of the Tsukuba experimental hall). The size of this room is 9.5m long, 4m wide and 2m high. In Fig.7, the room is shown as the hatched area located at about 90m from the emission point. By using this room we can avoid any large-scale construction work, such as the construction of a radiation shield. Only by making holes which connect the third basement to the fourth, we can introduce the SR beam for the experiments and send electricity, water and other items for the beamline operation. This room serves practically the same role as the experimental hutch in the SR experimental halls at the PF and the AR. Entrance to this room is to be allowed even in the on-beam condition of the MR, provided that the shutters are closed.

2.3 Monochromator

The SR beam is led to the experimental station after it is kicked down by a double-crystal monochromator. The monochromator has a special structure to meet the above-mentioned aim. The first crystal of the monochromator is set in the third basement, and the second crystal is put in the experimental station in the forth basement (Fig.8). The available range of the Bragg angle of this monochromator is limited to be from 18.5 to 27degrees, because of a height difference of 4.5m between the incident and out-going beams and the restricted space allowed. We need to exchange diffraction orders or diffraction crystals appropriately so as to obtain photons of the required energy.

The first crystal is cooled by liquid nitrogen in a vacuum. The second crystal is put in helium gas isolated by beryllium windows. Due to the following reasons, we have adopted liquid-nitrogen cooling method.

a) In this method, the monochromator crystal does not distort easily, since block crystals can be used. The quality of the SR beam is not deteriorated due to a distortion of the monochromator crystals.
b) This method is suitable for third- and forth-generation light sources, since the cooling efficiency is very high. We can use silicon single crystals that have the highest crystalline quality.

A beam shutter and XY slits for the monochromatic x-rays are installed between the first and second crystals of the monochromator. We can enter the experimental station while the first crystal is being irradiated, provided that the monochromatic x-ray shutter is closed. In order to reduce the background noise for the experiments, any unnecessary part of the x-ray beam should be cut off by the XY slits.

References

1) The Tristan Super Light Facility, Conceptual Design Report 1992, KEK Progress Report No. 92-1 (1993).
2) "The Tristan Super Light Facility", Photon Factory Activity Report 1992 # 10, S-1, (1993).

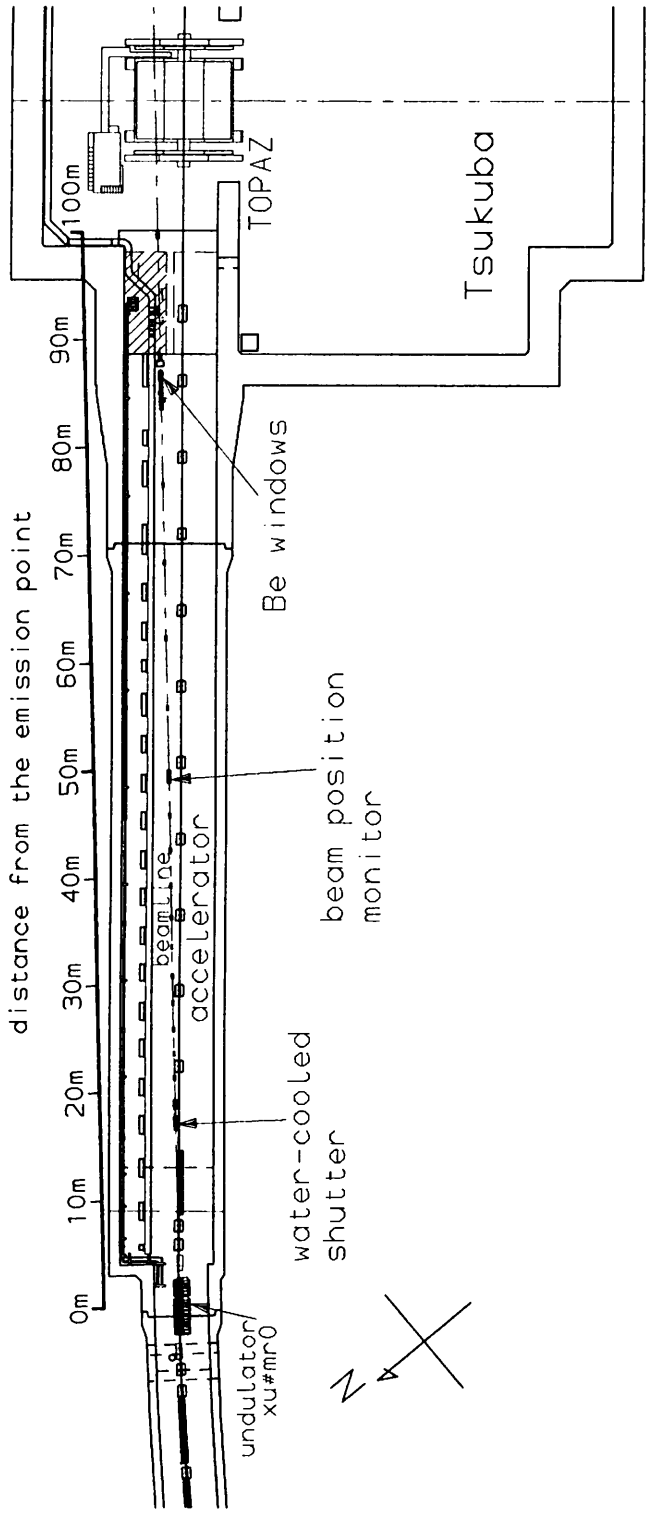

Fig. 7(a) Plane view of beamline BL-BW-TL. The scale indicates the distance from the emission point. The entire beamline and vicinities of the Tsukuba experimental hall are shown. The hatched area is the SR experimental station that is located about 90m from the emission point.

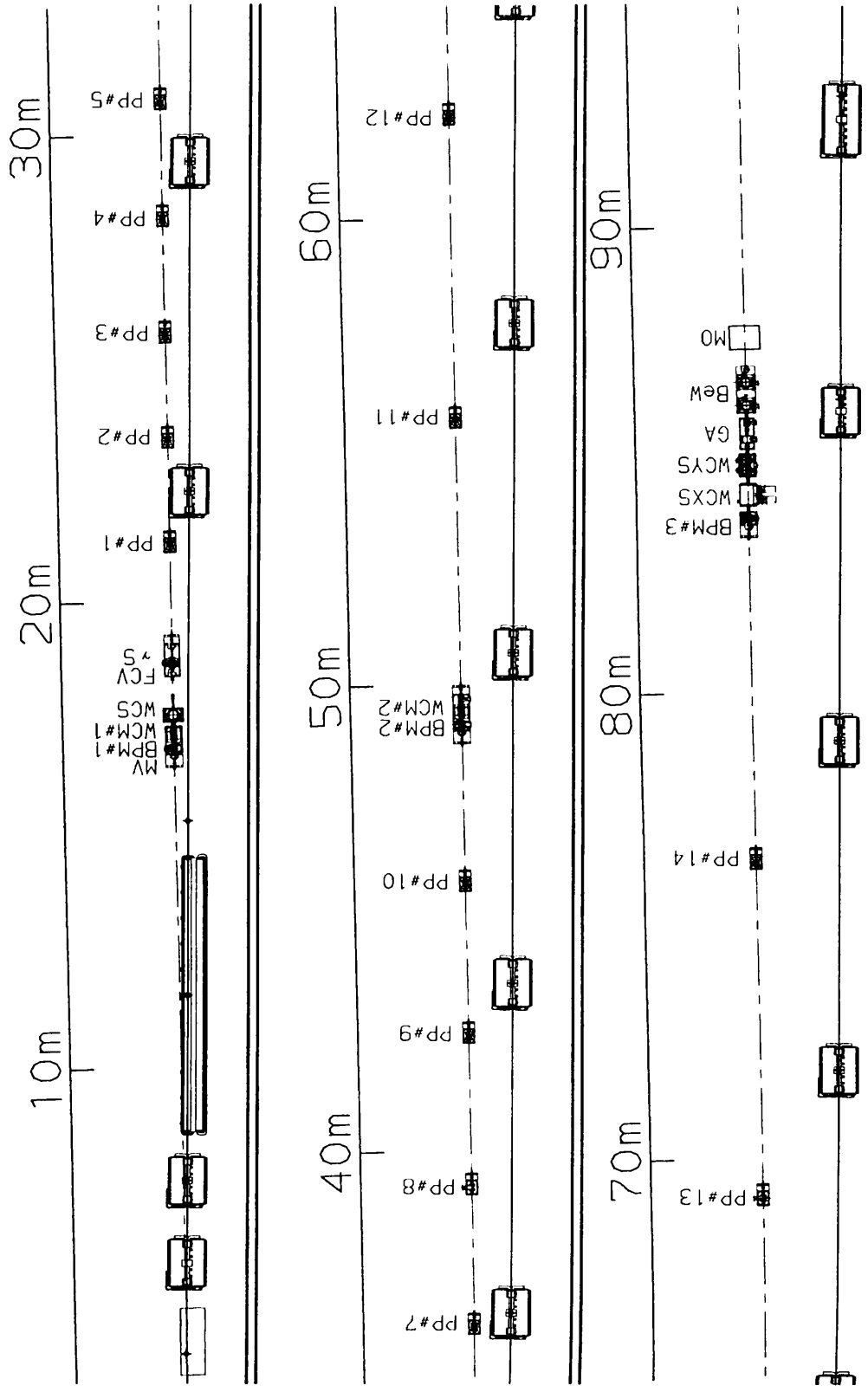

Fig. 7(b) Plane view of beamline BL-BW-TL. The scale indicates the distance from the emission point. An enlarged view of the selected part of Fig.7a is shown. The beamline is separated and given in three rows. The abbreviations are as follows: MV is a manual gate valve; BPM, a beam-position monitor; WCM, a water-cooled mask; WCS, a water-cooled shutter; FCV, a fast closing valve; γS, a γ-ray shutter; PP, a port for a vacuum pump; WCXS, water-cooled X slits; WCYS, water-cooled Y slits; GA, graphite absorbers; BeW, beryllium windows; and MO, a monochromator.

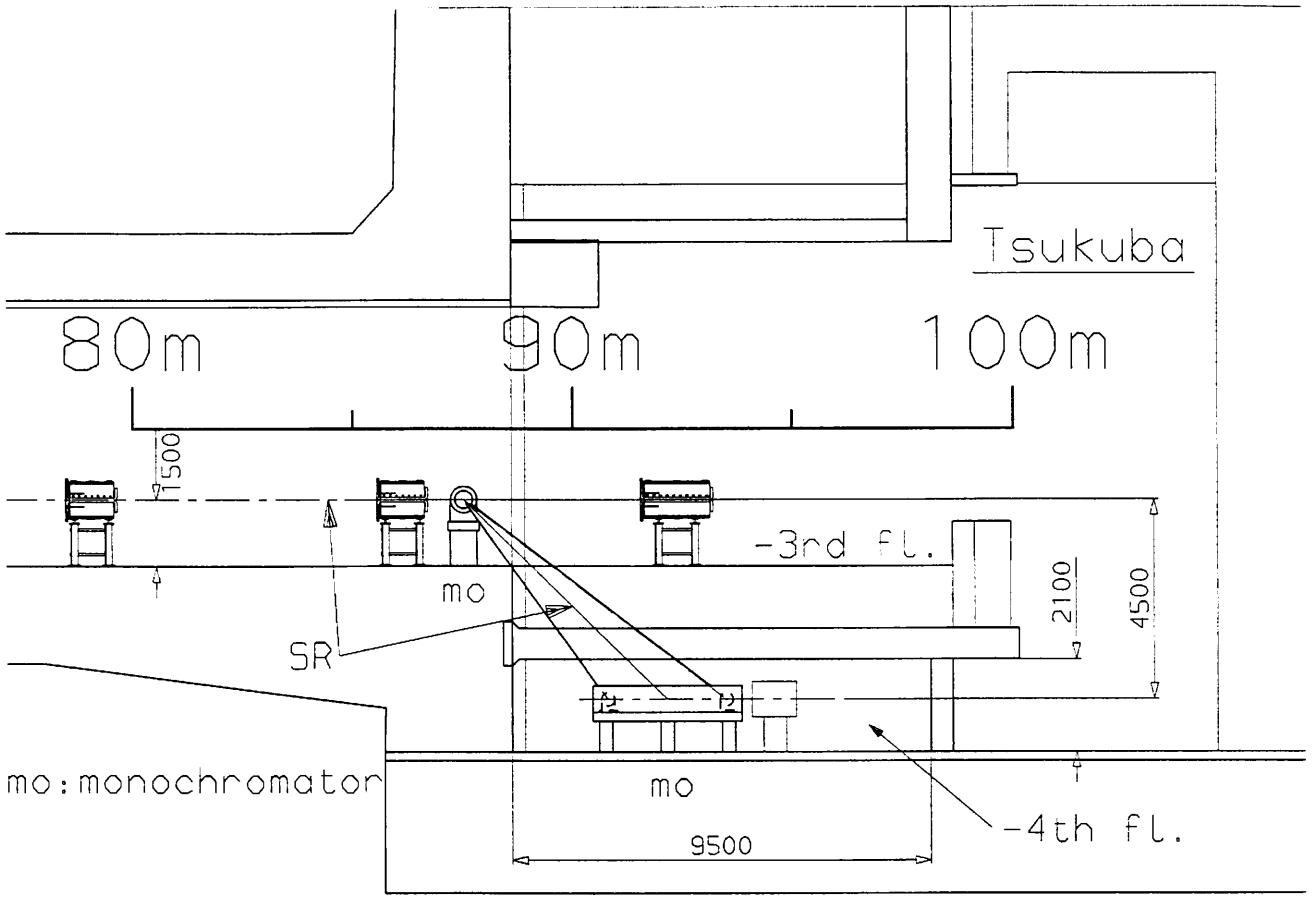

Fig. 8 Cross-sectional view of the SR experimental station viewed from the center of the MR. The scale indicates the distance from the emission point.

E. RESEARCH AND DEVELOPMENT IN RELATED FIELDS

1. LONGITUDINAL FEEDBACK SYSTEM DEVELOPED FOR THE FEL PROJECT AT THE PF STORAGE RING

Achievement of a low-emittance electron beam is one of very important key factors for advancing the Tristan Super Light Facility, the fourth-generation coherent light source project at KEK. Construction of an effective feedback system for the electron beam will facilitate it strongly. For this purpose we are carrying out a R&D study for developing a longitudinal feedback system at the PF ring where a free electron laser (FEL) in the VUV region is under development

The present FEL study (the target wave length is 177 nm) requires high-quality beams at low beam-energy (0.75 GeV). Although the gain measurement will be carried out using a single-bunch, further experiments concerning the FEL oscillation require four-bunch operation. At a low-beam energy, problems due to beam instabilities are serious because the radiation damping time becomes long. Therefore, cures for the instabilities are particularly important at low energy.

Studies on the low-energy operation at the PF storage ring have been carried out since 1989. Positron beams were injected at a beam energy of 2.5 GeV, and then slowly decelerated to 0.75 GeV. A beam current of 40 mA was stored at 0.75 GeV in a single-bunch operation mode. However, the currents and beam quality were greatly limited by the longitudinal coupled-bunch instabilities, particularly under four-bunch operation. In order to suppress these instabilities, a longitudinal feedback system was developed.[1,2)]

The feedback system was initially tested under single-bunch operation at 2.5 GeV. A strong longitudinal dipole-oscillation of a bunch was excited by tuning one of the main accelerating

cavities, which was not powered, to a frequency of about $f_{rf} + f_s$. The oscillation was successfully damped by using the feedback system (see reports on Light Source Division of this volume).

As the next step, a single-bunch beam was decelerated to 0.75 GeV. Due to a change in the synchrotron frequency during deceleration, we needed additional phase shifts on the feedback signals, which were controlled so as to retain total shifts of 90 degrees. Then, the longitudinal oscillation at 0.75 GeV was successfully damped.

Finally, the system was tested under four-bunch operation. The gate timings of an analog-multiplexer were adjusted so as to apply the correct voltage to each bunch when crossing the feedback cavity. The stored beam was then decelerated to 0.75 GeV. The instabilities were greatly suppressed during the deceleration, so that currents of 40 mA were achieved under four-bunch operation at 0.75 GeV. The feedback system is capable of controlling the longitudinal instabilities on four bunches, and are now routinely used during low-energy operation for FEL studies.

References
1) Photon Factory Activity Report #10 (1992), R-5.
2) S. Sakanaka, A. Ueda, K. Haga and H. Kobayakawa, The 9th Symposium on Accelerator Science and Technology (1993), 395.

2. X-RAY MICROBEAM

An x-ray microprobe has been expected to be a promising analytical tool for spectroscopic and structural studies of the elemental constitution of matter with spatial resolution. Detectable signals are fluorescent x-rays, photoelectrons, micro-x-ray diffraction, EXAFS and so on. Recent advances in x-ray optical elements have made it possible to design various types of x-ray microprobes.

Among them, grazing-incidence mirrors are the most convenient focusing elements, since they can be used for a wide spectral range. Due to the large optical aberrations inherent to a single grazing-incidence mirror, it was difficult to produce a small x-ray spot of less than one micron. In order to produce a much smaller microbeam, these aberrations must be reduced. A Wolter type-I mirror is one of the best grazing-incidence mirrors, which reduce aberrations considerably. Figure 9 shows the parameters of a Wolter type-I mirror which is being developed for x-rays with a wavelength longer than 0.1nm. The Wolter mirror consists of a paraboloidal and a hyperboloidal mirror which compensate the aberrations of each other. If the complete 360-degrees surface of revolution is used for focusing x-rays, it is theoretically possible to obtain a microbeam smaller than 10nm. A submicron x-ray microbeam will be obtained by using only a small part of the aperture. For this optical system we do not need a very long source-to-mirror distance, which is usually required when an ellipsoidal mirror is used instead of a paraboloidal one. This system requires only a collimated beam. A high collimation of better than 10 microradians can be accomplished by using a combination of Si crystals, that is, double-parallel crystals and an asymmetric one. This also produces a relatively large coherent area, which is suitable for the production of a diffraction-limited microbeam.

Some preliminary tests with a single paraboloidal mirror of small aperture have been carried out at the beam line BL-6C2 (see a user's report No.93G110).

S. Aoki, University of Tsukuba

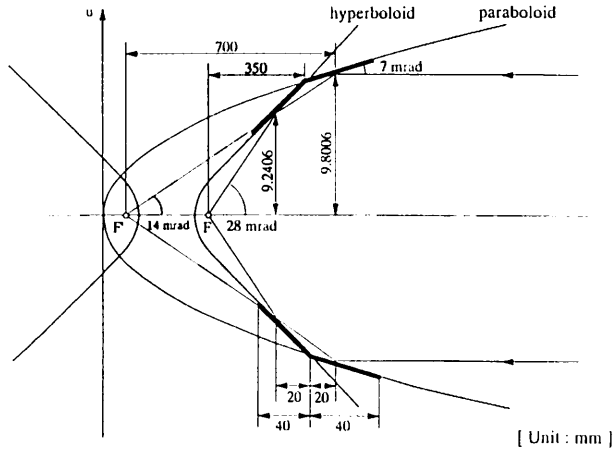

Fig.9 Parameters of a Wolter mirror.

3. BEAM-POSITION MONITOR FOR INSERTION DEVICES

Precise monitoring of the position of an SR beam from an insertion device is quite necessary not only for precision x-ray diffraction experiments, but also for the operation of the next-generation SR sources. Some ideas based on a pair of triangular photo-emission electrodes with an

analogue electric arithmetic circuit to monitor the SR beam position have been applied at several facilities. Although they have been successfully used for bending-magnet sources, they can not be applied to an SR beam from an undulator due to the following reasons: (1) It is technically difficult to design a pair of water-cooled electrodes irradiated by a high-power-density beam, the position of which is to be monitored. (2) The beam position is detected through subtraction of photo-currents produced by the individual electrodes. When the deflection parameter of the undulator is changed, the spatial (and spectral) distribution of the radiation is also changed. This change may generate a false signal of the change in the beam position. Therefore, this type of monitor can be used for undulator radiation only when its calibration is made precisely with respect to the deflection parameter, which changes continuously.

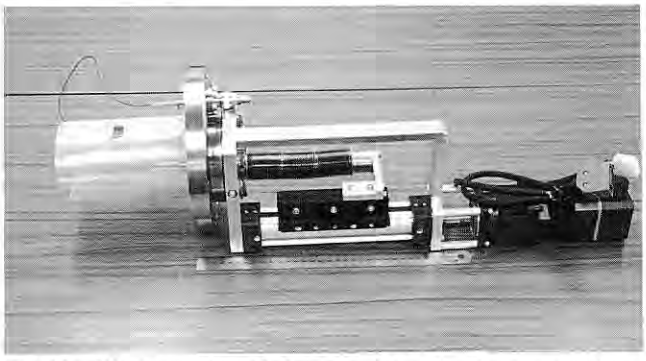

Fig.10 Photographs of the graphite-wire beam position monitor:

On the basis of a different and new idea, we devised a wire-type beam-position monitor for an x-ray undulator (Fig. 10), and examined its feasibility and operational limitation in beamline BL-NE3 in the AR by using radiation from the x-ray undulator U#NE3. Using this monitor we can observe an SR power profile as a photo-current distribution produced in the wire by scanning the wire in a direction perpendicular to the beam axis

The beam position (Y_0) is defined by a spatial distribution function (f(y)) of the SR power as its center,

$$Y_0 = \frac{\int f(y)\, y\, dy}{\int f(y)\, dy}, \qquad (1)$$

where y is a coordinate in the desired direction. Although this definition should be made for a certain photon energy to be used in general cases, we can use the total power distribution function which is contributed from the entire photon energy as f(y) in common cases, such as utilization of odd harmonics of the undulator radiation or the bending radiation.

The observed center (Y_0') of the SR beam by the wire is given by

$$Y_0' = \frac{\int f(y)\, g(y)\, y\, dy}{\int f(y)\, g(y)\, dy}, \qquad (2)$$

where g(y) is a photo-emission characteristic function of the wire at position y. If the function g(y) does not depend on the position, or it is vertically symmetric, then $Y_0=Y_0'$. This means that we can obtain the true position of the SR beam regardless of the wire width. When g(y) depends on the position, Y_0' is not always equal to the true beam position. However, the correspondence between Y_0' and Y_0 is a one-to-one relation, and the wire can be used as beam-position monitor

Graphite is a suitable material for the wire, due to its electrical conductivity and high sublimation temperature. If the wire is made of graphite we do not need any cooling systems for it, and the heat load to the wire can be taken away through thermal radiation. The heat load is proportional to the third power of the wire's dimensions, whereas the outgoing heat is proportional to the square of the dimensions. Thus, when the wire's dimensions are sufficiently, there is an optimum condition of the dimension at temperature T where the thermal radiation power is higher than the heat load on the wire. For example, let us consider a graphite wire 0.1 mm thick and 0.5 mm wide which is irradiated by very intense SR having a power density of $22W/mm^2$. The impinging power is 11W per unit length of wire. The power fraction absorbed by a wire having a thickness of 0.1 mm is only approximately 10%, since the higher energy portion of the radiation passes through the wire without absorption. If the heat load in the present case (=1.1W) is taken away by only thermal radiation, the power density should be $0.9W/mm^2$. The Stefan-Boltzmann law for a black body tells us that an equilibrium power density to this value for a graphite is achieved at 2000 K, which is far below the sublimation temperature of graphite. If we use the wire at 3000 K, the present simple estimation shows that the allowed power density of the impinging light beam should be $110W/mm^2$!

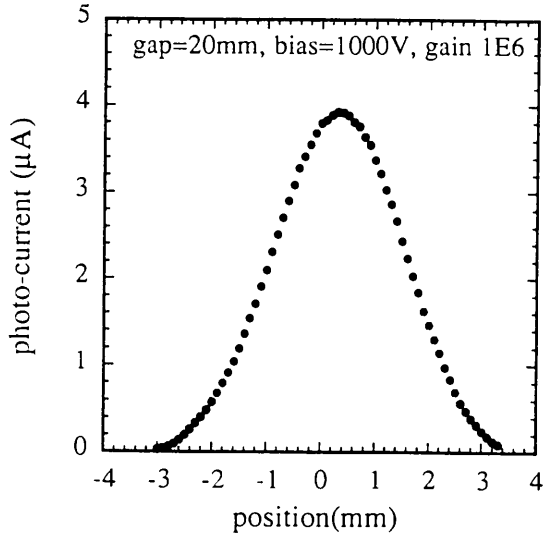

Fig.11(a) Photo-electron current versus the wire position: the graphite wire of 0.1-mm thickness and 0.5-mm width used in the condition of the electric shield bias of 1000V and the undulator gap of 20 mm.

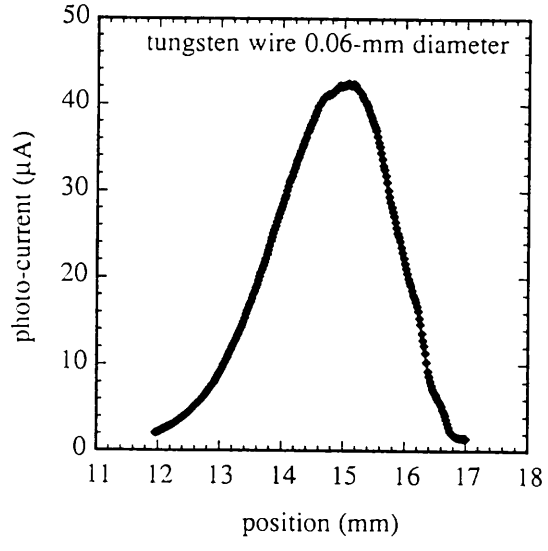

Fig.11(b) Photo-electron current versus the wire position: tungsten wire of 0.06-mm diameter used under the same conditions.

The test results obtained for the light beam from the x-ray undulator U#NE3 by the wire-type position monitors are given in Fig.11: Fig.11a corresponds to a result obtained by a graphite wire of 0.1-mm thickness and 0.5-mm width, and Fig.11b was obtained by using a tungsten wire of 0.06-mm diameter as a preliminary test material. The wires were scanned by ball-bearing screws which are driven by a stepping motor with a position resolution of 0.001 mm. The FWHM of the experimental result is 2.7 mm, which almost corresponds to a summation of the wire width and the FWHM of the SR power distribution at the location of the monitor. With several observations using different conditions of the deflection parameter, we found that the monitor was not sensitive to the spectrum structure, but was sensitive to the radiation power. Now, one of the graphite-wire monitors is being continuously tested and operated at beamline BL-NE3 by setting it at the half maximum of the peak intensity.

4. LIQUID-NITROGEN COOLING METHOD FOR THE FIRST DIFFRACTION CRYSTAL IN A MONOCHROMATOR FOR SUPER-BRILLIANT SR

The power density of synchrotron radiation from an x-ray undulator is very high, and is usually a hundred-times stronger than that of a bending magnet source. Although many ideas concerning crystal-cooling for monochromators have been proposed so far (they are summarized in the reference (1)), they were not completely satisfactory for high-power-density radiation. Also, in the PF and AR, where all x-ray monochromators are based on water-cooled silicon crystals, these diffraction crystals are not able to give an ideal performance when powerful SR hits them.

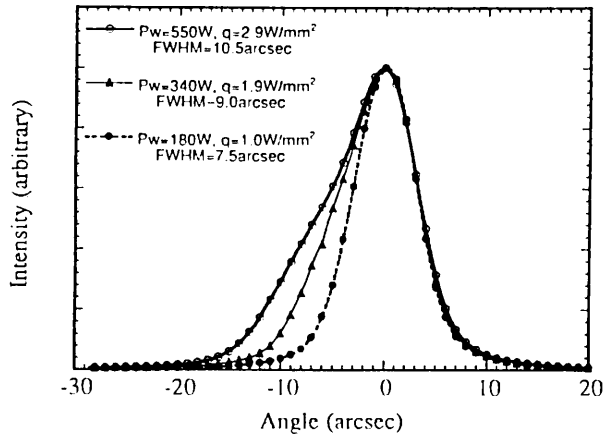

Fig. 12 Rocking curves of directly water-cooled silicon crystals. They are irradiated by SR with the various power densities under an atmospheric pressure of helium.

The power density of the undulator radiation amounts to $10W/mm^2$ or more at the location of the first diffraction crystal in a double-crystal monochromator, which is located at a few tens of

meters from the source. Even if we take a shallow incidence angle of a few degrees, the heat load will also be a few watts per square millimeter. We found that the performance of the diffraction crystals sensitively depends on the value of the power density on the surface of the crystals. This critical value is about $1W/mm^2$ in the case of silicon crystals. This situation is clearly indicated in Fig.12, which shows normalized rocking curves of Si (111) obtained with several different power densities using the x-ray undulator, U#NE3. We can find that the rocking curve of the diffraction is symmetric for a power load below $1W/mm^2$, but that for a higher power density the rocking curves become asymmetric. The lower angular part of the curves has been inflated and their height has become lower than in the symmetric case in practice.

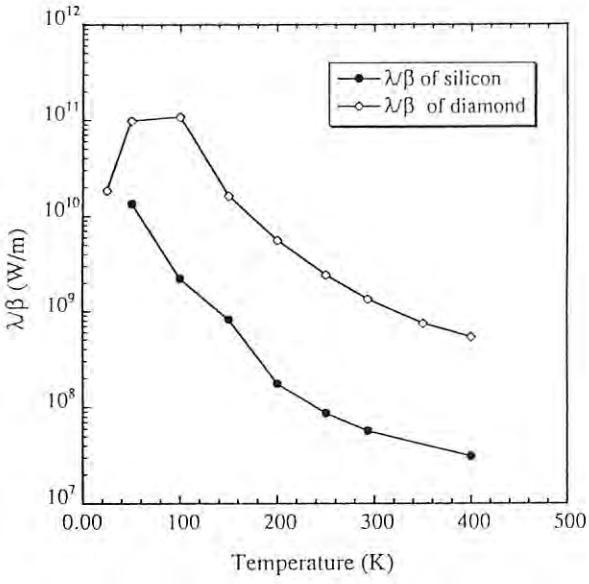

Fig. 13 Ratio of the thermal conductivity over the linear thermal expansion versus the temperature.

This is not fundamentally caused by the cooling method, but by the physical properties of the silicon crystal. When SR irradiates a crystal surface, a thermal field is produced with a temperature gradient toward the cool (or cooled) side of the crystal. The lattice constant was slightly distorted by thermal expansion due to the temperature gradient. The lower distortion results in the better reflectivity of the crystal. If λ and β are the thermal conductivity and the thermal linear expansion of the crystals, respectively, the ratio λ/β should be a figure of merit of both the cooling and the reflectivity of the crystals. Figure 13 shows the ratios of silicon and diamond crystals as a function of the temperature. From this point of view diamond crystals are very suitable as diffraction crystals in a monochromator under a high heat-load condition, since their λ/β is about 30-times higher than that of silicon at room temperature. It should be noted that when silicon crystals are used at about 100K, they have the same λ/β as that of diamond crystals at room temperature. This means that silicon crystals at 100 K have the same thermal toughness as diamond crystals at room temperature, and that they are able to maintain a high reflectivity under the 30-times higher condition of the power density than that of the above-mentioned critical value: under $30-W/mm^2$ condition.

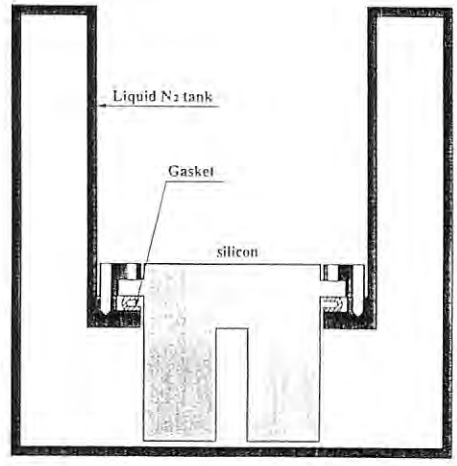

Fig. 14 Inside view of the liquid-nitrogen tank which contains the silicon first crystal.

According to the principle mentioned above, we have devised a new monochromator which has Si (111) double crystals and a liquid-nitrogen cooling system for them. A cross-sectional view of the liquid-nitrogen tank is shown in Fig.14. The silicon crystal is mounted directly in the tank with a special sealing gasket. The capacity of the tank is about 1 liter. At present, we adopt an open system for a nitrogen path, and the evaporated gas is discharged to the atmosphere. The new monochromator was installed in beamline BL-NE3, and was tested by using x-ray undulator radiation with various thermal loads. Figure 15 shows the result obtained at a maximum power density of $4.3W/mm^2$ with a total power of 800W; no change was observed in the width of the rocking curve of Si (111) (Fig. 15(a)), and no distortion pattern was observed on the

topography of Si (111) obtained at the same condition (Fig. 15(b)).

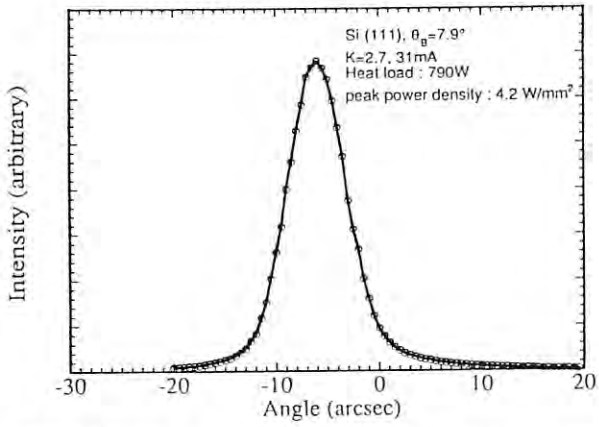

Fig. 15(a) Rocking curve of the liquid-nitrogen-cooled silicon crystal under a power density of 4.3W/mm^2, and total heat load of 790W.

Fig. 15(b) Topography of Si (111) diffraction.

When the silicon crystals are cooled to 100K, they can be used as ideal optical elements up to a power density of 30W/mm^2. Under these conditions they have the same performance as that of directly water-cooled silicon crystals which receive a power density below 1W/mm^2 at room temperature. A power density of 30W/mm$_2$ is about 10-times higher than the maximum produced by the x-ray undulator, U#NE3 in the AR. The cryogenic cooling method, which was developed in the present work, will be important and applied in a very high-power-density beamline, which will be constructed for super third- or fourth-generation light sources, such as the TSLF.

Reference

1) T. Mochizuki, doctoral thesis presented to the Graduate University for Advanced Studies (1993).

5. MICRO-AREA'S STRUCTURE ANALYSIS

R & D activities of TSLF also have been made at the PF ring. At its beamline 4B(BL-4B), an equipment and software system aimed at the crystallographic studies on submicrometer-sized samples was developed using the Laue method combined with an imaging plate (IP; Fuji Co. LTD.) as a two dimensional detector. This system has been successfully applied to analyze microtextures in complicated crystal aggregates, and to refine structures of submicrometer-sized crystal particles or twinned domains of some inorganic specimens. By making use of SR from MR, it is expected to analyze minuter samples. However in this case, it seems difficult to pick up such a small sample and attach it to a fine glass fiber under an optical microscope. When SR from MR will be available, submicron areas of specimens become subjects of our research in such cases as mentioned above.

The method for the crystallographic studies on such small areas has to be developed, and a preliminary experiment on micro area has been carried out at BL-4B. The brief introduction of the apparatus will be described in this report.

Taking the limited space around BL-4B as well as a small x-ray shield hutch into account, we produce a microbeam by using a micropinhole set just after the optical system which was installed in the beamline and the diffraction apparatus as shown in Fig.16. The newly developed equipment was designed to be installed with the micropinhole and with the IP readout system. Even though the equipment is placed in a vacuum chamber to minimize air scattering, a diffraction pattern at a different crystal orientation can be obtained without opening the vacuum chamber.

On the way to submicron area's crystallography, a pinhole with diameter of about 10 μm was made in trial. Its beam size was measured to be 8 μm in diameter as the full width at half maximum at the sample position by scanning an ion chamber with a slit. The equipment with this pinhole was applied to a mineral included in a thin section of a meteorite, and its structure was successfully refined by a least-squares program which was also developed. Three smaller pinholes were then produced with beam sizes of 3.5, 2.4 and 1.5 μm. Laue pattern of minerals in a thin section of meteorite taken with 3.5 μm pinhole is shown in Fig.17.

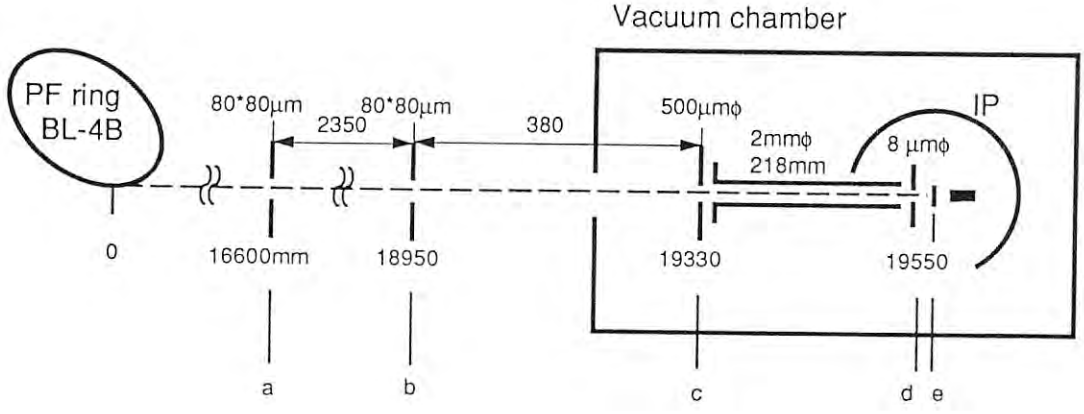

Fig.16 A schematic drawing of the layout of an optical system and a diffraction equipment. Letters a, b and c denote first and second and third pinhole, respectively. A micro-pinhole is shown as d. Sample of thin section and imaging plate are indicated by e and IP respectively. The figures below the horizontal dotted line are distances from the source point.

Fig.17 The Laue pattern of 3.5 μm area of a thin section of a meteorite taken for 60min. with the ring current from 176 to 175mA.

If we compare brilliance and emittance in case of using MR with an undulator to those of using BL-4B (PF; 2.5GeV), and also the distances between source points and sample positions, the number of photons at the sample position in case of MR is expected to be as much as six orders of magnitude higher than those of BL-4B. Taking into account of peak height of Laue function as well as volume ratio of samples, micro areas of samples with volume of 2×10^{-4} μm^3 (600A in edge length if its form is cubic) can be analyzed. By using such SR from MR, crystal structures and textures as observed by transmission electron microscopy (TEM) will be refined and analyzed in detail by an X-ray diffraction method.

F. TENTATIVE PROPOSALS OF SR EXPERIMENTS

1. MECHANO-CHEMICAL X-RAY DIFFRACTION EXPERIMENTS ON A SINGLE SKELETAL MUSCLE FIBER

1.1 Scientific Background

X-ray diffraction studies on skeletal muscles have been greatly advanced since intense x-rays from synchrotron-radiation sources became available. Many lines of evidence obtained during the last 14 years indicate that myosin heads can interact with actin molecules with various conformations during contraction. This conclusion seems to be inconsistent with a model of muscle contraction in which each chemical state corresponds to a unique conformation of the actin-myosin complex, and suggests flexibility in the actin-myosin interaction.

One major task in future x-ray diffraction studies on skeletal muscles is to observe any structural changes that accompany force generation, and to correlate them to the chemical states of the ATPase reaction of actin and myosin. For this purpose, it is necessary to measure any intensity changes of the x-ray reflections when the myosin

heads change their states and develop force simultaneously. A single muscle fiber is the most desirable specimen in this kind of experiment, since the tension can be controlled far better than in a whole muscle, which has been mainly used in fast x-ray diffraction studies.

In single-fiber experiments currently being carried out at the Photon Factory (see below), the equatorial reflections, which are the most intense in a whole x-ray diagram, can be recorded in about 0.2 sec. A 30-sec exposure is necessary to record a two-dimensional diffraction pattern on an imaging plate. To investigate the force-generating reaction which takes place at a sub-millisecond time scale, it is necessary to repeat an experiment more than 1000 times. The physiological condition is not ensured in so many repetitions of contraction.

Use of caged-compounds is a new technique developed during the last 10 years to study the kinetics of muscle contraction. Caged compounds can be split by UV-irradiation and yield biologically active chemical substances, such as ATP, Ca^{2+} and inorganic phosphate. The structural changes after the photolysis of caged-compounds are caused by the interaction of these substances with muscle proteins. This reaction typically takes 1-100 msec. The specimen used for this kind of experiment is usually a single skinned muscle fiber into which the caged compounds can quickly diffuse.

A single muscle fiber is the most common specimen in many physiological studies on skeletal muscles and, therefore, many applications are envisaged.

1.2 Experimental Requirements

The diameter of a single frog skeletal muscle fiber is typically 0.1 mm. Since the tension can be controlled better when a fiber is placed horizontally, the vertical size of the x-ray beam must be about 0.1 mm. The horizontal size should be less than a few mm. A monochromatic x-ray beam with a wavelength of 0.10-0.15 nm is suitable. The intensity of the beam should be at least 100-times higher than that currently available at the Photon Factory, which is about 10^{10} photons/sec on the area of a single fiber.

These requirements are met by the x-ray beam from an undulator of the Tristan MR.

1.3 Proposed experiments

The most serious problem of this experiment is the radiation damage on the muscle fiber. Since intact muscle fibers are known to be readily damaged by intense x-ray radiation, a skinned single fiber is a more preferable specimen. For this reason, experiments using caged compounds are proposed.

Currently, experiments using caged ATP are carried out at the Photon Factory. When ATP is liberated by photolysis of caged ATP in a muscle fiber in the absence of Ca^{2+}, it relaxes during the initial few seconds, and then contracts in the next 10-30 msec before it finally relaxes. This contraction in the absence of Ca^{2+} has been extensively studied in physiological experiments, and interpreted as being due to a cooperative behaviour of myosin heads in their binding to actin. At the Photon Factory, the photon flux limits the time resolution of the experiment to 5 msec. With a more intense beam from the Tristan MR, the time resolution is expected to be better than 1 msec. At this time resolution, it will become possible to study the x-ray intensity changes associated with the initial relaxation phase, during which an ATP-induced conformational change of the myosin molecule takes place.

A linear x-ray detector suitable for high time-resolution experiments with a high counting rate has been developed and tested. A combination of an x-ray image intensifier and a CCD video camera will also be adequate as an area detector with a moderate time resolution (1/60 sec).

N.Yagi, Tohoku University

2. HARD X-RAY SCANNING MICROSCOPY WITH KIRKPATRIK-BAEZ OPTICS

Achieving an x-ray microprobe with a sub-micrometer spot size is expected to add a new dimension to various x-ray analysis methods, such as scanning microscopy, diffraction, absorption spectroscopy and fluorescent X-ray analysis. Many types of focusing devices have been proposed and developed. Fresnel zone plates, Bragg Fresnel lenses, multilayer reflectors, bent crystals and total-reflection mirrors are used to produce hard x-ray micro-focus beams. Among them, the grazing-incidence total-reflection mirror system has several advantages. A broad wavelength band can be accepted with high reflectivity (nearly 100%). The short-wavelength limit is determined only by the critical angle for total reflection. The optical elements can be used at a fixed focal length during a wavelength scan. The latter is suitable for

applications to absorption-edge subtraction techniques, x-ray absorption spectroscopy experiments, and x-ray diffraction analysis by means of wavelength scanning.

We have developed a total-reflection focusing optics[1-4] which uses a pair of elliptical-cylinder-shaped mirrors arranged in the Kirkpatrick-Baez (KB) configuration. In a preliminary experiment at a bending magnet beam line (BL-8C) of the PF 2.5GeV storage ring, a focused spot size of about 1 μm is achieved, and a periodic resolution test pattern with 0.6 μm line and space is resolved in scanning microscopy experiments.[2,3] The present probe size (resolution) is considered to be limited by both the characteristics of the x-ray source and by the accuracy of the optical elements. If focusing mirrors with a sufficient accuracy are available and an SR source with sufficient brilliance can be used, a micro-focus x-ray beam with a spot size less than 0.1 μm can be achieved by using an elliptical Kirkpatrick-Baez mirror system.

Here, we discuss the elliptical KB system for generating a hard x-ray microprobe and possible applications to industrial materials.

2.1 Elliptical KB Total-Reflection Optics

A schematic diagram of the elliptical KB optics is shown in Fig.18. An x-ray beam from a light source (S) is monochromatized by a double-crystal monochromator (CM) and focused by a pair of elliptical-cylinder-shaped mirrors (M_1 and M_2). The first mirror (M_1) focuses the beam in the horizontal direction, and the second mirror (M_2) focuses the beam vertically. A demagnified image of the light source is generated at a focal point (F) where the samples are set. Elliptical mirrors made of high-purity copper are fabricated by the fly-cutting technique.

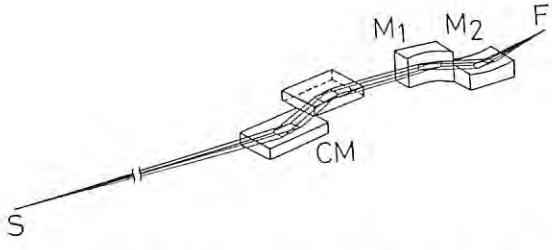

Fig. 18 Schematic diagram of an elliptical Kirkpatrik-Baez microprobe. S, an x-ray source; CM, a double crystal monochromator; M_1 and M_2, elliptical mirrors; and F, the focal point.

In the hard x-ray region, the value of the critical angle for total reflection (θ_c) is usually less than 10mrad. Therefore, the focused spot size is limited mainly by the strong astigmatism and spherical aberration in grazing-incidence optics. Comparing with the Wolter mirror, the single ellipsoid or the elliptical KB has a strong coma and field distortion (or field obliquity). However, their on-axis focusing properties are perfect, *i.e.*, radiation from a point source is focused on a point by the single ellipsoid or by the elliptical KB mirror system. Therefore, diffraction-limit-focusing can be achieved, if light sources with a sufficiently small source size are available.

All of the focusing systems, except for optical guided tubes, form a demagnified image of an x-ray source in order to generate micro-focus beam, and there is a conservation rule on brilliance. Therefore, the maximum flux available at a sample position is calculated simply by using the following equation for an elliptical KB system:

$$I = B\,(2NA)^2\,(\Delta\lambda/\lambda)\,S\,,$$

where I(photons/s) is the photon flux at the sample position, B(photons/s/mm^2/mrad^2/band width) is the brilliance of the light source, NA is the numerical aperture of the objective, $\Delta\lambda/\lambda$ is the wavelength band width determined by a monochromator, and S(mm^2) is the cross-sectional area of the focused beam. A factor $(2NA)$ should be replaced by $\pi(NA)^2$ for a circular aperture. When crystal monochromators are used, $\Delta\lambda/\lambda$ is usually about 10^{-4}. In the hard x-ray region, since the reflectivity of total reflection mirrors is nearly 100%, the reflection-loss is negligible.

Assuming $B=1\times10^{19}$(photons/s/mm^2/mrad^2/0.1%bandwidth), $NA=1\times10^{-3}$, $\Delta\lambda/\lambda=10^{-4}$, and $S=(1\mu m)^2$, we can have

$$I = 4\times10^{12}(\text{photons/s}).$$

This photon flux is much higher than the total photon flux available at the bending magnet beamlines of the PF 2.5GeV storage ring. It is considered that any experiments (spectroscopy, diffraction, fluorescence analyses, etc.) can be performed with a spatial resolution of less than 1 μm.

The design value of a microprobe with the elliptical KB system for the Tristan MR test beamline is shown in Table 5. Other types of

optical devices, a sputter sliced FZP and KB optics with multilayer mirrors, are also being tested.

Table 5. Design values of an x-ray microprobe

Optics:	single stage elliptical Kirkpatrick-Baez
Monochromator:	Si(111) double crystal
Pinhole or collimator:	none
X-ray wavelength range:	from 1.0Å to 2.0Å
Source size (assumed) (rectangular shape):	1mm × 1mm
Distance between the source and the focusing mirror:	100m
Divergence of radiation accepted by mirrors (half angle):	0.9μrad × 0.9μrad
Focal length:	120mm for the 1st mirror (M_1) 60mm for the 2nd mirror (M_2)
Mirror length:	60mm (both the M_1 and M_2)
Average glancing angle:	3mrad
Critical wavelength:	0.9Å (copper mirror)
Nominal demagnification:	1.2×10^{-3} for the M_1 0.6×10^{-3} for the M_2
NA:	0.8×10^{-3} for the M_1 1.8×10^{-3} for the M_2
Calculated spot size (FWHM):	1.2μm × 0.6μm
Diffraction limit:	60nm × 30nm at 1.0Å 120nm × 60nm at 2.0Å
Photon flux at sample point:	about 10^{12} photons/s

($B=10^{19}$photons/s/mm^2/mrad^2/0.1%bandwidth is assumed)

2.2 Applications to Industry

It is considered that the micro-structure in semiconductors (LSI) and magnetic storage will approach 0.1 μm in the future. These sub-micrometer structures are usually observed and inspected by a scanning electron microscope (SEM). However, only surface regions can be detected by an electron probe, and radiation damage is very serious. The hard x-ray microprobe has following advantages:

(1) large penetration depth (detection of underlying layers),
(2) low damage,
(3) imaging of lattice strain fields by diffracted x-ray detection (scanning topography),
(4) sample environment (observations in the air or in the water are possible, and observations under strong electric or magnetic fields are also possible),
(5) trace element mapping because of low background (mono-atomic layers are easily detected by a fluorescent x-ray analysis),
(6) quantitative mapping of elements by absorption-edge subtraction (evaluation of stoichiometry),
(7) spectroscopy (micro-XAFS (x-ray absorption fine structure) for structure analysis of small samples or small area in a sample), and
(8) chemical-state imaging by utilization of absorption-edge chemical shifts and/or differences in XAFS.

By utilizing the above-mentioned advantages, for instance, the relation between the lattice strain (or dislocation) and the deposited patterns (or impurity mapping), can be studied by simultaneous imaging with scanning diffraction topography and trace-element analysis by fluorescent x-ray spectroscopy. The sensitivity for trace elements will be much higher than 10^{12} atoms/cm^2, and submicron resolution will also be achieved by using the Tristan MR test beamline. It is also possible to analyze the chemical states and/or crystal structures of a small region of interest in a mm-scale size by means of a micro-XAFS technique and micro-diffraction methods.

Y. Suzuki, Advanced Research Lab., Hitachi, Ltd.

References

1) Y. Suzuki et al., Jpn. J. Appl. Phys. **28** (1989) L1660.
2) Y. Suzuki and F. Uchida, Jpn. J. Appl. Phys. **30** (1991) 1127.
3) Y. Suzuki and F. Uchida, Rev. Sci. Instr. **63** (1992) 578.
4) F. Uchida et al., J. Jpn. Soc. Prec. Eng. **58** (1992) 546.
5) F. Uchida et al., J. Jpn. Soc. Prec. Eng. **57** (1991) 152.

3. SOLID-PHASE CRYSTALLIZATION WITH X-RAY IRRADIATION

The irradiation of brilliant x-rays from synchrotron radiation drives non-thermal solid-phase crystallization of amorphous silicon (a-Si). This x-ray crystallization technique has several advantages compared with the current photo-excitation method using conventional laser irradiation: (1) Thick films or bulk materials can be treated. (2) Treatments on the nano-scale can be expected using the micro-beam techniques. (3) Selective crystallization of composite materials can be made by tuning the energy of x-rays to the absorption edge of the component material, etc. The non thermal-effect of x-rays has been attributed to an enhancement of vacancy-mediated self-diffusion in a-Si. These vacancies have been

considered to be produced non thermally during the relaxation processes of the multiply-ionized state such, as Si^{+4}, Si^{+5} and Si^{+6}, formed as a result of inner-shell electron excitations. However, the detailed mechanism for this crystallization is not known.

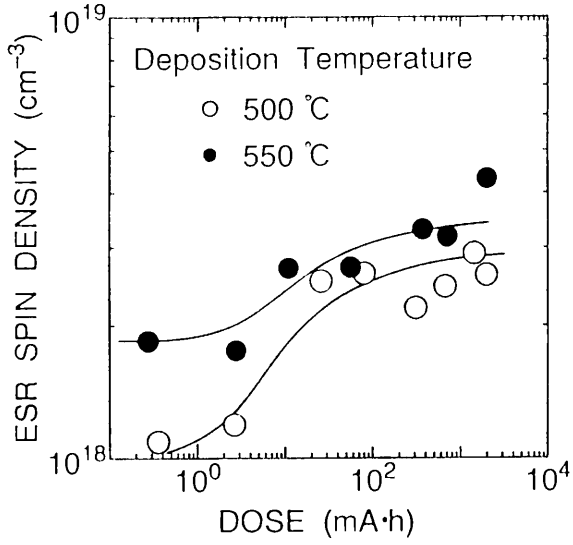

Fig. 19 X-ray dose dependence of the ESR spin density for hydrogenated a-Si.

To clarify the atomic processes of this type of crystallization, the formation of dangling bonds in a-Si by x-ray irradiation has been investigated. For both hydrogenated and ion-implanted a-Si films, the dangling bonds are formed at nearly room temperature. Figure 19 shows the dependence of the x-ray dosage absorbed by a-Si films (hydrogenated) on the dangling-bond density measured by electron-spin resonance at room temperature (BL-15B, white x-rays: 2.5 GeV, ~300 mA). The dangling-bond density tends to saturate to a certain value along with an increase in the dosage. Both the formation rate of the dangling bonds before saturation and the saturation value are much higher than those for conventional light illumination (Kr^+ laser; $h\upsilon$ =1.91 eV) when a comparison is made under the same absorbed power condition. Similar results were obtained for non-hydrogenated (ion-implanted) a-Si.

Because the dangling bonds are formed and stabilized so as to relax the elastic strain in a-Si at low temperatures, a large amount of atoms are required to move by vacancies in the formation process, especially for non-hydrogenated a-Si. Therefore, it is suggested that the formation of the dangling bonds is determined by the balance between the non-thermal formation of vacancies due to inner-shell electron excitations and their thermal annihilations. In fact, a higher formation rate of the dangling bonds has been obtained when the irradiation was performed at lower temperatures, and with higher photon densities (BL-NE3 undulator, and BL-16 multi-pole wiggler). On the other hand, at elevated temperatures, those movements of atoms by vacancies act for crystallization as a process involving the energy relaxation of a-Si.

When such a vacancy-mediated diffusion process is assumed for the solid-phase epitaxy of a-Si, the activation energy for this x-ray crystallization can be expressed in terms of two contributions: non-thermal vacancy formation by a radiation effect and their thermal formation through electron-phonon interactions. Therefore, a large non-thermal effect is expected only when the thermal energy can be removed during irradiation with a high photon density. Detailed investigations by using x-rays over wide range of photon densities are required to confirm these speculations.

F. Sato,
NHK Science and Technical Research Labs.

4. X-RAY PARAMETRIC SCATTERING

X-ray quantum optics is an important subject in coherent x-ray physics, which will be developed fully by an x-ray FEL in the near future. Most of the characteristics of the quantum optics appear in non-linear optical phenomena. Because of the poor coherency of the synchrotron radiation at present, there is little hope to observe an x-ray non-linear phenomenon that includes an induced process. Only a few observations of x-ray non-linear phenomena have been performed, and their nature have not yet been revealed.

X-ray spontaneous parametric scattering[1] is a well-known quantum optical phenomenon; an incident x-ray field couples with a field due to the vacuum fluctuation through the higher order susceptibility of materials, resulting in two-photon scattering. These phenomena in which both scattered photons are in the x-ray region[2] or one photon is in the x-ray region and the other photon is in the VUV region[3] have already been observed. However, the case in which one of the two photons is in the optical region has not yet been observed, because of its small scattering probability; it is an

order of 10^{-9} compared to the one-photon scattering.[4] We can expect the emission of an optical photon to occur as an induced process, provided that an intense laser field exists. In this case, the probability of x-ray parametric scattering can be enormously enhanced. According to the theory of the laser-assisted x-ray absorption under a 10^7 W/cm^2 laser field,[5] the probability of x-ray parametric scattering amounts to 10^{-2} of the one-photon scattering. An investigation of these phenomena would lead to a better understanding of the characteristics common to x-ray non-linear phenomena.

Adopting a GGG single crystal as a sample, we presume such a resonance scattering process in which a 2p electron in Gd is excited into an empty 5d band; an intra-band transition then takes place by the stimulated emission of two optical photons; finally, an emission of x-ray photon takes place. This process occurs effectively when the following so-called phase matching conditions are satisfied:

$$\omega_{x'} = \omega_x - 2\omega_l \qquad (1)$$

and

$$k_{x'} = k_x - 2k_l + G, \qquad (2)$$

where, x and x' are the incident and scattered x-rays, respectively, the suffix l means the optical photon and G is a reciprocal lattice vector. From eqs (1) and (2), we can expect a satellite to appear at the tail of the higher angle side of the Bragg scattering.

A preliminary experiment was performed using the x-ray undulator U#NE3 installed in the AR, which is operated in a single-bunch mode. Incident x-rays have been monochromated by a Si(111) double-crystal monochromator within a resolution of 2 eV to an energy higher by 4.66 eV (=double of the energy of the optical photons) than that of the Gd L2 absorption maximum. The second higher harmonic of a pulsed Nd-YAG laser 50 Hz in repetition and 2 nsec in width has been utilized as the laser beam. Under the condition described above, a satellite has been expected to appear at a 268" higher angle side of the 444 Bragg reflection. Simultaneous irradiation of the x-ray beam and the laser beam has been performed while referring to the ring control timing signal. The intensity profile has been measured with respect to the rotation of the crystal. Two kinds of profiles have been measured simultaneously: one was gated by the laser Q-switch trigger; the other was ungated.

The gated profile normalized by the ungated exhibits an intensity enhancement at the region expected by the phase-matching conditions. The profile of the satellite enhancement, consisting of two peaks, agrees well with that of the 444 Bragg reflection consisting of two peaks due to the domain structure (accidentally). The enhancement amounts to about 1.3% of the background intensity in this region. This value corresponds to 1×10^{-5} of the intensity of the 444 Bragg reflection. The scattering probability of the relevant phenomenon amounts to 10^{-3} of that of the normal one-photon scattering, which is nearly the same order of magnitude of the estimated value, if we consider the effective number of atoms contributing to the relevant structure factor. These results strongly suggest that the observed intensity enhancement is due to x-ray parametric scattering induced by a strong laser field.

The advanced nature of the x-ray in Tristan Super Light Facility is characterized by its ultra-small beam size, super-high brilliance, very narrow pulse width and long pulse interval. As a result, a distinguished improvement in the spatial coherence is realized in TSLF radiation. Thus, the phase-matching condition is satisfied over a wide region of the crystal. The radiation damage is diminished by using a laser pulse as short as that of the TSLF x-ray pulse. In this way we can focus the laser beam upon the sample with less radiation damage. In this case, the scattering probability increases bilinearly to the laser beam brilliance. These characteristics of the x-ray parametric scattering, stimulated by an intense laser field, enhances the scattered intensity. Investigations of these characteristics reveal in the x-ray region the meaning of the concept peculiar to such nonlinear phenomena as the phase-matching condition, non-linear susceptibility and the temperature inversion in the induced process. These concepts are the key factors for opening the field of x-ray quantum optics when the x-ray FEL is realized in the near future.

K. Namikawa, Tokyo Gakugei University

References

1) I. Freund and B. F. Levine, Phys. Rev. Lett. 23 (1969) 854.
2) P. Eisenberger and S. L. McCall, Phys. Rev. Lett. 26 (1971) 684.
3) H. Danino and I. Freund, Phys. Rev. Lett. 46 (1981) 1127.
4) I. Freund, Phys. Rev. A7 (1973) 1849.

5) I. Freund, Opt. Commun., 8 (1973) 401.

5. NUCLEAR RESONANT SCATTERING

Experiments concerning nuclear resonant scattering have been carried out using an x-ray undulator at the Tristan Accumulation Ring.[1] The time evolution of nuclear Bragg scattering of $^{57}Fe_2O_3$(777) was observed over a wide time range. The hyperfine parameters were determined from the quantum beats of its time spectrum. Nuclear forward scattering of ^{57}Fe-enriched foils was observed under various conditions. For instance, two foils were set in a beam path, one of which was Doppler-shifted; the time spectrum showed intensity modulation due to a slight change in the nuclear transition energy. Further, the interferometric experiments of the nuclear forward scattering were made by means of an x-ray interferometer.

On the basis of the results mentioned above, we are planning to carry out the experiments on nuclear resonant scattering to be executed at the Tristan MR. Synchrotron radiation from an undulator which will be installed in the MR has the properties of high brilliance and high coherence. It has a long pulse interval. In addition, high-energy photons are available from a high harmonic. In this project the themes were selected aiming at making best use of such prominent properties, as follows.

5.1 Photon correlations in the x-ray region

A nuclear resonant scattered beam is highly monochromatic, and is thus highly temporally coherent. Since the source size in the MR is very small, the spatial coherence of the beam is high. By using highly coherent x-rays the measurements of photon correlations of the Hanbury-Brown-and-Twiss type[2] may be realizable in the x-ray region.[3,4] The nuclear Bragg-scattered beam from a TmIG crystal will be suitable for this experiment, because the resonance energy of ^{161}Tm is low (8.42keV). The beam splits into two using diffraction by a crystal. Two fast detectors are arranged so as to detect photons coming from the crystal along two directions. The distribution of the time difference of photons arriving at two detectors is measured. It is expected to observe the bunching effect of photons in the x-ray region. This experiment is also useful for the characterization of the SR source.

5.2 X-ray interference in case of different optical path lengths

Since the nuclear Bragg-scattered beam has an extremely long coherence length, an x-ray interferometer with different optical path lengths will be realized by modifying the Bonse-Hart type. With the interferometric technique, the temporal and spatial coherence of the beam can be characterized. The phase information of a diffracted wave from a crystal may be extracted from x-ray phase optics.

5.3 Production of an extremely monochromatic x-ray beam

By using long interval (10ms) of the SR pulse in the MR the time spectrum of the nuclear resonant scattering from ^{181}Ta, which has an exceptionally long life time ($t_{1/2}$=6.8ms), can be observed.

The nuclear Bragg scattering from a single crystal enriched in ^{181}Ta provides an extremely monochromatic x-ray beam (E = 6.23keV, $\Gamma = 6.7 \times 10^{-10}$eV). This highly collimated Mössbauer beam may be useful to carry out gravitational red-shift experiments with a long base line.

5.4 Coherent excitation of the cascade nuclear x-ray transition

The coherent deexcitation of nuclei via a cascade of nuclear x-ray transitions exhibits unusual angular characteristics of coherent x-ray emission.[5] To study these phenomena, SR photons of high energy are required. These photons can be obtained as a high harmonic of SR from an undulator at the MR. Single crystals containing, for example, ^{161}Dy (excitation energy: 74.6keV) or ^{73}Ge (68.8keV), are candidates for this experiment. An investigation of such cascades may be interesting for studying the processes of coherent pumping of low-lying nuclear levels.

S.Kikuta, University of Tokyo

References
1) S.Kikuta et al., Hyp.Int.,71(1992)1491.
2) R.Hanbury-Brown and R.Q.Twiss, Nature 177(1956)27.
3) E.Ikonen, Phys.Rev.Lett., 68(1992)2759.
4) E.Gluskin et al., Nucl.Instrum. and Meth., A319(1992)213.
5) V.A.Belyakov et al., Nucl.Instrum and. Meth., A261(1987)1322.

6. FAST MONOCHROMATIC X-RAY CRYSTALLOGRAPHY FOR TIME-RESOLVED KINETIC STUDIES OF PROTEIN STRUCTURES

This proposal aims at obtaining the time-resolved high-quality electron density from protein crystals in enzymatic transition states for a structural elucidation of dynamic interactions among proteins, substrates and water molecules. Utilizing monochromatic and highly brilliant x-rays, fast monochromatic data-collection techniques for time-resolved studies of protein crystals will be developed for this purpose. The techniques will suffice problems in Laue-diffraction techniques, which have been extensively exploited in recent years. The proteins to be analyzed are hydrolytic enzymes which cleave peptides and nucleic acids by adding nucleophilic water molecules. In order to identify intermediates of enzymatic reactions at a time-resolution of several milliseconds, the exact locations of protein atoms, substrate atoms, and water molecules must be analyzed based on high-quality electron density maps.

The Laue-diffraction technique, which utilizes the broad x-ray spectra of synchrotron radiation, enables crystallographers at the Photon Factory to presently collect diffraction data in the millisecond range. Although progress in the Laue methodology has been achieved, many problems associated with it have been realized. Compared to the conventional technique combined with monochromatic x-rays and rotation methods, although a few exposures taken at different orientations of the crystal yield Laue data sets, both the accuracy and completeness of the Laue data sets are low. Furthermore, the Laue techniques require well-ordered crystals, and the Laue data sets lack low-resolution reflections. These setbacks are inherent in this techniques, and result in poor-quality electron density maps, which often hinder any quantitative interpretation of subtle structural changes.

In our recent time-resolved study of the enzyme bovine trypsin, which hydrolyzes peptide and ester bonds, very high-quality of electron-density maps were obtained using monochromatic x-rays and rotation methods. The electron-density maps clearly revealed the acyl-intermediate trypsin, generated during the cleavage of ester substrates, as well as the nucleophilic water molecule which has long been sought, even with the Laue-diffraction experiment. Since a rotating-anode x-ray generator was applied in this study, the attained time-resolution was 6 hours. Based on our considerations, the time-resolution attainable through this proposal will be in the millisecond range, with highly brilliant synchrotron x-rays. Both acylation generating the acyl-intermediate and subsequent deacylation in trypsin hydrolysis proceed rapidly at a physiological pH. Therefore, fast monochromatic techniques must be applied for a complete understanding of the catalytic cycle of the hydrolysis.

The proposal involves two-step projects; the development of a fast monochromatic diffraction data-collection system, and then time-resolved diffraction experiments to study any structural changes during enzyme catalysis. The data-collection system required is simple: it will consist of a fast mechanical shutter with a time-resolution of few milliseconds, a fast-rotating single-axis goniometer which rotates a crystalline specimen at a speed of up to 600 rpm, an imaging-plate x-ray detector with 2000×2000 pixels, and a timing electronic control system which synchronizes the operations of these components to the catalytic steps in the specimen.

Monochromatic techniques will be developed during the course of experiments; by the use of shorter wavelengths and beam parallelism of synchrotron x-rays of about 15 keV, typical protein crystals such as trypsin could be rotated by about 10 degrees during a single exposure on the x-ray detector. By a data-editing technique that we recently invented, full and redundant time-resolved monochromatic data sets could be obtained with a minimized number of exposures. When finer time-resolutions are required, monochromatic diffraction has another advantage over Laue diffraction: from a single monochromatic exposure, time information can be assigned to each reflection recorded at a definite orientation angle. This advantage of monochromatic diffraction could exploit new techniques for time-resolved studies of crystal structures.

Y. Satow, University of Tokyo

ISSN 0912-1803

PHOTON FACTORY ACTIVITY REPORT

1993

#11

PHOTON FACTORY ACTIVITY REPORT 1993

#11